The Hidden Hazard Of Melting Ground Ice In Northern Iceland

Thesis

The hidden hazard of melting ground ice in northern Iceland

Costanza Morino

A thesis submitted to the Open University

in the subject of Environment, Earth and Ecosystem Sciences

for the degree of Doctor of Philosophy

June 2018

Environment, Earth and Ecosystem Sciences

Open University

L'importante non é sapere, ma cercare.

Umberto Veronesi

Abstract

This thesis explores the morphology, dynamics and causes of landslides and debris flows in mountainous regions of northern Iceland. The primary objectives are to define the initiation and evolution of Icelandic landslides and debris flows, and to understand the link between ground-ice thaw and rapid mass movements. Slopes are predicted to react more intensely to global warming, so improving our knowledge of rapid mass movements in cold environments, which are even more sensitive to climate change, is crucial, as they could pose at risk local population in Iceland and other mountainous periglacial areas.

I first perform a detailed study of debris flows in north-western Iceland, distinguishing through quantitative geomorphological methods the different mechanisms of debris-flow initiation and the associated geomorphic features. The approach of this study is easily applicable to similar settings, and its results could help in anticipating new potentially destructive events. Secondly, I describe and quantify the morphometric characteristics of two landslides in northern Iceland, whose source materials comprised ground ice-cemented deposits. This study reveals different dynamic landslide processes and the crucial role of thawing ground ice in landslide emplacement. I then analyse meteorological and seismic data near these two landslides. I define and distinguish precipitation, seismic activity and permafrost degradation as the preparatory and triggering factors for the failures. Finally, through a geomorphic approach I analyse molards, conical mounds of debris that I found in both landslides deposits. I show conclusive evidence that molards form from thawing of blocks of ice-rich sediments that degrade into cones of debris. I demonstrate that molards are the 'fingerprint" of permafrost degradation, and their different morphology and

distribution can reveal different types of landslide processes in periglacial terrains.

This thesis widens our knowledge of the conditions and processes controlling rapid mass movements in cold environments, which is crucial in the perspective of hazard assessment, and opens up new avenues for the study of potentially hazardous geomorphic responses of cold landscapes to changing climate conditions.

Acknowledgements

Usually, when you start a PhD, you do not know your supervisors, particularly if you come from another country. If you are lucky, you meet them before your interview (on Skype, wearing a smart blazer while no one can see your pyjama pants), when you are trying to beat your nerves and instead you are quivering like you have been sent to the gallows. So I did not know Susan Conway before I started my PhD. But she is the supervisor that I would have chosen if I had the choice. I want to thank Susan for allowing me to explore this project the way I wanted, providing me with guidance and support, particularly at the most difficult time, for all the things that she taught me (let's not forget: evidence~~s~~! explain TO me!), and for showing me an inspiring way of thinking and doing science.

I would like to thank my supervisor Matt Balme, who has always been there to give me advice and warm encouragement when most needed, and whose door was always open when I needed to talk (and let off steam).

I would like to express my gratitude to all my external supervisors. Thanks to Þorsteinn Sæmundsson for the invaluable assistance and suggestions, and for having tried to teach me Icelandic pronunciation and failed miserably. Thanks to Colm Jordan and John Hillier for the great discussions, the constructive comments, and the help that they always gave me. Thanks to Tom Argles for the great contribution, and for being my idol in writing.

I am deeply grateful to my collaborator Jón Kristinn Helgason, for providing essential data, and for the invaluable help and the illuminating discussions. My sincere gratitude goes also to Frances Butcher for the constructive comments and the insights on Mars.

I owe my deepest gratitude to Susan, Francesco, Silvia and Sydney for having been the best, most tolerant and patient field assistants one can possibly imagine.

I want to thank all the new friends, housemates and colleagues that I have found in these four years. Thanks to Ilaria, Manu, Matt S-C., Laura, Jon, Katie, Matt K., Wes, Sam and Stacy for having made Milton Keynes a surprisingly wonderful place where to live: you are great. A special thank you goes to Matt S-C. for being the best officemate ever, for having fed the Ebola paranoia to make me laugh, and for the uncountable attempts to kill me with a sneeze.

I am deeply grateful to my friends in Italy and all around Europe. Thanks for bringing me home with a phone call and for making this PhD a lighter weight to carry.

My deepest thanks go to my family. Thanks to Mamma and Papà, because they have always been there for me not to get lost. Thanks to Edoardo and Maria, for the phone calls at the airport when you stopped me from coming back and for making me laugh.

And finally, thanks to Francesco. There are too many things I have to thank you for. Thanks for believing in me more than I do, for choosing this difficult path together, for showing me the view, and for not giving up.

This work has been funded by a postgraduate studentship grant (NE/L002493/1) from the Central England Natural Environment Research Council Training Alliance (CENTA). This project forms part of and is funded by a British Geological Survey BUFI CASE Studentship (GA/14S/024, Ref: 284). I thank the Natural Environment Research Council Airborne Research Facility Data Analysis Node (NERC-ARF-DAN) and EUropean Facility for Airborne Research (EUFAR) for obtaining the air photography and LiDAR data on which this thesis relies. Thanks go to NERC Geophysical Equipment Facility (GEF) for the Loans 1048 and 1064 through which differential GPS surveys were possible. I thank Airbus Defence and Space for the Pléiades images.

Table of Contents

List of Figures

List of Tables

Chapter 1. Introduction

1.1 Focusses and aims

The objective of this work is to study landslides and debris flows occurring in mountain regions in northern Iceland. The term landslide is widely used to indicate different types of movement of a mass of rock, debris, or earth down a slope (Varnes, 1978). Debris flows are a particular type of landslide and are commonly defined as “poorly sorted sediment agitated and saturated with water, surge down slopes in response to gravitational attraction” (Iverson, 1997).

Rapid mass movements such as debris flows (Figure 1.1) pose a potential risk to the local population in Iceland (Decaulne, 2005). The first focus of this thesis is to explore the geomorphological processes that characterise the release of debris flows, their impact on the Icelandic landscape and the potential risk that they pose to the local communities.

Figure 1.1. Oblique aerial view of the slope above the town of Ísafjörður (north-western Iceland) affected by debris flows.

A second focus of this thesis is to understand the possible connections between the thawing of shallow ground ice in mountainous areas of Iceland with discontinuous permafrost and the occurrence of landslides. Ground ice was found in the deposits of landslides in the northern regions of the country (Figure 1.2) immediately after they had been deposited. This can indicate that permafrost is present in these areas, and it is degrading. Although models of permafrost extent showed it was present in the central-northern regions of the island (Etzelmüller et al., 2007), little information exists on its state and on the possible consequences on the Icelandic landscape due to its degradation. Therefore, this thesis aims to understand the geomorphological impact of landslides in permafrost terrains, their origin and evolution, with the goal of increasing our knowledge on this type of potentially hazardous phenomena in general.

I developed the thesis with the intent of:

i) defining the release processes of debris flows in north-western Iceland and their geomorphological and hazardous impact (Chapter 3);

ii) testing whether the morphological signature of the landslides in northern Iceland where ground ice was found can be used to prove the presence of permafrost and its degrading state, and to reconstruct the dynamics of the landslides and to evaluate their potential hazard (Chapter 4 and 6);

iii) identifying the exogenous and endogenous factors that determined the release of these landslide, including permafrost degradation (Chapter 5).

Figure 1.2. Oblique view of the Árnesfjall landslide (north-western Iceland), where ground ice was found in the failure deposits after its occurrence.

1.2 Methodology and technical approach

Geomorphology is the science concerned with the study of landforms and the processes that create and modify them. I have analysed debris flows and landslides that occurred in recent years in northern regions of Iceland using a geomorphological approach. This has allowed me to analyse the geomorphic characteristics of debris flows and landslides in Iceland, and to reconstruct their origin and evolution.

In order to accomplish the objectives of this thesis, I used fieldwork and remote sensing. The fieldwork involved field observations and measurements, and used high accuracy differential Global Positioning System (GPS) and (where possible) ground penetrating RADAR. Remote sensing comprised two types of data. The first was acquired in the field through the Structure from Motion photogrammetric

technique, which allowed the production of high resolution topographic data and orthoimages. The second type of data was airborne laser altimetry and aerial photography. These approaches were supported by complementary analysis, such as weather data analysis. Both fieldwork and remotely-sensed data allowed the accurate and detailed quantification of the morphological signatures left by debris-flows and landslides. This allowed me to measure the magnitude of the mass-movement phenomena, the characterisation of their features and structures to trace back to their emplacement processes and evolution, and, finally, to the understanding of their causes, dynamics and their geomorphological and hazardous significance.

1.3 Published or submitted work

Parts of this thesis have been published or are in review in international peer-reviewed journals (Table 1.1). Chapter 3 is in review in the international journal *Earth Surface Processes and Landforms*. Chapter 5 includes parts of a manuscript which I am second author of and that has been published on the international journal *Science of the Total Environment*. Chapter 6 is in review on the international journal *Earth and Planetary Science Letters*. These publications are detailed in Table 1.1, which also shows the contribution of the co-authors to each of the papers. The co-authors reported in Table 1.1 are in addition to my supervisors Susan J. Conway, Matthew R. Balme, Þorsteinn Sæmundsson, Colm Jordan, John Hillier and Tom Argles.

Except for Chapter 5, the content of the manuscripts remains essentially unchanged from the version in review. Some minor changes have been made to avoid repetition and to maintain consistency throughout the thesis. The first

person plural in the manuscripts has been changed to the first person singular where appropriate. Numbering of figures and tables has also been changed. In Chapter 5, parts of the manuscript have been deleted to avoid redundancy of the content of other chapters. Finally, parts of Chapter 5 were expanded for completeness and coherency with the rest of the thesis. A summary of the changes made to each manuscript is given at the start of each chapter.

Table 1.1 - Summary of published work contained in the thesis and contribution of co-authors.

Chapter	Manuscript title	Co-authors	Contribution (%)		Journal	Status
Chapter 3 - Debris-flow release processes revealed through the analysis of multi-temporal LiDAR datasets in north-western Iceland	Debris-flow release processes revealed through the analysis of multi-temporal LiDAR datasets in north-western Iceland	—	—	C.M.=100%	Earth Surface Processes and Landforms	Reviewed and awaiting minor corrections
Chapter 5 - The preparatory and triggering factors of the Móafellshyrna and Árnesfjall landslides in northern Iceland	The triggering factors of the Móafellshyrna debris slide in northern Iceland: Intense precipitation, earthquake activity and thawing of mountain permafrost	Jón Kristinn Helgason, Halldór G. Pétursson	J.K.H. provided the data, contributed to their manipulation and interpretation. H.G.P. contributed to finalise the manuscript.	C.M.=85%, J.K.H. =15%, H.G.P.=<1%	Science of the Total Environment, 621, 1163-1175 (2018)	Published
Chapter 6 - Molards as a marker of permafrost degradation and landslide processes	Molards as a marker of permafrost degradation and landslide processes	Jón Kristinn Helgason, Frances E.G. Butcher	J.K.H. contributed to data collection and manuscript preparation. F.E.G.B. provided the data for Mars and contributed to manuscript preparation	C.M.=90%, J.K.H. =5%, F.E.G.B.=5%	Earth and Planetary Science Letters	Moderate corrections after review

1.4 Thesis structure

Chapter 2 presents a review of the state of the art on rapid mass movements in cold environments, with a focus on these processes in Iceland. It provides also an account of the up-to-date knowledge on the state of permafrost in the island, and a consideration of the hazard presented by rapid mass movements in cold environments. Chapter 3 presents a quantitative geomorphological study of debris flows in north-western Iceland based on the comparison between two

datasets of high resolution (1 m/pixel) airborne laser altimeter data. This study allowed me to identify the release mechanisms of debris flows in the area, and to analyse the implications for their potential mobility and hazard, resulted in a paper submitted to *Earth Surface Processes and Landforms* (and is in review at the time of writing of this thesis).

Chapter 4 presents the measured geomorphological characteristics of two recent landslides in northern Iceland, whose deposits were found to be partially cemented by ground ice. The analysis of field evidence and high resolution remote sensing data from Structure from Motion and airborne laser altimetry data reveals how the presence of ground ice affected the dynamics of these landslides.

Chapter 5 examines the same two landslides as Chapter 4, but details the analysis of the preparatory and triggering factors of these mass movements, leading to the identification of precipitation, seismic activity and permafrost degradation as the main factors that brought to the release of the landslides. More than half of this chapter was published in *Science of the Total Environment*.

Chapter 6 describes the morphometric characteristics of peculiar landforms that were found in both the landslides featured in Chapter 4 and Chapter 5: molards. Molards are cones of debris that can be found in landslide deposits. Through field observations and the quantitative analysis of Structure from Motion and airborne laser altimetry data, the chapter shows that molards can be used in the field and through remote sensing as a marker of permafrost degradation and landslide processes in cold environments. This chapter resulted in a paper under review in *Earth and Planetary Science Letters*.

The thesis concludes with Chapter 7: a synthesis of the work in the thesis, including final conclusions and potential avenues of future research. The

appendices include supporting materials including data obtained by auxiliary techniques and raw data.

Chapter 2. Rapid mass movements in cold environments

2.1 Introduction

In 2012, a landslide occurred on the north-western slope of the Móafellshyrna Mountain. Blocks of ice-rich sediments were found on the landslide deposits immediately after its occurrence, a phenomenon that was never officially reported in Iceland before the occurrence of this event. Immediate questions rose after this event: Is the Móafellshyrna failure an evidence of degrading permafrost in Iceland? Is the cementing ground ice seasonal frost or perennial ice? Is this landslide the harbinger of similar future failures threatening the population and infrastructures around the island? The Móafellshyrna event was the trigger for the research presented in this thesis, which focusses on rapid mass movements in Iceland. In particular, as stated in Chapter 1, the two main focusses of the thesis are the study of ground ice-thaw-induced landslides and the analysis of the release and geomorphic and hazardous impacts of debris flows in northern Iceland. Therefore in this chapter, a review of the current state of knowledge on rapid mass movements in Iceland (Section 2.2) then in cold environments generally (Section 2.3) is performed, with a particular focus on periglacial ones (with "periglacial" defined as "the conditions, processes and landforms associated with cold, non-glacial environments, Permafrost Subcommittee, 1988). The chapter then continues with, a summary on the current state of art regarding the knowledge of permafrost in Iceland (Section 2.4), and ends with some considerations on the hazard of rapid mass movements in cold environments (Section 2.5).

Mass movement is a term that refers to the processes that imply a downslope movement of rock, debris and soil under the influence of gravity (Crozier, 1989; Hutchinson, 1968). Mass wasting, mass movement, slope movement or slope failure are commonly used as synonyms. Apart from processes of subsidence and creep that can lack discrete failure boundaries, for discrete slope movements Crozier (1989) uses the general term landslides. Mass movements can be divided into slow and rapid mass movements (e.g., French, 2007). Slow mass movements comprise, among the many, gravity-induced processes evolving over very long periods of time such as deep-seated gravitational slope deformations (e.g., Dramis and Sorriso-Valvo, 1995). They also include phenomena like solifluction, a process that originates from the action of freeze–thaw cycles that induce downslope displacement in general at a rate of at most 1 m/year of soils in cold environments, where vegetation is lacking or sparse (e.g., Andersson, 1906; Ballantyne and Harris, 1994; Washburn, 1979). This thesis focusses on rapid mass movements, a term that refers to geomorphological processes that involve a transfer of slope material downwards and that can be extremely fast moving (up to the scale of 5 m/s; Hungr, 1981) and that may affect different parts of a slope.

Various types of processes involved in rapid mass movements may be distinguished, according to the type of material, the type of movement, the volume of displaced material, and the extent of the material's spreading area (Cruden and Varnes, 1996; Hungr et al., 2014; Varnes, 1978). Varnes (1978) developed a classification system for slope movements, based on five possible types of movement (fall, topple, slide, spread and flow) and on the type of material (rock, debris and earth). Varnes' (1978) classification has been revised by several authors (Cruden and Varnes, 1996; Hungr et al., 2001; Hutchinson, 1988; Julian

and Anthony, 1994), but remains probably the most compelling and widely used classification system for mass movements. In Varnes' (1978) classification, slow processes such as subsidence, creeping and solifluction are not accounted for, and are considered by other authors (Sidle and Ochiai, 2006). In this chapter, and for the whole thesis, I adopt the updated Varnes landslide classification from Hungr et al. (2014) (see Table 2.1) , where the most significant changes from the initial Varnes' version are: i) the use of textural classes to replace the term "earth", which has no standard definition in either geological or geotechnical material description schemes; ii) the reintroduction of "ice" as type of material, because many destructive mass movements on mountain slopes contain varying proportions of glacial ice (note that Hungr et al. (2014) do not introduce "snow" as a type of material to maintain separation from the field of snow science); iii) the introduction of slow mass movements under the movement type of "slope deformation".

Table 2.1 - Summary of the Varnes (1978) classification system updated following Hungr *et al.* (2014).

Movement type	Definition	Type of material	
		Rock	Soil
Fall	The detachment of rock and soil from a cliff or steep slope, where the detachment takes place with little or no shear displacement along the failure surface	Rock/ice fall*	Boulder/debris/silt fall*
Topple	The forward rotation of a mass of rock or soil out of a slope around a point or axis below the center of gravity of the displaced mass, usually at or near the base of the slope	Rock topple*	Gravel/sand/silt topple*
Rotational slide	The relatively coherent downslope movement of a mass of rock or soil along a circular concave upward shear surface	Rock rotational slide*	Gravel/sand/debris rotational slide*
			Clay/silt rotational slide
Translational slide	The relatively coherent downslope movement of a mass of rock or soil along a planar shear surface	Rock translational slide*	Gravel/sand/debris translational slide*
			Clay/silt translational slide
Spread	The near-horizontal spatial dilation or extension of a cohesive rock or soil mass generated by shear or tensile fractures and coupled with subsidence into underlying material	Rock slope spread	Sand/silt liquefaction spread*
			Sensitive clay spread*
Flow	A spatially continuous turbulent movement of disaggregated rock or soil over a rigid surface	Rock/ice avalanche*	Sand/silt/debris dry flow
			Sand/silt/debris flowslide*
			Sensitive clay flowslide*
			Debris flow*
			Mud flow*
			Debris flood
			Debris avalanche *
			Earth flow
			Peat flow
Slope deformation	Large-scale gravitational deformation characterised by a slow or unmeasurable movement rate of steep, high mountain slopes lacking a fully defined shear surface	Mountain slope deformation	Soil slope deformation
		Rock slope deformation	Soil creep
			Solifluction
Complex	The combination in space and/or time of one or more of the principal movements described above	—	—

*Movement types that usually reach extremely rapid velocities as defined by Cruden and Varnes (1996). The other landslide types are most often extremely slow to very rapid.

2.2 Rapid Mass Movements in Iceland

2.2.1 Paraglacial mass movements in Iceland

Landslides are a process that occurs in many mountainous landscapes over an extensive range of temporal and spatial scales. Their spatial distribution, frequency, and magnitude control the effects that they have on the landscape

(Densmore and Hovius, 2000; Palmquist and Bible, 1980). Mass movements are one the main sources of erosion, affecting the sediment budget and the morphological evolution of hillslopes (e.g. Burbank et al., 1996 Beylich et al., 2004; Beylich and Kneisel, 2009; Cendrero and Dramis, 1996; Hovius, et al., 1997; Schmidt and Montgomery, 1995). Paraglacial rapid mass movements (with paraglacial referring to non-glacial earth-surface processes, sediment accumulations, landforms, land systems and landscapes that are directly conditioned by glaciation and deglaciation; (Ballantyne, 2002)) have shaped the landscape of Iceland. Falls, debris flows, and debris slides have been recognised among the main phenomena that have contributed to mass transfers in eastern Iceland in the Holocene (Beylich and Kneisel, 2009). The retreat of rock walls and the continued accumulation of talus cones at their foot due to slope processes caused the gradual erosion of hillslopes and valley widening (Beylich, 2000).

Ancient slope failures in Iceland (see Figure 2.1 for an example) have been recently reported and analysed by different authors (Coquin et al., 2015, 2016; Decaulne et al., 2016; Feuillet et al., 2014; Jónsson et al., 2004; Jónsson, 1957; Líndal, 1936; Mercier et al., 2017; Peras et al., 2016; Thorarinsson et al., 1959; Þorarinsson, 1956). Ancient mass movements are widespread, particularly in the Tertiary basalt formation of the northern, eastern and north-western regions of Iceland (Jónsson, 1957; Sæmundsson, 1973; Whalley et al., 1983; see Chapter 3 and Chapter 4 for the details of the Tertiary basalt formation). The abundance of slope failures in these areas of Iceland has been linked to post-glacial rebound (Cossart et al., 2014) and dated to the paraglacial phase in the early Holocene (Decaulne et al., 2016; Mercier et al., 2017). In the northern central parts of Iceland, the majority of the slope failures occurred before 12ka (Mercier et al., 2012, 2017), thus during the early stage of the Late Weichselian deglaciation,

when the uplift rate was at a maximum (Coquin et al., 2015; Cossart et al., 2014; Jónsson, 1957; Mercier et al., 2017). It has also been recognised that in these areas of Iceland, some paraglacial landslides were probably initiated from propagation of deep-seated gravitational slope deformations (also known as mountain slope deformations, see Table 2.1) related to post-glacial rock-stress release (Coquin et al., 2016). Coquin et al. (2016) also report the favourable dip of the lava layers of the Tertiary basalt formation and interbeds of poorly cohesive palagonite — which they infer act as weak horizons for the landslides to exploit — predisposing the release of landslides generated by paraglacial topographic readjustments. Other predisposing factors for failure such as slope inclination, valley depth and curvature could have influenced these ancient mass movements as well (Feuillet et al., 2014). In the Westfjords of Iceland, slope failures are preferentially distributed on hillslopes close to the coasts, where steep slope gradients, availability of cohesion-less material and excess moisture to saturate and mobilise the material favour gravitational mass movements (Decaulne, 2001, 2007; Decaulne and Sæmundsson, 2003).

Nearly two hundred slope failures have been identified in area this area, which deglaciated during the Last Glacial Maximum to Younger Dryas transition, meaning that potentially their origin could be related to the deglaciation patterns of northern central regions (Peras et al., 2016).

Against this backdrop of ancient landslides, Iceland has experienced many landslides within human timescales. These are different in scale, causes and morphology, but that have equally shaped the landscape of the country, and are the object of the following Section 2.2.2.

Figure 2.1. Lateral view of one of the paraglacial slope failures in northern central Iceland (the dashed line in the bottom panel marks the perimeter of the slope failure). The length from the headscarp to the toe is roughly 1600 m.

2.2.2 Recent mass movements in Iceland

Landslides can cause environmental damage (e.g., Blaschke et al., 2000) and be a major risk to population, infrastructure and land use (e.g., Geertsema et al., 2009; Kjekstad and Highland, 2009; Petley, 2012; Schuster, 1996; Selby, 1993). Rapid mass movements, whether involving debris, snow and/or water, are a direct threat to many towns in Iceland, where, in the last century, they have caused the death of nearly 200 people (Jóhannesson and Arnalds, 1992) and considerable damage to the road system and buildings, both in rural and urban areas (Pétursson et al., 2010). It should also be taken into account that some proportion of disastrous events may not have been recorded during the last

century, as in remote areas of Iceland urban sites are sometimes not older than 40 years (Decaulne, 2004). Coastal villages and towns of north-western, northern and eastern Iceland are subject to recurrent snow-avalanche and debris flow activity, whose catastrophic effects are increasing with time (Decaulne, 2004). The increasing awareness of this hazard has been attributed to the snow avalanches that killed 35 people in three successive winters between 1994 and 1995 in the Westfjords (Decaulne, 2005). Most of the fatalities in the last decades have been caused by snow avalanches, but the hazard of other rapid mass movements should not be neglected (Arnalds et al., 2001, 2002, 2004; Jóhannesson and Arnalds, 1992; Pétursson, 1999)

Debris flows, rock falls, rock and debris slides and avalanches are widespread, particularly in the weathered Tertiary basaltic area (Sæmundsson and Pétursson, 2000). This bedrock (see Chapter 3 and 4 for detailed description) is easily erodible by phenomena like frost shattering, creating a constant supply of new debris on the mountain slopes, which recent glaciations have steepened, forming the perfect conditions for the occurrence of rapid mass movements (Pétursson et al., 2010).

Four main triggering factors promote rapid mass movements in Iceland: heavy precipitation, snowmelt, permafrost thaw and earthquakes (Decaulne et al., 2005; Decaulne and Sæmundsson, 2007; Sæmundsson et al., 2003, 2014a, 2018). The first three of these factors depend on the climate of Iceland, where the Mean Annual Air Temperature (MAAT) for the period 1971–2000 was 4–5°C in the south, 3–4°C in the east and west parts, and 2–3°C in northern coastal parts of the country (Tveito et al., 2000). The whole country experienced a warming of between ~0.7–1.6 °C during 1871–2002 (Hanna et al., 2004). Easterly and southerly prevailing winds bring the majority of the precipitation (Einarsson, 1984). Consequently,

mean annual precipitation increases from about 400 mm in the central and northern parts of the country to more than 5000 mm in the southeast (Figure 2.2; Crochet et al., 2007).

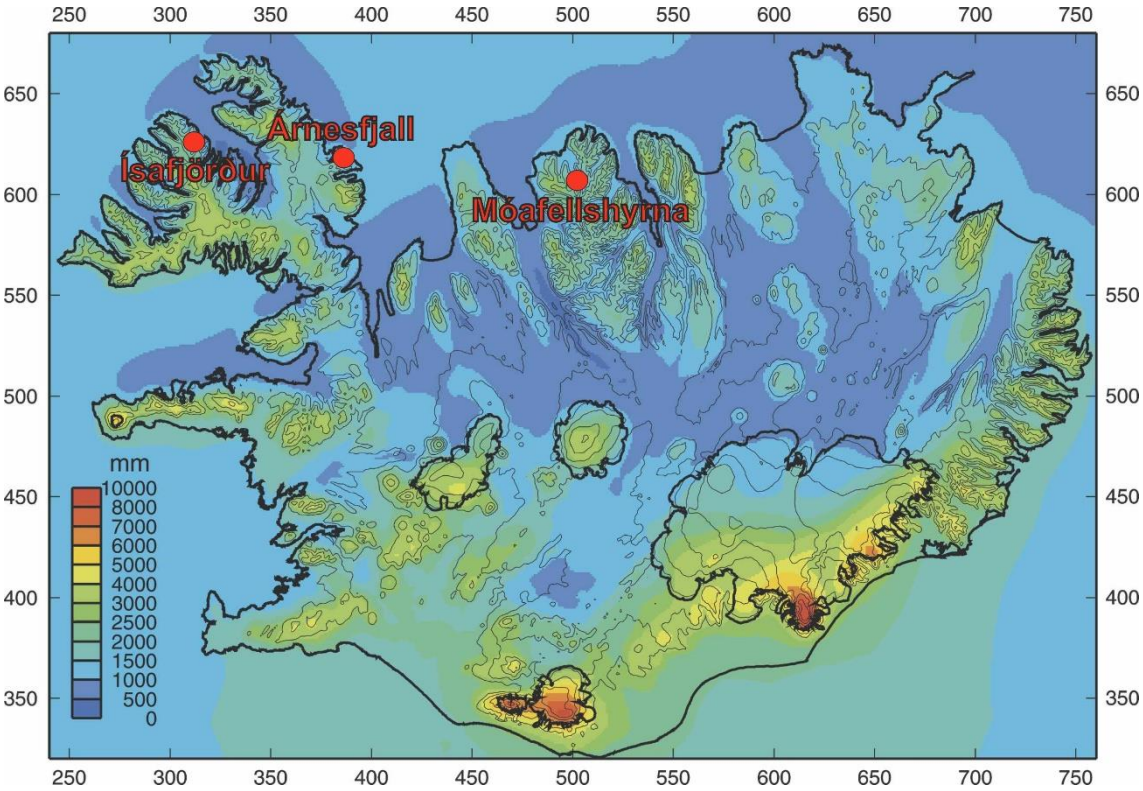

Figure 2.2. Mean annual precipitation of Iceland in 1971-2000; thick black lines outline the main four ice caps, in red are marked the study sites of this thesis (modified from Crochet et al., 2007).

From October to May, heavy snowfall and snowdrift cause snow avalanches (Jonsson et al., 1992). From May to October, heavy precipitation generates debris flows and rock falls, with a peak during the autumn (Valsson and Sigurbjornsson, 1996). Rapid mass movements, particularly debris flows, are reactive to snowmelt (most intensive period from April to June) in north-western and central northern Iceland (Decaulne and Sæmundsson, 2007; Jonsson et al., 1992; Sæmundsson et al., 2003), and have a high frequency of occurrence (a debris flow every 4-5 years; Decaulne et al., 2005). Rapid mass movements related to earthquakes are usually observed locally around the epicentres in the volcanic

zones and in the fault zones of the southern lowlands (e.g., Valsson and Sigurbjornsson, 1996). The relationship between permafrost-thaw and the occurrence of rapid mass movements in Iceland has been highlighted by recent studies (Sæmundsson et al., 2014a, 2018), but has not been routinely studied, and is one of the two main focusses of this thesis (see Section 2.4 for the state of art on permafrost in Iceland). Finally, further factors that can lead to rare but high-magnitude rock avalanches on glaciers in Iceland are glacial erosion and glacier retreat. These are thought to be the causes of a ~4,000,000 m^3 rock avalanche that occurred in 2007 on the Morsárjökull glacier on the southern part of the Vatnajökull ice cap, in south Iceland, leaving one fifth of the glacier surface buried and extending over the eastern flow unit and the medial moraine (Decaulne et al., 2010; Evans et al., 2017; Sæmundsson et al., 2011; see Figure 2.3).

Figure 2.3. The deposits of the Morsárjökull rock avalanche (in the foreground) that fell on the Morsárjökull glacier (in the background) in 2007. Photo taken on the surface of the rock avalanche.

The literature on rapid mass movements in Iceland shows that the Icelandic landscape is prone to their occurrence, particularly debris flows, rock falls, and rock/debris slides and avalanches. Slope movements have high frequency of occurrence in northern, eastern and western regions of the country, presenting a significant threat to the local inhabitants, as many settlements in Iceland are located on the coast in a limited space between steep rockwalls and the sea (Decaulne et al., 2005). The investigation and quantification of the sediment sources of rapid mass movements, and the analysis of their transfer and reproduction are the forefront of the research in natural hazard posed by hillslope processes. These have been attempted by different studies in the Westfjord of Iceland – an area particularly prone to debris-flow events (Conway et al., 2010; Decaulne et al., 2005; Glade, 2005) - as the definition of the magnitude of these phenomena is crucial in the prospective of hazard assessment. Deaculne et al. (2005) produced volume estimates of a singular debris-flow event in Ísafjörður from field inspections, and at the same location Conway et al. (2010) defined erosion and deposition patterns along the slope of multiple debris flows from DEMs and dGPS measurements (Figure 2.4). Glade (2005) used an empirical model to assess the sediment available for debris-flow occurrence in Bíldudalur, to define potential run-out zones and depositional areas of new debris-flow movements. However, new more accurate methods could improve these estimates. The geomorphological study of rapid mass movements in these regions of Iceland, and in particular the quantification of sediment supply and transfer of rapid mass movements can aid in evaluating risks and designing protection measurements. In Chapter 3 and Chapter 4, I produce a quantitative volume assessment of material mobilised by debris flows and landslides in

northern and western Iceland, with the final aim of better understanding their release, evolution and hazard.

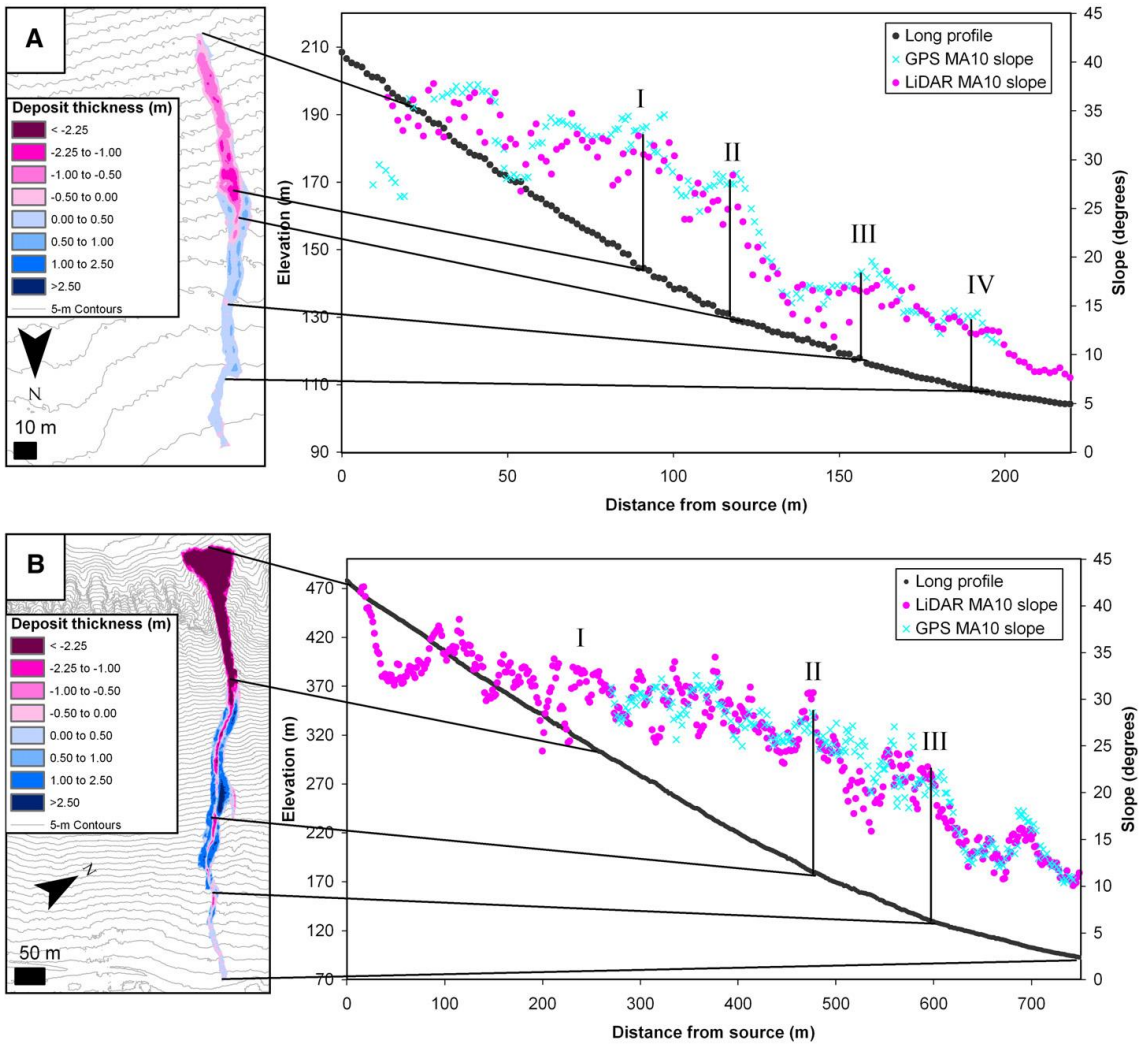

Figure 2.4. Long profile and isopach map of two debris flows in Ísafjörður, Westfjord. Contours on the isopach maps are at 5-m spacing (MA10 stands for Moving Average over 10 data points). Black points correspond to elevation on the right-hand axis, and pink/blue points correspond to slope represented on the right-hand axis (Conway et al., 2010).

2.3 Rapid Mass Movements in permafrost terrains

Permafrost is defined as soil or rock with a temperature below 0°C continuously for >1 year (Permafrost Subcommittee, 1988). Ground ice is a potential, but not

essential, component of permafrost: “All types of ice formed in freezing and frozen ground” fall within this term (Permafrost Subcommittee, 1988). Pores, voids and cavities in soil and rock can all contain ground ice, whose formation is controlled by air and ground temperature, water content and soil grain size (MacKay, 1972). The spatial variability of ground ice and the absence of surface manifestations make it difficult to detect (French, 2007; Pollard and French, 1980). Rapid changes in local climate, snow cover, topography, incoming radiation, ground and soil characteristics determine the variability of ground thermal regimes at local scale (e.g., Harris et al., 2009; Harris and Pedersen, 1998; Hasler et al., 2015; Thomas et al., 2009). Different techniques can be used to detect permafrost, to map its extent and define its state, such as geophysical investigations, mapping and GIS probability maps, numerical distribution modelling, and physical modelling of thaw-related slope processes (e.g., Haeberli et al., 2011; Harris et al., 2009, 2001; Hauck et al., 2003; Kaab, 2008; Kneisel et al., 2014; Lewkowicz and Harris, 2005; Mühll et al., 2002).

In the last thirty years, rapid mass movements such as active-layer detachment slides (the active layer is “the layer of ground that is subject to annual thawing and freezing in areas underlain by permafrost”, Permafrost Subcommittee, 1988), retrogressive-thaw-slumps, debris flows, rock/debris falls, slides and avalanches have been studied in relation to possible interactions with changing permafrost conditions (e.g., Ashastina et al., 2017; Blais-Stevens et al., 2015; Deline et al., 2014; Fischer et al., 2006; Gruber and Haeberli, 2007; Haeberli et al., 2017; Huscroft et al., 2003; Pedersen et al., 2002). There are various reasons why rapid mass movements are particularly effective under periglacial conditions (French, 2007): i) frost action promotes mechanical fragmentation of rocks, with resulting loose material available for transport; ii) shallow sediment movements are

accelerated by short-term free-thaw cycles of the ground surface; iii) moisture content produced by active-layer thaw reduces cohesion; iv) permafrost limits infiltration of water into the ground, generating high pore-water pressures in the near-surface; and v) the active layer can act as slip plane.

Active-layer-detachment slides are localised slope failures confined to the permafrost active layer in ice-rich terrains (Lewkowicz, 1990; Lewkowicz and Harris, 2005a). They occur due to a reduction in shear strength resulting from progressive soil weathering and an increase in ice content of the active layer usually during rapid spring thaw or prolonged summer precipitation, genereting shallow (~1 m deep) failures (French, 2007).

Retrogressive-thaw slumps are semi-circular depressions resulting from thawing of ice-rich permafrost terrains (Pollard, 2005; Van Everdingen, 2005; see Figure 2.5A).They occur where ice-rich permafrost is exposed to thaw, and are generally triggered by wave action along coasts, undercutting erosion of banks along streams or lakes, or active-layer-detachment slides (de Krom, 1990; Lantuit and Pollard, 2008). Thaw slumps can cover areas of 50,000-40,000 up to 800,000 m^2, expose ground ice to thaw, modify the landscape, and can erode and transport thawed material to lakes, valley-bottoms or coastal zones (Kokelj et al., 2015, 2013; Lantuit et al., 2012; Murton et al., 2017). Thaw slumps cannot be classified as “rapid movements” — they can develop over decades (Lacelle et al., 2010) — but phenomena like falls or flows can transport thawed material from the slump headwall as secondary movements (Lantuit et al., 2012; Murton, 2001). As they are one of the most rapid erosion processes in permafrost terrains, their accelerated activity due to global warming is causing concern in different periglacial environments, from western Canadian Arctic to Siberia (e.g., Ashastina et al., 2017; Segal et al., 2016).

Debris flows are rapid, downslope flows of poorly sorted debris mixed with water (e.g., Iverson, 1997), and can severely affect periglacial environments. Debris flows can travel over long distances and transport large amounts of material at great speed (Zimmermann and Haeberli, 1992). They are characterised by a distinct failure scar, a central channel, the construction of levees on one or both sides of channel, and a terminal depositional lobe or lobes (e.g., Costa, 1984). Steep slopes, loose materials and wet conditions are favourable for the occurrence of debris flows (Lewin and Warburton, 1994). This combination of factors is extremely common in periglacial mountain environments, such as the Swiss Alps, where climatic warming during the 19th and 20th centuries has indirectly increased the frequency of debris flows (Haeberli et al., 1990; Rebetez and Lugon, 1997; Zimmermann, 1990; Zimmermann and Haeberli, 1992). This increased frequency is not directly linked to the thaw of perennially frozen debris in the source areas (i.e., meltwater producing a source of fluid), but it has been shown that there is a link between the initiation zones and the thickening of the active layer as a reaction to the increase in atmospheric temperatures (Sattler et al., 2011). This has also been observed in Yukon, where the interface between frozen and unfrozen ground seems to control the depth of movement in debris flows (Huscroft et al., 2003; see Figure 2.5B).

Rock falls are bedrock mass movements on steep slopes, rockslides are bedrock mass movements that occur along discrete surfaces, and rock avalanches are large-volume (>1M m^3) bedrock mass movements which cause fragmentation during rapid transport (Cruden and Varnes, 1996; Hungr et al., 2014). These phenomena are frequent in mountain glacial and periglacial environments, where glacial over-deepening, stress-release fracturing after

removal of glacial ice (McColl, 2012), glacial debuttressing (Cossart et al., 2008) and degrading permafrost (Deline et al., 2015; Fischer et al., 2006; Gruber and Haeberli, 2009; Huggel et al., 2012; Krautblatter et al., 2013) can destabilise rock walls (Figure 2.5D). These factors can induce changes in the stress field of the rock walls and expose previously insulated surfaces to altered mechanical and thermal erosion (Haeberli, 1997; Wegmann et al., 1998). In particular, when permafrost degrades due to climate change, physical changes also occur in the rock mass. After permafrost thaw, the shear strength of a rock significantly reduces with warming (minimum factor of safety is between −1.5°C and 0°C) (Davies et al., 2001). Ice segregation and volume expansion subsequent to increased temperatures can lead to failures (Gruber and Haeberli, 2007). Elevated water pressure and reduced frictional strength can result from meltwater or ground-water flow in previously frozen rock masses (Harris, 2005).

The processes of fall, slide and avalanche where loose debris is main the transported material are underreported in permafrost environments in the literature. However, these types of mass movements can reveal permafrost degradation in a similar way to processes involving bedrock, as permafrost in loose deposits has a role in controlling terrain drainage and strength (Huscroft et al., 2003). Ground ice was observed in the landslide deposits of the Little Salmon Lake landslide in central Yukon (Brideau et al., 2009; Lyle et al., 2014, 2004; see Figure 2.5), a zone characterised by sub-arctic continental climate and discontinuous permafrost (Heginbottom et al., 1995). The authors infer that the degradation of ground ice produced high pore-water pressure and triggered the landslide. Another example is the Chita landslide, in the central Andes, whose source is thought to be the deposits of an active rock glacier terminus, whose lack of cementation due to permafrost thaw caused the release of the slide (Milana,

2016). Exposed ground ice was found also in the Ram Plateau slide, Yukon, a sliding process similar to a retrogressive-thaw-slump and thought to be caused by permafrost thaw (Jermyn and Geertsema, 2015).

Ice-rich permafrost occurs in loose-deposits landforms such as rock glaciers, ice-cored moraines and talus slopes (e.g., Isaksen et al., 2000; Kenner et al., 2017; Lukas et al., 2005; Monnier and Kinnard, 2015; Schwamborn et al., 2008). Its degradation can cause a reduction in cementation, which can lead to the occurrence of rapid mass movements. As shown in this literature review, there is paucity of studies on loose-deposit landslides in periglacial environments and of the role of permafrost thaw in their release and evolution. This opens up a fruitful area for progress in landslide geomorphological analysis and hazard. To explore this area, in Chapter 4 and Chapter 6 I describe a quantitative geomorphological study of landslides involving ice-cemented loose deposits in Iceland, and a geomorphic analysis of their features, with the aims of (i) determine how ground-ice thaw influence the landslide dynamic processes, (ii) to characterise landslide features that can be recognised and used to detect permafrost degradation, revealing permafrost degradation, and (iii) widen the knowledge of landslide behaviour and hazard in periglacial environments.

Figure 2.5. Examples of mass movements in cold environments. (A) Scar zone and headwall of a retrogressive-thaw-slump on the Peel Plateau, Canada (from Kokelj et al., 2015); (B) Debris-flows channel on Mount Sumanik, Yukon, related to permafrost thaw (from Huscroft et al., 2003); (C) the Little Salmon Lake landslide, Yukon, a rare example of loose-debris failure in permafrost terrain (from Brideau et al., 2009); the Crammont rock avalanche in the Mont Blanc massif, Italy, resulted from permafrost degradation (Deline et al., 2013).

2.4 Permafrost in Iceland

Permafrost is present in Iceland as “mountain permafrost” (Brown et al., 1997; Etzelmüller et al., 2007) as defined by Haeberli et al. (1993) and the Permafrost Subcommittee (1988) “permafrost existing at high altitudes in high, middle, and low latitudes”. The nature of mountain permafrost, which is extremely heterogeneous (Hauck et al., 2004) and whose temperature is close to the freezing point, makes it particularly vulnerable to climate variations (Haeberli et al., 1993; Nelson et al., 2002). Due to the problems related to recognition (spatial variability and absence of surface expression), the distribution of ground ice in

Iceland is not well-constrained. In the past, many studies have focussed on geomorphological features related to permafrost or active periglacial processes (Clark, 1983; Feuillet et al., 2012; Priesnitz and Schunke, 1983, 1978; Stötter, 1991; Thorarinsson, 1951; Van Vliet-Lanoë et al., 1998). Priesnitz and Schunke (1983) and Clark (1983) gave a detailed report on different periglacial landforms, distinguishing features non-indicative of permafrost, such as micro-relief features, sorted and non-sorted patterned ground (stone polygons and stripes, thufur, frost mounds; see Figure 2.6), stone pavements, gelifluction forms, and features directly indicative of permafrost aggradation, i.e. palsas, and degradation, i.e. thermokarst depressions and mounds. Patterned grounds show spatial distribution and geomorphic characteristics controlled by altitude, insolation, grain size characteristics and type of drift in northern Iceland (Feuillet et al., 2012; Stötter, 1991).

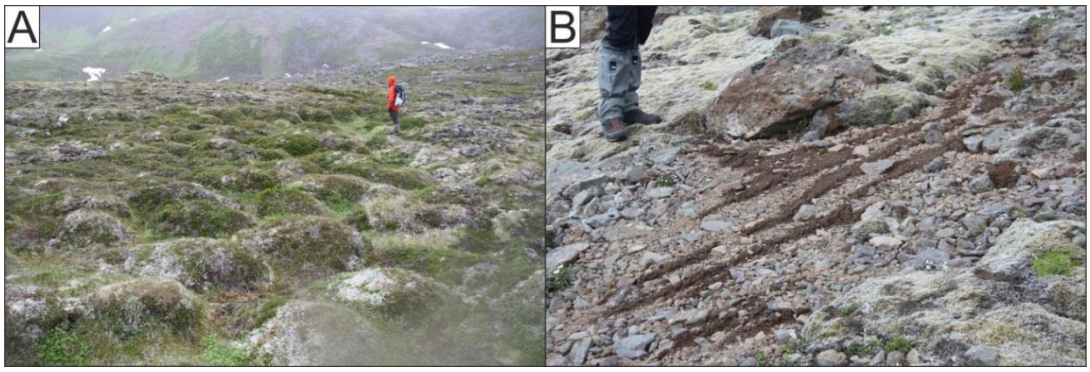

Figure 2.6. Patterned ground in Iceland. (A) Thufur patterned ground in northern central Iceland; (B) patterned stone stripes in the north-western fjords of Iceland.

The first attempts to geographically define the extension of permafrost in Iceland were by Harris (1981), who highlighted that permafrost is present in Iceland as discontinuous ("Permafrost occurring in some areas beneath the exposed land surface throughout a geographic region where other areas are free of permafrost", Permafrost Subcommittee (1988)), in accordance to Priesnitz and

Schunke (1978), and confined in the central highlands. Whalley and Martin (1994) suggested that permafrost was likely to exist on high-elevation plateaus above 1200 m a.s.l. A census and characterization of active rock glaciers and ice-cored moraines was performed in northern Iceland (Farbrot et al., 2007a; Lilleøren et al., 2013; Wangensteen et al., 2006; Whalley et al., 1995a, 1995b). In the Circum-Arctic map of permafrost and ground-ice conditions of the official International Permafrost Association (IPA) (Brown et al., 1997), the palsa-rich areas of central Iceland are within the zones of sporadic discontinuous permafrost (subcategory of discontinuous permafrost defined as "permafrost underlying 10 to 35 percent of the exposed land surface", Permafrost Subcommittee (1988)), with isolated patches on the north-eastern side of the Vatnajökull ice cap and the on the eastern side of the Drangajökull ice cap.

Etzelmüller et al. (2007) developed a simplified regional permafrost distribution model for Iceland, which for the first time attempts to constrain the potential distribution of ground ice. They used mean annual air temperature (1961–90), topography, ground surface temperature and the presence of typical features of mountain permafrost, such as active rock glaciers and creeping ice-cored moraines (Guodong and Dramis, 1992; Hoelzle and Wagner, 1998; Washburn, 1979b), to compile their map. The study by Etzelmüller et al. (2007) revealed the presence of widespread mountain permafrost outside the already known permafrost zone in central Iceland. In their map, the lower altitude limit of permafrost increases in elevation towards the southeast, with elevations between 800 m and 900 a.s.l. in the north and more than 1000 a.s.l. in the southern part of Iceland (see Figure 2.7). The largest continuous area on the map is on the peninsula of Tröllaskagi and southwards towards the area between Hofsjökull and Vatnajökull. The mountain permafrost zone covers an area of 7000–8000

km^2. The cryosphere in terms of glacier and permafrost is estimated to cover around 15% of the total land area of Iceland at present.

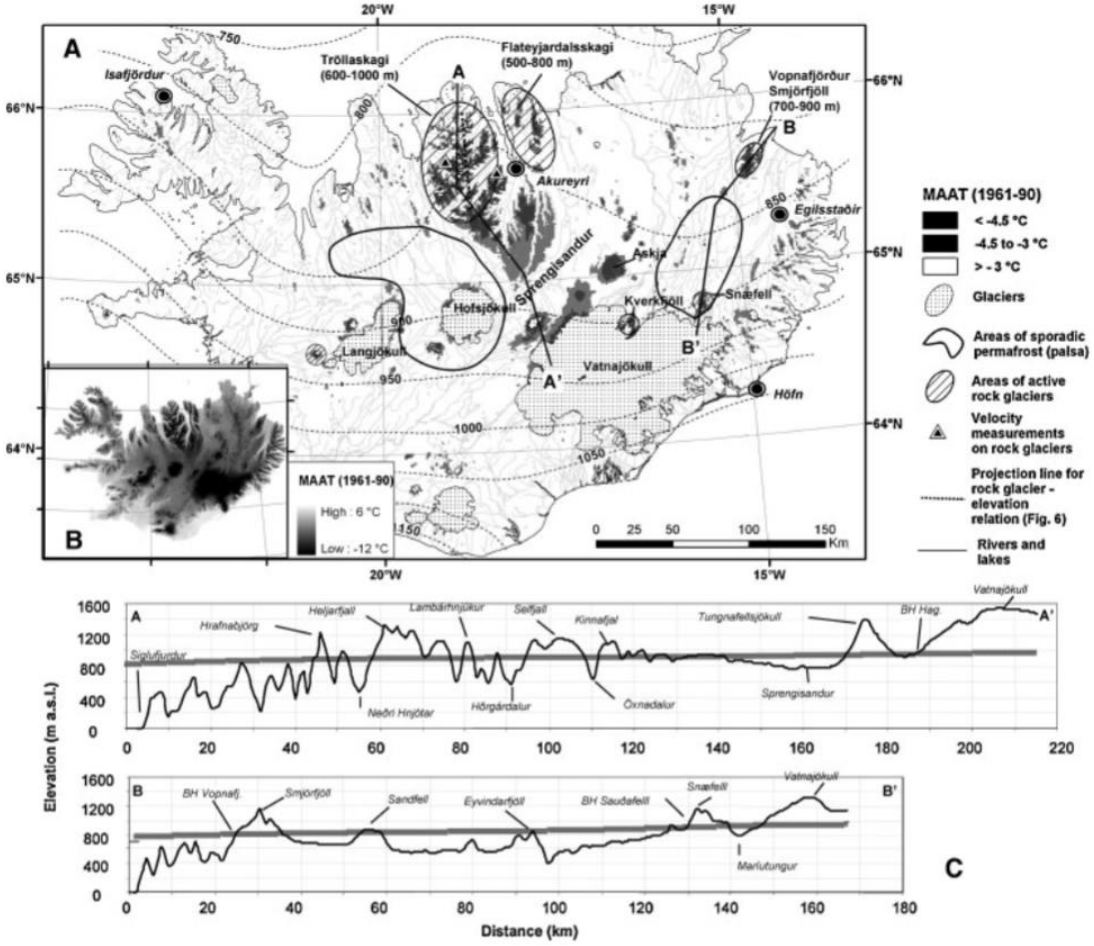

Figure 2.7. Regional mean annual air temperature (MAAT)-based map of mountain permafrost distribution in Iceland. The contours indicate the lower limit of potential mountain permafrost. The shaded areas show the distribution of predicted permafrost based on topography extending to elevations with MAAT <3°C. The hatched ellipses denote areas of active rock glaciers and their elevation range. The triangles indicate the location of rock glacier's velocity measurements. (B) The inset map shows the original map of MAAT. (C) Topographic profile lines with proposed lower limit of mountain permafrost (from Etzelmüller et al. (2007)).

Etzelmüller et al. (2007) were the first to hypothesise that permafrost is probably degrading, as indicated by the surface offset between air and ground surface temperatures. This was also confirmed by Farbrot et al. (2007b), who

suggested that the northern central regions of Iceland could expect permafrost degradation within decades (Farbrot et al., 2007b). The suggestion of an ongoing degradation of permafrost was also supported by the study of Kneisel et al. (2007), who in central Iceland detected shallow and spatially heterogeneous permafrost, an indication of likely rapid reaction of permafrost to changes in climate, confirmed in the same area by the detection of degrading permafrost in palsas (Sæmundsson et al., 2012). However, so far relatively little attention has been paid to the consequences of the recent climate change on the possible degradation of mountain permafrost in Iceland. The relationship between permafrost-thaw and the occurrence of rapid mass movements in Iceland has been highlighted by recent studies (Sæmundsson et al., 2014a, 2018), but not routinely studied, and is the main focus of this thesis.

2.5 The hazard of rapid mass movements in cold environments

According to the definition of (Varnes, 1984), landslide hazard is defined as the probability that a landslide event of a certain magnitude occurs within a period of time in a given area. Landslide risk refers to the expected degree of loss due to a landslide event, and is the result of the product of the landslide hazard and the vulnerability, with the latter defined as the degree to which a community, a structure, a service or an area is likely to be damaged by a hazardous phenomenon. Mass movements represent can be extremely dangerous, as they are processes that can severely threaten human life and affect infrastructures (Crozier, 1989; Geertsema et al., 2009; Haque et al., 2016; Kjekstad and Highland, 2009; Petley, 2012). Slope failures can involve different types of

materials and can have a great diversity of velocities and fluid contents making it hard to understand them and produce the appropriate countermeasures. Even if high level of uncertainty of global-climate predictions and the lack of spatial resolution of the available downscaled projections, there is a strong theoretical basis for increased landslide activity as a result of climate change (e.g., Crozier, 2010; Guzzetti et al., 2005; IPCC, 2007). This increased activity could also affect cold environments, which are particularly sensitive to variations in atmospheric temperatures (e.g., Clague et al., 2012; Huggel et al., 2012), leading to an enhanced reaction of mountain slopes to glacial retreat and permafrost degradation (e.g., Deline et al., 2014; Gruber et al., 2017; Gruber and Haeberli, 2007; Schoeneich et al., 2011). While glacier volumes in most cold mountain environments rapidly decrease due to climate change, degradation of permafrost at altitudes above and below glaciers is much slower (Haeberli et al., 2017), causing disequilibria and consequent hazardous phenomena like those described above. The frequency of rapid mass movements in cold periglacial environments has particularly increased during the past two decades, as reported from the European Alps (Ravanel and Deline, 2011), New Zealand (Allen et al., 2009), and northern British Columbia, Canada (Geertsema et al., 2006a). In these geographical contexts, although permafrost degradation could have played a role in some of these failures, isolating its effects from those of glacier thinning and retreat is difficult (Clague et al., 2012).

Several catastrophic mass movements in cold environments have occurred in the recent past. Disastrous debris flows have occurred in periglacial environments with permafrost degradation as one of the main causes (e.g., Haeberli et al., 1990; Harris and Gustafsson, 1993; Rapp and Nyberg, 1981; Zimmermann M, 1992). Several rock falls, rock slides and rock avalanches

triggered by permafrost degradation threaten the mountain populations of the European Alps (Bottino et al., 2002; Deline et al., 2013, 2015; Dramis et al., 1995; Fischer et al., 2006; Gruber and Haeberli, 2007; Phillips et al., 2017; Schoeneich et al., 2011). Rock/ice avalanches are one of the most catastrophic mass movements in cold environments (Davies and McSaveney, 2012; Evans and Clague, 1988; Geertsema et al., 2006b, 2006a; Hungr and Evans, 2004).

Several examples with volumes ranging up to a few million cubic metres include the Thurwieser rock avalanche in the Italian central Alps (Sosio et al., 2008), the Brenva rock avalanche that detached in the Mont Blanc range in 1997 (Barla et al., 2000), the rock slide from Monte Rosa in the western Italia Alps in 2007 (Fischer et al., 2011), the rock avalanches at Mount Munday in 1997 and at Kendall Glacier in 1999 in British Columbia (Delaney and Evans, 2014; Geertsema et al., 2006a). Rock/ice avalanches with volumes of 30 to >100 million m^3 include cases like a rock/ice avalanche of about 100×10^6 m^3 volume occurred at at Kolka/Karmadon, Russian Caucasus, causing in 2002 destruction and the death of ca. 140 people, or the 2005 Mt. Steller rock avalanche in Alaska that mobilised 40 to 60 million m^3 volume in the Alaska Range (Huggel et al., 2007). The consequences of landslides in cold environments can be more unexpected and severe than the events themselves, generating hazardous consequences because of dam-creation (e.g., Strom and Korup, 2006), or tsunami if they reach the water (e.g., Dahl-Jensen et al., 2004; Evans et al., 2006).

In Iceland, as reported in Section 2.2.2, the death of 35 people between 1994 and 1995 because of snow avalanches was the turning point for improving the work on landslide and snow-avalanche hazard assessment. Thorough reports of landslide and snow avalanche risk in different zones of the country are regularly updated by the local and state authorities, as the current Icelandic regulation on

hazard zoning requires the same individual phenomenon risk criteria to be used for landslides and for snow-avalanche hazard zoning (i.e., landslide hazard zoning is done jointly with avalanche hazard zoning), and the combined risk is presented on one map (e.g., Arnalds et al., 2001, 2002, 2004). Detailed assessments of snow-avalanche and debris-flow risk have been produced by the Icelandic Meteorological Office (IMO) for the main town and villages of Iceland and by independent researchers for towns in the northwest fjord regions of Iceland (see an example in Figure 2.8), producing risk maps pointing out critical regions in relation to the different hazardous processes and the elements at risks (Bell and Glade, 2004; Decaulne, 2004, 2005, 2007; Glade and Jensen, 2004). These are directly used by decision makers to identify the need for and then plan the emplacement of mitigation measures.

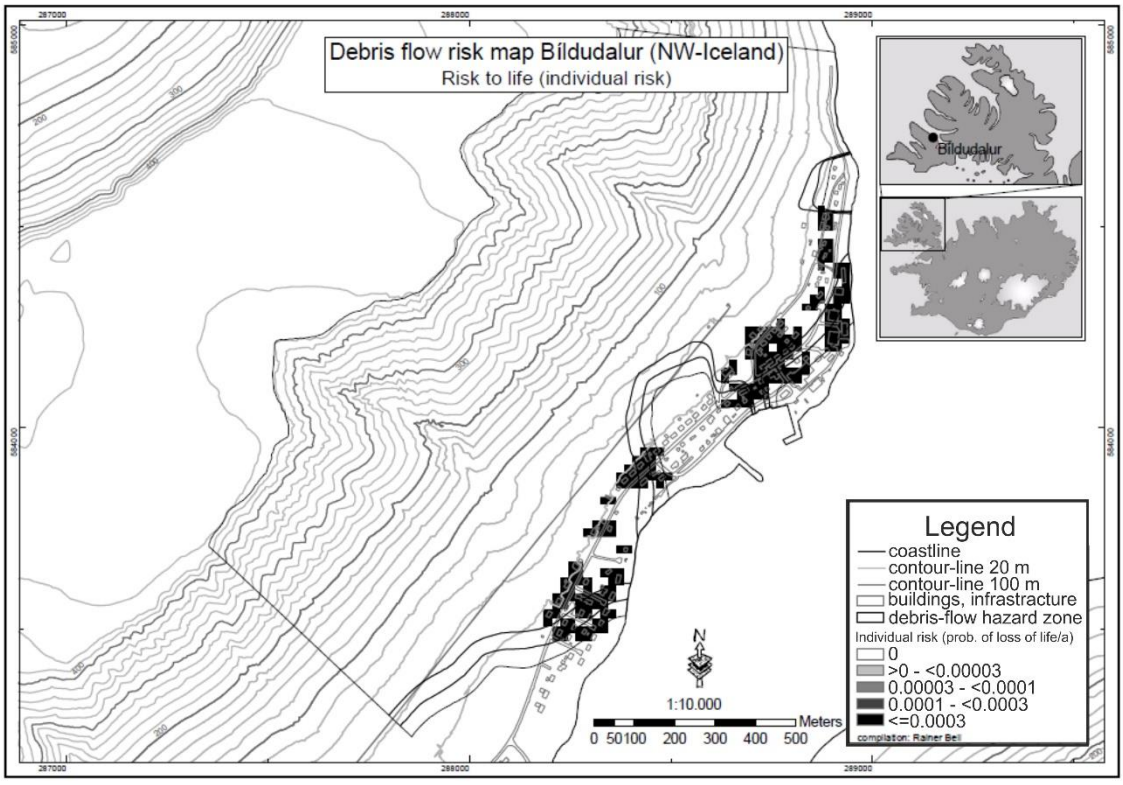

Figure 2.8. Debris flow risk map for the town of Bíldudalur in the Westfjords, showing the individual risk to life (from Bell and Glade, 2004).

Solutions that offer a reduction of risk to population exposed to the hazard of rapid mass movements in cold environments are various. Preventive solutions can be either structural physical defences or non-structural measurements, such as land-use planning (e.g., integrated spatial information on glacier/permafrost evolution, rapid mass movements susceptible areas and vulnerability; Haeberli et al., 2017) and increasing the awareness of the population at risk. However, structural and non-structural risk-reduction measurements as designed nowadays are likely to be insufficient in the framework of a changing climate, so existing historical records, monitoring datasets, modelling and computational means should be implemented to adapt to the new, predicted climate conditions (Gariano and Guzzetti, 2016), particularly in more sensitive cold environments.

This thesis is not designed with the purpose of offering direct prevention-risk solutions to potentially hazardous slope movements, but provides a detailed investigation of debris flows and landslides that, being so frequent in Iceland, need to be fully characterised. Landslide management involves prediction, prevention, and risk assessment (Dai et al., 2002), and none of these steps can be achieved without the characterisation of the landslide as a process. The analysis performed in this thesis can contribute to widen the information on rapid mass movements in Iceland and other cold environments, and can be correlated to the existing knowledge to enhance our ability to predict, prevent and mitigate these gravity-induced hazardous phenomena.

2.6 Conclusions

One of the most obvious reactions of permafrost-affected terrains to climate change is rapid mass movement. From my literature search I have ascertained that:

- the landscape of Iceland has been shaped by ancient and recent slope failures, with the latter being frequent and potentially disastrous. In Chapter 3 and 4, I report the analysis of the morphology and processes of some of these potentially hazardous rapid mass movements;
- the influence of the changing cryosphere on the stability of rock walls are well documented, since the number of periglacial rapid mass movements has increased over the past century in periglacial environments worldwide. However, little is known about how the dynamics of rapid mass movements involving loose deposits are conditioned by thawing ground ice, which is the topic of Chapter 4;
- permafrost in Iceland is expected to be located in the central-northern regions of Iceland generally at altitudes above ~800-900 m a.s.l.. It is estimated that permafrost is degrading in the island, but the consequences on the landscape of this decay are so far unknown. Permafrost as trigger of rapid mass movements in Iceland is the topic of Chapter 5, and the possible morphological signatures as consequences of this process are analysed in Chapter 4 and 6;
- as degrading permafrost is predicted to increasingly affect mountain regions in the future, improving our knowledge on rapid mass movements in cold environments is important, since they could be a new source of risk for local population in Iceland and other mountainous periglacial areas,

where rapid mass movements are a significant source of risk for local population and infrastructure.

Chapter 3. Debris-flow release processes revealed through the analysis of multi-temporal LiDAR datasets in north-western Iceland[1]

3.1 Introduction

Debris flows are among the most dangerous and damaging of all landslide phenomena (Hungr, 1995), and can pose a severe threat to many towns in Iceland, causing life loss and damage to infrastructures (Jóhannesson and Arnalds, 1992; Pétursson et al., 2010). In Chapter 2, I have reported that in wide areas of Iceland the frequency of debris flows is increasing with time (Decaulne, 2004). This highlights the need to of detailed geomorphic analysis of debris flows, as they provide information for future hazard assessment, as scenario modelling are dependent on processes and sediment availability. A clear identification of the geomorphic signatures of different debris-flow release styles and a precise quantification of their magnitude is necessary when evaluating risks and designing protection measurements, and is one of the final aims of this thesis.

[1] The work contained in this chapter of the thesis is based on a paper that has been published on the journal Earth Surface Processes and landforms entitled “Debris-flow release processes investigated through the analysis of multi-temporal LiDAR datasets in north-western Iceland”. The full citation of this paper is:

Morino, C, Conway, S. J., Balme, M. R., Hillier, J., Jordan, C., Sæmundsson, Þ., Argles, T. 2018. Debris-flow release processes investigated through the analysis of multi-temporal LiDAR datasets in north-western Iceland. Earth Surface Processes and Landforms. DOI: 10.1002/esp.4488

Typological changes to the paper have been made to ensure consistency with the rest of the thesis. These changes are: removal of the abstract, the use of the first person singular instead of the first person plural where appropriate.

Debris flows are rapid (e.g., 0.8-28 ms^{-1}; Rickenmann, 1999) and potentially destructive mass movements composed of a cohesion less mixture of water and poorly sorted sediments (Iverson, 1997). To initiate, debris flows require the availability of unconsolidated material, excess moisture to saturate and mobilise this material, and slopes greater than 15°-20° (e.g., Costa, 1984; Imaizumi et al., 2006; Rickenmann, 1999; Terzaghi et al., 1996). Hundreds of thousands of cubic metres of sediment can be transported for distances of over tens of kilometres, even on moderate (~5-10%) gradients (e.g., Iverson, 1997; Rickenmann and Koschni, 2010). They are distinct from other forms of landsliding due to their periodic occurrence on established paths, usually in gullies or first order drainage channels (Hungr et al., 2014).

Debris flows can initiate in several ways, e.g. by shallow translational or rotational sliding (e.g., Costa, 1984; Innes, 1983), by the erosion and mobilisation of accumulated material on hillslopes or in pre-existing depressions (e.g., Cannon et al., 2001; Davies, 1986), or by sediment entrainment in channels (e.g., Hungr et al., 2005). Different styles of triggering and propagation processes of debris flows have inherently different preconditioning factors. It is important to understand which triggering processes (or combination of processes) are active during the formation and evolution of debris flows to anticipate their behaviour in zones exposed to their hazard, and hence to design mitigation and prevention measures.

Direct observation of the initiation processes of debris flows is the best way to identify them, but is seldom possible. In recent years, the development of high-resolution topographic data from Laser Scanning (or “LiDAR”, Light Detection And Ranging) and other photogrammetric datasets has facilitated the study of

debris flows. Monitoring of debris flows through multi-temporal LiDAR data is becoming more and more common, particularly for sediment budget analysis and for studying debris-flow initiation (e.g., Blasone et al., 2014; Bossi et al., 2015; Bull et al., 2010; Cavalli et al., 2017; Scheidl et al., 2008). Bremer and Sass (2012) used a combination of Terrestrial Laser Scanning (TLS) and Airborne Laser Scanning (ALS) to quantify and map the sediment volume transported by a single debris-flow event in the Austrian Alps. Erosion and deposition generated by channel-bed entrainment of sediments by debris flows in the Swiss Alps have been calculated by differencing two ALS Digital Elevation Models (DEMs) (Frank et al., 2015). Loye et al. (2016) used time series TLS data to quantify the sediment budgets of two debris-flow events in the Manival catchment (France). They were able to distinguish between the seasonal debris recharge produced by rock fall in winter, and the debris produced by hillslope sediment reworking in spring and autumn. In the same area, Theule et al. (2015) used TLS to quantify erosion and deposition caused by debris flows, and ALS to detect unstable sediment deposits that could be a source for new events. In all these studies, the number of the debris-flow events was known and the debris-flow catchments were monitored by other means. However, when catchment changes are not easily identifiable - in the absence of monitoring systems or witnesses - knowing how and when individual or multiple debris-flow events occur is challenging. A possibility that has not been fully explored in literature is the identification and quantification of different debris-flow release processes from multi-temporal laser altimetry datasets, where the conditions for their development are poorly monitored.

Two debris-flow triggering processes were previously hypothesized for the site of Ísafjörður (Conway et al., 2010; Decaulne et al., 2005): (i) slope failure,

characterised by landslides evolving into debris flows, and (ii) the fire-hose effect, in which debris accumulated in pre-existing, steep-sided bedrock passages is transported by a surge of water. It is unknown which process dominates and determines the local risk. In this chapter, I investigate how two debris-flow initiation processes (slope failure and fire-hose effect, which have been previously proposed for my study area in the Westfjords of Iceland; Conway et al., 2010; Decaulne et al., 2005) manifest themselves in terms of geometric properties and geomorphological features recognisable and measurable in remote sensing data. Specifically, I quantify the geomorphic effects of debris flows on the slope above the town of Ísafjörður through the comparison of two repeat aerial photograph and airborne laser altimetry datasets from 2007 and 2013. In particular, I use the airborne LiDAR data to calculate the volumes eroded and deposited along debris-flow tracks by potential multiple debris-flow events, and I couple these volume quantifications with the analysis of changes in slope and geomorphic observations and interpretations from the aerial photographs. This allows us to assess and distinguish the role of two release mechanisms in debris-flow generation: slope failure and fire-hose effect.

Identifying and characterising different debris flows processes is useful for understanding both sediment cascades and the implications of the potential risk posed by debris flows where they occur near inhabited areas. This can be achieved by LiDAR differencing, which in my case has permitted the detection and quantification of debris accumulated at high gradients without the assistance of any other monitoring system or information on the evolution of the hillslope. From remote sensing interpretation alone, I do not know if one or several debris-flow events have mobilised the material between 2007 and 2013 in the tracks that

I analyse, but this debris could be the source-material for potentially large debris flows in the future. This kind of study, implemented with *in situ* channel survey and monitoring, can improve both our understanding of how debris flows develop and mitigate the risks associated with them.

3.2 Debris-flow activity in the study area

Slopes in the north-western region of Iceland, the Westfjords (Figure 3.1A), are prone to debris flows (Decaulne, 2005). Ísafjörður is the largest town of the peninsula, with a population of approximately 2600 inhabitants over an area of 4.2 km² in 2016. It has more than 150 buildings (including houses, a hospital, a church, two schools, two elderly residences, and three kindergartens) less than 50-300 m from recently emplaced debris-flow runout deposits. Although in this century debris flows have not caused major loss of life in the Westfjords, they do pose at serious risk local infrastructure and population (Decaulne, 2004). In mid-June 1999, six debris flows occurred after a sudden and intensive snowmelt period on the slope overlooking the town of Ísafjörður, damaging houses and infrastructure (Decaulne et al., 2005). Moreover, at least 24 debris-flow events occurred on this slope between 1900 and 1999, giving a return period for debris flows of 4-5 years (Decaulne et al., 2005).

My study site is located above the town of Ísafjörður in the Gleiðarhjalli area, situated on the western side of the Skutulsfjörður fjord (Figure 3.1A). The fjord was shaped by Pleistocene-age glaciers and is carved into the Tertiary Basalt Formation, comprised of 2 to 30 m thick jointed basaltic lava flows separated by lithified sedimentary horizons (from a few centimetres up to tens of meters thick;

Thordarson and Hoskuldsson, 2002), which are gently dipping towards the southeast (Kristjánsson et al., 1975; Sæmundsson, 1980).

The Gleiðarhjalli bench, which is located on the south-eastern side of Eyrarfjall Mountain at a height of 470 m above sea level (a.s.l.), is 1500 m long and 450 m wide (Figure 3.1B). Deposits of poorly sorted glacial till 20-35 m thick (surveyed and measured by visual inspection in the field) are perched on this bench (Figure 3.2A), at whose margin they are unstable. The till deposits are composed of subangular to subrounded clasts varying in size from pebbles to metre-scale boulders and lying in a matrix of clay, silt and sand. The deposits are covered by centimetre to metre-sized angular clasts from talus deposits, which are either lying scattered on the bench or leaning against the rockwall (Figure 3.2B). Chutes (i.e., steep-sided passages scoured in bedrock along which the debris flows can move) are incised into the exposed rockwall at the edge of the bench (Figure 3.2), forming areas through which most of the transfer of sediment to the lower parts of the slopes takes place.

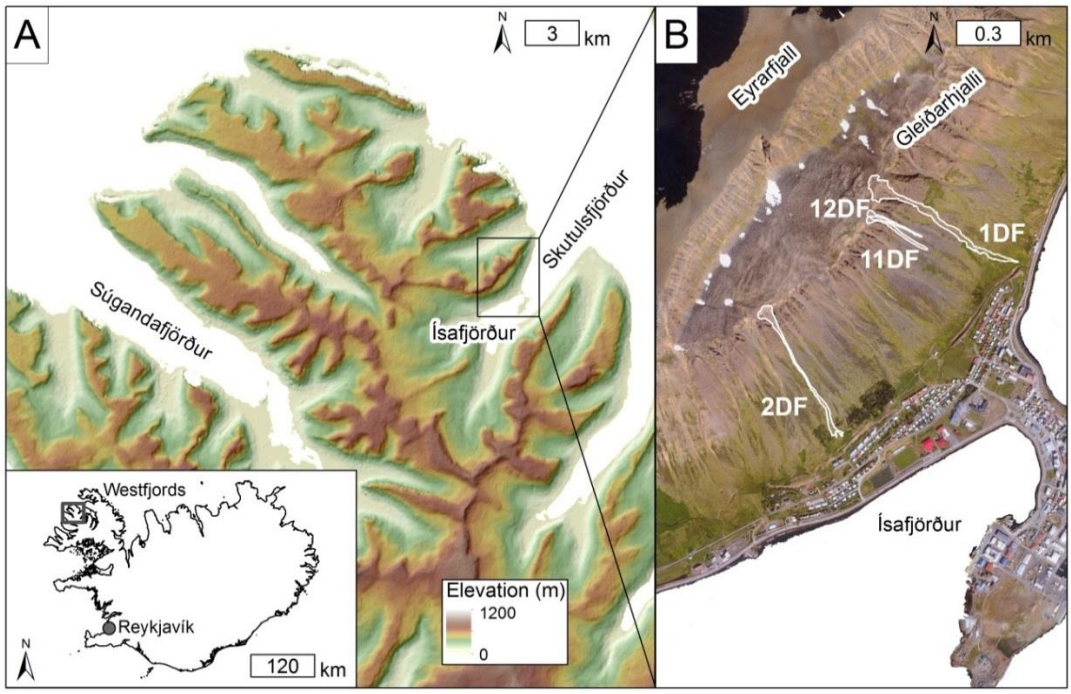

Figure 3.1. The study site in Ísafjörður, Westfjords. (A) The study area in the Icelandic Westfjords. Elevation data are from the Digital Elevation Model over Europe (EU-DEM) from the Global Monitoring for Environment and Security service for geospatial reference data access project (GMES RDA). (B) Aerial photograph shows the town of Ísafjörður, with debris flows analysed in this study marked with white outlines.

The SE-facing hillsides above Ísafjörður have steep slopes in the range 25° to 35°, and slightly concave profiles. Below the exposed rockwall, the slope is covered by talus material and relict debris-flow deposits (Figure 3.2). Grass, moss and patches of dwarf birches and bilberries (30-40 cm high) cover the slope of Ísafjörður in its lower part. Trees are absent, apart from two small artificially forested areas at the foot of the slope (covering ~43,000 m^2 and 6,800 m^2 respectively), planted with spruce (3-4 m high on average) as wind-breaks and for aesthetic reasons. The lack of substantial vegetation in the upper part of the slope favours erosional processes (e.g., Elwell and Stocking, 1976; Wells, 1981, 1987).

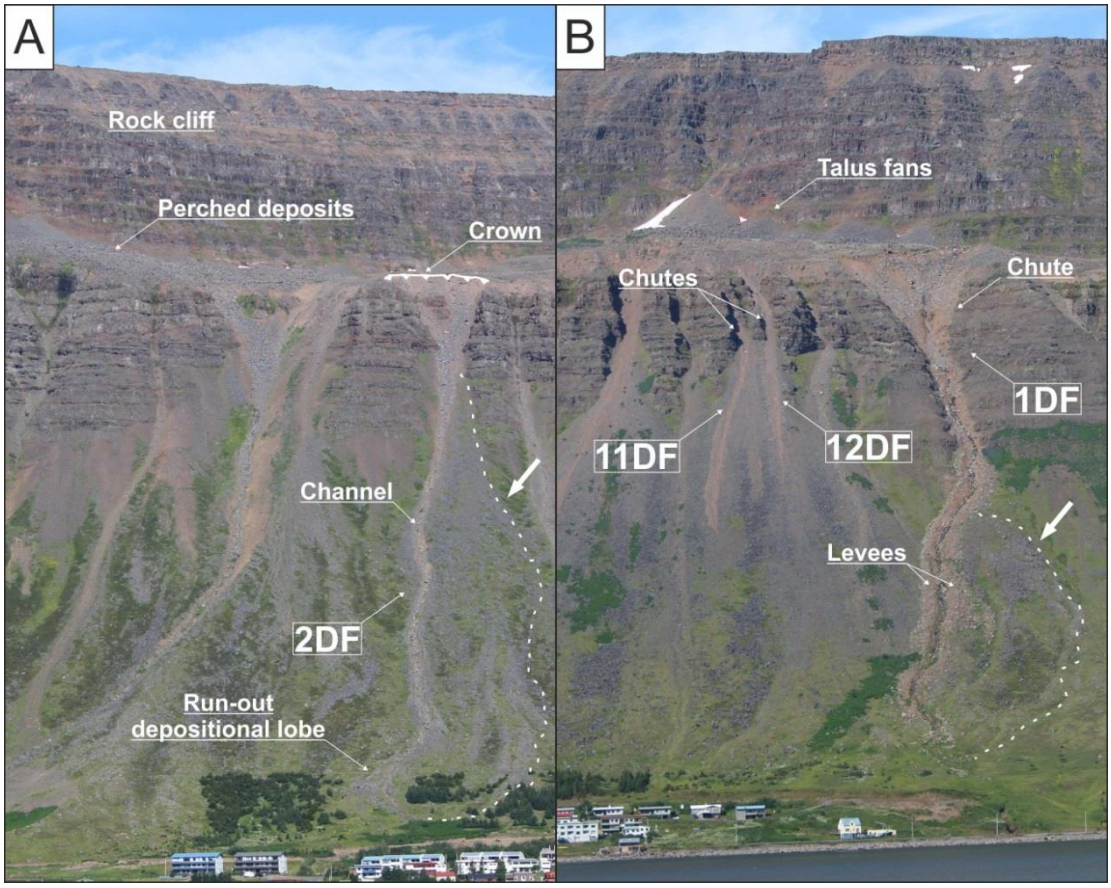

Figure 3.2. Southeast flank of the Eyrarfjall mountain above the town of Ísafjörður showing the four debris-flow tracks analysed for this study (debris flow 2DF in (A), debris flows 1DF, 11DF and 12DF in (B)). Above the rock cliff it is possible to observe talus fans and perched deposits on the Gleiðarhjalli bench; chutes are scoured in the bedrock below the bench ridge and the debris flows' channels incise the deposits from talus material and relict debris flow deposits. Arrows and dashed lines indicate the migration of the channels of 1DF and 2DF in the terminal parts, leaving fan-shape debris accumulation. Some of the run-out depositional lobes reach the inhabited areas. The white dotted line marks an example of chute area, the white indented line an example of crown overlying the main failure scarp. Photograph taken on July 26, 2013.

In Ísafjörður, heavy and prolonged rainfall and rapid snowmelt have been recognised as the main factors that promote rapid mass wasting phenomena, which are also favoured by the steepness of the slope (Decaulne and Sæmundsson, 2003, 2007; Sæmundsson et al., 2003). However, the exact physical mechanisms by which debris flows are initiated have been hypothesised but not studied in too much detail. This is partially due to the difficulties in

accessing and observing the phenomena directly, which is only rarely possible in Ísafjörður (Decaulne et al., 2005), and other mountain environments (e.g., Berti et al., 1999; Coe et al., 2008; McArdell et al., 2007).

Among the many possibilities, two processes are most commonly considered responsible for triggering debris flow here: slope failure and the fire-hose effect (Conway et al., 2010; Decaulne et al., 2005). Initiation by slope failure is characterised by one or more discrete slope failures, instigated by changes in pore water pressure due to gradual *in situ* infiltration of rain or snowmelt (e.g., Hungr et al., 2001). As failure proceeds, contraction of debris causes an excess in pore water pressure, weakening the debris mass and resulting in the transformation from localized failure into a debris flow (Iverson, 1997). It is believed that this initiation style is experienced in the Gleiðarhjalli area; Decaulne et al. (2005) observed that intense precipitation and snowmelt caused the saturation of the debris mantle covering the bench. Decaulne et al. (2005) further observed that the debris flows begin with rock falls originating from the edge of the bench. This implies a subsequent loss of support, leading to the perched deposits sliding and then forming channelized debris flows. The authors report that, between the rock-fall phase and the debris-flow phase, the uppermost part of the tracks were temporarily blocked by the collapsed material from upslope, being prone to be re-mobilised by further events.

Initiation by the fire-hose effect (Johnson and Rodine, 1984) is characterised by a concentrated flow of water that entrains loose deposits, which are generally located in a steep bedrock channel, torrent or chute (e.g., Godt and Coe, 2007). An increase in pore-pressure results in their conversion into a debris flow (e.g., Coe et al., 1997; Griffiths and Webb, 2004; Johnson and Rodine, 1984). The

recurrence interval of such flows is controlled by the debris accumulation rate in the source area and the timing of triggering precipitation. The fire-hose effect has been inferred to have been active in the Westfjords based on field inspections (Conway et al., 2010; Decaulne and Sæmundsson, 2006), but has never been fully characterized and quantified.

3.3 Methods

3.3.1 Dataset-processing and Digital Elevation Model generation and interpolation

In 2007 and 2013, the U.K. Natural Environment Research Council's Airborne Research Facility Data Analysis Node (NERC-ARF-DAN) collected aerial photography and LiDAR data for Súgandafjörður and Skutulsfjörður areas in Iceland. Details of both aerial surveys are reported in Table 3.1. As the methods of remote sensing data collection differed between the two years, including the location/type of the reference GPS base stations on the ground, the two LiDAR datasets needed further processing to attain a satisfactory comparison. Alignment and filtering are required when comparing different type of datasets, in order to achieve sufficient accuracy for producing volumetric differencing (e.g., Bremer and Sass, 2012; Roberti et al., 2017). Furthermore, co-registration error between flightlines needs to be corrected. Approaches such as morphometric parameter distributions (Sofia et al., 2013) or spatially variable error models (Schaffrath et al., 2015) have been developed to correct these errors. Fuzzy inference system (Fis) has also been used to estimate the spatial variability of elevation uncertainty in individual DEMs, in order to propagate the uncertainties into the so-called DEM of Differences (DoD) map (e.g., Blasone et al., 2014;

Bossi et al., 2015; Moss, 2000; Scheidl et al., 2008; Theule et al., 2012), and then assess the significance of the propagated uncertainty (Bangen et al., 2016; Cavalli et al., 2017; Wheaton et al., 2010). The Iterative Closest Point (ICP) algorithm has been successfully used to ameliorate co-registration errors where data from individual flightlines can be used (Besl and McKay, 1992; Chen and Medioni, 1992; Zhang, 1994). The correction is based on a least squares adjustment (similar to that of Akca, 2007), which matches the surface shape between each track to individually align the tracks relative to a reference point cloud (e.g., Brasington et al., 2000; Lane et al., 2003; Milan et al., 2007). The ICP procedure allows to obtain the alignment between two point clouds to be as close as possible (e.g. James and Robson, 2014; Micheletti et al., 2015). Since I have reliable LiDAR data collected in 2013, and I could use this as the reference elevation dataset for aligning the 2007 LiDAR flightline(s), I chose to apply ICP procedure. In order to assess the DEM accuracy I assumed the propagated DEM uncertainty in the DoD as uniform, and determined a minimum level of detection of above which changes were considered real (Brasington et al., 2000, 2003; Fuller et al., 2003). This approach has been successfully used in recent analogue case studies (e.g., Bossi et al., 2015; Cavalli et al., 2017).

Table 3.1 - Details of airborne survey of Súgandafjörður and Skutulsfjörður fjords for year 2007 and year 2013.

Date of collection	Type of data	Survey instrument	Survey details
05 August 2007	Aerial photography	Leica-Wild RC10	63 photographs
	LiDAR data	Optech ALTM3033	17 lines, 68 M Points, 2.5 points/m²
12 August 2013	Aerial photography	Leica RCD 105	340 photographs
	LiDAR data	Leica ALS50-II	23 lines, 287 M Points, 1.5 points/m²

The 2007 LiDAR point data have horizontal and vertical shifts of up to 2 m between flightlines caused by a lack of between-track corrections in the initial processing (such errors are particularly problematic in steep terrain, see Favalli et al. (2009) for a full analysis). The 2013 data by comparison have averagely 6 cm vertical and horizontal differences between overlapping flightlines. I used only one flightline from the 2007 LiDAR data and cropped out the area of interest in order to reduce the errors from the LiDAR data processing. Cropping the dataset into a relatively short along-track segment (1.5 km) reduces the errors introduced by poorly integrated flight navigation and positional information. I then corrected the mis-alignment between the 2013 and 2007 datasets by means of the open source CloudCompare software, using an implementation of the ICP algorithm. I used the point cloud from the 2013 LiDAR data as the reference data for the 2007 data, as the 2007 cloud had more severe co-registration issues. Once corrected, the mean value of the normal distances of the 2007 point cloud from the 2013 reference is 0.49 m (standard deviation 0.28 m); from this value I defined the minimum level of detection as ±0.5 m.

After the co-registration, I imported the point clouds into ArcGIS and gridded the LiDAR data at 1 m/pixel, using the return time of the last peak of light to reach the receiver from the LiDAR laser shot, which is generally assumed to be the ground return. To do so, I used the LAStools extension for ArcGIS, which temporarily triangulates the LiDAR points into a Triangulated Irregular Network (TIN), and then rasterises the TIN into a Digital Elevation Model. The rasters were constructed so as to be orthogonal, i.e. so that the pixel-size and pixel-centres were the same. Finally, using ArcGIS, I calculated elevation changes and

volumes by subtracting the 2007 gridded data from the 2013 data, producing the DoD.

3.3.2 DEM of Difference Error Propagation

Any individual errors in the DEMs derived from the LiDAR, generated during surveying and post-processing, are propagated into the DoD (Goulden and Hopkinson, 2010). The DoD error varies spatially and arises from factors such as steepness of the terrain (causing data-gaps), the growth/change of dense vegetation, the varying density of the point clouds (data-gaps or false-smoothing) or misalignment between datasets (which causes an increase in error with the measurements between different datasets; Reuter et al., 2009). On the majority of the hillslope of Ísafjörður, between 2007 and 2013 there are few changes in elevation above the minimum level of detection (less than 0.5 m vertical change for 89% of the area analysed), and those that do occur are usually caused by noise or artefacts in the data (e.g., Figure 3.3A-D). Figures 3.3A and B show areas with no observable differences in the aerial photographs between 2007 (Figure 3.3A) and 2013 (Figure 3.3B), yet detectable differences in the DoD. Apparent elevation changes of up to ±5 m in the DoD are caused by the steepness of the bedrock cliff – where different (sub-pixel) horizontal positions of the laser spots between years result in large differences in the height values. Artefacts with a magnitude of ±2.5 m can be caused by growth and/or changes in vegetation, but such example can be easily identified by comparison with the aerial photographs (Figure 3.3C-D).

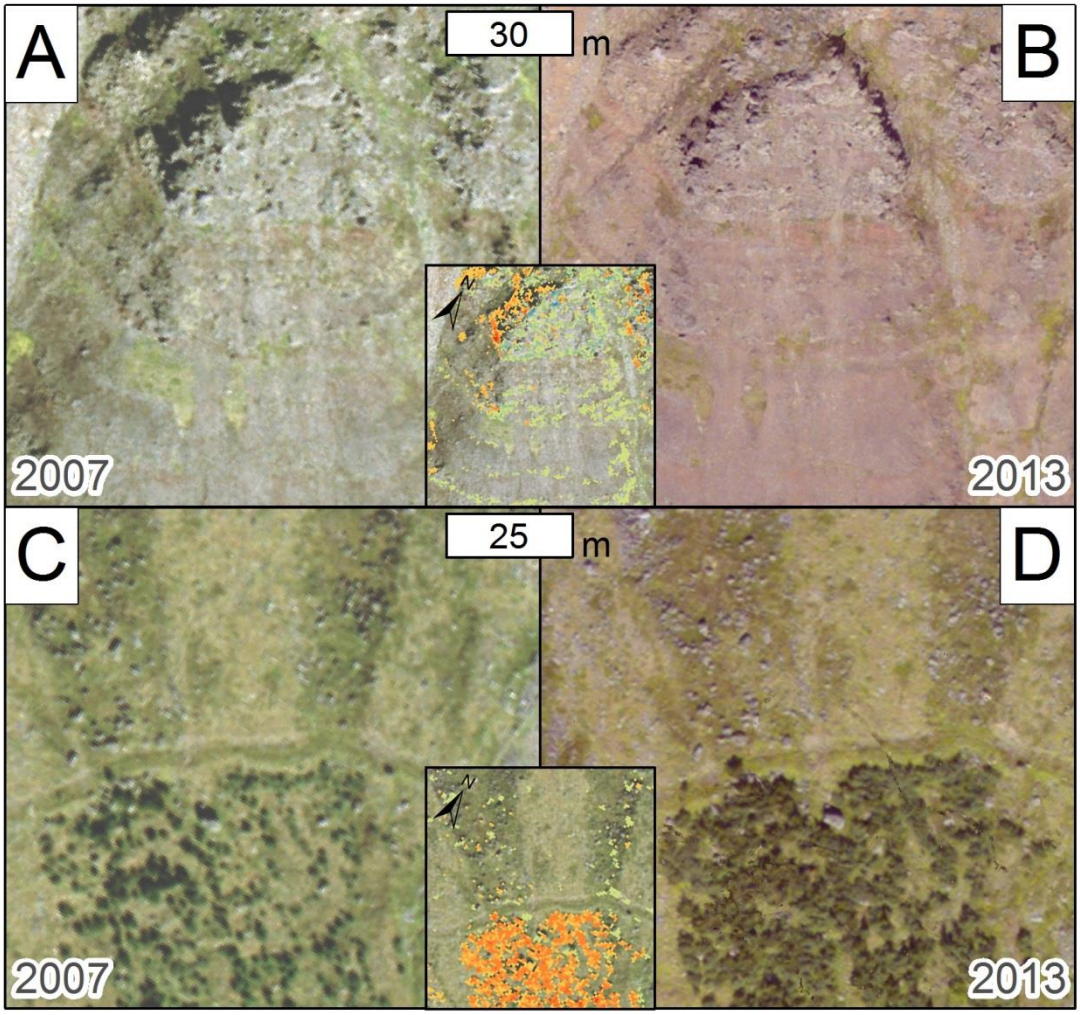

Figure 3.3. DEM of difference error propagation. Aerial photographs from 2007 (left side) and 2013 (right side) of a portion of the steep cliff above Ísafjörður (A, B) and of the forest on ESE side of the town (C, D) showing different sources of noise in the map of difference in elevation (in the centre, see Figure 3.5 for legend). Noise has been cleaned by checking for changes in the aerial photographs and distinguishing the signal.

The deposited and eroded volumes along and within the debris-flow tracks are key metrics in this study, so I explicitly derived the effects of errors on my volume calculations, using the DoD to determine the relative absolute and percentage errors in the estimates (Table 3.2). Firstly, I manually selected areas lacking visible change from aerial photographs ("stable areas") and with similar setting (i.e., slope angles and vegetation/materials) to the debris flows analysed, and I

calculated their volume changes. I then divided the volumes of the sampled debris flows obtained from the DoD by the area of the selected zones that showed no changes in the aerial images, and multiplying the results by the area of the sampled debris flows. The volume error calculated with this approach depends on the scale of the process (when the uncertainty on the measurements have minimum values, errors are not proportional to the measurement), so errors are low for medium-scale flows (volumes between 1000-100,000 m^3; Innes, 1983), ranging between ±3% and ±5% for deposited volumes and ±4% for eroded volumes. Small-scale flows (volumes of 1-1000 m^3; Innes, 1983) often have higher relative error because they cover smaller areas and mobilise less material, giving calculated errors of ±9-11% for deposited volumes and ±5-7% for eroded volumes. Particularly high values of error occur where small volume flows cover large spatial areas. Furthermore, some of the error values for volumes are relatively large (see Table 3.2), because I have used a fixed vertical uncertainty, so zones whose volume values are dominated by vertical changes with magnitudes close to that of the minimum level of detection (±0.5 m) have large percentage errors.

Table 3.2 - Results of the measured eroded and deposited volumes and other parameters of debris flows.

Debris flow ID		Erosion (m^3)	Error (m^3)	Error(%)	Deposition (m^3)	Error (m^3)	Error (%)	Area (m^2)	Maximum lenght (m)	Chute width (m)	Elevation drop (m)
Debris flow 1DF		8552	± 322	± 4	4079	± 223	± 5	23952	803	125	406
Subareas ID	**1DFa**	5622	± 132	± 2	629	± 91	± 15	9845	168	-	-
	1DFb	256	± 31	± 12	2234	± 21	± 1	2300	129	-	-
	1DFc	2674	± 159	± 6	1216	± 110	± 9	11807	506	-	-
Debris flow 2DF		5001	± 183	± 4	3760	± 127	± 3	13596	727	74	411
Subareas ID	**2DFa**	3601	± 28	± 1	63	± 19	± 31	2077	51	-	-
	2DFb	201	± 43	± 22	3058	± 30	± 1	3225	156	-	-
	2DFc	1198	± 111	± 9	639	± 77	± 12	8294	520	-	-
Debris flow 11DF		862	± 46	± 5	339	± 32	± 9	3394	325	29	235
Subareas ID	**11DFa**	832	± 31	± 4	70	± 21	± 30	2303	187	-	-
	11DFb	30	± 15	± 49	269	± 10	± 4	1091	138	-	-
Debris flow12DF		628	± 42	± 7	271	± 29	± 11	3131	286	32	207
Subareas ID	**12DFa**	549	± 24	± 4	82	± 16	± 20	1777	137	-	-
	12DFb	78	± 18	± 23	188	± 13	± 7	1354	149	-	-

3.3.3 Track selection, naming and segmentation

I studied four debris-flow tracks on the slope above Ísafjörður (Figure 3.1B). I adopted and extended the naming protocol for debris-flow tracks used in Conway et al. (2010), who studied debris flows in the same area. They named 10 debris-flow tracks using numbers from 1 to 10 followed by the acronym “DF”. As two of the debris-flow tracks coincide with two tracks analysed in this study, namely debris flows 1DF and 2DF, I used those names. I continued the same numbering system for two newly developed debris flows: debris flows 11DF and 12DF (Figure 3.1B).

I selected these four tracks because they show substantial (>±0.5 m) geomorphic changes between 2007 and 2013 in the differenced LiDAR datasets. These include morphological changes in the chutes at the front edge of the Gleiðarhjalli bench and in the upper part of the channels. I focussed my analysis at these locations, being the zones of the debris flows where the majority of the changes occurred. Two of the four tracks, 11DF and 12DF (Figure 3.2B), did not

exist in the 2007 data. The other two, 1DF and 2DF tracks (Figure 3.2A-B) were already present in 2007, but they had changed their form by 2013. Because 1DF and 2DF are different from 11DF and 12DF in their size, morphology and the processes that controlled their formation (as discussed below), I treat the two pairs of debris flows separately in the “Results” and “Discussion” sections.

Having differenced the LiDAR datasets, I observed that, within the four debris-flow tracks, elevation changes occur in clearly defined, down-flow spatial domains. Since the debris flows tracks present an atypical distribution of volumes, I segmented them and outlined different subareas according to the predominance of negative or positive elevation change from visual inspection; for example, negative elevation change was predominant in the upper part of 2DF track, so I split it from the strongly contrasting area below, characterised by a positive change in elevation (see Figure 3.5A in “Results” section). This in turn allowed us to calculate the eroded and deposited volumes for these subareas and for the debris-flow tracks as a whole (see Table 3.2 in “Results” section).

3.3.4 2007-2013 Comparison

In order to analyse the changes occurring along each debris-flow track, I adopted the following approaches:

i) in order to evaluate the deposited and eroded volumes within each debris-flow track, I derived the volumetric changes in these zones (i.e., debris-flow tracks and debris-flow sub-areas);

ii) I visually identified geomorphological changes occurred along the tracks in aerial photographs. Additionally, I performed repeated field observations (summer 2012, 2013, 2016) in order to check what I observed and mapped from remote sensing;

iii) I created a slope map at 1 m/pixel using the standard tools provided in Spatial Analyst of ArcGIS; the slope angle was derived using the steepest downhill slope as calculated by fitting a plane through the eight nearest neighbours (neighbourhood slope algorithm, also known as the average maximum technique; e.g., Burrough et al., 2015). Slope was evaluated for each sub-areas of the four debris flows: I took topographic profiles along the line of steepest descent, then extracted both the elevation values and the slope values for both the 2007 and 2013 DEMs along those lines. Accumulation of boulders could generate high slope angles where they pile onto each other, but in my case boulders do not register in the slope map as they are smaller than its resolution.

3.4 Results

3.4.1 Morphology and morphometry of debris-flow tracks 1DF and 2DF

1DF and 2DF are the largest debris-flow tracks analysed in this study, having mobilised volumes up to 14 times larger over areas up to 8 times wider than 11DF and 12DF (see dimensional details in Table 3.2). They are deeply incised and have chutes carved in bedrock in their upper part, with channels cutting slope deposits (Figure 3.2). In their terminal parts it is possible to observe fan-shaped debris accumulations (Figure 3.2). Over the whole debris-flow tracks, total erosion volumes are larger than their total deposition volumes. 1DF has an erosion volume more than twice the depositional volume, while 2DF has 25% less deposition than erosion over the whole volume mobilised (see Table 3.2). The net sediment budget should be near zero, but the deposits of the terminal lobes that reached the defensive protections were removed by the local authorities.

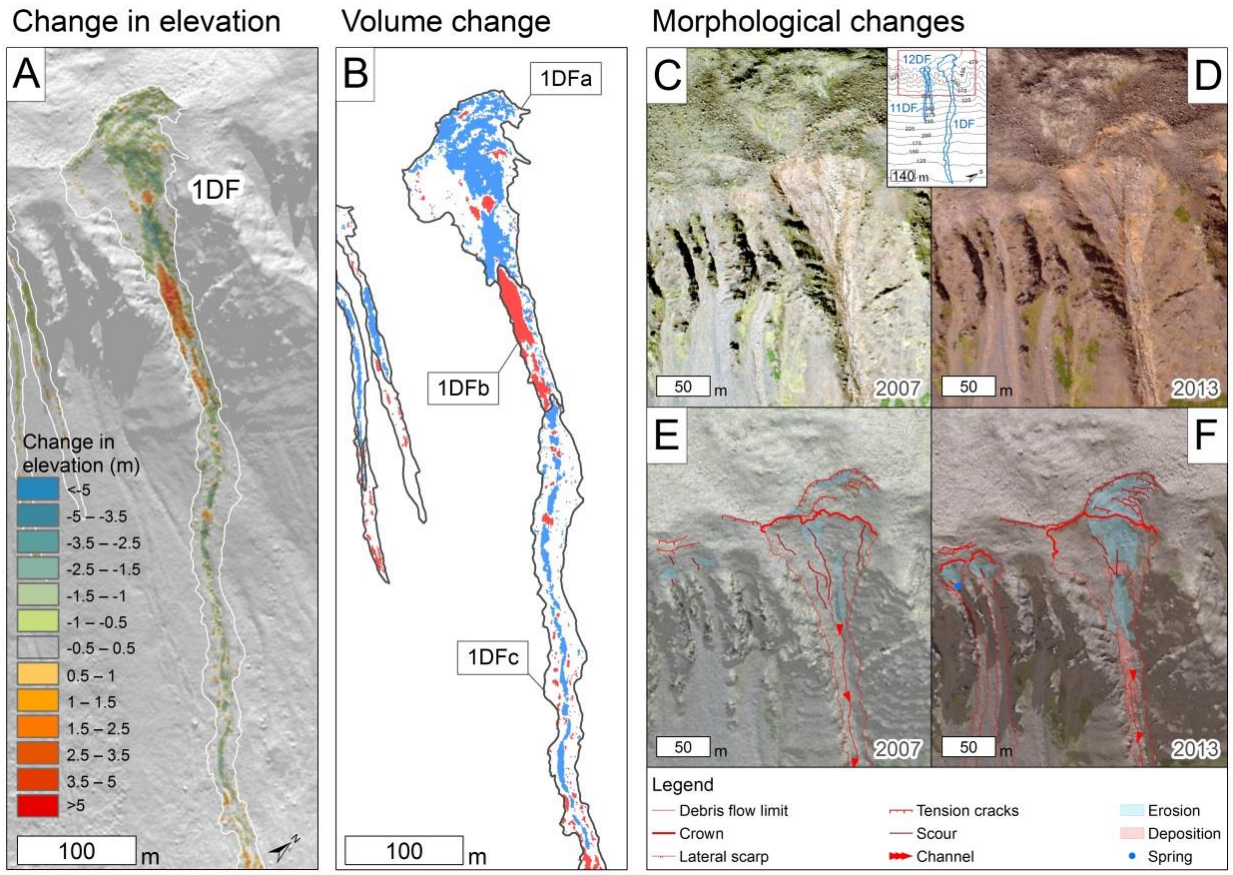

Figure 3.4. Morphology and morphometry of debris -flow track 1DF. (A) Elevation-difference map of debris-flow track 1DF obtained calculating the difference in elevation occurred between 2007 and 2013, overlying the hillshade model derived from 2013 LiDAR. (B) Maps of the erosion and deposition distribution of debris-flow track 1DF derived by differencing the LiDAR generated topography from 2007 and 2013. The debris flow was segmented in subareas of prevailing erosion and deposition along its length. Distal lobes extensively modified during protection works (Figure 3.10) are omitted to avoid confusion. (C-F) Aerial photographs of the upper zones of debris flows 1DF, 11DF and 12DF from 2007 (C) and 2013 (D) compared, with simplified sketches of the main observable features (E and F, where the hillshade models derived from 2007 and 2013 LiDAR data respectively are overlain by aerial photographs in transparency).

1DFa and 2DFa: Most of the erosion in 1DF and 2DF occurs in their upper subareas (designated as “a”), namely in the perched material at the edge of the bench and in the apical chutes carved into the bedrock. Erosion occurs in sub-areas 1DFa and 2DFa, amounting respectively to 5600 m^3 and 3600 m^3 (Figure 3.4B for 1DF, Figure 3.5B for 2DF, Table 3.2), over a great range of slope (Figure

3.6). For both the debris-flow tracks in the time span between 2007 and 2013, the slope angle below the scarps and in the apical chutes remains on average above 35° (Figure 3.6A-H, Table 3.3). Erosion is also evident from the morphology of the upper sub-areas 1DFa and 2DFa. In 1DFa in 2007, tension cracks, associated with areas of erosion located directly below them, cut the bench above the crown (Figure 3.4C, E), with three more appearing in 2013, concomitant with enlarged erosion areas (Figure 3.4D, F). In 2DFa, the main failure scarp in 2013 originated from two already well defined release scarps that since 2007 regressively eroded 22 m (Figure 3.5E, F; note the paler material marking the main scarp below the crown in Figure 3.5D). Tension cracks that are present above the crown in 2DFa in 2007 had been partially erased by regressive erosion by 2013. Springs rise at the contact between the deposits perched on the bench and the underlying bedrock (Figure 3.5D, F).

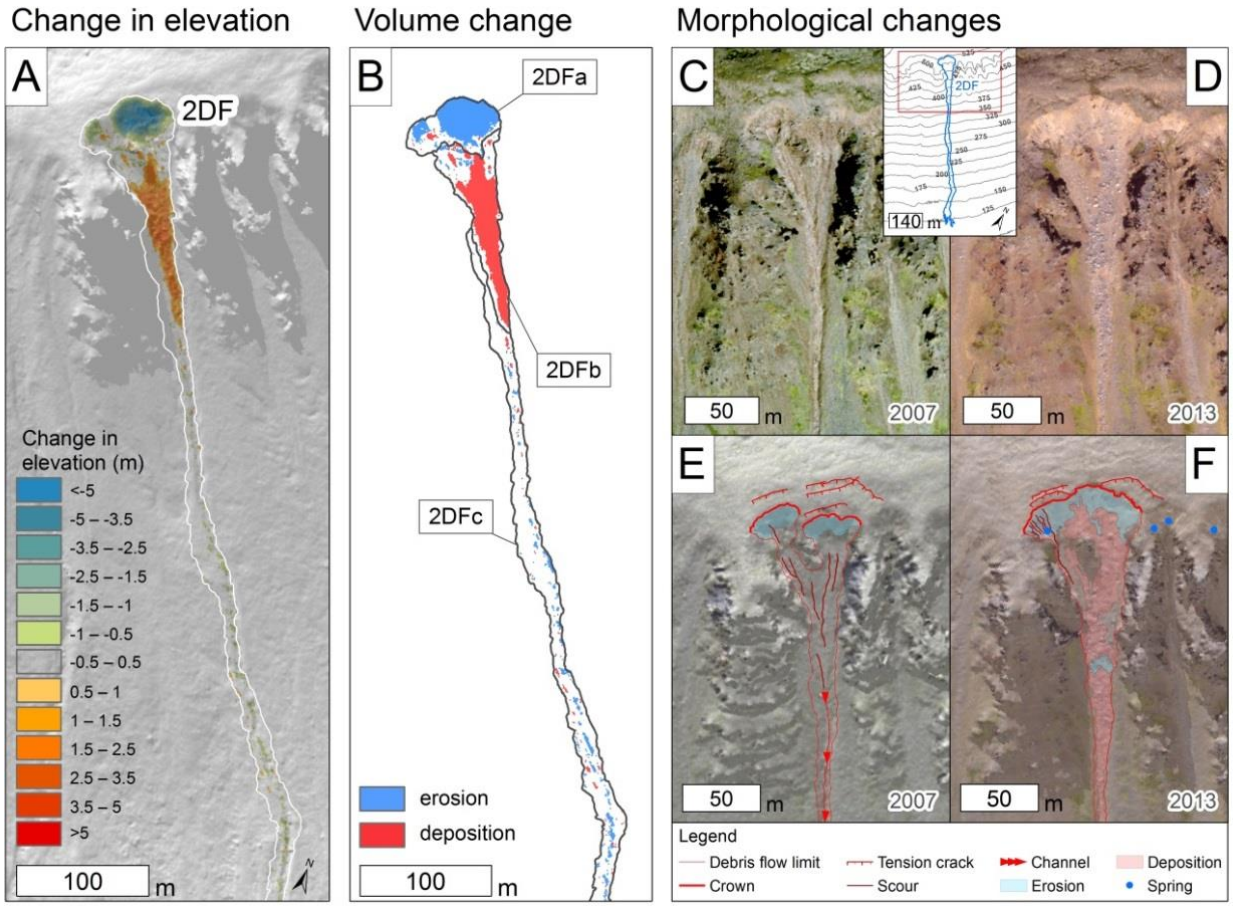

Figure 3.5. Morphology and morphometry of debris -flow track 2DF. (A) Elevation-difference map of debris-flow track 2DF obtained calculating the difference in elevation occurred between 2007 and 2013, overlying the hillshade model derived from 2013 LiDAR. (B) Maps of the erosion and deposition distribution of debris flow track 2DF derived by differencing the LiDAR generated topography from 2007 and 2013. The debris flow was segmented in subareas of prevailing erosion and deposition along its length. Distal lobes extensively modified during protection works (Figure 3.10) are omitted to avoid confusion. (C-F) Aerial photographs of the upper zones of debris flow 2DF from 2007 (C) and 2013 (D) compared, with simplified sketches of the main observable features (E and F, where the hillshade models derived from 2007 and 2013 LiDAR data respectively are overlain by aerial photographs in transparency).

1DFb and 2DFb: Immediately below 1DFa and 2DFa, positive elevation change of up to ~5 m occurs in the chutes and in the upper channels (Figure 3.4A for 1DF, Figure 3.5A for 2DF). The majority of the accumulated deposits of 1DF and 2DF, 2200 m^3 and 3100 m^3 respectively (Table 3.2), lie in these subareas (designed as “b”). In 1DFb, the slope angle values for 2013 are equal to or less

than those of 2007, with deposition occurring at a high slope gradient (mean of 38° in 2013, 49° in 2007, Table 3.3). In subarea 2DFb, slope angle values remained constantly high along the profile between 2007 and 2013 (mean is 37-38°, Table 3.3, Figure 3.6E-H). In 1DFb, the aerial images show that new deposits have been transferred into the chute by 2013, obliterating the scours and filling the zones of erosion that were present in 2007 (Figure 3.4C-F). In 2DFb, the upper catchment, the chute and the upper channel were largely empty of debris in 2007, whereas by 2013 they are filled by a deposit of blocky material (Figure 3.5C-F).

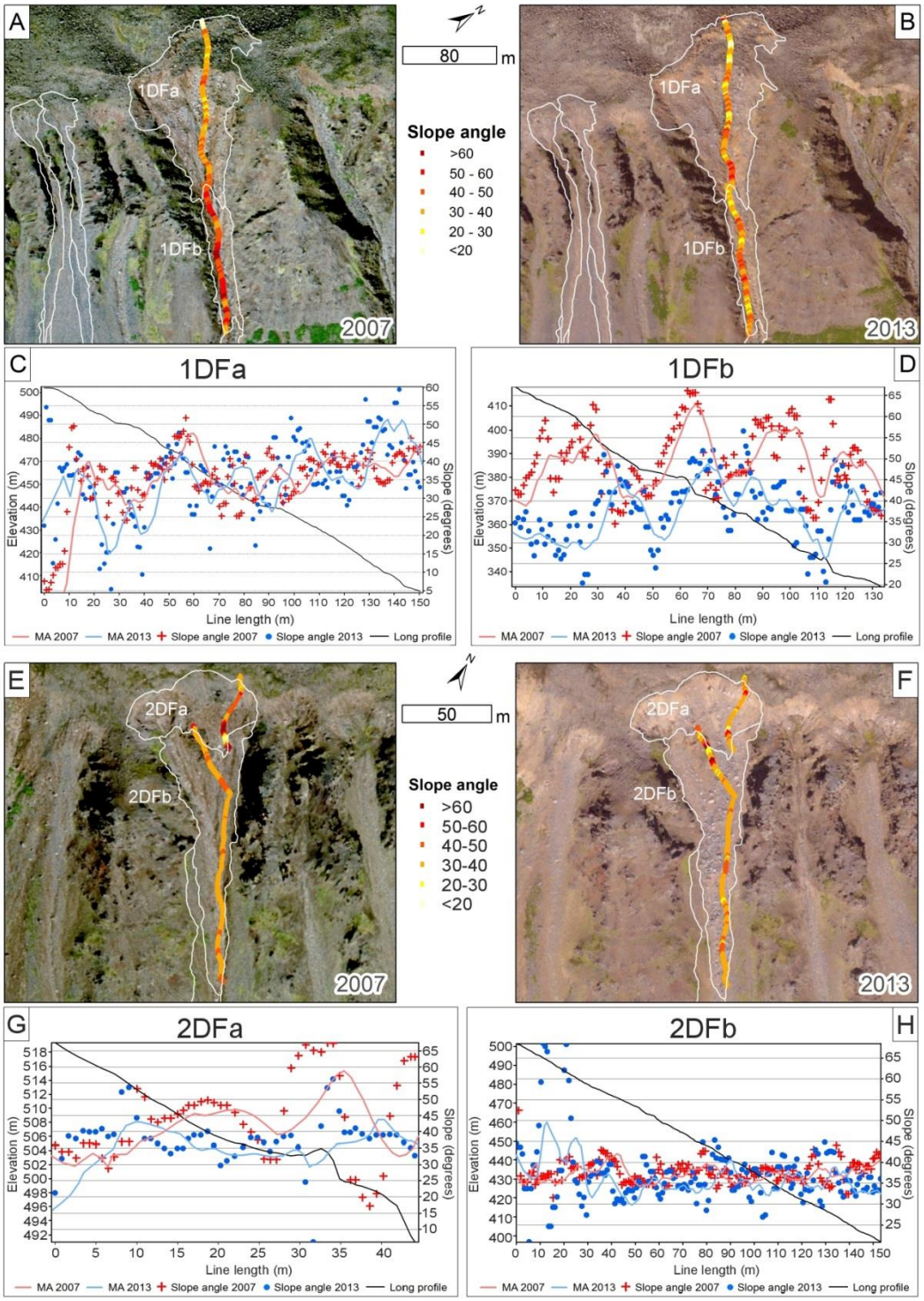

(Figure continues in the next page)

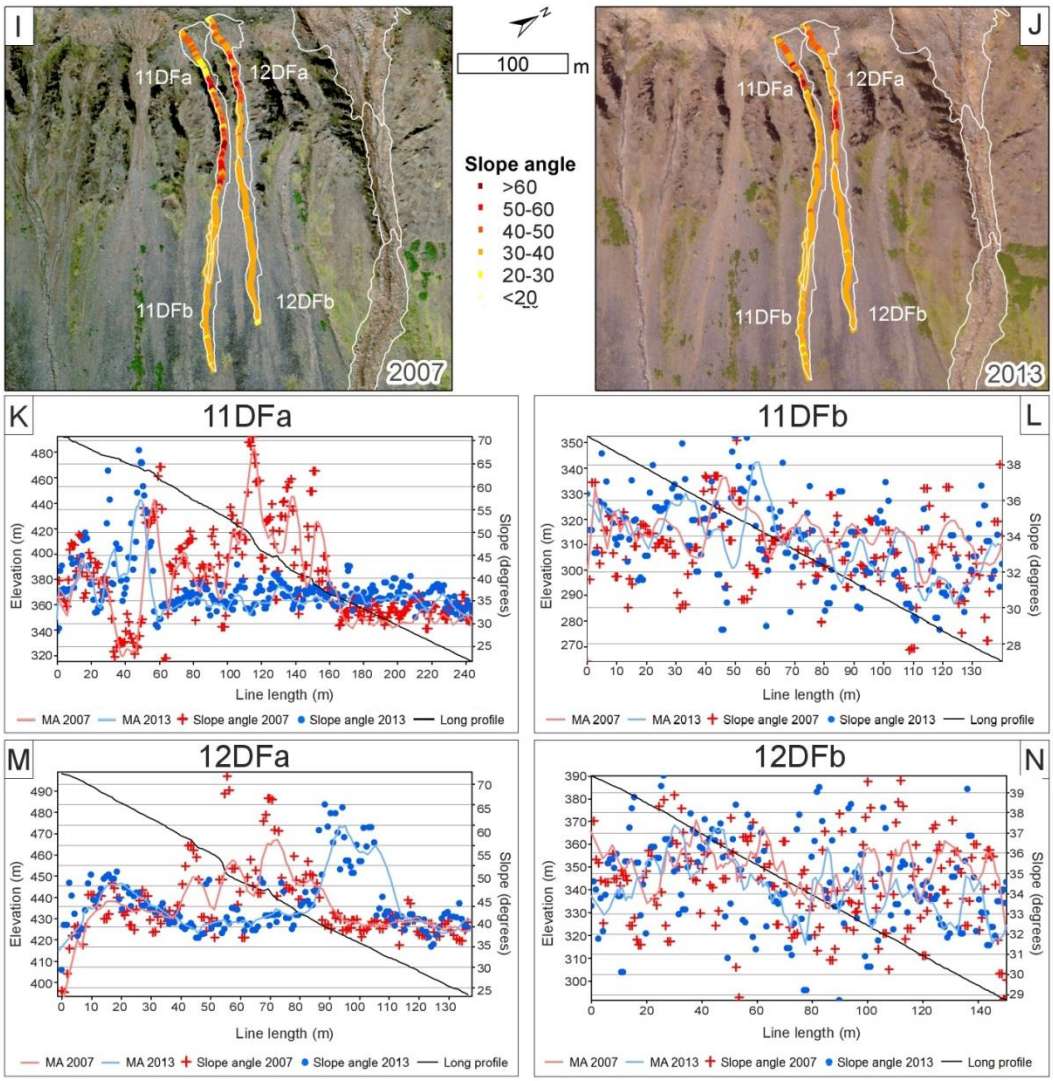

Figure 3.6. Slope analysis of debris flows. Aerial photographs of the upper zones of debris flows from 2007 (A, E, I) and 2013 (B, F, J) showing the steepest slope lines with colour indicating the slope values. Below, plots of the slope angles from 2007 (in red) and 2013 (in blue) against the long profile representing the terrain elevation in 2013 (black continuous line) for subareas "a" (C, J, K, M) and "b" (D, H, L, N). Red and blue continuous lines indicate the moving average (MA) for year 2007 and 2013 respectively.

1DFc and 2DFc: Further downstream, I have grouped smaller, more discontinuous zones of negative and positive elevation change of up to 1 m in magnitude in the sub-areas 1DFc and 2DFc (Figure 3.4A-B for 1DF, Figure 3.5A-B for 2DF). These zones of erosion and deposition do not correspond to the position of the channel and levees, but they alternate along the channel, almost

as far downslope as the terminal lobes. Levees are built up in association with discrete zones of erosion. Part of the debris transferred between 2007 and 2013 was deposited here (1200 m^3 in 1DFc and 600 m^3 in 2DFc, see Table 3.2). In both the subareas, the slope angle values do not greatly vary between 2007 and 2013 (Table 3.3).

Table 3.3 - Analysis and uncertainty values for slope angle values plotted on profiles in Figure 3.6

Debris flow subareas ID	2013			2007		
	Median slope	Mean slope	Standard Deviation	Median slope	Mean slope	Standard Deviation
1DFa	36.91	35.98	±10	37.29	35.33	±8
1DFb	37.96	38	±7	48.83	49.44	±8
1DFc	30.18	30.19	±11	25.83	25.95	±10
2DFa	38.08	37.61	±7	44.21	43.83	±13
2DFb	35.97	37.08	±7	37.34	37.81	±3
2DFc	32.57	31.15	±7	30.73	32.4	±12
11DFa	36.37	37.52	±5	37.58	40.43	±10
11DFb	33.85	33.74	±2	33.33	33.24	±2
12DFa	34.31	40.86	±7	37.1	40.22	±9
12DFb	34.31	34.48	±2	34.65	34.46	±2

3.4.2 Morphology and morphometry of debris-flow tracks 11DF and 12DF

Debris-flow tracks 11DF and 12DF are smaller than 1DF and 2DF (see morphometric properties in Table 3.2). They originate from the edge of the bench, and their channels are only moderately incised into the existing slope deposits. The spatial distribution of negative elevation change extends from the upper catchments, along the chutes and into the upper part of channels newly incised into the slope deposits (Figure 3.7). 11DF and 12DF tracks are unconstrained by previous levees in their mid-sections and have newly formed levees and depositional lobes in their lower reaches (Figure 3.7).

11DFa and 12DFa: On the failure scarps, the negative elevation change between 2007 and 2013 is up to 2.5 m, whereas in the chutes and channels it is up to 5 m (Figure 3.7A). Erosion is dominant in these sub-areas: 800 m^3 in 11DFa and 500 m^3 in 12DFa (Table 3.2). Both 11DFa and 12DFa erosional subareas (Figure 3.7B) show an anti-correlation in their slope profiles between the two observation dates: low slope values in 2007 match increased slope angle in 2013, and vice versa (Figure 3.6I, K, M, Table 3.3). Between 2007 and 2013, in both the upper catchments and chutes of 11DF and 12DF the slope angle in the chutes generally remained above 35°. In the 2007 aerial photographs, the presence of tension cracks and material different in colour and with fewer blocks than the surroundings in the scarp area of 11DF indicates that erosion had already occurred (Figure 3.4C, E). A well-defined main failure scarp and associated erosion are observable in the upper catchments in 2013, and two new channels overlay the coarse grey deposits of the talus slope (Figure 3.4D, F). Springs rise at the contact between deposit mantle on the bench and the underlying bedrock (Figure 3.4D, F)

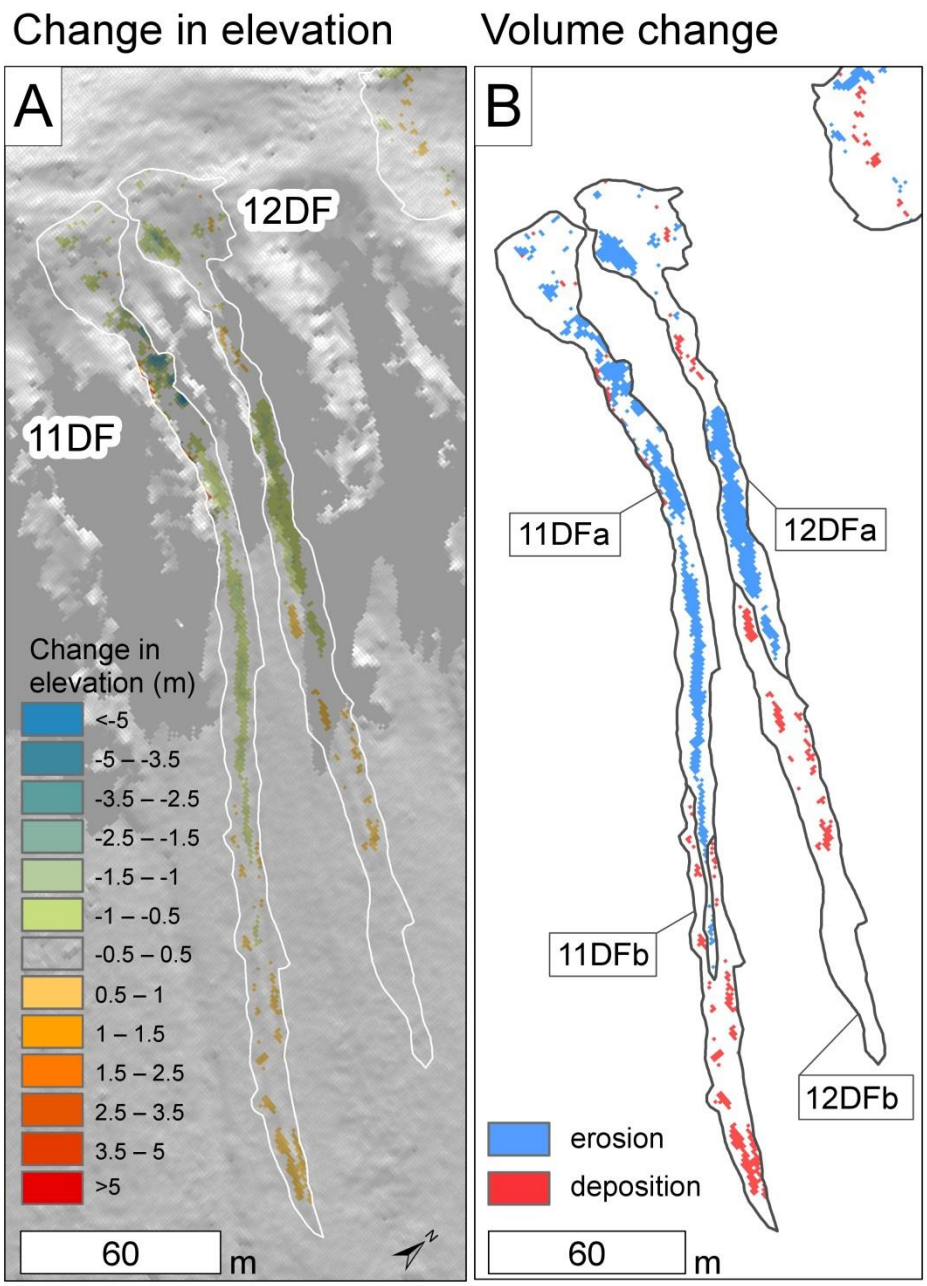

Figure 3.7. Morphology and morphometry of debris -flow tracks 11DF and 12DF. (A) Elevation-difference map of debris-flow tracks 11DF and 12DF obtained calculating the difference in elevation between 2007 and 2013, overlying the hillshade model derived from 2013 LiDAR. (B) Maps of the erosion and deposition volume distribution of debris-flow tracks 11DF and 12DF derived by differencing the LiDAR generated topography from 2007 and 2013. The debris flows were segmented in subareas of prevailing erosion and deposition along their length.

11DFb and 12DFb: These sub-areas (Figure 3.7B) show zones of positive elevation change (up to 1 m), and these take the form of slightly outlined lateral

levees and a straight terminal lobe (Figure 3.7A). These depositional landforms constitute 300 m^3 of material in 11DFb and 200 m^3 in 12DFb. The slopes along the steepest profiles of 11DFb and 12DFb show a steady trend with high average values (33°-34°) in both years (Figure 3.6J, L, N, Table 3.3).

3.5 Discussion

3.5.1 Analysis of debris-flow initiation: 11DF and 12DF

A debris flow originates by slope failure when individual failures, or numerous small failures, coalesce, transforming into a debris flow (e.g., Fairchild, 1987; Iverson, 1997; Rodolfo et al., 1996). Slope failure-initiated debris flows require the availability of loose material on steep slopes and an accumulation of water in the deposits, so they occur when rainfall and snowmelt cause an increase of pore-water pressures (Anderson and Sitar, 1995; Sidle and Swanston, 1982). This can commonly cause the rise of a water table at the contact of the debris cover with the impermeable bedrock or on top of impermeable layers (Campbell, 1975; Decaulne et al., 2005; Iverson, 1997). In the Westfjords of Iceland, long-duration rainfall and/or snowmelt associated with rain are the two main sources of water for triggering debris flows. For example, extreme rainfall of 63 mm/24h after one month of rainy days (about 140 mm of cumulative precipitation) triggered the debris-flow event in Ísafjörður in September 1996 (Smith et al., 2009). Over 40 mm of one month-cumulative precipitation related to snowmelt triggered a debris-flow event in Ísafjörður in June 1999, after a sudden (two weeks) increase in air temperature from 1-4°C to 14-17°C (Decaulne et al., 2005; Smith et al., 2009). In Decaulne et al. (2005), the initiation for the debris flow-

events in Ísafjörður in June 1999 is identified by the appearance of the subsurface runoff at the edge of the Gleiðarhjalli bench, causing erosion of material and generation of rotational slide evolving into debris flows downslope. Debris flows 11DF and 12DF — that were not present at the time of observations made by Decaulne et al. (2005) — have these characteristics. Springs coming out between the sediment mantle and the bedrock are visible in aerial images in the scarp of 11DF (Figure 3.4D,F) showing that runoff could have initiated erosional processes. This is a condition that has been observed in other environments; Bremer and Sass (2012) in the Austrian Alps identified the starting zones of debris flows at the bedrock-debris interface where runoff is concentrated. The combination of springs and loose debris has also been reported in the Alpine environment as one of the most important preparatory factors for slope failure (e.g., Marchi et al., 2002; Wieczorek and Glade, 2005). This is a plausible mechanism in Ísafjörður for the weakening and saturation of the deposits, leading to the development of discrete slope failures evolving into debris flows.

Debris flows 11DF and 12DF have a simple morphology: erosion in the upper part (11DFa with -832 ±31 m^3, and 12DFa with -549 ± 24 m^3) and deposition in the terminal part (11DFb with 268 ±10 m^3, and 12DFb with 188 ± 13 m^3). Erosion extends from the edge of the bench, to the chutes, into the newly formed channels on the hillslope. Simple curved main scarps and crown-parallel tension cracks are due to rotational sliding process (Figure 3.4C-F, Figure 3.8A). A negative elevation change of up to 5 m in the chute and in the channel shows that, once slope failure started from the front of the bench, it mobilised material that was already in transfer, and with saturation evolved into a debris flow, forming a terminal lobe and lateral levees. Sediment transfer is further evidenced by the

fact that in the chutes and upper channels, low slope values in 2007 match increased slope angles in 2013, and vice versa. The entrainment and transport of debris from the chutes and channels is also expected because of their gradient above 35° both in 2007 and 2013. Debris-flow tracks 11DF and 12DF are short: <250 m long.

My suite of observations and measurements for 11DF and 12DF tracks fits with the characteristics of the slope failure process reported in literature. Theule et al. (2012) used multi-temporal topographic surveying from TLS and ALS to monitor sediment transport by two debris flows in the French Alps. Low rainfall intensity events caused short-runout debris flows (less than 100 m) generated by talus slope failure (magnitude of erosion 266 m^3, magnitude of deposition 268 m^3). Cannon et al. (2001) reported ~84 debris flows in Colorado initiated by landslides; they back-traced the debris-flow paths to discrete landslide-scar sources and estimated their volumes, which had a range of ~95 to 2500 m^3. Debris flows in Switzerland have been shown to originate from individual shallow rotational slides on slopes with angles between 25° and 45°, and with volumes of tens to a few hundred cubic meters (Hürlimann et al., 2003). The order of magnitude of the volumes and the size and morphological characteristics of the debris flows analysed in these three studies match well with my quantification and observations of debris-flow tracks 11DF and 12DF (Figure 3.8A).

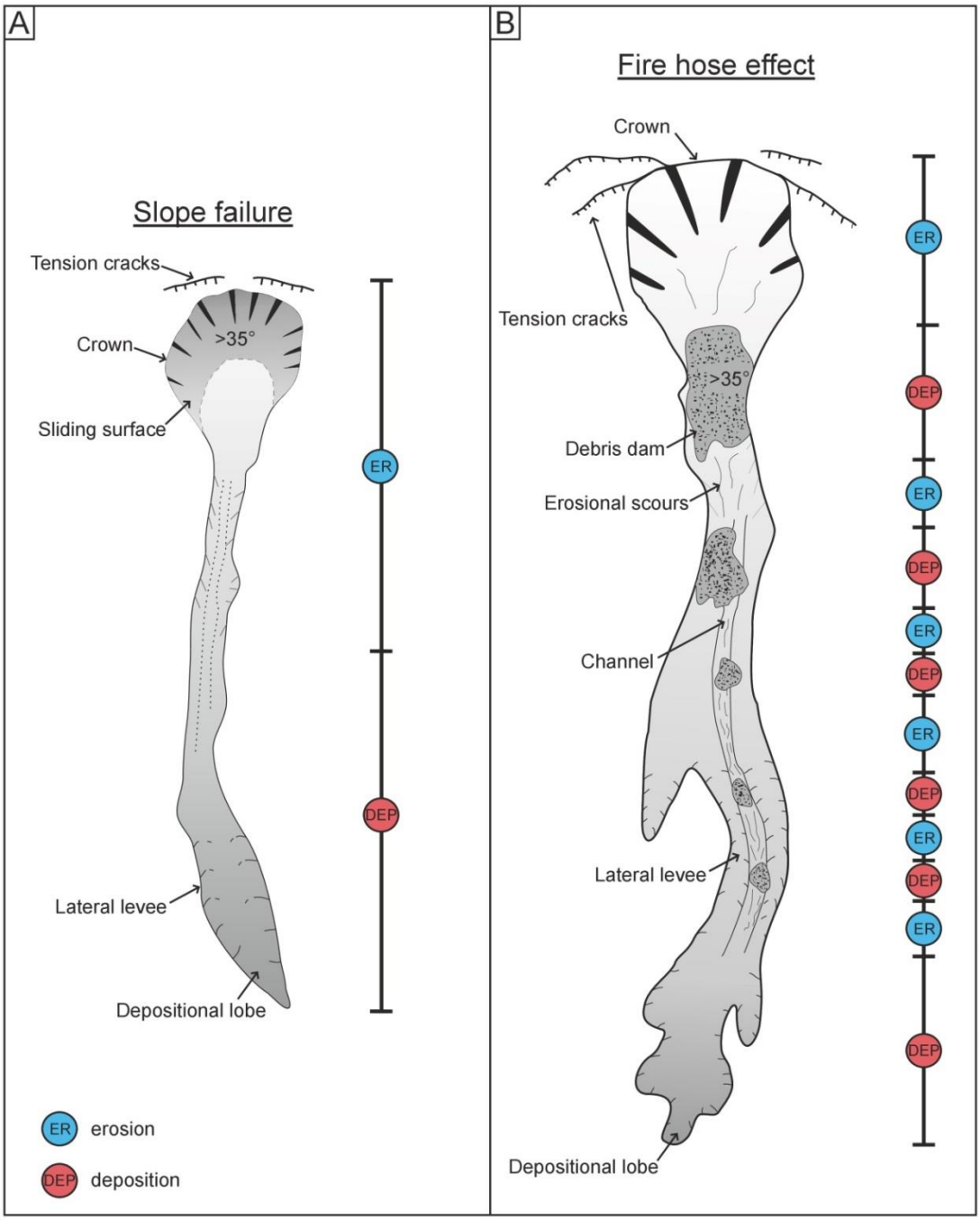

Figure 3.8. Simplified sketch of the main geomorphological characteristics of the slope failure (A) and the fire-hose effect (B).

3.5.2 Analysis of debris-flow initiation: 1DF and 2DF

Material released by slope failure can be transferred into a channelized area. Then, debris can either be transferred down slope, if saturated, evolving into a debris flow, or can cease to be mobile, generating a debris dam and obstructing the channel (Bovis and Jones, 1992; Iverson et al., 2000). Formation of such a debris dam creates the optimal conditions for the development of the fire-hose effect. This mechanism occurs when an overland flow is concentrated by chutes or depressions in the bedrock and becomes a debris flow when impinging on loose debris accumulated in those depressions (Berti et al., 1999; Berti and Simoni, 2005; Coe et al., 1997, 2008; Curry, 1966; Fryxell and Horberg, 1943; Glancy and Bell, 2000; Godt and Coe, 2007; Johnson and Rodine, 1984; Larsen et al., 2006). Coe et al. (2008) reported that the initiation via the fire-hose effect is controlled by the sediment supply, rather than by the moisture level.

In the Westfjords, Decaulne and Sæmundsson (2006) link the presence of release scars to debris flows originated by rotational slides. In Ísafjörður, debris flows tracks 1DF and 2DF – not of new formation as 11DF and 12DF, but already formed at the time of the surveys – have curved release scarps showing signs of regressive erosion, ephemeral springs at the contact between loose debris and bedrock, erosion in the upper catchment (subareas 1DFa and 2DFa), and a main depositional area in the chute (subareas 1DFb and 2DFb). These are all evidence of slope failure, which through rotational sliding eroded material in the upper catchments and dammed the chutes depositing up to 3000 m^3 of debris at high slope angles (>35°). The slope failure process in this case has generated the

preparatory conditions for future debris flows to occur. It is improbable that the deposits currently located in the chutes remains stable.

In particular, I believe that the debris-flow tracks 1DF and 2DF show the preparatory conditions for the fire-hose effect. 54.7% and 81.3% respectively of the overall deposited volumes in 1DF and 2DF are gathered in the chutes. It has been observed that hundreds to few thousand cubic meters of loose deposits reflects pulses of sediment supply from upslope catchments (Theule et al., 2015), and that these pulses can be induced and fed by processes such as rock falls (Loye et al., 2016). Cascades of processes leading to slope failure has been observed in the field and in experiments, where surface water runoff causes erosion and accumulation of material, subsequently mobilised by shallow slides. Depending on the topography, sediment can be re-accumulated and periodically released as a debris flow surge when impinged on by water flow (Hu et al., 2016; Kean et al., 2013).

Debris flows can be initiated by saturation and breaching of dams of sediment located in channels. I suggest that in 1DF and 2DF tracks there has been scarp failure and sediment storage in the chutes and channels, a setting that is favourable to fire-hose debris flows. I hypothesise that some of the accumulated debris has already been transported downslope by the fire-hose effect. This is suggested by a trend of alternating zones of erosion and deposition throughout the 1DF and 2DF tracks and at different scales in the different subareas (Figure 3.8B). For example, in the lower parts (1DFc and 2DFc) of debris-flow tracks 1DF and 2DF, small zones of deposition and erosion are aligned within the channel, and along the central steepest path in the upper catchments and apical chutes, particularly clearly in 1DFa (Figure 3.4B, Figure 3.5B). I infer that this

setting cannot be due to the failure of pre-existing material, such the collapse of lateral levees or lateral banks (Frank et al., 2015; Hu et al., 2016), as in the DoD erosion of these features would be visible in correspondence of deposition in the chute or the channel. Therefore, I interpret these alternating zones of erosion and deposition to be likely the result of the transport of debris by the fire-hose effect: this has caused instantaneous sediment-entrainment, as the built-up of the lateral levees occurs in association of discrete erosion zones in the chutes and channels (potential impact points; Coe et al., 2008). The presence of these fire-hose events is also supported by the erosion volume being larger than the deposited one (i.e. debris has left the survey zone).

In Table 3.4, I compare my volume calculations to the volume results obtained by Decaulne et al. (2005) and Conway et al. (2010). My deposition results for 1DF (4079 m^3) and 2DF (3760 m^3) are similar to those of Conway et al. (2010): 8287 m^3 and 1925 m^3 respectively for the same tracks. The deposition value calculated for debris flow 2DF by Decaulne et al. (2005) matches fairly well with my calculation, but the event described by these authors extended to the base of the slope. In my study, much of the total deposited volumes for 1DF and 2DF lies in the chutes (1DFb with 2234 ± 21 m^3 and 2DFb with 3058 ± 30 m^3 in Table 3.4), rather than along the tracks, or in the depositional lobes as measured by Decaulne et al. (2005) and Conway et al. (2010). These volumes are of the same order of magnitude as the material mobilised by a debris flow in 1999 (estimates at 3000 m^3 for 2DF; Decaulne et al., 2005) and from 1999 to 2007 (1925 m^3 for 2DF; Conway et al., 2010). Previous studies (Conway et al., 2010; Decaulne and Sæmundsson, 2006; Glade, 2005) recognised debris flows that had originated through the fire-hose effect in other areas of the Westfjords in Iceland, but with a

lower frequency (~10 years return) than the mean return period of Gleiðarhjalli area (4-5 years; Decaulne et al., 2005). Those previous studies considered the fire-hose effect to only involve smaller volumes of material (700-1000 m^3), based on debris collected in the chutes by weathering and erosion of the bedrock (i.e. those flows are most likely supply-limited). Since 2007, much larger volumes gathered in the chutes of 1DF and 2DF tracks (subareas “b”) at high slope angle (~37-38°, see Figure 3.6). This setting is vulnerable to the fire-hose effect, and shows high potential mobility of the debris in the chutes of the 1DF and 2DF tracks.

Table 3.4 - Data regarding the debris flows described in this study, compared with the data of Conway et al. (2010) and Decaulne et al. (2005).

Debris flow ID	Years of activity	Years of data collections and authors	Method of survey	Estimated deposition m^3 (standard error)	Deposition m^3 (relative uncertainty) - This study	Estimated erosion m^3 (standard error)	Erosion m^3 (relative uncertainty) - This study
1DF	June 2006, 2007-2013	Summer 2007, Summer 2008: Conway et al. (2010)	LiDAR/airborne photographs, DGPS	8000 (±66%)	_	41000 (±38%)	_
		Summer 2007, Summer 2013: This study	LiDAR/airborne photograph	_	4079 (±5%)	_	-8552 (±4%)
2DF	1965, June 1999, June 2006, 2007-2013	Summer 1999: Decaulne et al. (2005)	Aerial photographs, field survey	3000	_	_	_
		Summer 2007, Summer 2008: Conway et al. (2010)	LiDAR/airborne photographs, DGPS	2000 (±134%)	_	16000 (±62%)	_
		Summer 2007, Summer 2013: This study	LiDAR/airborne photographs	_	3760 (±3%)	_	-5000 (±4%)
11DF	2007-2013	Summer 2007, Summer 2013: This study	LiDAR/airborne photographs	_	339 (±9%)	_	-862 (±5%)
12DF	2007-2013	Summer 2007, Summer 2013: This study	LiDAR/airborne photographs	_	271 (±11%)	_	-628 (±7%)

3.5.3 Summary of debris-flow initiation processes identified in Ísafjörður

I have shown that the use of differenced LiDAR datasets for volume change detection, integrated with slope and geomorphic analysis from remote sensing data, and demonstrate its potential for identifying debris-flow initiation processes. The deposits in the chutes described by us would be “invisible” in the datasets of Conway et al. (2010) and Decaulne et al. (2005), since in their field-based studies they could not quantify the material in the chutes of the flows. My approach of identifying pre- and post-events changes in topography, volumes, slopes and morphology allowed us to distinguish between slope failure initiation process and the formation of preparatory conditions for the fire-hose effect without having to witness them, making possible a discrimination that would have been virtually impossible otherwise.

The slope failure and the fire-hose effect as initiating processes for debris flows in the Westfjords were previously only hypothesised (Conway et al., 2010; Decaulne et al., 2005; Decaulne and Sæmundsson, 2006). The comparison of airborne datasets with a six-year separation shows that the four debris-flow tracks analysed are geomorphically distinctive (see Figure 3.8) and show two different modes of flow initiation and evolution:

(1) Slope failure is the mechanism that triggered the newly-developed debris flow 11DF and 12DF, and that caused erosion in the upper catchments and deposit transfer in the chutes of the already-formed 1DF and 2DF tracks.

(2) I have been able to quantify the magnitudes of the volumes of material stored within debris-flow chutes and tracks above Ísafjörður by slope

failure: this has produced debris dams at high slope angle, forming the preparatory conditions for the fire-hose effect. Part of this debris has probably already been transported by this mechanism. The large volumes of material stored in the chutes and channels of 1DF and 2DF (2000-3000 m^3 in subareas 1DFb and 2DFb) in the past were moved in a single sudden event, so they provide a substantial amount of material that could be mobilised by the fire-hose effect, leading to potentially hazardous debris flows, as cyclic damming has been proved to enlarge the size of new debris-flow pulses (Hu et al., 2016). This further suggests that this repeated storage of large volumes of sediment in the upper parts of the slope could result in longer runout debris-flow tracks, compared to smaller flows that are formed by single slope failures.

3.5.4 Implications for potential mobility and hazard

In general, slope angles exceeding 20°–40° are sufficient for the development of slides in dry conditions, and these values can be much lower in saturated conditions, depending on the nature of the material (Anderson and Anderson, 2010). Mean values of slope angles in 2013 in the upper zones of all the analysed debris flows are high (Table 3.3; 36° in 1DFa, 38° in 2DFa, 37° in 11DFa, 41° in 12DFa). Instead of decreasing since 2007, the slope angle in the scarp zones is maintained, hence prone to new slides. I also found such high angles in other debris-flow chutes along the slope above Ísafjörður (Figure 3.9). Over an area of 0.55 km^2 defined along the edge of the bench, I calculated that ~17% is occupied by deposits perched on slopes exceeding 35° and ~4% exceeding 45°. This means that all these areas could be prone to failures.

In geomorphologic studies, the mobility of gravitational movements has been related to the volume and angle of repose (Corominas, 1996; Legros, 2002; Rickenmann, 1999; Toyos et al., 2008). Steep slopes and initial failure volume have previously been shown to be important factors with respect to debris-flow initiation (Bovis and Dagg, 1992; Iverson, 1997; Brayshaw and Hassan, 2009). Steep channels are intrinsically less stable than low-angle channels, thus debris-flow initiation is more likely. Additionally, large sediment volumes — which can self-increase as they travel downslope if runoff-initiated, as with fire-hose or sediment bulking (Godt and Coe, 2007) — usually travel at a higher flow speed than small failures when they enter the channel. Large volumes acquiring high speed are also more likely to impinge catastrophically on saturated deposits stored in the channel, triggering a further debris flow. Furthermore, the incision of the channel can progressively increase the volume of the flow during different debris-flow surges, with further material supplied in the flow by processes like channel scouring (e.g., Berti et al., 1999; Hungr et al., 2005; Rickenmann and Zimmermann, 1993). For these reasons, deeply incised pre-existing tracks like 1DF and 2DF in Ísafjörður are a further source of instability for the material upslope, and constitute a preferential path for sediment delivery downstream.

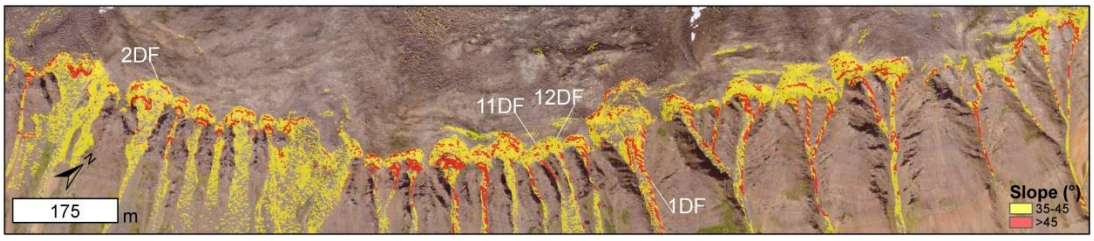

Figure 3.9 - Slope map calculated from DEM 2013, showing loose deposits with angle higher than 35° and 45°.

A high mobility debris flow, such as those that could be initiated by the fire-hose mechanism in tracks 1DF and 2DF, poses at potential risk people and properties. The construction of new engineering solutions (in Figure 3.10 barriers A, 4A and 4B realised with gabions) and the improvement of old ones (barrier 3) to protect Ísafjörður from debris flows and snow avalanches were commissioned in 2012 by the municipality of Ísafjörður (report in icelandic) and constitute a substantial improvement to the risk mitigation of the town. Old barrier 3 has been raised from 3 m to 5 m, while the new ones reach heights of up to 14 m. As barriers A and 3 are positioned beneath debris flow 2DF, they have the potential to retain a new flow in this track. However, there is no protection apart from the ditch beneath debris flow 1DF, whose terminal lobe deposits are located just 90 m above the main road (Figure 3.10).

The presence of these engineering solutions suggests that previous studies contributed to planning the measures of risk mitigation for the town of Ísafjörður. Further efforts should be made in understanding debris-flow initiation, as the reliance of runout distance, flow volume, and frequency of repeat for debris flows on their initial triggering mechanisms has broad implications for assessment of debris-flow hazards.

Finally, I note that the high quality topography data that can be obtained from airborne LiDAR surveys can be effectively used for hazard-monitoring purposes, but they are expensive and time-consuming to process. In this perspective, the use of Unmanned Aerial Systems (UAS) able to collect topography data (usually from photogrammetry) and remote sensing images has been proven a valuable resource for high-resolution hazard surveys (Jordan and Napier, 2015; Lucieer et al., 2014; Mancini et al., 2013), and could be used as a data source for the same

kind of analyses that I describe here. Annual UAS surveys of the debris-flow tracks above Ísafjörður could provide a flexible, cost-effective, and time efficient method for monitoring their evolution, especially the build-up of deposits in unstable parts of long tracks located above inhabited areas. Such data would also provide an important scientific resource for furthering the study of debris-flow initiation and evolution.

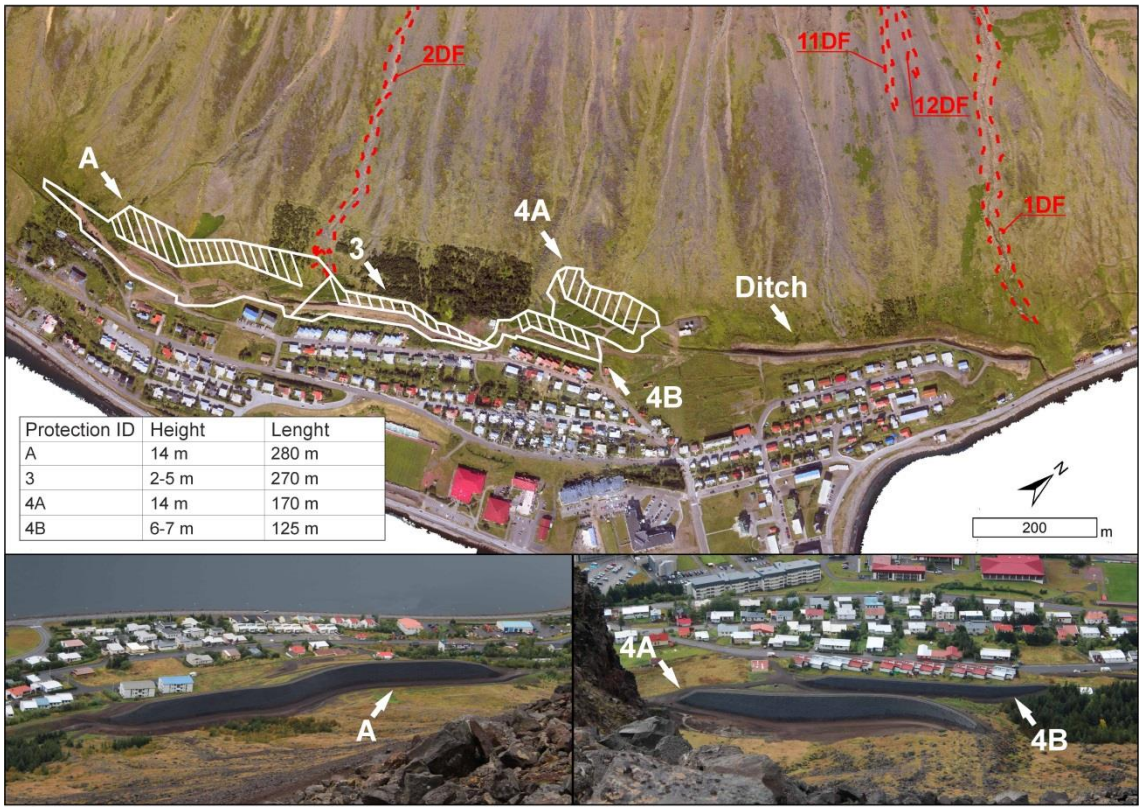

Figure 3.10. Plan of the snow avalanche and debris-flow protection measures ordered by the municipality of Ísafjörður in 2011 (protection measures have the same naming protocol used in the report in Icelandic from the municipality). Ditch and barrier 3 were already present in 2013 (ditch 2-3 m deep, barrier 3 3 m high). Dashed red line mark the perimeter of studied debris flows.

3.6 Conclusions

I have compared two airborne datasets (LiDAR topography and aerial images), collected in 2007 and 2013, that describe debris flows above the town of

Ísafjörður in Iceland. This multi-temporal high-resolution approach reveals details about debris-flow processes in the steepest source areas that previous studies using traditional survey techniques (i.e., Decaulne et al., 2005; Conway et al., 2010) were unable to fully analyse. My main conclusions are:

a) Slope failure of the deposits from the edge of the Gleiðarhjalli bench is the dominant initiation process, leading to a new generation of debris flows above the town (11DF and 12DF) and mobilising debris now in transit in the chutes and upper channels of pre-existing tracks (1DF and 2DF). The fire-hose effect could re-activate older flows (1DF and 2DF), and has probably already mobilised debris within their channels.

b) The two mechanisms can be geomorphologically distinguished, with slope failure characterized by a simple upper-lower erosion-deposition pattern, defined scarps with possible regressive erosion, steep (>35°) discrete slide surfaces with ephemeral springs, modest (below 1000 m^3) mobilised volumes, and short-runout. Preparatory conditions for the fire-hose effect-triggered debris flows are discrete zones of deposited material at high angle (>35°) in the chute and along the channel, and alternating zones of fill and scour along their whole length.

c) Volumes of debris stored in the chutes and upper channels of medium-scale debris-flow tracks 1DF and 2DF (2200-3000 m^3) are stored at high angles (37-38°) and have the same order of magnitude as those estimated for single damaging events that happened in the past (Conway et al., 2010; Decaulne et al., 2005). I infer that these two debris dams have high potential mobility. This confirms hypotheses previously suggested (but not confirmed directly, nor precisely quantified) by Decaulne et al. (2005) and Conway et al. (2010) – namely that there are large volumes of material blocking steep channels in Ísafjörður.

More widely, I have shown that my geomorphic criteria applied on LiDAR differencing has permitted to detect, quantify and characterise debris accumulated at high gradients, without the assistance of any other monitoring system or information on the evolution of the debris flow and of their triggering conditions. This work accomplishes one of the final aims of the thesis, namely the identification of the different release processes of debris flows in Iceland, and the quantification of their geomorphological and hazardous impact. The slope of Ísafjörður is extremely prone to activation and re-activation of debris flows, so this kind of study in this and other debris-flow threatened areas, supported by *in situ* channel survey and monitoring, can improve our understanding of both how debris flows develop and how to mitigate the risks associated with them.

Chapter 4. The dynamics of landslides induced by ground-ice degradation: two case studies in northern Iceland

4.1 Introduction

In Chapter 2, I reported that rapid mass movements are one of the most obvious reactions to climate change of mountain slopes affected by permafrost. The influence of the changing cryosphere on the stability of rock walls is well documented (e.g., Gruber and Haeberli, 2007), and the frequency of periglacial rock falls has increased over the past century in cold mountain environments worldwide (e.g., Beniston et al., 2018; Clague et al., 2012; Haeberli et al., 2011; Huggel et al., 2012; Kellerer-Pirklbauer et al., 2012; Phillips et al., 2017). Active layer detachments and thaw slumps caused by permafrost degradation are also well-documented in areas with continuous permafrost (Blais-Stevens et al., 2015; Günther et al., 2016; Huscroft et al., 2003; Lewkowicz and Harris, 2005b; Segal et al., 2016). However, little is known about how the dynamics of rapid mass movements involving loose deposits, such as debris flows and debris slides, are conditioned by thawing ground ice in periglacial environments. This Chapter aims therefore to explore the morphological impact of two landslides in northern Iceland, where ground ice was found after their occurrence. This because understanding the geomorphological signatures of these underreported landslides can attest the presence of permafrost and its ongoing degradation, and can aid in reconstructing the dynamics of the failures and in evaluating their potential hazard.

Few examples of landslides involving loose debris in permafrost terrains are reported in the literature. In particular, direct observation of frozen landslide material during or after the occurrence of rapid mass movements that involve loose debris, such as talus or moraine deposits, is very rare (Brideau et al., 2009; Huscroft et al., 2003; Lyle et al., 2004, 2014; Sæmundsson et al., 2018). This is due to the fact that, once mobilised, frozen material thaws rapidly; furthermore, this type of landslide commonly occurs in remote glacial and periglacial areas, so they are either not witnessed, or reported a long time after their occurrence. Nevertheless, these observations are crucial, as they help to understand the effect of the presence of ice on the mobility of the landslide. The Little Salmon Lake landslide, a debris slide in Yukon that developed in ice-cemented deposits, is an exceptional example where debris cemented by ground ice was observed in the landslide deposits a few days after the occurrence of the failure (Lyle et al., 2004, 2014). The 800 m long landslide, involving metasedimentary rocks with minor metabasic and ultramafic rocks, occurred on a moderately steep (15-25°) north-facing slope in central Yukon (Brideau et al., 2009), a zone characterised by sub-arctic continental climate and considered affected by discontinuous permafrost (Heginbottom et al., 1995). At this location, ground ice was thought to provide cohesion to blocks of surficial material that were then “mobilized by high pore water pressure in the surrounding saturated sediments” (Brideau et al., 2009), and ground ice degradation was inferred to have caused the failure. However, it is not clear how the ground ice affected the mobility of the landslide. Different cases of debris slides, debris flows and thaw slumps related to thermal disturbance of the permafrost active layer have also been reported in Yukon (Huscroft et al., 2003). Here, in the last thirty years, rapid mass movement activity has involved surficial material such as colluvial till and lacustrine sediments

affected by shallow permafrost, and has impacted the surrounding environment and infrastructures. These failures were ascribed to permafrost and its thaw controlling terrain drainage and strength, but how permafrost affected the dynamics of the mass failures was not investigated.

The closest analogue for debris slides that mobilise ice-rich material are rock-ice avalanches. It is known that rock-ice avalanches have 20-35% higher mobility than rock avalanches of the same magnitude in non-glacial settings (Evans and Clague, 1988; Huggel et al., 2005; Schneider et al., 2011a; Sosio et al., 2012). This enhanced mobility is attributed to fluidization, caused by the reduction of granular friction due to ice melting, basal lubrication by frictional heating of ice (Davies and McSaveney, 2012; Evans and Clague, 1988), and internal mass and momentum exchange (Pudasaini and Krautblatter, 2014). Laboratory experiments with a rotating drum show that the ice in a moving mass of a gravel affects the mobility of the mass as the thaw of that ice supplies water to the flow (Schneider et al., 2011b). In particular, the friction coefficient of a granular moving mass containing ice decreases linearly with increasing ice content, and this has also been shown to be the case in numerical modelling (Sosio et al., 2012). A volume of ice in the mixture greater than 40% causes an increase in pore-water pressure and liquefaction, consequently generating a transition from a dry granular mass to a debris flow-like movement, and eventually to a hyperconcentrated flow (De Blasio, 2014; De Blasio and Elverhøi, 2008; Schneider et al., 2011b). However, laboratory studies do not consider the scale effects introduced by ice on the friction angle — Schneider et al. (2011b) recognised to have a stronger dependence on ice content for mixtures with larger grains; this could have important implications for natural scale events. Also, it is not known if debris slides or flows affecting loose deposits cemented by ground

ice would have the same dynamics as rock-ice avalanches, due to the different distribution of the ice within the material that could make the ice melt progress differently.

Two landslides in ice-cemented sediments have occurred in the last decade in northern Iceland. The first landslide occurred on 20th September 2012 on the north-western facing side of the Móafellshyrna Mountain in the Tröllaskagi peninsula; the second one occurred on 10th July 2014 on the northern slope of the Árnesfjall Mountain in the northern Westfjords. Immediately after their occurrence, blocks and ridges of ice-cemented debris were found in the landslides' deposits (Figure 4.1). This observation has given rise to the hypothesis that these landslides were related to permafrost degradation (Sæmundsson et al., 2014a).

Figure 4.1. Blocks and ridges of ice-cemented sediments. (A) An oblique view of the Móafellshyrna landslide on the day of its occurrence, with one of the blocks of ice-rich sediments found in its deposits (see red circles); (B) a close-up photo of the block of ice-rich sediments shown in Figure 4.1A, taken nine days after the occurrence of the Móafellshyrna landslide (in the yellow circle a close-up image of the ground ice

cementing the deposits with a walking pole for scale); (C) one of the ridges of ice-cemented deposits found two days after the Árnesfjall failure; (D) ground ice found at one meter of depth in the landslide deposits two days after the occurrence of the Árnesfjall landslide.

In this chapter, I describe and discuss how the presence of ground ice has affected the mechanical behaviour of these landslides. Specifically, I analyse the geomorphology and dynamics of the two landslides, whose source material was composed of ice-cemented talus deposits. A volume percentage of 20-30% ground ice has been estimated from visual inspection of the material mobilised by both landslides (see Chapter 6 for theoretical estimations). I assess if this relatively low ice content has affected the mechanical behaviour of the debris compared to "normal" rock/debris slides/avalanches. I describe and quantify the morphometric characteristics of these two landslides, which have different mobilities, and assess how the thawing of ground ice could have affected their emplacement. Geophysical investigations (Ground Penetrating Radar) and runout modelling have been also performed to obtain a better characterisation of the Móafellshyrna landslide. However, the results obtained have not been considered conclusive or satisfactory (see Sections 4.4.2.1 and 4.4.2.3.). This study contributes to our understanding of this complex type of landslide, where ground ice has an unknown impact on the landslide dynamics and may be an additional factor that needs to be included when predicting the hazard posed by rapid mass movements in permafrost areas.

In Chapter 5, I complete my analysis of the Móafellshyrna and Árnesfjall landslides, identifying and discussing their main preparatory and triggering factors: heavy precipitation, seismic activity and permafrost degradation. As degrading permafrost is predicted to increasingly affect mountain regions in the

future (e.g., Haeberli et al., 2011; Stoffel and Huggel, 2012), improving our knowledge on this type of landslide is important, since they could be a further source of risk for local population in Iceland, and in general in other mountain periglacial areas.

4.2 Setting of the case studies

4.2.1 The Móafellshyrna Mountain, Tröllaskagi peninsula

The first case study is the Móafellshyrna landslide, which occurred on the north-west facing slope of the Móafellshyrna Mountain. The site is in the Tröllaskagi peninsula in northern Iceland, a mountain plateau with summits up to 1550 m high located between the Skagafjörður fjord in the west and the Eyjafjordur fjord in the east, which both strike north-south (Figure 4.2A). The Móafellshyrna Mountain is located in the Móafellsdalur valley, a tributary valley of the Stífludalur valley in the north-western part of the peninsula, located 21 km southwest of the town of Ólasfjörður, and 26 km south of the town of Siglufjörður (Figure 4.2A). The Þrasastaðir farm, the innermost inhabited farm in the Stífludalur valley (Figure 4.2B), is situated on the northern side of the Fljótaá River, facing the Móafellshyrna Mountain (Figure 4.2C). The occurrence of the Móafellshyrna landslide was first reported by the farm residents, who witnessed the event (see Chapter 5). In the Móafellsdalur valley, the Galtará river flows from SSW to NNE, joining the Fljótaá river that flows from SE to NW (Figure 4.2C), ultimately draining into the Denmark Strait. The Móafellshyrna ridge is 1000 m high and strikes NNE, extending 5 km between the Fljótaá valley in the north and the Móafellsjökull glacier in the south.

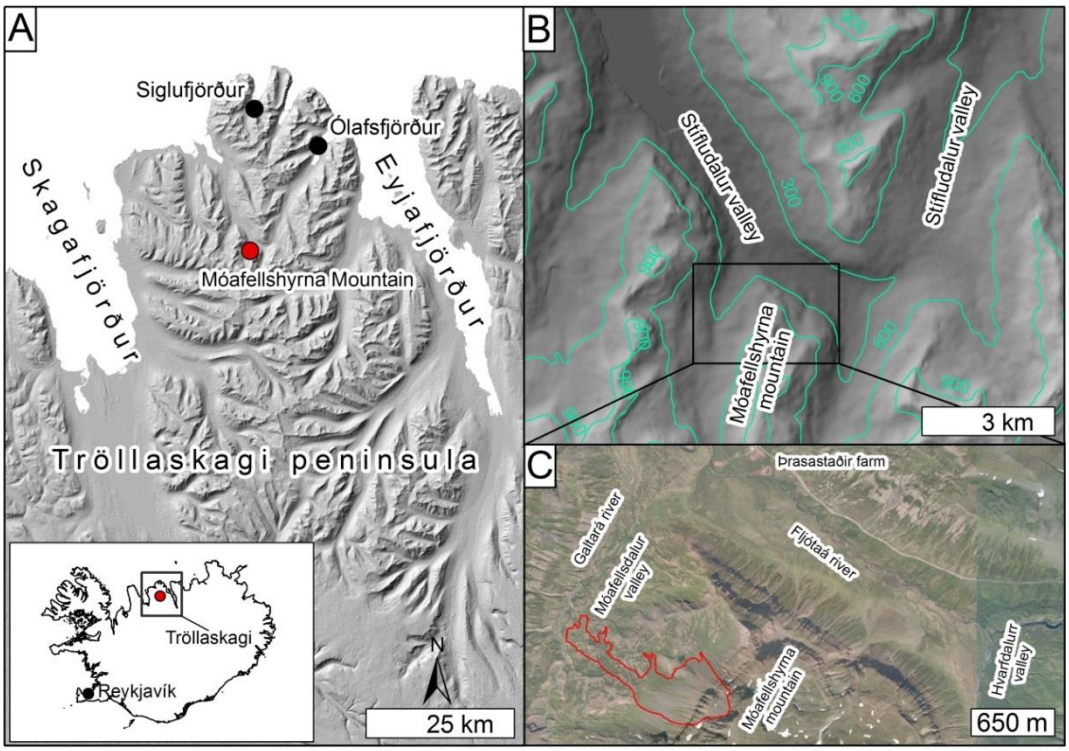

Figure 4.2. The geographic setting of the Móafellshyrna site, Tröllaskagi peninsula, northern Iceland. (A) A hillshaded digital elevation model (DEM) showing the main geographic locations of Tröllaskagi peninsula and the Móafellshyrna Mountain (DEM source EU-DEM from the Global Monitoring for Environment and Security service for geospatial reference data access project (GMES RDA). (B) Hillshaded DEM and contours (in green, metres above sea level) of the Móafellshyrna region. (C) Aerial photograph (source samsyn.is) of the Móafellshyrna Mountain before the landslide (perimeter of the landslide marked by a red line) in 2012, showing some of the main geographic features of the area.

The bedrock of the mountain is within the Tertiary basalt series, and consists of closely-jointed basaltic layers, composed of 2 to 30 m thick individual flows (Figure 4.3A). These are interbedded with poorly cohesive red to yellow hyaloclastites, with thicknesses from a few centimetres up to decametres (Figure 4.3C). Horizons of red lithified paleosols up to meters thick are also observable in the basaltic sequence (Figure 4.3B). The basaltic layers dip 5-10° towards SW-WSW on average, are 15 to 10 Ma old (Jóhannesson, 2014), and are cut by 3 and 7 Ma old dikes, sills and faults (Garcia et al., 2003).

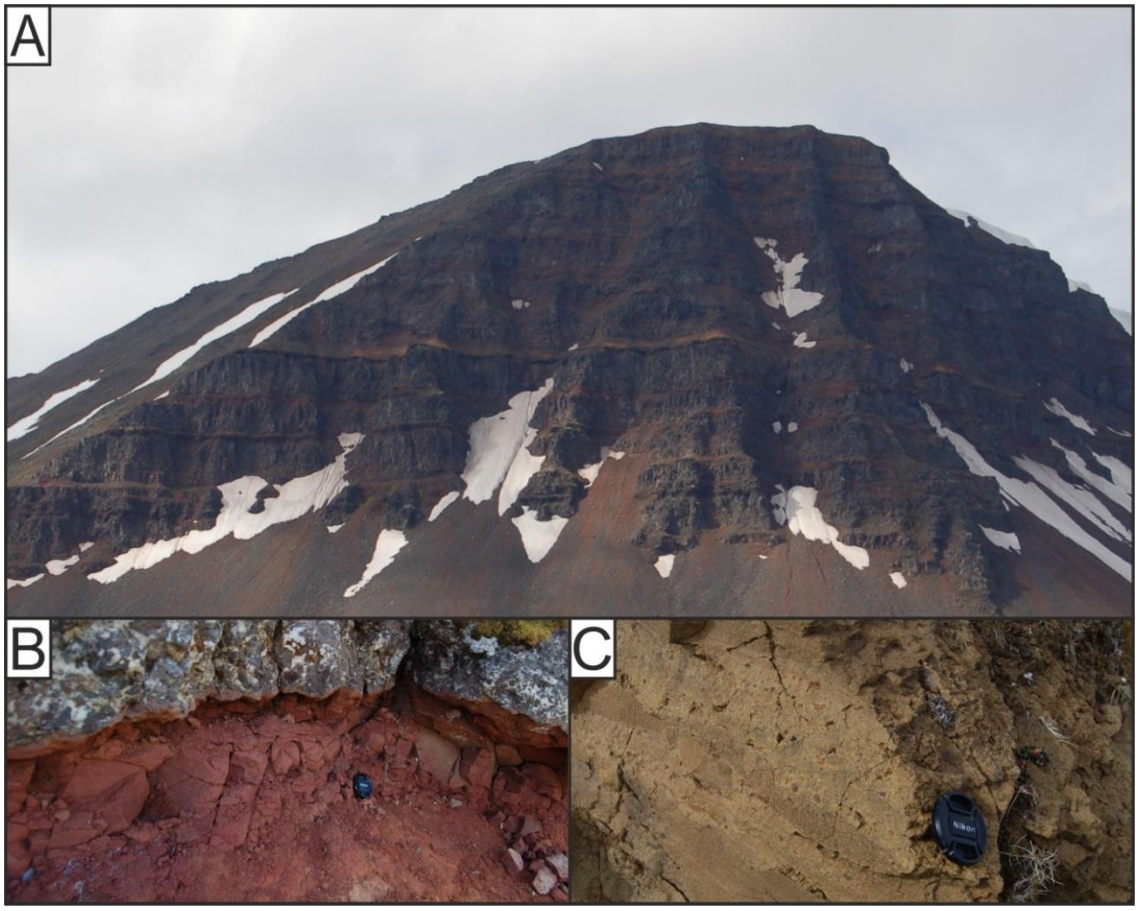

Figure 4.3. The bedrock of Móafellshyrna region. (A) Basalt layers interbedded with red paleosols and yellow hyaloclastite forming the Lambahnjúkur mountain on the south-eastern side of the Móafellsdalur valley; (B) a layer of red lithified paleosols on the northern crest of Móafellshyrna mountain; (C) yellow hyaloclastite interlayered with the basaltic lava layers forming the Móafellshyrna mountain.

After the Last Glacial Maximum (LGM), when the Icelandic ice sheet extended to the submarine shelf break (Einarsson and Albertsson, 1988; Eiríksson et al., 2000; Hubbard et al., 2006; Spagnolo and Clark, 2009), the last major deglaciation of Iceland occurred (Pétursson et al., 2015) between 15 ka (Andrews et al., 2000) and 10.2 ka (Caseldine et al., 2003; Caseldine and Stotter, 1993; Geirsdóttir et al., 2009; Stötter et al., 1999). The landscape of the whole Tröllaskagi peninsula has been sculpted by the Icelandic Ice sheet, and is characterised by deeply incised glacial valleys and cirques. 167 glaciers, mostly debris-covered, are catalogued on the peninsula; all are in regions above 800 m

a.s.l. (Andrés et al., 2016). Rock glaciers and ice-cored moraines are abundant in the region (Lilleøren et al., 2013; Whalley and Martin, 1994), as well as several other periglacial features such as sorted and non-sorted stripes, thufur, and sorted nets or polygons (Clark, 1983) observed in field investigations). As I report in detail in Chapter 2, discontinuous permafrost has been predicted in the area above 800-900 m elevation using numerical models calibrated by observations (Etzelmüller et al., 2007; Farbrot et al., 2007a, 2007b; Lilleøren et al., 2013). In the Tröllaskagi peninsula, rock-slope failures and deep-seated gravitational slope deformations dating from the early Holocene onwards are very common, and they provide evidence of the destabilization of the slopes during the paraglacial phase (Coquin et al., 2016; Cossart et al., 2014; Decaulne et al., 2016; Feuillet et al., 2014; Mercier et al., 2012, 2017).

The precipitation in the Tröllaskagi peninsula is estimated to be 2000–2500 mm/year, of which the majority falls as snow on the glaciers (e.g., Lippert et al., 2003); however, this region of Iceland receives less precipitation than the rest of the island, being sheltered from the prevailing south-western wind by the great central volcanoes. See Chapter 5 for a detailed description of the weather data in the Móafellshyrna area before and during the occurrence of the failure.

The Móafellshyrna landslide originated at 870 m a.s.l. and travelled 1,320 m on the north-west facing slope of the mountain. The topographic long profile of the landslide can be subdivided into five distinct sections (Figure 4.4):

– Section 1 is the detachment zone. It includes the headscarp, the topographic bench where the source deposits detached, and the bedrock cliff over which the mass fell. The highest elevation of the headscarp is 873 m a.s.l., and its elevational extent is 183 m. This section has a stair-case shaped profile: the headscarp has an average slope of 36°, then there is a break-in-slope leading

to the bench, which has an average slope of 14°, and then further downslope the cliff has a slope of 44°;

- Section 2 is the first transport zone. It consists of the talus slope below the topographic bench, with an average slope of 31°. The top of this section is at 690 m a.s.l., and the elevation drop is 180 m;
- Section 3 is the first low slope (16°) accumulation zone, and its top is at 510 m a.s.l. with an elevation drop of 30 m;
- Section 4 is the second transport zone. The topographic profile has a convex-up shape, with its top located at 480 m a.s.l, an elevation drop of 90 m, and an average slope of 23°;
- Section 5 is the second accumulation zone. Its top is at 390 m a.s.l., and it has an average slope of 14°. The landslide toe is located at 329 m a.s.l..

Later in this chapter I will show that the Móafellshyrna landslide does not comprise thick deposits. Therefore, its step-like topographic profile is not caused by the morphological changes produced by the failure, but follows the underlying topography, typical of periglacial landscapes that have undergone recent deglaciation. This kind of profile is known as the “free-face model” and is composed of a rockwall above 40° below which there is, first, a talus slope, and then, second, a footslope or a basal complex (French, 2007; King, 1953).

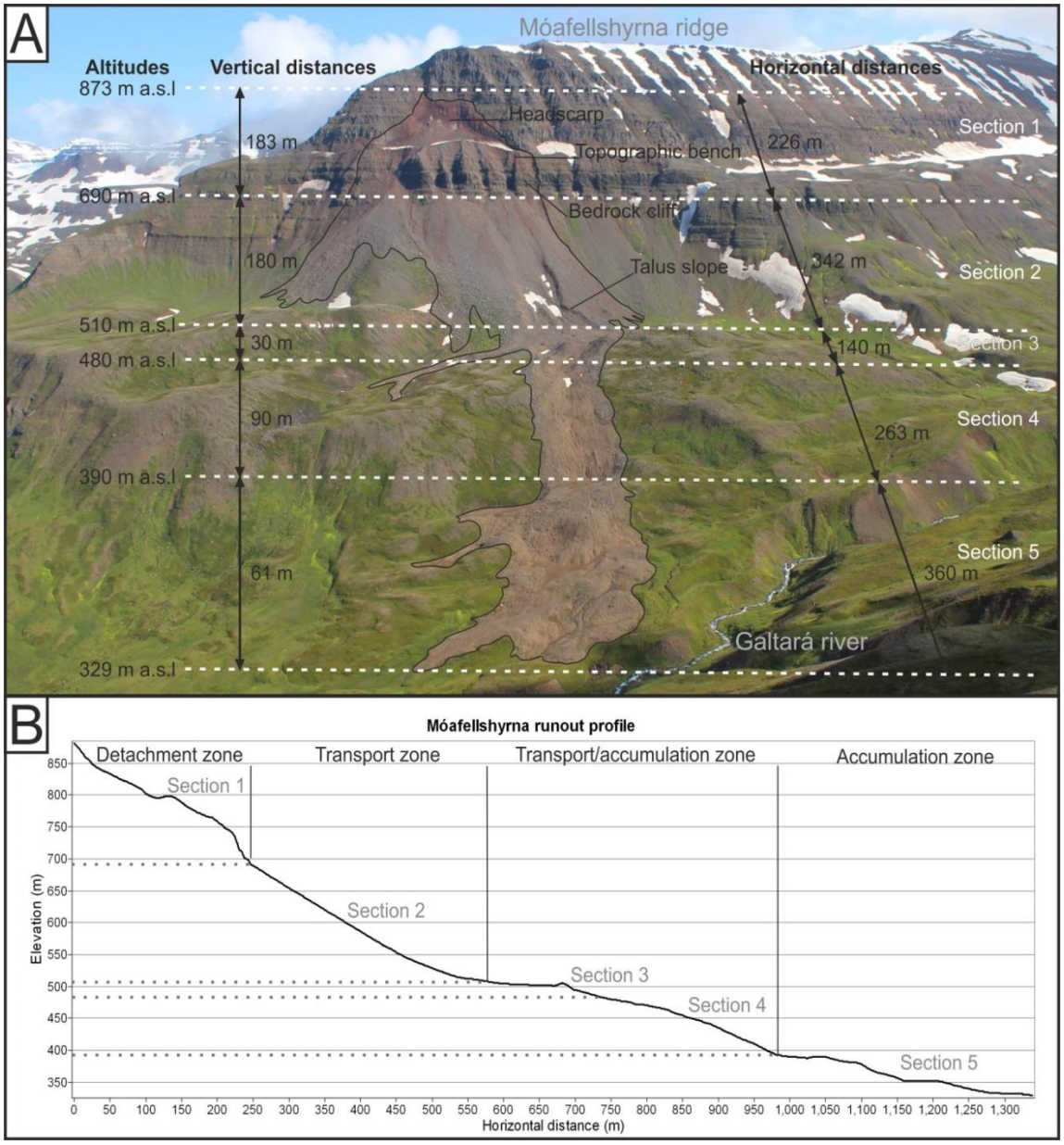

Figure 4.4. The division of the Móafellshyrna landslide into sections based on topography and whether erosion, transport or accumulation dominates. (A) Oblique view looking south-east of the Móafellshyrna landslide with the different sections outlined; (B) longitudinal topographic profile divided into five sections, corresponding to the detachment, transport, transport/accumulation and accumulation zones detailed in the text and marked in A.

4.2.2 The Árnesfjall Mountain, Westfjords

The second case study is the Árnesfjall landslide, which occurred on the north facing slope of the Árnesfjall Mountain. This site is located in north-western

Iceland on the Westfjords peninsula, between the Húnaflói bay in the east and the Breiðafjörður bay in the SSW (Figure 4.5A). The Árnesfjall Mountain is located on the coast of Norðufjörður fjord in the north-eastern part of the peninsula, 26 km east-south-east of the southern terminus of the Drangajökull glacier, and 34 km north-north-east of the town of Hólmavík. The Árnesfjall ridge rises from the sea level to 490 m of elevation and strikes north-east, extending 1.7 km between the Meladalur valley in the north-west and the Árnesdalur valley in the south-east (Figure 4.5B).

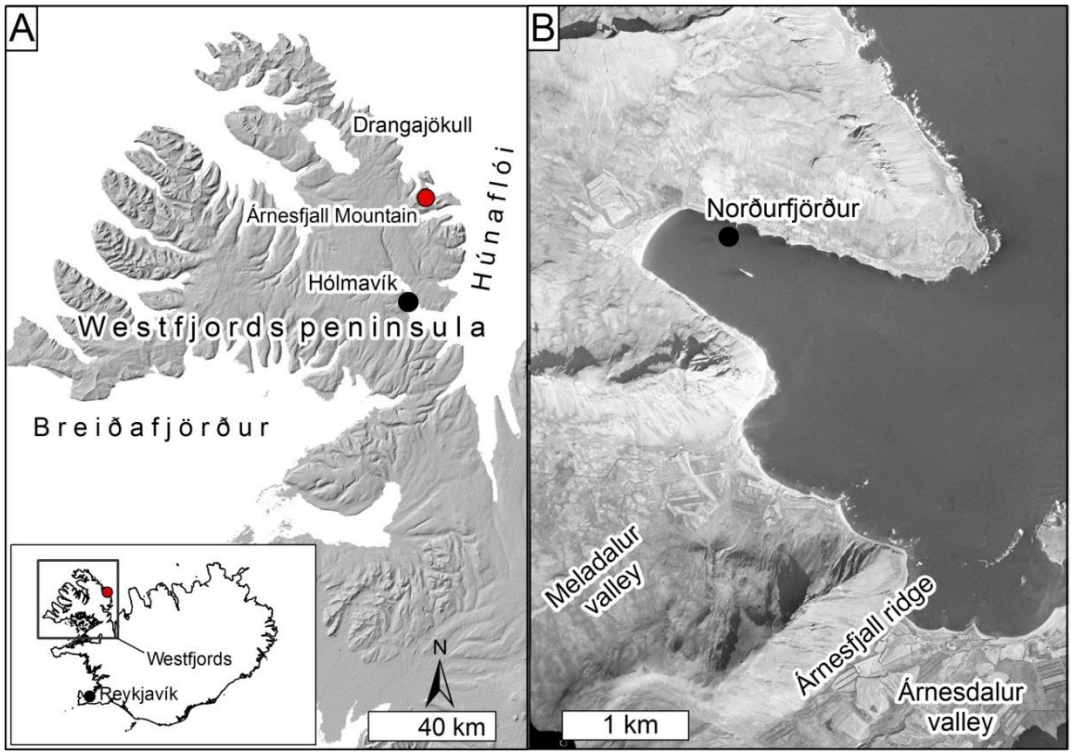

Figure 4.5. The geographic setting of the Árnesfjall site, on the Westfjords peninsula, north-western Iceland. (A) The hillshaded DEM showing the main geographic locations of Westfjords peninsula and the Árnesfjall Mountain (base map from the EU-DEM from the Global Monitoring for Environment and Security service for geospatial reference data access project (GMES RDA)). (B) Aerial photograph from 1981 (source National Land Survey of Iceland - Landmælingar Íslands) of the Árnesfjall Mountain before the landslide in 2014, showing some of the main geographic features of the area.

The bedrock of the mountain is within the Tertiary basalt series and consists of superimposed basaltic lava flows, dating from the Miocene and Lower Pliocene epochs (Jóhannesson, 2014). Individual lava layers are sub-horizontal (locally dipping 5-10° towards ESE), 2 to 30-40 m thick (Figure 4.6), and are interlayered by red lithified paleosols, a few centimetres to a few meters thick, and sometimes volcanoclastic sedimentary horizons. Intrusions of rhyolite crop out on the northern slope of the mountain (Figure 4.6B).

Figure 4.6. The bedrock of the Árnesfjall area. (A) Basaltic lava layers visible on the Hlíðarhúsafjall Mountain, north of the Meladalur valley. The red-brown colour indicates the presence of paleosols and/or volcanoclastic sedimentary layers interbedded with the basaltic ones; (B) an example of a rhyolite intrusion on the northern slope of the Árnesfjall mountain.

The Westfjords are characterised by deep fjords, glacial valleys and wide cirques, while the mountains have flat summits (up to 998 m a.s.l.) and steep flank-slopes (25-35°, Decaulne et al., 2005), a landscape shaped by the glacial history of the area. During the Last Glacial Maximum, the Icelandic ice sheet extended up to 30 km out onto the shelf beyond the Westfjords peninsula (Andrews et al., 2002; Geirsdóttir et al., 2009, 2002). The Icelandic ice sheet retreated rapidly between 15 ka and 10.2 ka in the Westfjords (Andrews et al., 2000, 2002; Bovis and Jones, 1992; Brynjólfsson et al., 2015; Geirsdóttir et al., 2002; Ingolfsson et al., 2010; Norddahl and Pétursson, 2005; Pétursson et al.,

2015). An extensive ice cap remained over the eastern peninsula in the Drangajökull region until at least 9 ka (Brynjólfsson et al., 2015). Today, Drangajökull is the only ice cap present in the Westfjords. 186 rockslides have been mapped in the Westfjords: they are concentrated along the coasts and are thought to be primarily paraglacial (Peras et al., 2016; Whalley et al., 1983) and might be associated with slope debuttressing and isostatic rebound as are other rockslides in northern Iceland (Coquin et al., 2015, 2016, Mercier et al., 2012, 2017).

As specified in Chapter 2, permafrost is not predicted in the Westfjords (e.g., Etzelmüller et al., 2007). However, a number of periglacial features are found around Árnesfjall mountain, including sorted stone polygons in flat areas, sorted and non-sorted stripes in steep areas, and solifluction lobes. The presence of these features cannot be used as an indication of present-day permafrost, but their presence does suggest discontinuous permafrost could be present in this area of Iceland, as other authors also have inferred (Brynjólfsson et al., 2015; Glade, 2005).

The Árnesfjall landslide originated at 420 m a.s.l. from the north facing slope of Árnestindur and travelled 563 m. The topographic long profile of the landslide can be subdivided into three sections (Figure 4.7):

- Section 1 is the detachment zone, which consists of the headscarp and the bedrock exposed from underneath the landslide mass. The top is located at 418 m a.s.l., the elevation drop is 60 m, and the section has an average slope of 37°;
- Section 2 is the depletion zone (as defined by Cruden and Varnes (1996), namely the area of the landslide where the displaced mass overlies the rupture surface and underlies the original ground surface), with the top at 358 m a.s.l., an elevation drop of 42 m, and an average slope of 23°;

- Section 3 is the accumulation zone, with the top at 316 m a.s.l., an elevation drop of 246 m, and an average slope of 32°.

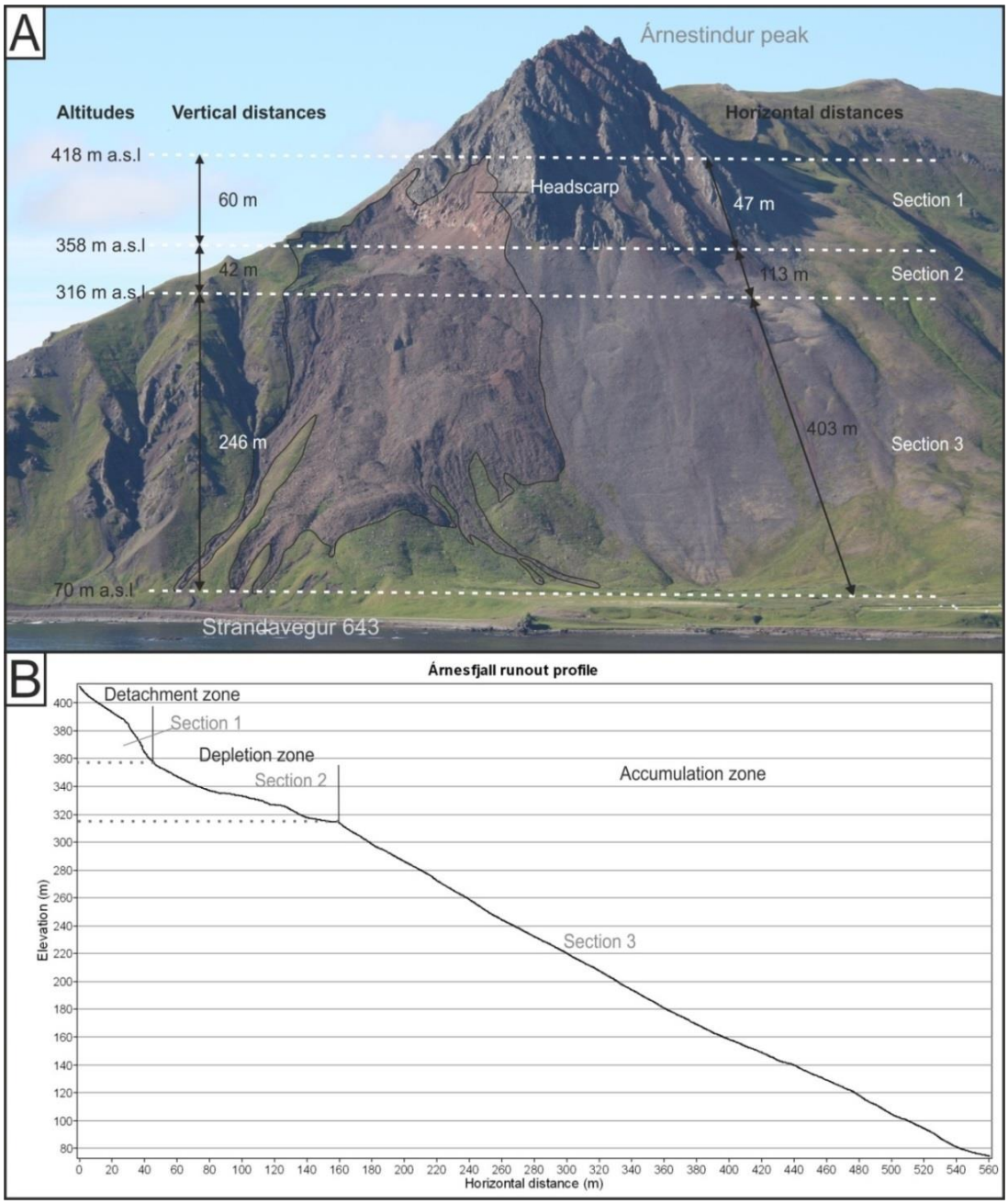

Figure 4.7. The Árnesfjall landslide divided into sections based on topography and dominant process.Oblique view looking south towards the Árnesfjall landslide showing its local geographic setting; (B) Topographic long profile divided into three sections, corresponding to the detachment, depletion, and accumulation zones.

4.3 Methods

4.3.1 Fieldwork

I performed fieldwork at the Móafellshyrna landslide in summer 2015. I also used personal communication and photographs collected by my supervisor Þ. Sæmundsson and colleagues from the Icelandic Meteorological Office, who visited the site a few hours, four days and nine days after the Móafellshyrna event. I performed fieldwork at the Árnesfjall landslide in summer 2016, and I received photographic documentation of the landslide from Jón Kristinn Helgason at the Icelandic Meteorological Office, who visited the site two days after the occurrence of the landslide.

Detailed fieldwork was conducted with the purpose of identifying, characterising and classifying geomorphic features and structures of the landslides, in order to reconstruct the failure history, and to compare field observations with remote sensing datasets. I performed geological and geomorphological field analyses in every section of each landslide (see Sections 4.2.1 and 4.2.2 above), observing and measuring the thickness (using a measuring tape), composition and texture (using comparative charts) of the deposits. Debris thickness measurements made at the edges were validated for the centre of the mass using Ground Penetrating Radar profiles in different zone of the landslide (see Section 4.3.6). In both field sites, I performed differential GPS (dGPS) surveys of the landslides using two GNSS Leica System 1200 in Móafellshyrna and two GNSS Leica VIVA GS10 Systems in Árnesfjall (one as rover unit and one as base station; average accuracy of samples is around 1cm in the horizontal and 2 cm in height). In Móafellshyrna, a base GPS unit was positioned on the landslide deposits, always within 1 km of the rover GPS unit,

whose antenna was attached to a helmet worn by the operator. These GPS measurements were collected to survey the landslide perimeter, the thickness of the deposits and the main geomorphic features of the landslide, recording a sample every 10-15 m for at least 5 epochs (seconds) per sample. In Árnesfjall, a base GPS unit was positioned at the foot of the northern slope of the Árnesfjall mountain, within 500 m of the rover GPS unit, whose antenna was positioned on a pole. The dGPS measurements were used to survey the perimeter of the landslide, logging data when the rover was static and moving, with a record rate every 1 second. Samples were recorded every 20-30 m, recording for at least 10 epochs every sample. To ensure high quality, at both field sites date were not collected when the Global Dilution of Precision (GDOP) value (which is calculated real-time from relative satellite positions) was > 7. Finally, dGPS units were also used to support Structure from Motion and Ground Penetrating Radar data collection (see Section 4.3.3 and 4.3.6 respectively).

4.3.2 Airborne data

In September 2015, the U.K. Natural Environment Research Council's Airborne Research Facility (NERC-ARF), on behalf of the European Facility for Airborne Research (EUFAR), collected aerial photography and airborne light detection and ranging (LiDAR) data for the Móafellshyrna area in Iceland, three years after the Móafellshyrna landslide occurred. 170 aerial photographs were collected with a Leica RCD105 digital camera, and 15 lines were flown to collect 126 million LiDAR points with (a mean of 1.7 points/m^2) using a Leica ALS50-II instrument. A GNSS Leica VIVA GS10 dGPS was used in a fixed location at 1 Hz during the flight to collect base station data for the on-board dGPS. The processing of the LiDAR point cloud was performed by NERC-ARF-DAN (Data

Analysis Node). I used the LAStools extension for ArcGIS to convert the point clouds into gridded data at 1 m/pixel, using the return time of the last peak of light to reach the receiver from the LiDAR laser shot, which is usually assumed to be the ground return. I used Agisoft Photoscan Professional 1.3.5 software to produce a seamless orthomosaic from the airphotos, where the position of the images was controlled using ten well-spread ground control points, derived by locating matching positions in a hillshaded version of the LiDAR Digital Elevation Model and the air photos.

Aerial photographs of the Móafellshyrna area from August 1985 and of the Árnesfjall area from August 1981, both collected at 5486 m of elevation (provided by the National Land Survey of Iceland), were also used to analyse the pre-failure morphology of the mountain, in order to compare the source area before and after the failure, and to improve the estimate of the volume of debris mobilised.

4.3.3 Structure from Motion

With the recent advances in digital photogrammetry and availability of low-cost high-resolution cameras, topographic modelling produced by ground-based photogrammetric techniques is becoming more accessible (James and Robson, 2012; Micheletti et al., 2015; Remondino et al., 2014; Smith et al., 2015). For this study, to produce a base map for geomorphic mapping and analysis for the Árnesfjall site, I processed digital photos with the ground-based Structure from Motion (SfM) photogrammetry technique (Westoby et al., 2012). The SfM technique uses a series of input images with overlapping view perspectives to simultaneously reconstruct three dimensional (3-D) camera pose and sparse scene geometry using an iterative bundle-adjustment procedure (Fonstad et al., 2013; James and Robson, 2012; Micheletti et al., 2015; Snavely et al., 2008;

Westoby et al., 2012). A point cloud is then produced, increasing the density by two orders of magnitude using the estimated camera positions and image clustering, and multi-view stereo methods (e.g., Furukawa and Ponce, 2010). The quality of Digital Elevation Models (DEMs) produced using the SfM technique can be comparable to, or better than, models derived from aerial or terrestrial LiDAR data (Fonstad et al., 2013; James and Robson, 2012; Micheletti et al., 2015; Remondino et al., 2014; Smith et al., 2015; Westoby et al., 2012). However, the construction of the DEM and orthomosaic using SfM is an automated workflow, in which errors can be difficult to quantify (Fonstad et al., 2013; James and Robson, 2012; Micheletti et al., 2015; Remondino et al., 2014).

I collected photographs in July 2016, two years after the Árnesfjall landslide occurred. The photographs were taken from ground-based oblique perspective (at approximately 3 km from the landslide), using a single-lens reflex (SLR) camera (Canon EOS 450D, 12.2-megapixel image sensor) set to a fixed focal length of 200mm and automatic exposure settings enabled. I identified clearly visible blocks and features on the landslide – a total of 19 ground control points (GCPs) – and obtained their coordinates by using differential GPS measurements, whose errors are detailed in Table 4.1. Photographs were inspected manually, blurry images were deleted, and the sky was masked out of each image manually. The remaining 73 photographs were imported into Agisoft Photoscan Professional 1.4.1, which uses an algorithm based on the Scale Invariant Feature Transform (SIFT) object recognition system (Lowe, 2004) to identify key points for photograph alignment. I removed any misaligned photographs at this stage and then identified the GCPs recorded in the field in the image set, importing their GPS coordinates, in order to apply an absolute coordinate system to the 3D model. Scaling and georeferencing the point cloud

was achieved by applying a linear similarity transformation, which was then optimised by adjusting the camera parameters and the 3D points in order to minimize the sum of the re-projection error and the georeferencing error (Javernick et al., 2014). For the 19 ground reference points I obtained a horizontal positional accuracy ranging from 0.05 m to 0.08 m, and a vertical uncertainty ranging from 0.05 to 0.15 m. This processing procedure allowed me to produce a 3D topographic model, from which I derived an orthomosaic at 9 cm/pixel and DEM at 18 cm/pixel. The 3D model has reconstruction errors of 0.9–1.8 pixels and an absolute precision of 0.5–1.5 m. I then imported the DEM and the orthomosaic into ArcGIS for further analysis.

Table 4.1 - Summary of estimated measurement and processing error generated during GPS data collection and processing.

	Vertical error (m)	Horizontal error (m)
Instrument error	0.02	0.01
Human error	0.05	0.05
Wobble of antenna	0.1	0.1
Error in identifying the GCP in processing phase	0.5	0.5

4.3.4 Volume analysis

In order to quantify the material deposited and eroded by the landslides, I calculated the volume of debris that both landslides mobilised. Firstly, I calculated an estimation of the entire volume mobilised by the landslides and the volumes eroded or deposited by their different features by multiplying the estimated thickness of the deposit/depth of the erosional scar for the area that they cover. The thickness was obtained either using tape measurements in the field, by dGPS measurements, or using GPR profiles (see Section 4.4.2.1).

I also made another volume calculation using the 3D topographic data of the source material of the landslides and the different geomorphic features that they produced, such as molards (see Chapter 6) and secondary lobes. I calculated these volumes following Conway and Balme (2014), reconstructing the pre-failure surface, and deriving the deposited or eroded volumes by subtracting the pre-failure surface from the landslide surface (Figure 4.8). I defined the pre-failure surface by different means: i) field observations and tape measurements, ii) dGPS measurements of the perimeter of the landslides and of the molards, ii) GPR profiles to define the thickness of the deposits (see Section 4.4.2.1). I have used the contour lines of the morphology not affected by the landslides as a reference to draw the estimated topographic contours of the pre-failure topography. This task was possible because both landslides' features have well-defined edges; in the case of Árnesfjall, the talus slope next to the landslide serves this purpose particularly well, as its surface is smooth and homogeneous, and the edges of the source area are well-defined. The topographic contour intervals used to reconstruct the pre-failure surface for the landslides and their features are reported in Table 4.2.

Table 4.2 - Summary of the topographic contour values used to reconstruct the pre-failure surfaces of the landslides.

Móafellshyrna landslide and features	Topographic contour interval	Unit
Source mass	5	m
Entrained talus deposits	2	m
Secondary lobe	2	m
Árnesfjall landslide and features	**Topographic contour value**	**Unit**
Landslide	10	m
Source mass	5	m

I used the reconstructed topographic contours and the topography adjacent to the landslides — or their surface features — as input data for a natural neighbour interpolation to estimate the pre-failure surface. This allowed me to obtain a new DEM with the same resolution as the original DEM. I then calculated the difference between the original DEM and the pre-failure surface in order to obtain the volume of material transported, eroded or deposited by the landslides. Error propagation calculations by Conway and Balme (2014) suggest that such volume estimates are accurate to within 25%. However, since the features analysed in this study are not always well defined, it is possible that this measurement might only be accurate to within 50%. Finally, to calculate the volume mobilised by the whole landslide, in both the Móafellshyrna and Árnesfjall cases, I coupled the volumes obtained with the method of Conway and Balme (2014) with estimates from field and DEM measurements for the parts of the landslides where reconstructing the pre-failure surface was not possible due to high uncertainty.

Figure 4.8. An example of volume analysis. Secondary depositional lobe (in red) in the Móafellshyrna landslide's body. In yellow are marked the extrapolated contours for the topography from before the landslide occurrence.

I have identified and measured the volumes of boulders that fell during the Móafellshyrna event. To distinguish them from earlier rock falls, I used blocks with freshly-broken surfaces and checked their presence in the photos taken just after the event. I have chosen only blocks that fell within the landslide perimeter, or at few meters distance from the boundary. The use of these data will be detailed in the Section 4.3.5. Whenever field measurements were not recorded, I selected boulders lying on top of the landslide deposits and measured their surface area from the aerial photographs and assumed a cubic shape to calculate their volume.

4.3.5 Fahrböschung

A broadly recognised method to quantify the mobility of a landslide is to calculate the Fahrböschung. Fahrböschung is the mobility index of a landslide and is defined as the ratio H/L, where H is the fall height and L is the horizontal length of the landslide (Abele, 1974; Scheidegger, 1973; Shreve, 1968). This ratio corresponds to the arctangent of the dip of the line connecting the source area to the distal fallen boulder of a rock fall or to the tip of a rock/debris slide/avalanche. This angle of dip is also known as the "Fahrböschung" angle (Heim, 1932), travel angle (Cruden and Varnes, 1996), reach angle (Corominas, 1996) and travel distance angle (Hunter and Fell, 2003). The Fahrböschung is adopted for different types of landslides, including rock and debris avalanches (Erismann and Abele, 2001; Hsu, 1975; Scheidegger, 1973), rock falls (Copons et al., 2009; Corominas, 1996), and debris flows (Iverson, 1997; Rickenmann, 1999). The longer the travel distance is for any given distance, the lower the value of the reach angle. Also, the ratio H/L is thought to vary inversely with the source volume (e.g. Hungr, 1990; Legros, 2002). For rock falls, the tangent of the reach angle is considered equivalent to the coefficient of friction of the ground surface where the rock fall starts (Scheidegger, 1973; Shreve, 1968). Therefore, we adopted this method for analysing the mobility of both Móafellshyrna and Árnesfjall landslides and the rock/debris fall activity associated with the Móafellshyrna landslide.

In the analysis of the Móafellshyrna molards and bedrock boulders, the source point from where they detached was not identifiable, although I assumed they originated from somewhere between the bedrock cliff and the topographic bench. Using the final position of the fallen boulders as a reference, I constructed a "centreline" path, connecting the boulder to the nearest point where this line

connects to the edge of the bench (Figure 4.9). The length of the centreline path was used as the horizontal travel distance L in the Fahrböschung calculation. I calculated the fall height subtracting the elevations of the two points connected by the centreline. I also evaluated the Fahrböschung using other 'potential energy' paths: I created 10-20 other possible lines connecting the bench with the boulder, spaced every 10 m along the edge of the bench (Figure 4.9), and used their median length as the length for the horizontal travel distance L. The fall height H was obtained in the same way as for the centreline. The deviation between the Fahrböschung value calculated using the length of the centreline path from the one using the median of the other potential fall lines was below 5%. Therefore, in the Results I show the Fahrböschung calculated using the centreline of the path as the horizontal travel distance.

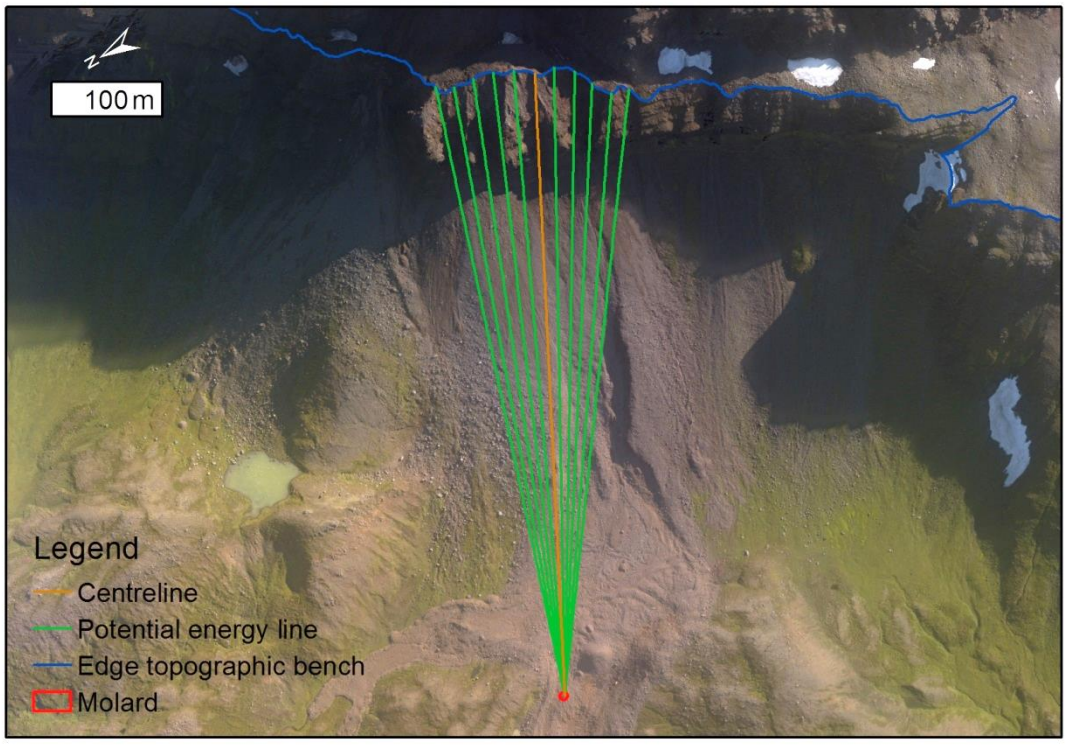

Figure 4.9. Illustration of the method applied for calculating the length L of the Fahrböschung for the boulders and molards that fell during the Móafellshyrna failure.

4.3.6 Ground Penetrating Radar

For detecting the subsurface of the Móafellshyrna site, I chose to use Ground Penetrating Radar (GPR), which uses an electromagnetic pulse emitted from a transmitter antenna to identify sub-surface interfaces. The GPR has allowed me to detect the sliding surface of the Móafellshyrna landslide, and I have used these measurements to calibrate the volume estimates of the landslide. The pulse is reflected by targets or interfaces buried within a visually opaque substance, and received by a second antenna after a measured travel time (Davis and Annan, 1989). In August 2015, I conducted a GPR survey to investigate the thickness of the Móafellshyrna landslide deposits, using a PulseEKKO™ Pro system with 50 and 100 MHz antennae. Survey lines covered 750 m of surface travel and were completed both parallel and perpendicular to the landslide runout direction (Figure 4.10). Antennae were aligned perpendicular to the survey direction and were towed manually across the landslide surface at 0.5 m and 1 m intervals for the two antenna frequencies mentioned above. Raw GPR data were processed in EKKO View Deluxe (Sensors and Software, 2003). Processing consisted of applying a dewow filter (time filter for signal saturation), band-pass filtering, 2-D migration, and topographic correction (using the 1m DEM from LiDAR data). A ground-wave propagation velocity of 0.075 m ns^{-1} was used for processing and interpretation of the profiles (the common midpoint (CMP) method was used to determine average velocity values for the landslide deposits).

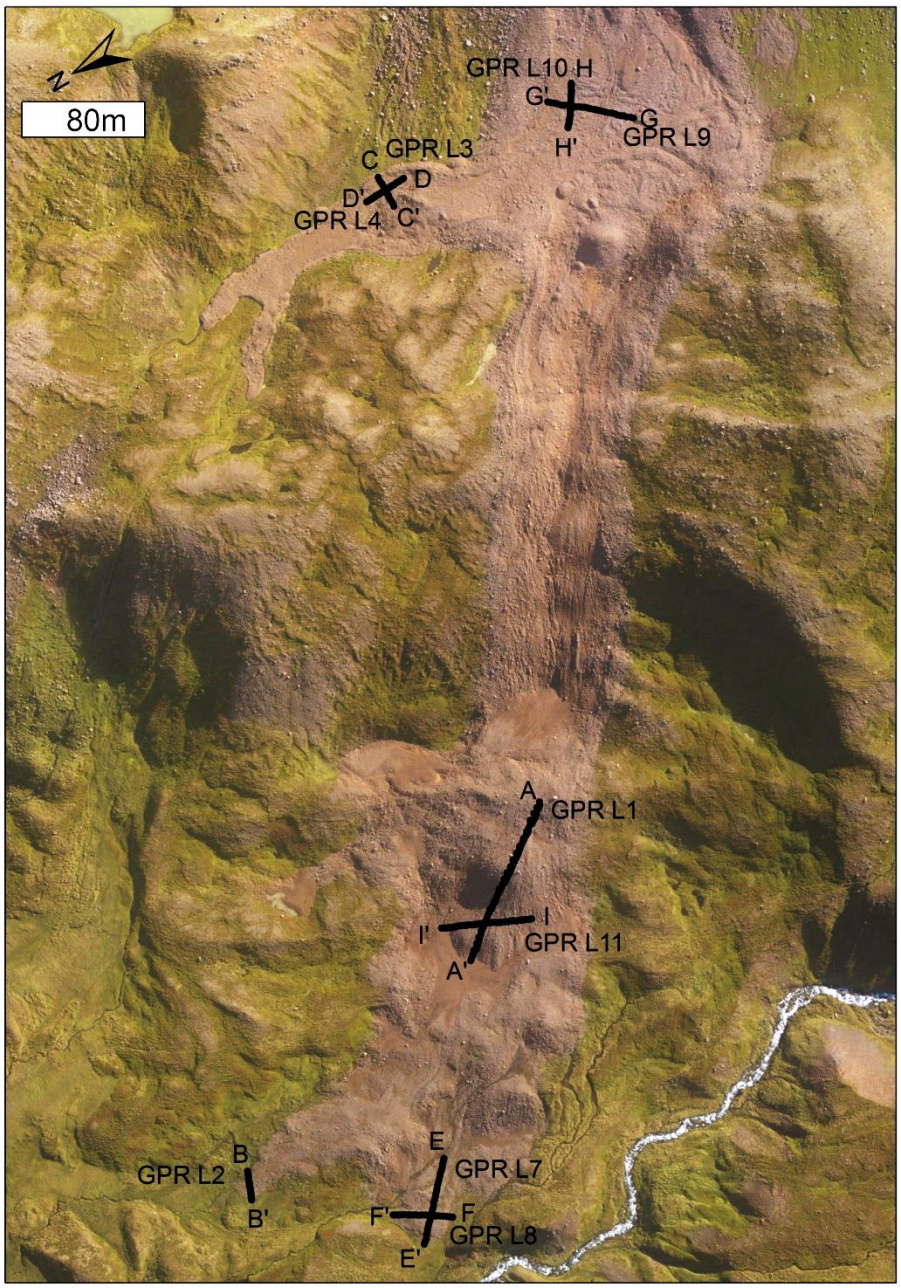

Figure 4.10. Location of the GPR profiles performed on the Móafellshyrna landslide deposits.

4.3.7 Rapid Mass Movements Simulation

I applied the Rapid Mass Movements Simulation (RAMMS) model (Christen et al., 2010) to simulate the runout of the Móafellshyrna landslide. I adopted the trial version of the RAMMS::DEBRIS FLOW module, which uses the two-parameter Voellmy relation to describe the frictional behaviour of the flowing debris. The

Voellmy friction law divides the frictional resistance into a dry-Coulomb type friction (coefficient μ) that scales with the normal stress, and a viscous-turbulent friction (coefficient ξ). The frictional resistance S (Pa) is then

$$S = \mu \rho H g \cos(\Phi) + \left(\frac{\rho g U^2}{\xi}\right) \quad (1)$$

where μ is the resistance of the solid phase or the tangent of the internal shear angle, ρ is the density, g the gravitational acceleration, Φ the slope angle, H the flow height, U the flow velocity and ξ is the viscous-turbulent friction coefficient. μ and ξ are responsible for the behaviour of the flow: μ dominates when the solid phase is prevailing, ξ when a viscous or turbulent fluid is prevailing.

I used as topographic data the 1 m Digital Elevation Model from LiDAR data. I calibrated the starting conditions of the simulation of a granular flow (solid dominated), in order to simulate a behaviour expected from a flow with talus deposits as source material and solid dominated, with the meltwater from the ground ice as the only source of fluid. I used the following parameters:

Table 4.3 - Calibrated RAMMS::DEBRIS FLOW parameters.

Release area	32,748 m^2
Released volume	151,395 m^3
Initial release deposits height	15 m
μ	0.100
ξ	200 m/s^2
ρ	1863 kg/m^3

Since RAMMS::Debris Flow uses a single-phase model, and therefore it is not possible to distinguish between fluid and solid phases, I used values for a bulk flow composed by 80% solid dominated granular flow (2100 kg/m^3; Iverson, 1997) and 20% ice (917 kg/m^3). I defined the percentage of ice from the content visually estimated in the field immediately after the occurrence of the landslide. A bulk density value of 1100 kg/m^3, simulating a higher content of ice (50%) and

estimating for the loose debris a 30% of porosity at saturation (based on rock-ice avalanche values (Evans and DeGraff, 2002)), was also applied, but the results of the module were completely unrealistic. The friction parameters μ and ξ were chosen in accordance with the values suggested by the authors of the RAMMS simulation, who suggest an initial value of 0.2 for μ and a value of 100-200 m/s^2 to calibrate the procedure. Varying μ around the initial value with steps of ±1 and ξ with steps of ±100 m/s^2, I found that the best-fit Voellmy friction coefficients for simulating a granular flow in Móafellshyrna were μ =0.100 and ξ=200 m/s^2. Finally, the release area was defined by digitising on the 1m DEM the perimeter of the source area, and using as a release volume the value calculated for the source volume in Section 4.4.2.1. I set as the release height the average thickness of the blocks of deposits perched on the topographic bench and of the biggest block felt in the accumulation area. To simplify the simulation, I did not consider sediment entrainment in the model.

4.4 Results

4.4.1 Morphology and structures of the landslides

4.4.1.1 Morphology and structures of the Móafellshyrna landslide

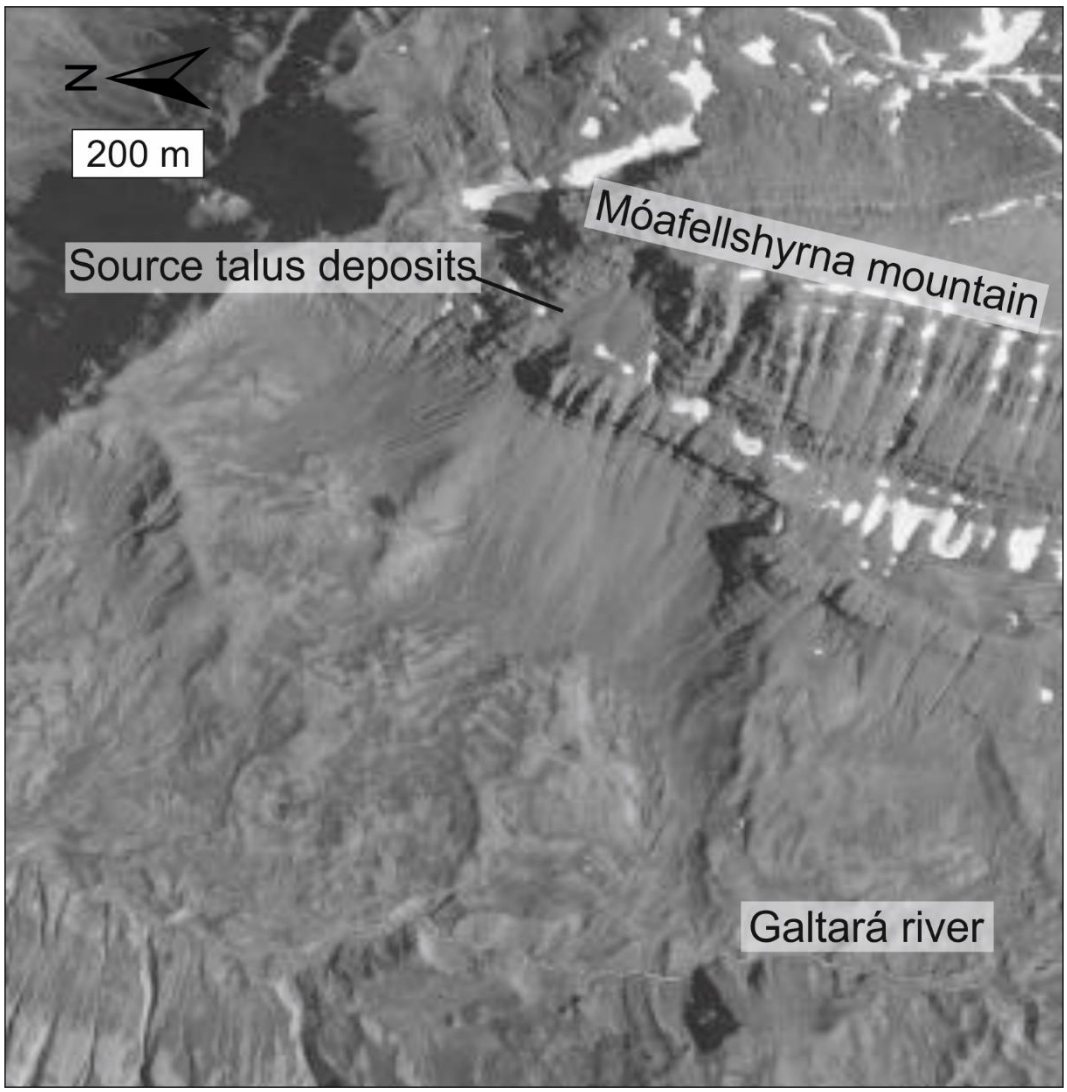

Figure 4.11. Aerial image of the Móafellshyrna mountain (photo LMI-Kort-J10-J-1733-qv taken in 1985, flight line Ármannsfell-Ámárhyrna, National Land Survey of Iceland - Landmælingar Íslands).

The highest point of failed debris in the Móafellshyrna source area is at 870 m a.s.l., and the toe of the debris is at 330 m a.s.l. (Figure 4.4), meaning a vertical

distance H of 544 m. The horizontal travel distance L is 1,320 m, so the Fahrböschung ($\tan^{-1}$ H/L) for the Móafellshyrna landslide is 22°. The landslide originated on a 665 m wide topographic bench on the north-western side of the Móafellshyrna Mountain. The failure mass consisted of ice-cemented talus deposits lying against the sub-vertical rockwall of the mountain. Figure 4.11 shows the appearance of the slope and the talus deposits located at the source of the landslide, 27 years before the occurrence of the failure. The landslide material ranges from fine clay to 1-3 m-sized boulders. At the time of the failure, the ground was covered by a ~20-30 cm of snow.

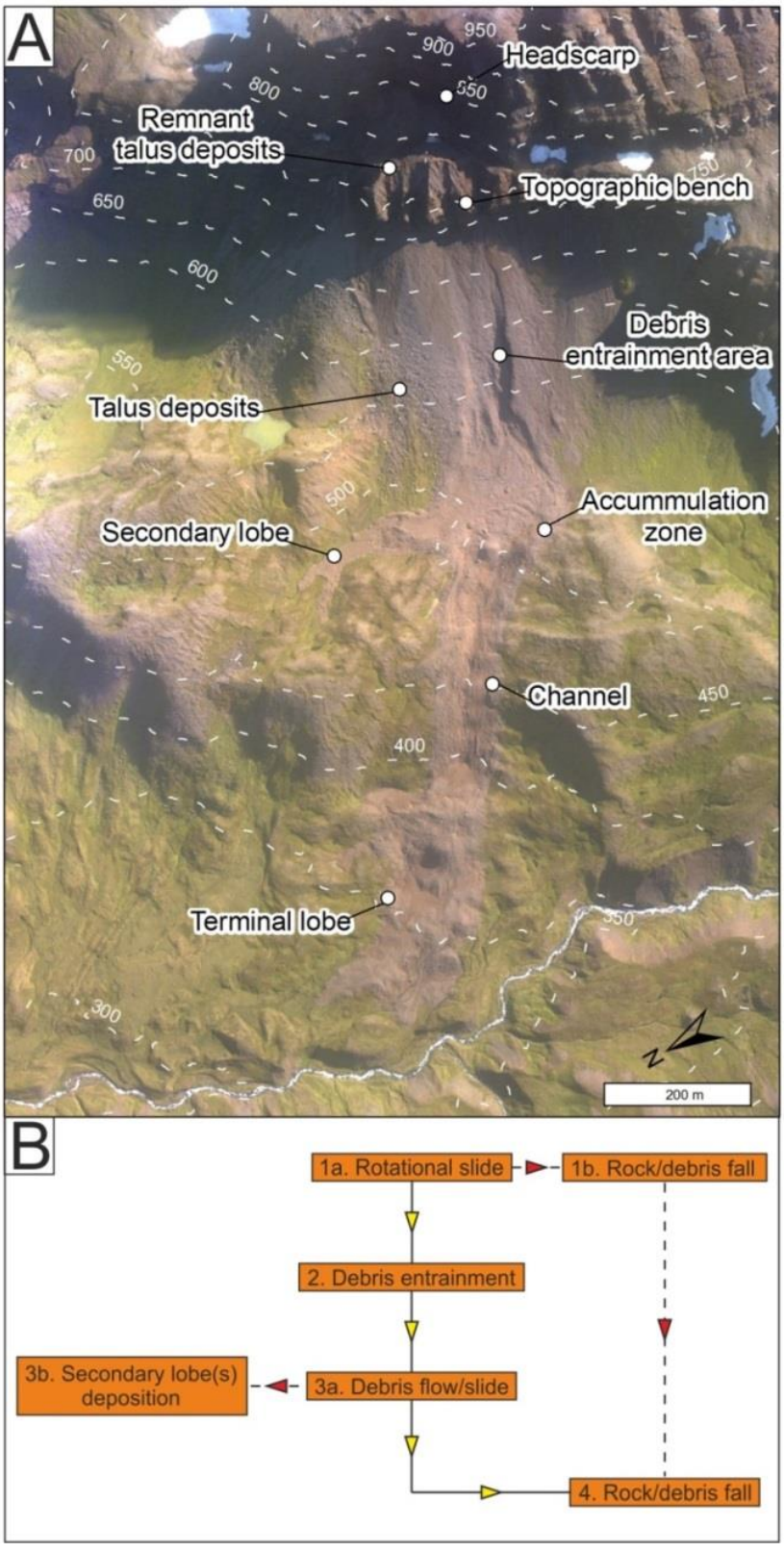

Figure 4.12. The main morphological features of the Móafellshyrna landslide and the flow chart summarizing the different processes that occurred during the Móafellshyrna landslide. The arrows in yellow indicate continuous and consecutive processes, while the dashed red arrows indicate intermittent and/or non-consecutive processes. Time goes from top to bottom of the diagram.

In Figure 4.12 the sequence of the different processes that occurred during the Móafellshyrna failure is illustrated. The first initial movement of the source material was by rotational sliding, accompanied at the same time by rock/debris fall. The debris mass fell on the talus cone downslope (Figure 4.12), entraining new material. Part of the material continued further downslope through a process analogous to debris flow/slide, while part of the material stalled on the first bench forming secondary lobes. After the deposition of the landslide deposits, prolonged rock/debris fail activity occurred intermittently over time. I will describe here the different morphologies and structures left by all of these processes.

The initial movement of the talus slope deposits was by rotational sliding. The initial movement direction of the detached talus deposit mass from the source area was N340°. The entirety of the talus deposits did not slide off the bedrock cliff, as remnants are still perched on a topographic bench in the source area (Section 1 in Figure 4.4). At the time of the failure the remnant talus material appeared as rectilinear blocks standing vertically at the edge of the bench. In photographs taken a few days after the occurrence of the landslide (Figure 4.13D and E), the blocks of frozen sediments perched at the edge of the topographic bench are clearly visible. Their vertical dimension has been visually estimated to be 15-20 m (see Chapter 6), and some of them have degraded in place, as they are today still observable in the field and in the aerial images, preserved as mounds of debris (Figure 4.13F,G). The debris deposits at the edge of the bench have an average slope angle of 39°, and a drop in elevation between their surface and their contact with the bedrock of 30 m. At this contact, in the field I observed the presence of active water springs Figure 4.13C).

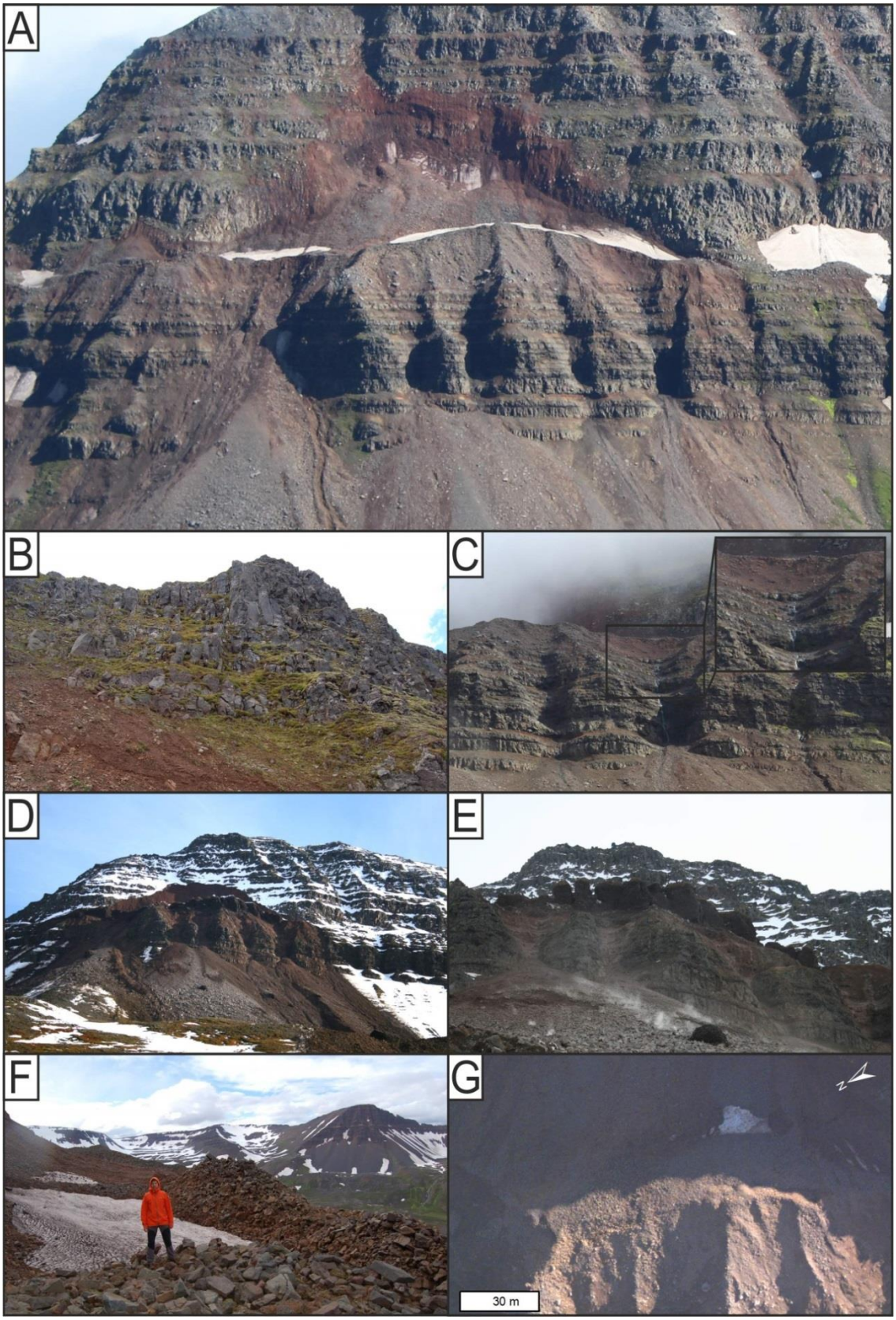

Figure 4.13. The geomorphology of the Móafellshyrna landslide's headscarp zone. (A) Oblique view of the headscarp of the Móafellshyrna landslide, with remnants of the source deposits lying against the rockwall and perched at the edge of the bench; (B) bedrock of the Móafellshyrna mountain dissected by sub-vertical

and sub-horizontal systems of discontinuities; (C) water spring at the contact between the bedrock and the remnant of the source talus deposits; (D) oblique view of the topographic bench and the headscarp of the Móafellshyrna Mountain four days after the failure; (E) unstable blocks of frozen talus deposits perched at the edge of the topographic bench four days after the failure; (F) one of the cones of deposits resulting from the degradation of blocks of ice-rich sediments, and perched at the edge of the topographic bench (picture taken in July 2015); (G) aerial photo of the remnants of the source talus deposits, with conical features at the edge of the topographic bench as result of the degradation of blocks of frozen talus deposits.

The bedrock of the mountain is dissected by sub-vertical and sub-horizontal systems of fractures, which are pervasive and spaced on the scale of tens of centimetres (Figure 4.13B). This orthogonal discontinuity geometry gives rise to multiple blocks that are prone to topple and fall. On the mountain ridge, I also observed a reverse fault with several metres of offset. Three years after the occurrence of the failure, the bedrock still appeared wet at the headscarp, and ice was visible on the headscarp wall (Figure 4.13A). This could reflect the presence of groundwater flow that exploits the intersecting discontinuity systems. The headscarp is marked by a distinctive red colour, caused by the fine silty clay deposits that compose the matrix of the original talus deposits, and which have not been completely removed (Figure 4.13; see Chapter 6 for full description of the ice-cemented talus deposits). The angle of slope of the headscarp, where bedrock is fully or partially exposed, is generally ~50°and the slip surface in the source area is upwards concave.

After the initial sliding movement, the debris mass encountered the edge of the topographic bench, and fell downslope through the process of rock/debris fall. The residents of the Þrasastaðir farm report debris fall activity for months after the occurrence of the landslide; this activity stopped over the winter, and new debris fall activity started again in the following spring. The debris mass was

probably transferred through the chutes that are carved in the bedrock cliff below the source area.

Topographically below, in Section 2, the debris mass encountered the talus deposits of slope angle of 30° that are located at elevations of 690 m to 510 m a.s.l. The falling debris mass entrained new material from these talus deposits, and eroded a channel down the middle of the talus slope (Figure 4.14). Measurements from the DEM reveal that the talus deposits were incised to a depth of up to 3 m from their original surface. However, visual estimations from pictures taken a few days after the occurrence of the failure show that the thickness of the talus debris entrained by the initial mass was probably much higher (up to 5 m, Figure 4.14), but this channel has been partially re-filled by material that fell subsequently on the talus slope. A minor debris flow 140 m long is also observable on the north-eastern side of the of the talus slope.

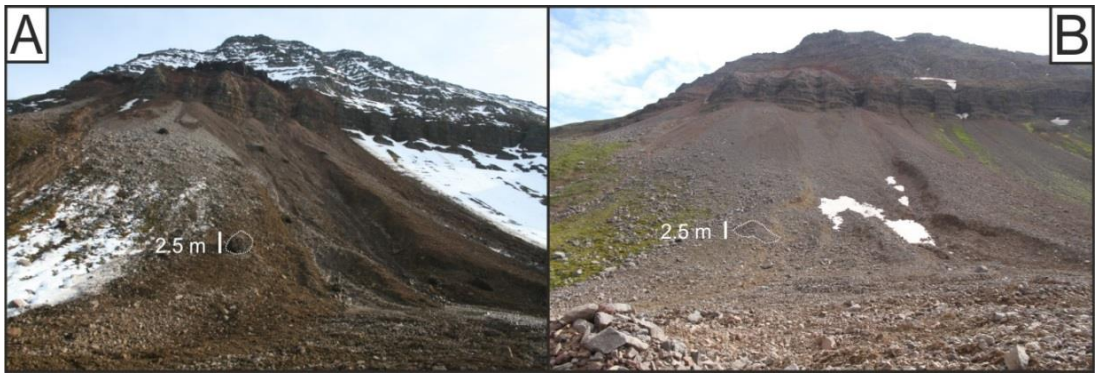

Figure 4.14. Entrained talus deposits. (A) The erosional area as result of the entrainment of talus deposits by the initial mass (the picture was taken on 29th September 2012); (B) the same view of the erosional area, partially re-filled by new talus material (the picture was taken in July 2015). Note the cone of debris as scale, resulting from the degradation of the ice-cemented block in panel A.

The debris mass then reached a low slope area in Section 3 at the foot of the talus slope (Figure 4.12), and then proceeded further downslope through a process similar to a debris flow/slide. It is likely that in a second stage – probably

a few minutes after the deposition of the main flow deposits – a second pulse of debris was transported in this intermediate flat area. This second pulse is recognisable by the granulometry, morphology and structures of the deposits in this flat area, and their geomorphic features have not been overprinted by newer flow features and therefore were the last to be formed. These deposits are characterised by the presence of multiple layers (at least 2). Distributed around this low slope accumulation area are thirteen relatively long (11-40 m) compressional ridges, separated by depressions (Figure 4.15). These compressional ridges are partially parallel to the runout direction of the flow (NW to WNW), but those towards the centre accumulation area verge towards NE, probably because the flow encountered a topographic obstacle to the west. The ridges are rounded and sinuous, are 5-10 m wide, and from the bottom of the intra-ridge depressions to the crest of the ridge they are 0.5-1 m high on average (Figure 4.16A). At the contact between the foot of the talus slope and the accumulation zone, there are lobate features, and discrete zones of well sorted fine or coarse deposits (Figure 4.15, Figure 4.16A). In this accumulation zone of the landslide, I found 17 cones of debris 4 to 39 m wide and tens of cm to 10 m high. These are called “molards”, and they are the result of the degradation of blocks of ice-cemented talus deposits that were observable a few days after the landslide occurred (Figure 4.16B). In Chapter 6, I reconstruct the formation of molards and I discuss their significance in periglacial environments. A fuller description of the geomorphological importance of molards is given in Chapter 6, but here I discuss their importance as pertains to the dynamics of the landslides. In this same zone of the landslide, at the foot of the talus slope, fresh boulders up to 1-3 m high are also present (Figure 4.15; see Section 4.4.2.2 for their runout analysis).

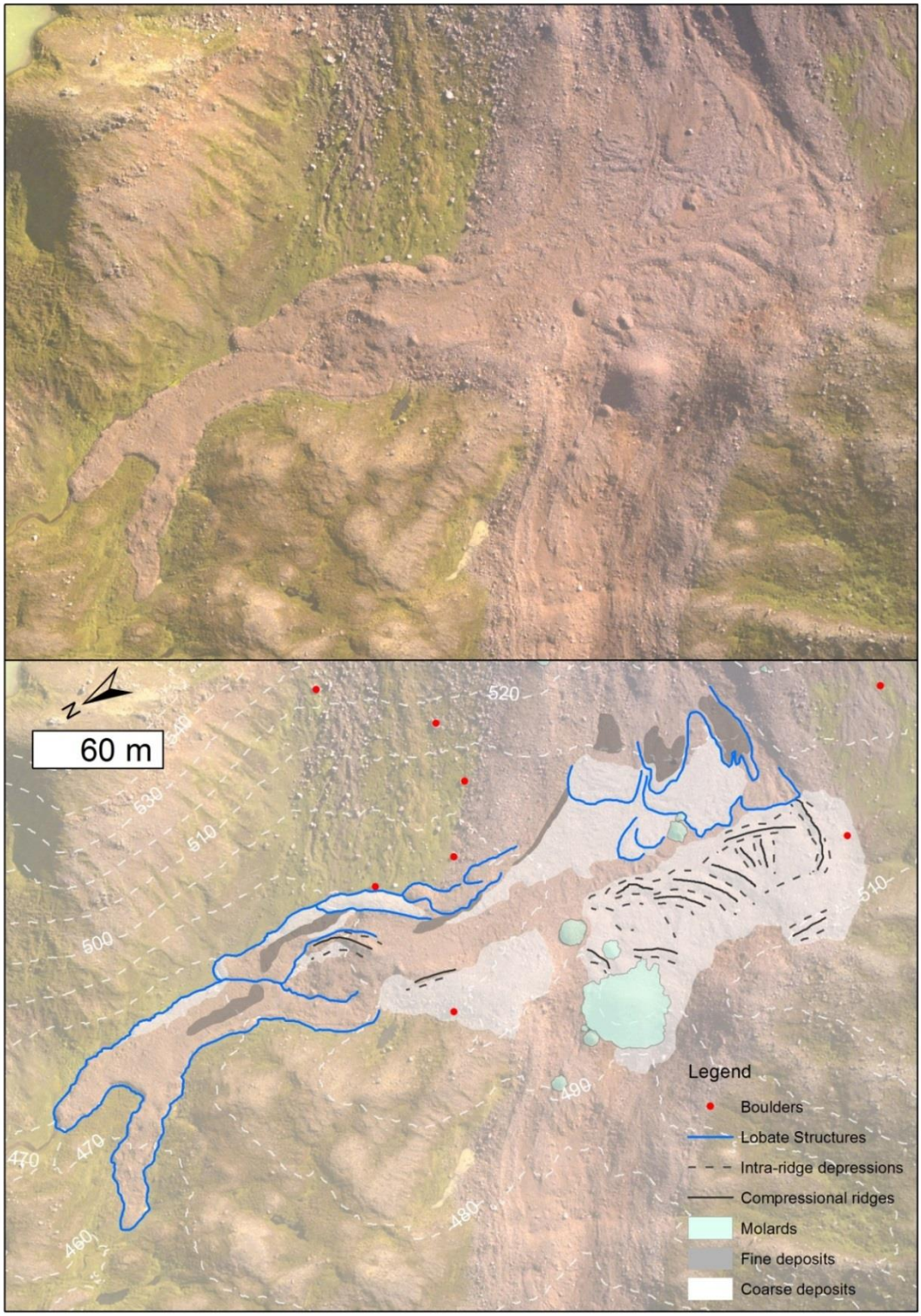

Figure 4.15. The main geomorphological features of the upper accumulation zone of the Móafellshyrna landslide with the black arrows indicating the main direction of the flow. Lighting angle from south.

In this flat accumulation zone of Section 3, a secondary lobe was deposited on the north-eastern side of the landslide, striking N260° (Figure 4.15). This secondary lobe has a distinctive “fish-tail” shape, characterised by a terminal bifurcation into two lobes. Other smaller secondary lobate features are also present further upslope. The lobate deposits have a thickness of 1 m up to 3 m (Figure 4.16C), and have abundant boulders and gravel in a fine (silty clay) matrix. There is a preferential distribution of coarse material at the edges of the lobe, while fine debris tends to be found towards its centre. Using aerial images, it can be seen that the fish-tail lobe is itself composed of lobate structures. From observations made four days after the failure, it also seems that the lobe bulldozed the snow as it travelled downwards on a slope of only 12° (Figure 4.16D).

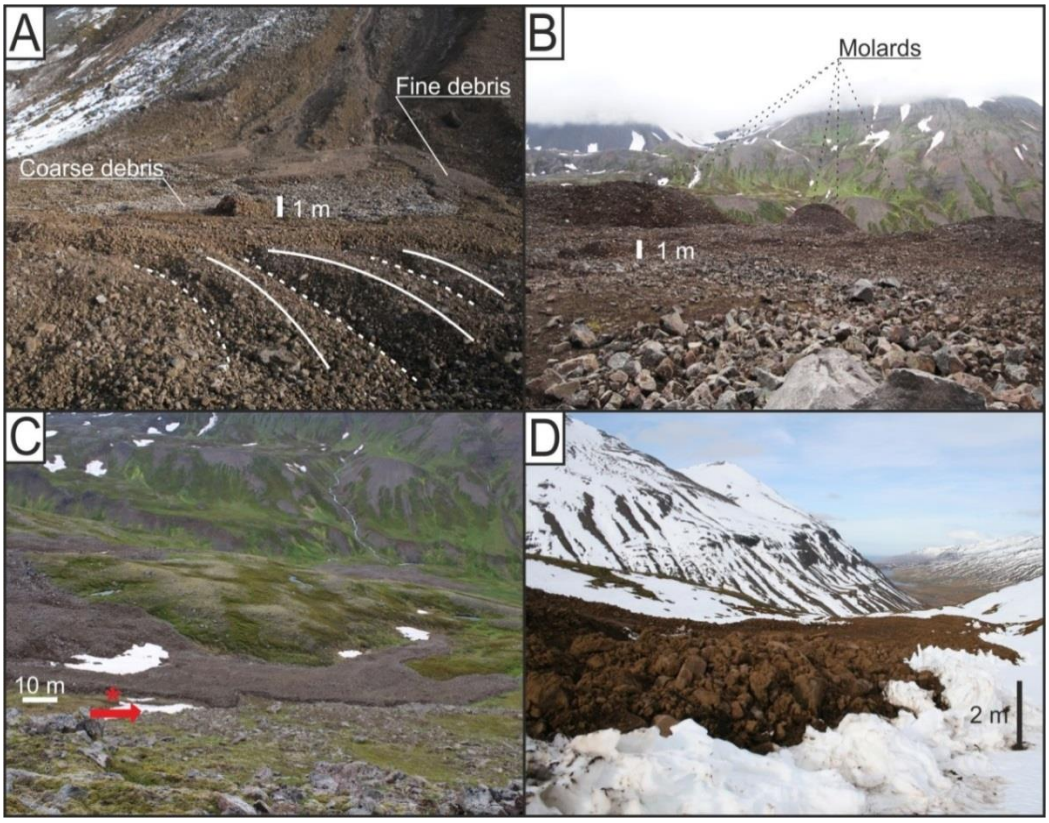

Figure 4.16. The morphology of the accumulation zone. (A) Ridges (crests marked with solid lines) and intra-ridges depressions (white dashed lines) in the first flat accumulation area encountered by the flow. In the background, discrete zones of coarse debris and lobes of fine debris are present; (B) some of the cones

of debris (molards) scattered on the accumulation area; (C) secondary "fish tail" lobe located to the east of the main accumulation zone (red asterisk and arrow show the perspective view of panel D); (D) snow bulldozed by the "fish tail" lobe (pictures taken 9 days after the landslide).

The main debris mass continued in a north-westerly direction and travelled downslope, forming a straight channel coated with debris (Figure 4.12). This is a zone where deposits were transferred (Section 4 in Figure 4.4), and the thickness of the deposited debris sheet is less than 1 m. This section of the landslide has a channel-form 263 m long and up to 107 m wide (Figure 4.17A). In the central part it is characterised by ridges and furrows with N145° direction (Figure 4.17B). The lateral margins show a different granulometry, being mainly composed by blocks, forming poorly-defined lateral levees (Figure 4.17C). The presence of a central "channel" with ridges and furrows might be an indication of erosion, because in the aerial images of the slope before the occurrence of the landslide (Figure 4.11) no channelized features seem to be present. The traces of lateral levees indicate deposition in this section of the landslide.

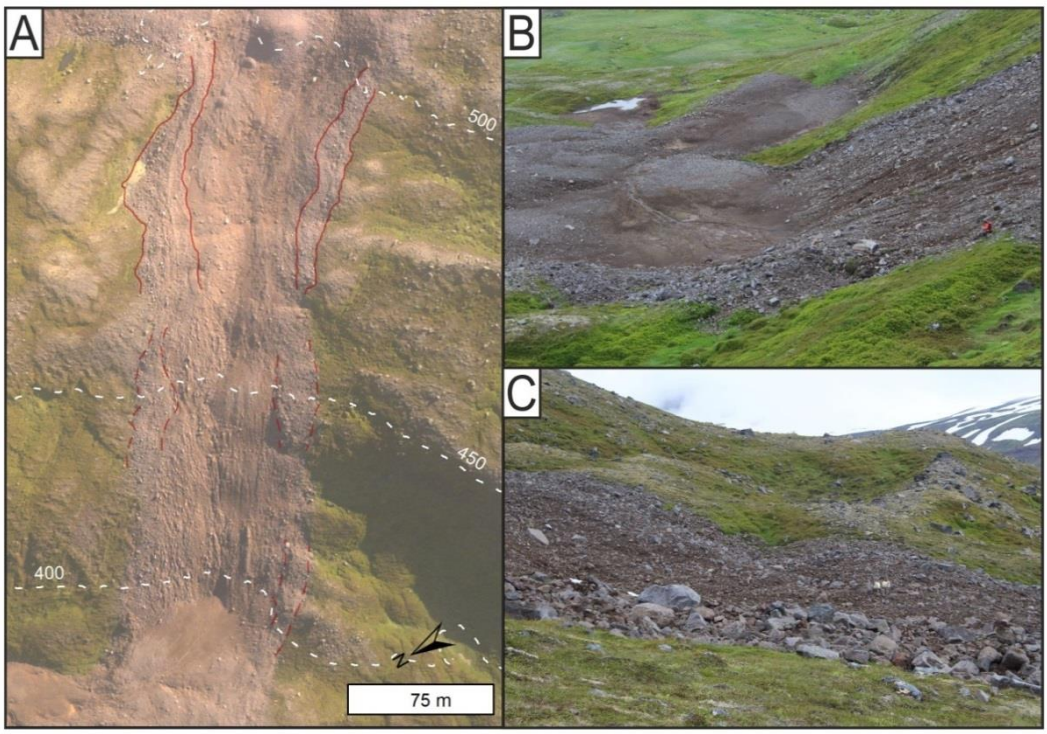

Figure 4.17. The channel of the Móafellshyrna landslide. (A) The channel has lateral levees, which are not-well defined downwards; (B) oblique view from south of the terminal part of the channel, with deposit-ridges and scours downslope; (C) oblique view from north-east of the upper part of the channel, with finer material in the centre (see the two sheep for scale) and the coarser material at the edge forming lateral levees.

The debris mass ended its path on a gently sloping surface in Section 5, almost reaching the Galtará river (Figure 4.4). The flow formed a terminal lobe 369 m long, up to 218 m wide, and with a thickness of at most tens of centimetres (10-50 cm). This terminal zone of the landslide is characterised by discrete flat areas where silty to clay material segregated from the gravelly material, sometimes forming secondary lateral lobes with ponded water, or pools of muddy sand, and sometimes infilling areas with topographic 'traps' (Figure 4.18A). Where the topography is steeper, longitudinal ridges and furrows (up to 40 m long) created by the transport of blocky material are observable (Figure 4.18B). The zones dominated by the fines show "sand boil" structures (4 to 5 m in diameter), which

result from the liquefaction of water-saturated fine sediment (Iverson et al., 2015; Xu et al., 2012), and cracks a few meters long (1-5 m) (Figure 4.17C,D).

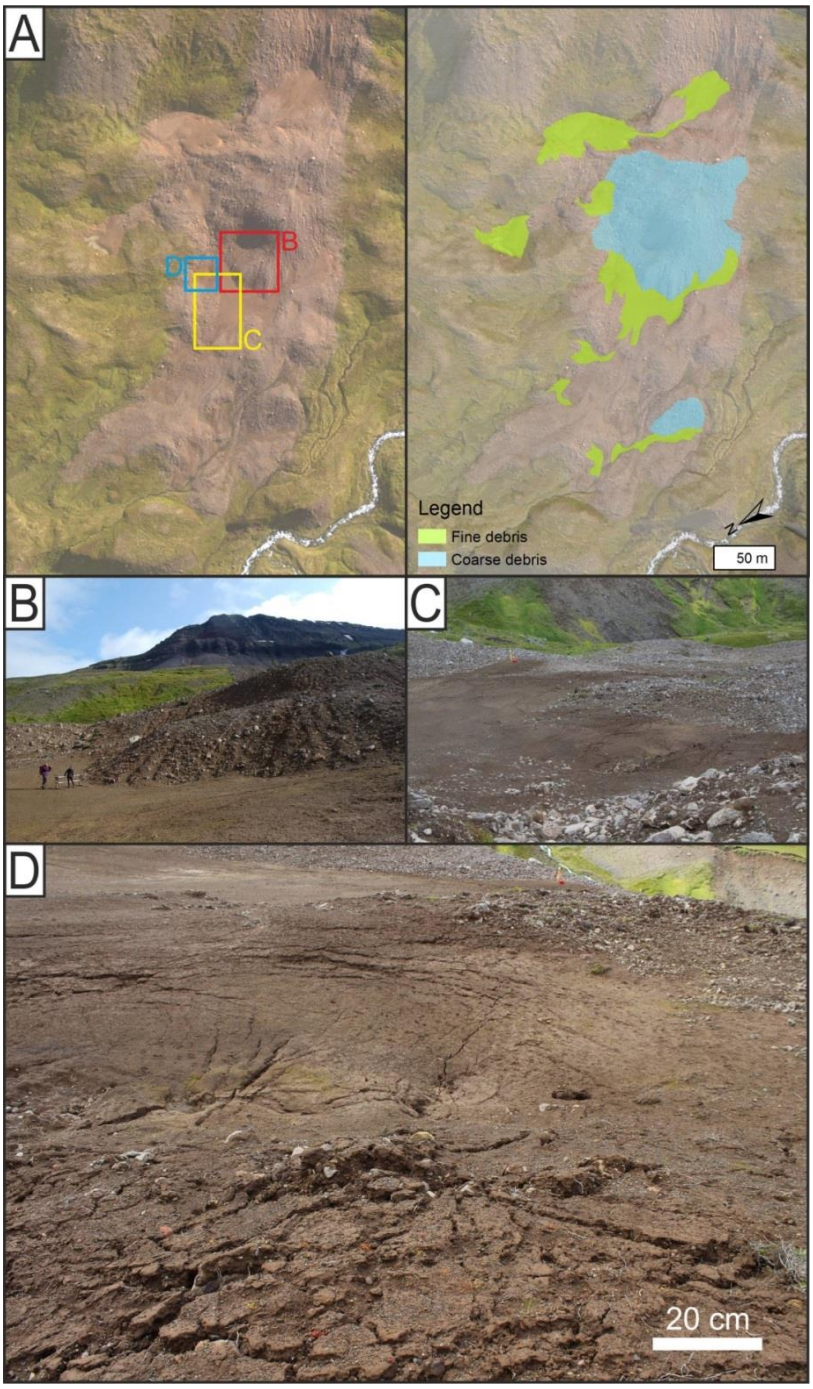

Figure 4.18. The terminal lobe of the Móafellshyrna landslide. (A) Aerial view of the terminal lobe, with the main zones where fine (silty-clay) and coarse (bouldery-gravelly) debris are dominant (the coloured squares indicate the different panels B, C, and D); (B) view from south-east of part of the terminal lobe with ridges and furrows and where coarse bouldery-gravelly deposits are dominant, in contact downslope with an area where silty-clay deposits are dominant; (C) view from east of an area where silty-clay material is dominant and where sand boil structures are located; (D) view from south-east of sand boil structures.

4.4.1.2 Morphology and structures of the Árnesfjall landslide

The Árnesfjall landslide detached from the northern flank of the Árnestindur peak (Figure 4.19A) at 418 m a.s.l., and its toe extends to the bottom of the valley at 70 m a.s.l., with a lateral debris flow that reached the road (Strandavegur 643) at a few meters above sea level (Figure 4.19B). The vertical distance H between the top and bottom of the landslide is 348 m, while the horizontal travel distance L was 560 m, giving a Fahrböschung of 32°. Similar to Móafellshyrna, the failure mass consisted of ice-cemented talus slope deposits, in this case lying against the north-facing, sub-vertical rockwall of the Árnestindur peak. Parts of the talus deposits were not mobilised by the landslide and still cover 75,000 m^2 of the northern side of the Árnesfjall Mountain. These preserved talus deposits show deformation features, such as transverse fissures (20-50 m long; Figure 4.20A,B) probably due to permafrost creep.

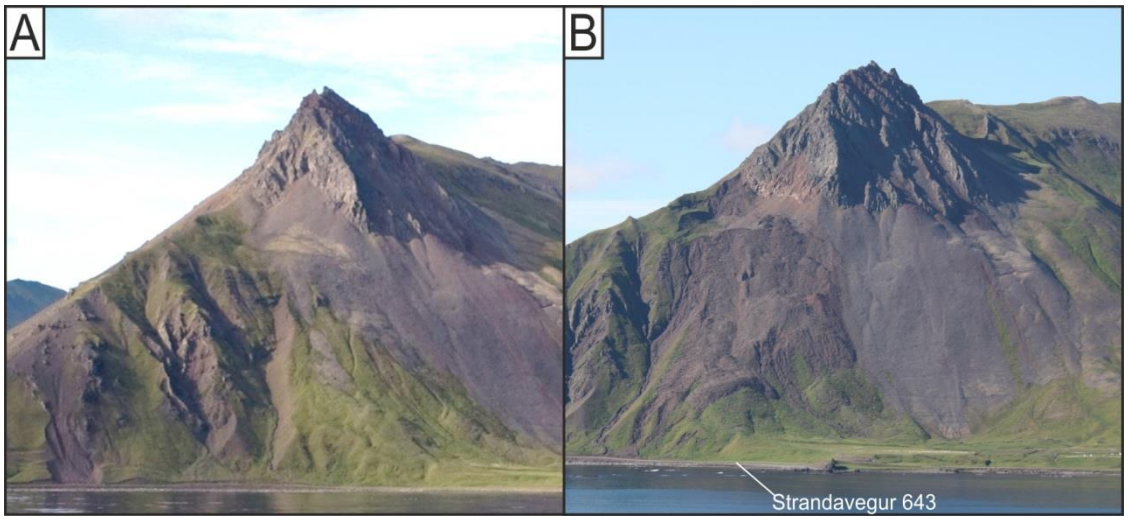

Figure 4.19. The Árnesfjall Mountain before and after the failure. (A) Oblique view from north-east of the Árnesfjall Peak (picture taken on 13-08-2008, courtesy of Ingvi Stígsson); (B) oblique view from north of the Árnesfjall landslide (picture taken in July 2016).

The landslide material ranges from clay to large boulders in grain size. On the western side of the landslide, the headscarp has a distinctive red colour due to remnants of fine material composing the matrix of the original talus deposits (Figure 4.20C; see Chapter 6 for full description of the ice-cemented talus deposits), and an average slope of 49°. On the eastern side, the landslide has three semi-circular and upwards concave minor scarps (50 to 85 m long), forming up to 15 m thick tilted blocks made from surficial colluvium (Figure 4.20D).

The basalt composing the bedrock of the mountain displays a pervasive (spaced on the scale of centimetres) primary foliation due to the movement of lava flow during its emplacement, dipping 30° towards SSW. This is cut by a pervasive discontinuity system (probably cooling joints) that dips sub-vertically between WNW and ESE, with typical joint spacing of 1-2 m (Figure 4.20D). Locally, particularly at the contact between the headscarp and the remaining talus deposits, the bedrock appears wet.

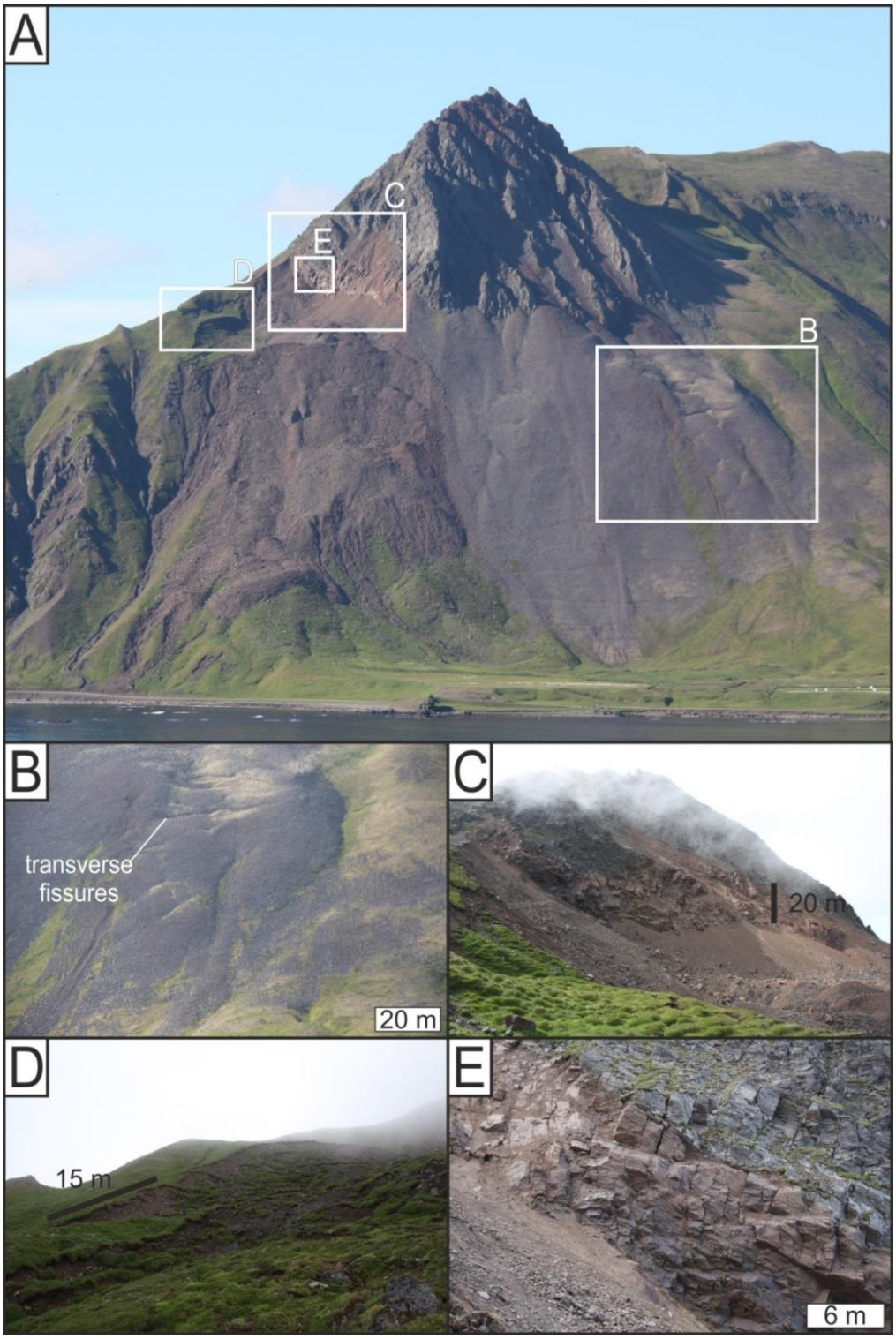

Figure 4.20. The morphology of the source area of Árnesfjall landslide. (A) Oblique view from north of the Árnesfjall landslide, with the white squares indicating the different panels B, C D, E; (B) Preserved talus deposits next to the landslide that show deformation features probably due to permafrost creep; (C) the headscarp with a distinctive red colour left the source materials; (D) lateral minor scarps on the eastern side of the landslide; (E) the bedrock in the headscarp exposed by the failure, showing two perpendicular discontinuity systems in the bedrock.

In Figure 4.21 the sequence of the different processes that occurred during the Árnesfjall failure is illustrated. The first initial movement of the source material was by rotational sliding, accompanied at the same time by lateral debris flows. After the deposition of the landslide, a secondary set of debris flows occurred, accompanied by the transport of an 'outrunner' (nearly intact blocks of debris that detach from a submarine landslide body (De Blasio et al., 2006); the term is also used for terrestrial landslides (Milana, 2016). I will describe here the different morphologies and structures left by these processes.

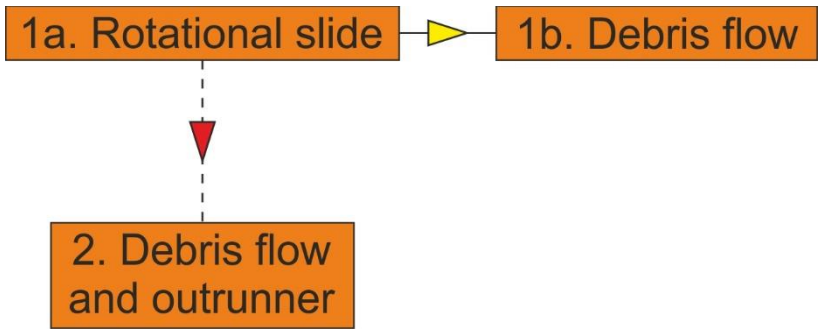

Figure 4.21. Flow chart summarising the different processes that occurred during the Árnesfjall landslide. The arrow in yellow indicates time continuous and consecutive processes, while the dashed red arrows indicate intermittent and/or non-consecutive processes.

In the depletion zone (Figure 4.22), the source material was tilted downwards, but part of the talus deposits are still perched in this area of the landslide (Figure 4.22A). In particular, multiple elongated cones of talus deposits lie here (Figure 4.22A,B), densely grouped ~40-150 m below the top of the headscarp. They are up to 27 m long and almost 4 m high, and are the result of the degradation of angular ridges composed of ice-cemented talus deposits (see Figure 6.2 in Chapter 6) that formed during the tilting downwards of blocks of source material during the failure. Four of these are located in the accumulation area downslope. I have identified these cones as molards. I discuss in Chapter 6 their

morphometric characteristics, and how they not only reveal permafrost degradation in the area, but also information on the landslide process. On the downwards-facing surfaces of the cones that are closest to the external edge of the depletion zone it is possible to observe lichens: hence this surface has not been greatly disturbed by the failure: its preservation reflects a homogeneous rotation of the whole debris mass (Figure 4.22C).

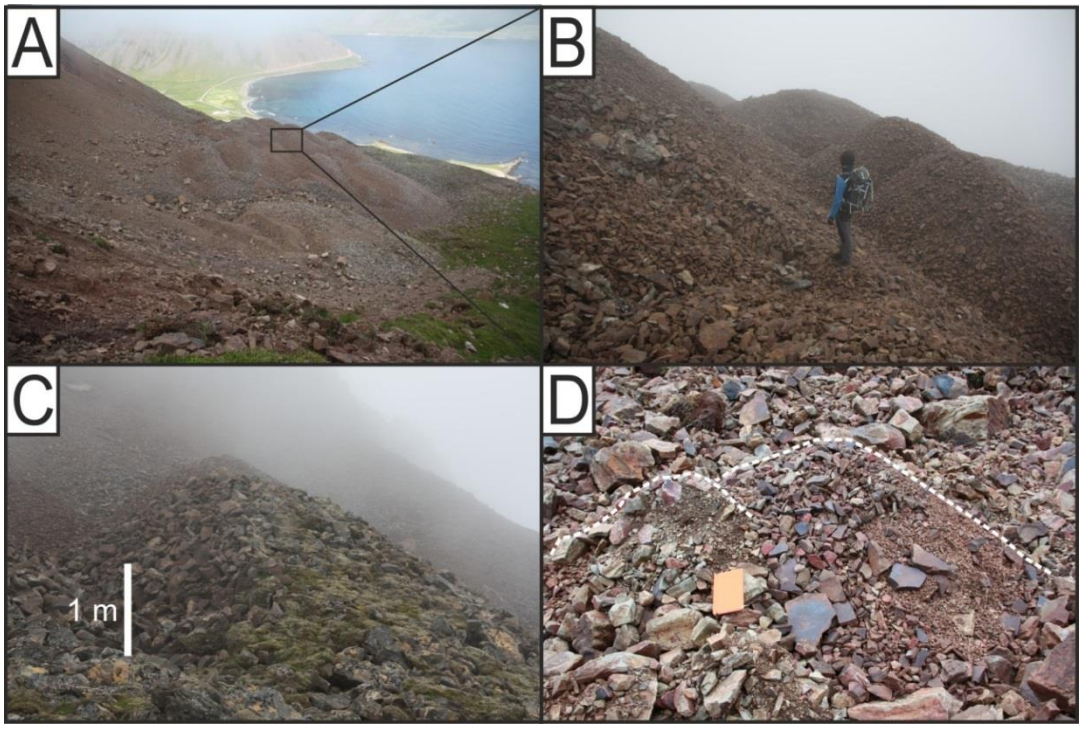

Figure 4.22. The cones of debris in the depletion zone of the Árnesfjall landslide. (A) The dense group of elongated cones of talus deposits perched below the headscarp; (B) the cones in the depletion zone are formed by bouldery talus deposits, can reach heights of 4 m, and are identifiable as molards; (C) the original surface of the source talus material is preserved in places in the depletion zone; (D) one of the circular isolated molards scattered on the surface of the accumulation zone, with a smaller molard sitting on top of it.

The slope transition between the depletion zone and the accumulation zone is quite abrupt, from an angle of ~18° at the edge of the depletion zone, to 33° in the upper part of the accumulation zone. The direction of movement of the whole mass was N58°. The accumulation zone is composed in the centre by a relatively

uniform debris mass, with debris flows around the periphery (Figure 4.23). The debris mass is 180 wide and 360 m long, and its thickness ranges from 5 m in the upper part to up to 15 m at the toe. It has two central terminal lobes and the eastern lobe ends with two small (66 and 70 m long) debris flows. The deposits are composed of clasts (ranging from 5 cm to tens of centimetres, rarely bigger than 1 m) and gravel, with scarce silty clay matrix. Some isolated molards are scattered on the surface of the debris mass (Figure 4.23D). They are more circular and less elongated than those in the depletion zone, are generally composed of bouldery-gravelly material (with a couple of exceptions where they are matrix supported by silty-clay material), and range in height from 20 cm up to rare cases of 1 m. As opposed to Móafellshyrna, the molards in Árnesfjall sometimes preserve the original stratification of the talus deposits, evidence that the material was tilted downwards as a single mass (see Chapter 6 for the description and discussion of molard morphology and formation).

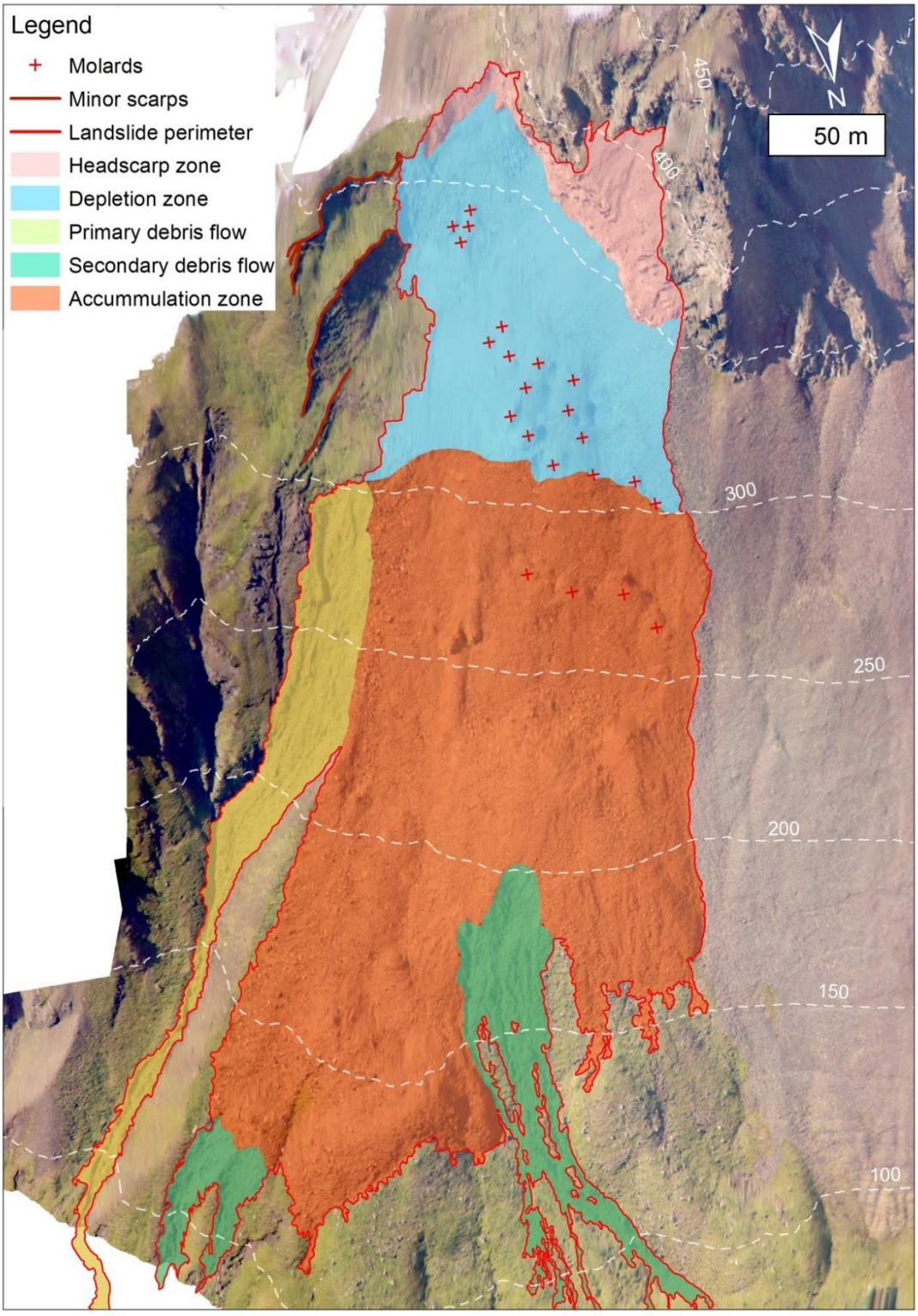

Figure 4.23. Map of the main morphological features of the Árnesfjall landslide.

The north-eastern debris flow, which happened at the same time as the landslide, originates at the top of the debris mass (Figure 4.23), so spans the

whole accumulation zone, and then extends to the Strandavegur 643 road (Figure 4.24C). It is 30 m wide at its head, where abundant clasts from 30-50 cm up to 1-2 m size are present, particularly at the contact with the debris mass (Figure 4.24B). The channel is 1 to 2 m deep, and shows 30-50 cm up to 1 m high lateral levees (Figure 4.24A). Secondary debris flows depart the foot of the east side of the accumulation zone as well, reaching the road downslope (Figure 4.24A). Other secondary debris flows on the north-north-western side of the landslide are 224 m long and develop at the terminal edge of the main debris accumulation zone. They bifurcate downslope into two channels less deeply incised (30-60 cm) that have 10 to 30 cm thick lateral levees. The terminal lobes reach the fields at a few tens meters from the coast. From visual comparison of pictures taken immediately after the occurrence of the landslide (Figure 4.24C) and two days after the failure, it is clear that this debris flow developed after the occurrence of the landslide in the two days between the photos being taken. It is likely that, as blocks of ice-rich sediments from the debris mass started to degrade, a mixture of debris and fluid was released. In one of the terminal lobes of the debris flow a molard is present (Figure 4.24D). This block is not visible in the photos taken on the day of the failure, but is visible in those taken two days later, so must have failed in this range of time, likely at the same time of the north-north-western secondary debris flow.

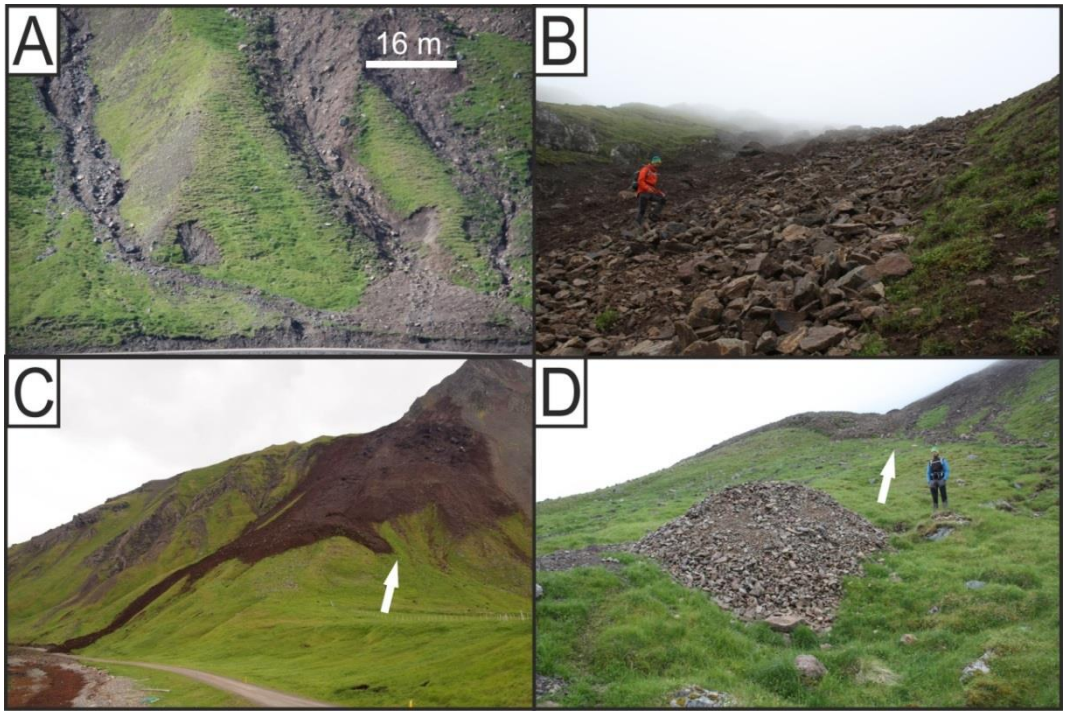

Figure 4.24. The accumulation zone of the Árnesfjall landslide. (A) The debris flows on the eastern side of the accumulation area; (B) Clastic material at the head of the debris flow on the eastern side of the accumulation zone; (C) a view from the road Strandavegur 643 of the landslide on the day of the failure. Note the square shape of the blocks of ice-rich sediments scattered on the landslide' surface. The white arrow points to the same place as the one in the next panel; (D) an isolated molard at the foot of the western debris flow (absent in Figure 4.24C), which developed two days after the occurrence of the failure.

4.4.2 Volume and runout analyses

4.4.2.1 Volumes and runout analysis of the Móafellshyrna landslide

Estimations from field observations of the deposit thickness indicate that the volume of debris that was mobilised by the Móafellshyrna landslide was between 295,000 and 440,000 m^3, considering that the landslide covers an area of 293,900 m^2. The Fahrböschung of the Móafellshyrna landslide is 22°. A further calibration of the volume estimates has been obtained using the GPR profiles. The GPR results give a rough estimate of the thickness of the deposits, particularly in the Sections 4 and 5 of the landslide. These results, however, are

unsatisfactory and not fully reliable, as they were affected by a strong attenuation of the radar waves. Thus, the penetration depth was restricted to 4-6 m (100 MHz) and 6-8 m (50 MHz). Furthermore, the data analysis was severely disturbed by signal scattering caused by the presence of voids in the coarse landslide material. However, near-surface sediment structures were detected at profile GPR L1 at 100 MHz frequency (Figure 4.25), which is located in the terminal lobe (see Figure 4.10) nearly parallel to the runout direction, and where the sliding surface is observable at 2 m of depth. The sliding surface is sub-parallel to the topography. The sliding surface is also observable at 1 m depth in profile GPR L2, which was run in the terminal lobe (see Figure 4.26). These results are confirmed by field inspections, as I dug a hole in the landslide deposits along profile GPR L2 and found a clod of earth with grass at 82 cm depths. Therefore I have used the GPR results only to have a rough estimate of the thickness of the deposits of the terminal part of the landslide (corresponding to Section 4 and 5). Other uncertain reflectors were recognized in the other GPR profiles (see Appendix 1) always sub-parallel to the topographic surface and always at depth between 0.5-4m.

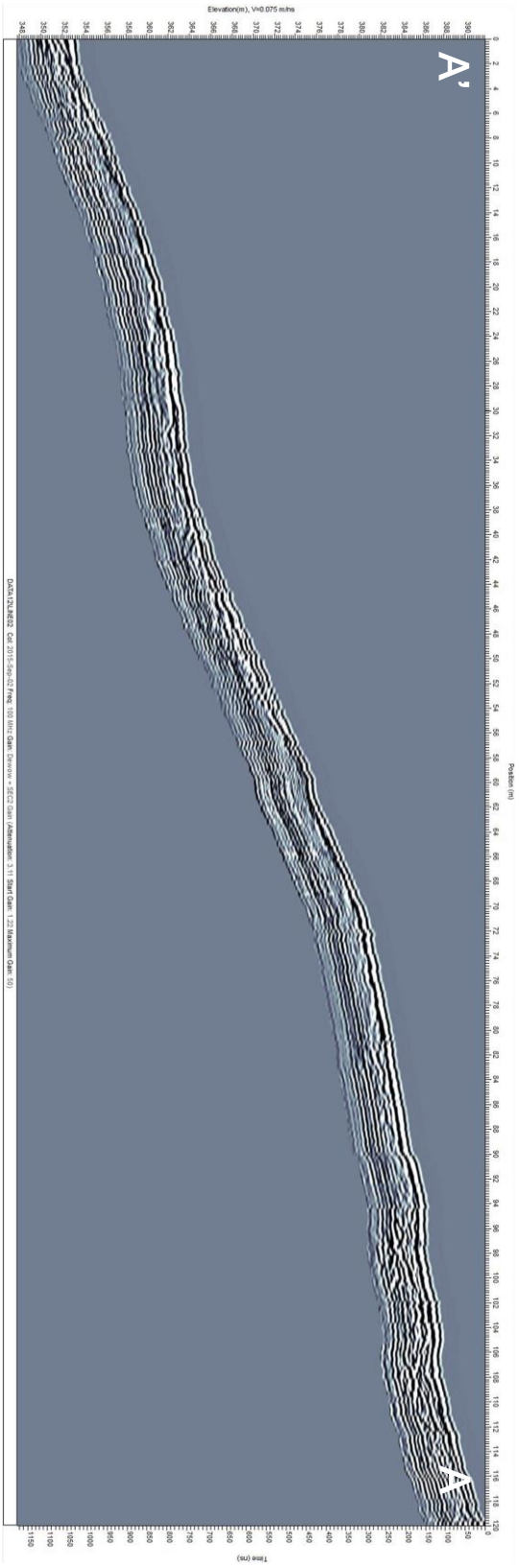

Figure 4.25. Results of GPR measurements at profile GPR L1.

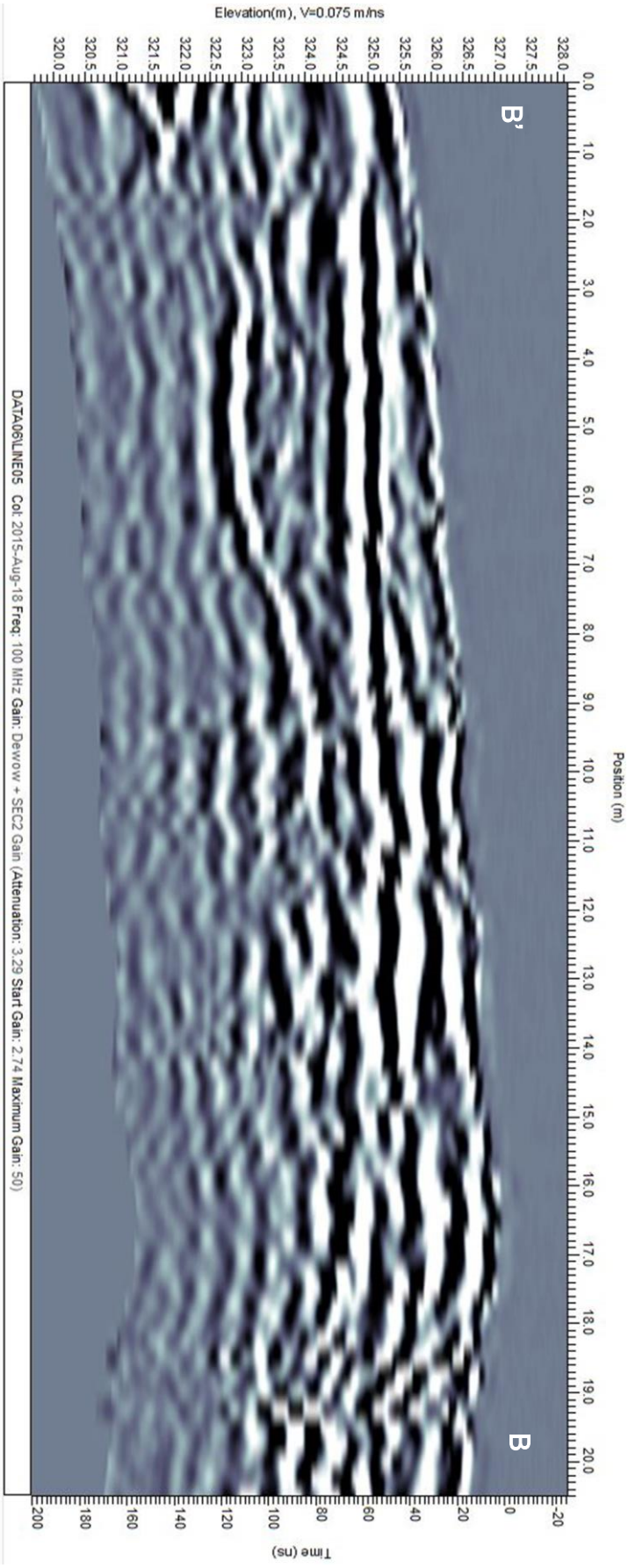

Figure 4.26. Results of GPR measurements at profile GPR L2.

Table 4.4 - Summary of the calculated parameters for the Móafellshyrna landslide and the DEM of difference (DoD) between the post-failure topography and the reconstructed pre-failure topography superposed on an aerial image.

Móafellshyrna landslide parameters	Value	Unit
Area of source debris	32,700	m^2
Debris thickness at the edge of topographic bench	15-20	m
Calculated source mass volume from DEM	151,400	m^3
Area of landslide	293,900	m^2
Flat accummulation area	24,000	m^2
Channel	25,000	m^2
Terminal lobe	47,000	m^2
Estimated average landslide debris thickness	1-1.5	m
Estimated landslide volume	295,000-440,000	m^3
Calculated landslide volume from DEM and field calculations/estimates	314,400	m^3
Length of landslide path (L)	1320	m
Height of landslide path (H)	544	m
(H/L)	0.41	
Fahrböschung (tan^{-1}(H/L)	22.43	°

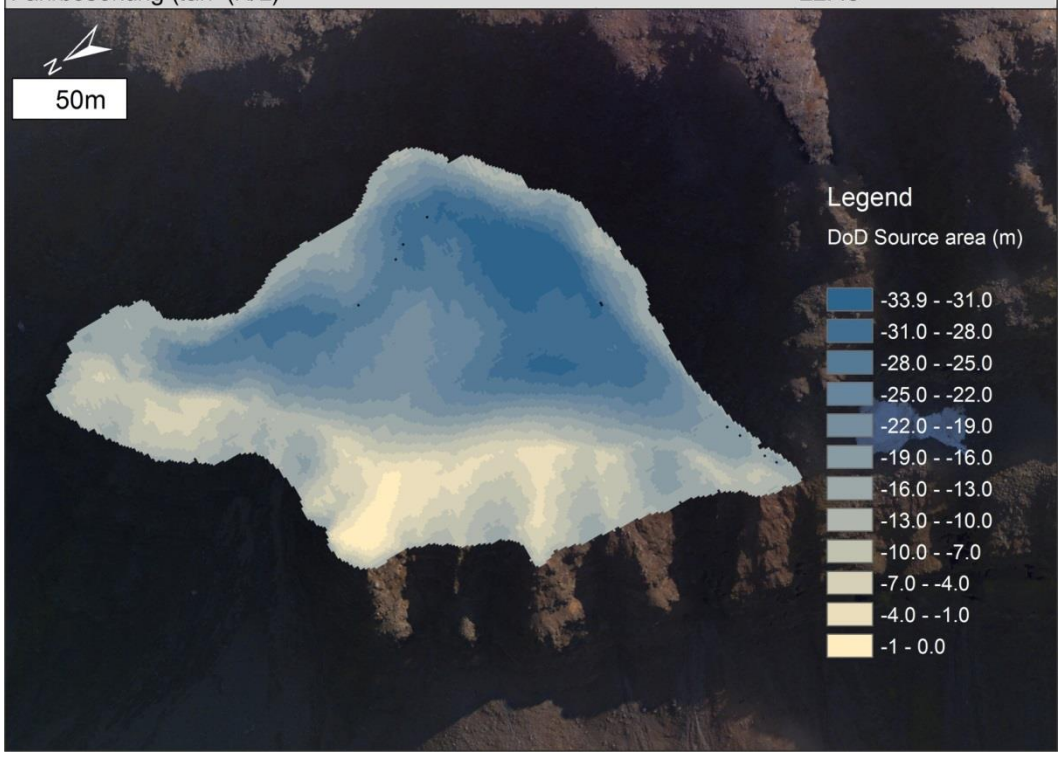

I reconstructed the pre-failure topography of the source deposits (see Section 4.3.4 for the method) to quantify the talus deposit volumes that were perched on

the topographic bench before the occurrence of the failure. The panel below Table 4.4 shows the DEM of difference (DoD) for the source area, obtained by subtracting the manually reconstructed pre-failure topographic surface from the post-failure topographic surface. The volume of source talus deposits obtained through this calculation is 151,400 m^3 (Table 4.4; Figure 4.27); in places, 15 to 20 m thick debris is still perched at the edge of the bench.

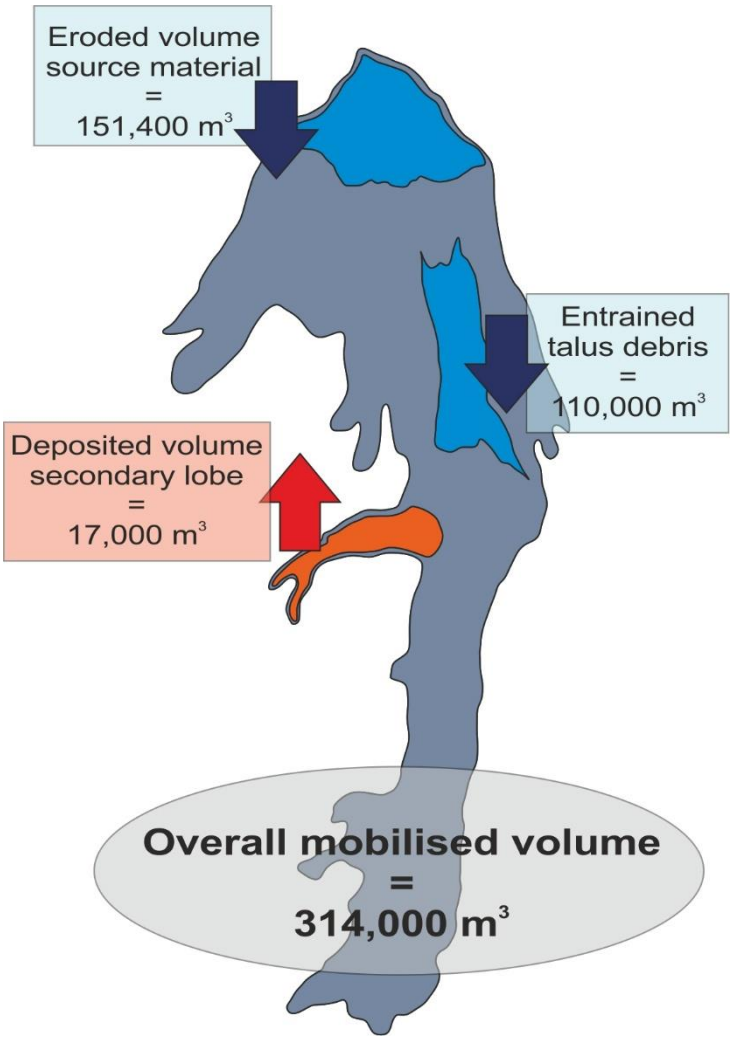

Figure 4.27. Conceptual diagram showing the eroded (blue) and deposited (orange) volume calculated for the main features of the Móafellshyrna landslide, which overall mobilised 314,000 m^3 of debris. The volume mobilised by the whole landslide does not equal the volumes eroded in the source area and entrained from the talus deposits because the volume of material entrained was higher than estimated and because the landslide entrained further shallow material in the transport zone.

The channel carved in talus deposits below the topographic bench shows that there was entrainment by the source mass, or bulking of the landslide, as also shown in the DoD in the panel below Table 4.5, in which the channel has caused up to 7.8 m of erosion. Assuming that the surrounding talus deposits were not mobilised, I have reconstructed the topography of the talus slope before the failure, calculating the volume of debris eroded by the failing mass. The calculated entrained mass is 110,000 m^3, which corresponds to 35% of the total mobilised material (Table 4.5; Figure 4.27). However, it is likely that the volume entrained was higher, since the visual estimations from the pictures taken a few days after the occurrence of the landslide reveal that the channel was more deeply incised than when the LiDAR data were collected — by at least 1 m on average, leading to an estimate of roughly 10,000 m^3 extra volume considering the lower part of the channel where most of the material was eroded. The field estimates are lower (52,200-87,000 m^3) than the volume calculated from the DEM probably because at the time of the field measurements, for safety reasons, I acquired data at the boundary of the channel and not at its centre, where it is at its deepest.

Table 4.5 - Summary parameters for the talus deposits entrained by the Móafellshyrna landslide and the DEM of difference (DoD) between the post-failure topography and the reconstructed pre-failure topography.

Entrained talus deposits parameters	Value	Unit
Area of entrained debris	17,400	m^2
Estimated thickness of entrained debris	3-5	m
Estimated entrained volume	52,200-87,000	m^3
Calculated entrained volume from DEM	110,000	m^3
Length of entrainment channel	307	m
Width of entrainment channel	65-105	m
Average slope angle	30	°

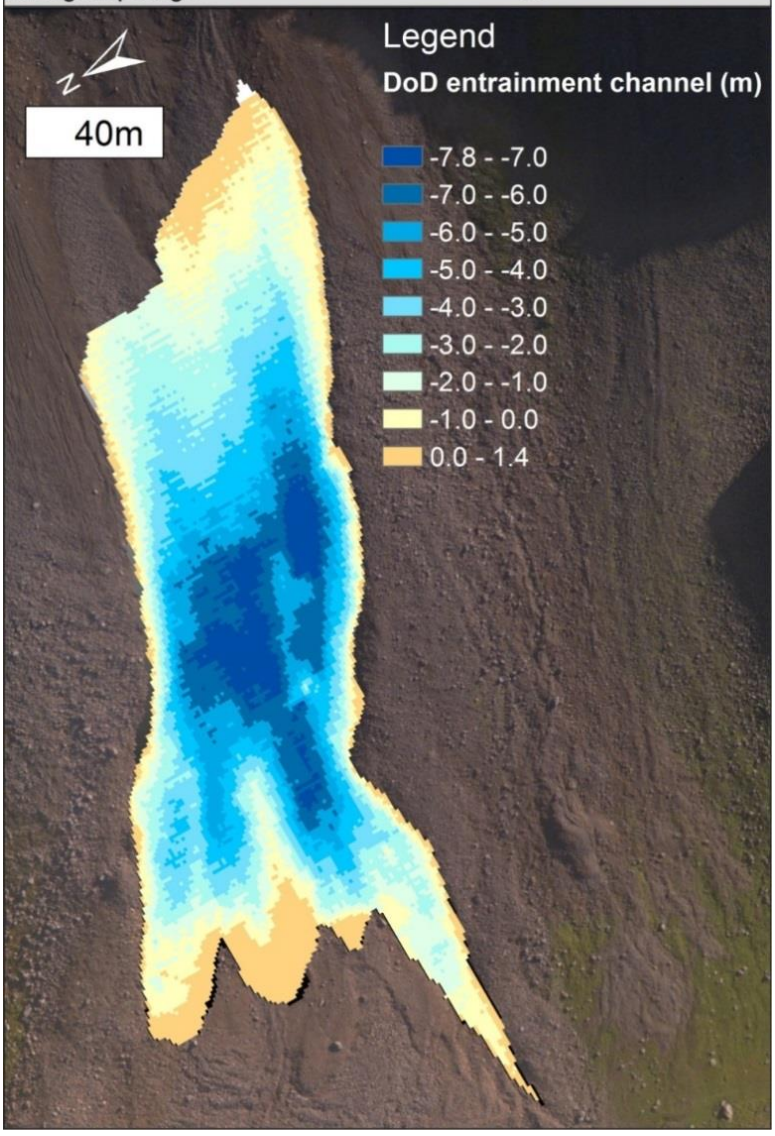

The distinct borders of the secondary lateral lobe “fish tail” that deviated laterally from the main runout path of the landslide allowed a better constrained

reconstruction of the topography before its deposition. The volume deposited in this area (see DoD in the panel below Table 4.6) of the landslide is 17000 m^3 (Figure 4.27), a value that is within the range estimated from field inspection (11,200-33,700 m^3; Table 4.6). The secondary lateral lobe travelled on a slope of only ~12° (Table 4.6) for 240 m, so with an estimated coefficient of kinetic friction (calculated according to the definition of Heim (1932) and Shreve (1966) as the tangent of the mean slope from the source to the distal margin of a landslide) of approximately 0.21.

The calculation of the volumes of the landslide features via (i) differencing the present topography from the reconstructed pre-failure topography, and (ii) field and DEM measurements of the areas where this calculation was not possible, give a total volume of ~314,000 m^3 (Table 4.6; Figure 4.27). The volume mobilised by the whole landslide does not equal the volumes eroded in the source area and entrained from the talus deposits (~261,400 m^3), most likely because the volume of material entrained from the talus slope was higher than estimated and because the landslide eroded and transported shallow material in the transport zone.

Table 4.6 - Summary parameters for the secondary lobe of the Móafellshyrna landslide and the DEM of difference (DoD) between the post-failure topography and the reconstructed pre-failure topography.

Secondary lobe parameters	Value	Unit
Area of entrained debris	11,200	m^2
Estimated thickness of debris	1-3	m
Estimated deposited debris volume	11,200-33,700	m^3
Calculated deposited debris volume from DEM	16,900	m^3
Length	240	m
Width	25-65	m
Average slope angle	12	°

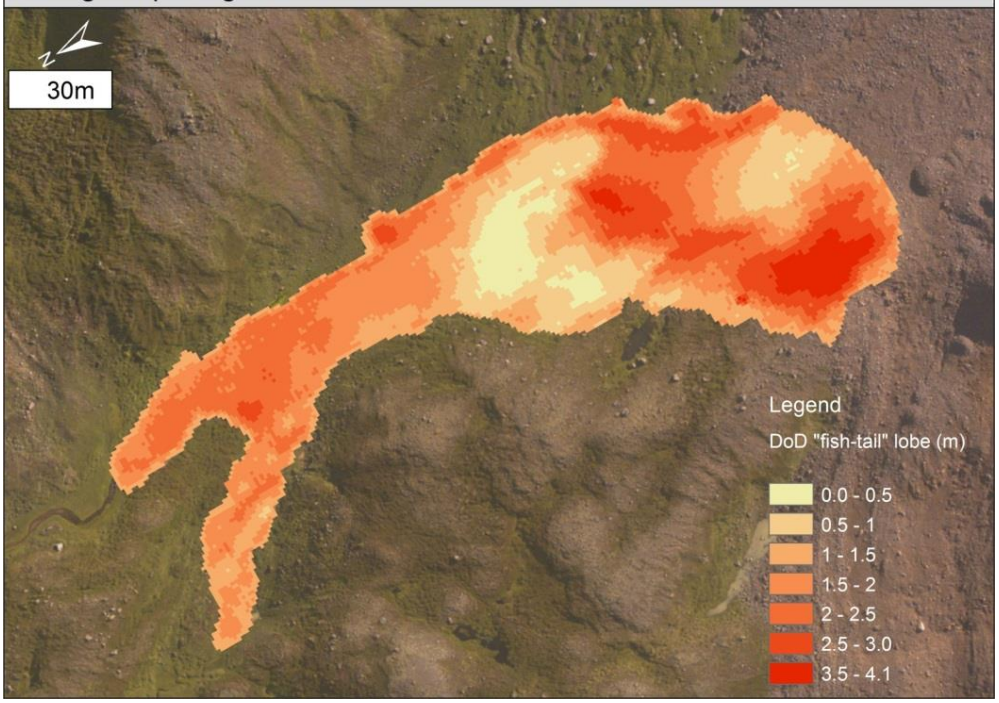

4.4.2.2 Runout analysis of molards and boulders of the Móafellshyrna landslide

The blocks of ice-rich sediment that fell at the foot of the talus slope during the Móafellshyrna event were deposited almost intact to their rest position because ground ice was still cementing them during transport (see Chapter 6 for further details on ice content). To analyse the mobility of the blocks of ice-rich sediment now visible as molards, I compared the reach angles and the volumes of the

debris cones with those of normal boulders that were mobilised during the landslide event that fell to the foot of the talus slope via simple rock fall (Figure 4.28). The debris cones show both travel distance and volumes coherent with those of boulders involved in common rock-fall processes.

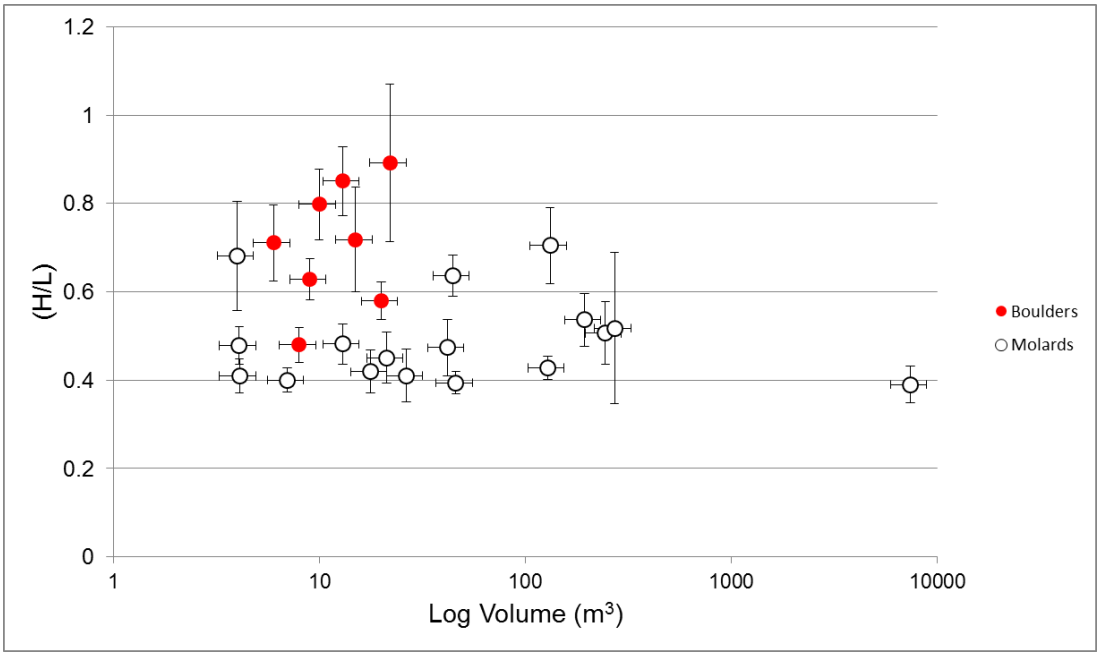

Figure 4.28. Semi-logarithmic plot of block and molards volume (m^3) versus the tangent of reach angle (H/L), The vertical error bar is the propagation of errors of L (whose error is the standard deviation of the length of the various potential energy lines of fall) and H (whose error is the thickness of the bedrock cliff for boulders and the thickness of the deposits perched on the topographic bench for the molards in correspondence of the centreline path of fall). The horizontal error bar is calculated using an accuracy of 25% according to Conway and Balme (2014) for molards, and is calculated arbitrarily using an accuracy of 20%of field and plan-view measurements for boulders.

4.4.2.3 Rapid Mass Movement Simulation applied on Móafellshyrna landslide

I applied the Rapid Mass Movements Simulation (RAMMS) model (Christen et al., 2010) to simulate the runout of the Móafellshyrna landslide. Since the source material of the landslide is composed of talus deposits, I calibrated the starting conditions simulating a granular flow, with the purpose of modelling the runout

distance of a solid-dominated flow (as expected from non-saturated talus slope material) with the same percentage of ground ice as that observed in the source deposits in the field after the failure. The output runout of the RAMMS calibrated model was compared to that of the Móafellshyrna event. The runout obtained by the RAMMS simulation deviates from the Móafellshyrna runout by 47%, while the modelled volume deviates by 10% from the volume calculated in Section 4.4.2.1. Figure 4.29 shows the outputs of the RAMMS runout model applied to the 1m gridded DEM from LiDAR data, where the modelled deposit height is projected, and where the area covered by the Móafellshyrna landslide is also reported. The model simulates the deviation of the secondary lobe due to the topography, but it underestimates the main runout path. Therefore, the model did not give satisfactory results with the input calibration parameters.

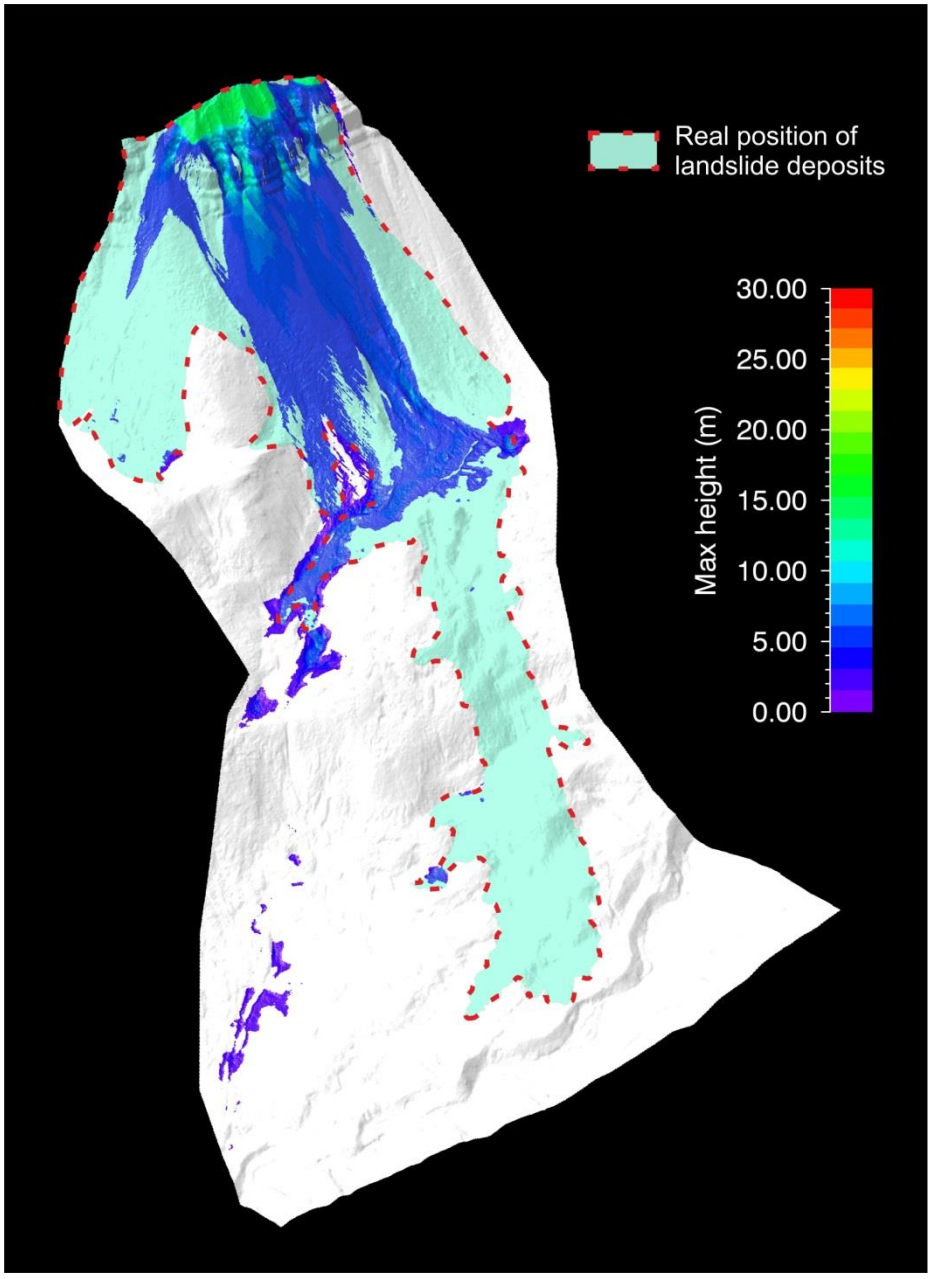

Figure 4.29. The RAMMS::DEBRIS FLOW model of the Móafellshyrna landslide from 1m gridded data.

4.4.2.4 Volumes and runout analysis of the Árnesfjall landslide

Covering an area of 71,700 m^2, the estimated volume mobilized by the Árnesfjall landslide is between 71,700 and 215,000 m^3, considering an average landslide deposit thickness of 1-3 m. The Fahrböschung of the landslide is 32°. As it is possible to observe in Figure 4.7, the landslide deposits now lie on a slope

that was once homogeneously covered by talus deposits. Since parts of the talus deposits have not been mobilised by the Árnesfjall event, I have used the elevation of these deposits (using the 18 cm gridded DEM) as a reference to reconstruct the pre-failure topography of its source area. The volume obtained through this procedure, and combining field and DEM measurements for the rest of the landslide body, is 151,400 m^3, giving an average debris thickness of 2 m, a value in agreement with field estimates (Table 4.7).

The defined borders of the source area have allowed the reconstruction of the quantity of eroded material (see DoD in the panel below Table 4.7). The value obtained is 77,400 m^3, which corresponds to almost half the volume mobilised by the landslide. From field and DEM measurements, I estimated a volume of debris deposited in the accumulation zone, excluding the debris flows, of 80,500 m^3. The thickness of the debris mantle in the accumulation zone is heterogeneous, being up to 5 m thick in the upper part, and in the terminal lobe just a few tens of centimetres near the western debris flow. However, field estimations for the deposited volume of 55,000 - 275,000 m^3 do not greatly deviate from the topographic calculation.

Part of the deposit transported by debris flows was removed by local authorities, (because these deposits covered the Strandavegur 643 road). The major part of the deposits of these debris flows is so thin (often few tens of centimetres) that reconstructing the topography before their emplacement is not possible. It is likely from field estimations that less than 500-800 m^3 of debris have been transferred via these debris flows. This volume is negligible in the overall sediment budget of the landslide, but is important in terms of hazard assessment purposes.

Table 4.7 - Summary parameters for the Árnesfjall landslide and its features and the DEM of difference (DoD) between the post-failure topography and the reconstructed pre-failure topography.

Árnesfjall landslide parameters	Value	Unit
Area of source debris	16,700	m^2
Calculated source mass volume from DEM	77,400	m^3
Area of accummulation zone	55,000	m^2
Estimated debris thickness in accummulation zone	1-5	m
Estimated debris volume in accummulation zone	55,000 - 275,000	
Debris flows area	12,740	m^2
Estimated average landslide debris thickness	1-3	m
Area of landslide	71,700	m^2
Estimated landslide volume	71,700-215,100	m^3
Calculated landslide volume from DEM and field calculations/estimates	151,400	m^3
Length of landslide path (L)	560	m
Height of landslide path (H)	348	m
(H/L)	0.62	
Fahrböschung (tan^{-1}(H/L)	32	°

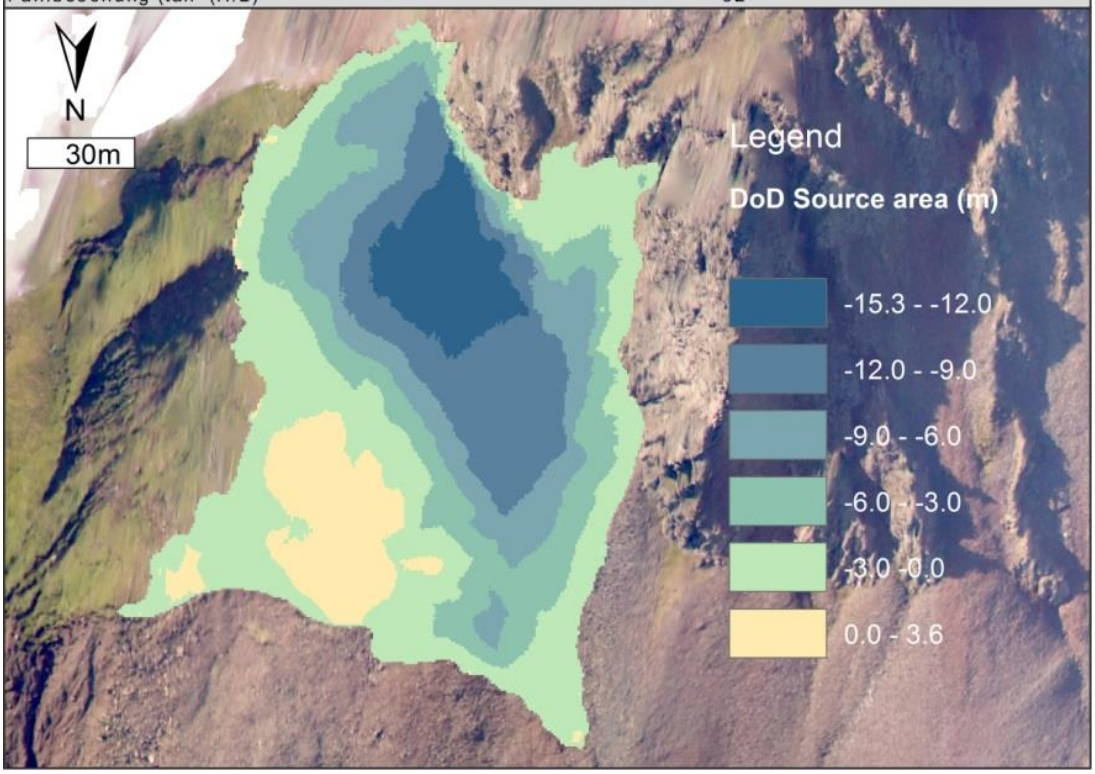

4.5 Discussion

Both the Móafellshyrna and Árnesfjall landslides can be broadly classified as complex landslides, where the downslope movement occurred. The initial movement occurred on a distinct curved surface in the source area. However,

both show morphological and morphometric characteristics that suggest other types of movement, due to the nature of the debris material, the topography and the presence of water and ice. In both landslides, the source material was weakly cemented (being formed of ice-cemented talus deposits), and perched on a steep slope, observations that can both be considered as preconditioning factors for the initiation of rapid mass movements (McColl, 2012). Despite the fact that these two landslides had similar preparatory and triggering factors (see Chapter 5), they developed quite differently.

4.5.1 The dynamics of the Móafellshyrna landslide

Detailed morphological analysis of the 2012 Móafellshyrna landslide (Fahrböschung of 22°) allowed me to infer emplacement mechanisms, since this landslide shows various forms and structures along its runout path. These give important information regarding the initiation, transport, deposition and evolution of the mass movement. I have recognised that the Móafellshyrna landslide evolved through three different types of dynamics: (i) rotational debris slide, (ii) rock/debris fall and (iii) debris flow/slide.

The local residents of the Þrasastaðir farm observed the opening of a semi-circular fissure at the crown of the Móafellshyrna landslide as one of the first signs of movement. The surface of the headscarp of the landslide is upward concave, a condition necessary for the development of a rotational slide. Once this material had propagated downwards over the cliff, the debris slide entrained the talus material below, a mechanism that is common in rock and debris slides/avalanches and that can cause liquefaction and an increase in flow volume (Geertsema et al., 2006b; Huggel et al., 2007; Hungr and Evans, 2004). This

entrained material must have had a strong impact on the emplacement of the debris, since it comprised at least ~35% of the total volume of the mobilised mass. The debris-slide dynamic is also evident from structures such as ridges and depressions in the flat accumulation area below the entrainment zone. Similar features have been observed in a debris avalanche in British Columbia and have been associated with a water-poor debris content (Roberti et al., 2017a). Ridges and intra-ridge depressions in Móafellshyrna show that the direction of the movement was affected by the topography and the fluid content. Coarse debris accumulated in this first flat accumulation area, as the debris mass encountered a topographic high (see Figure 4.12 and Figure 4.15); this made part of the debris mass deviate to the NW, creating new lobes of debris on a relatively flat surface (5-12°). The deviation of the secondary lobe with a fish-tail shape was predicted by the back analysis performed with the RAMMS numerical model where parameters of a granular (solid-dominated) flow were used. These predictions, and a coefficient of kinetic friction of 0.21, imply that the fish-tail lobe developed as a granular flow. The RAMMS model however gave for the landslide as a whole unsatisfactory results. This could be due to several reasons, including the complex morphology and rheology of the landslide, and the fact that the RAMMS model is not designed to include the behaviour of ice melting. Therefore, further investigation is needed in order to obtain better simulations of landslides involving ice thaw, as they would serve to the purpose of risk prevention and mitigation. The fish-tail lobe and the other lobate features are well delimited and are also present at the contact between the debris entrainment area and the flat accumulation area, revealing debris emplacement in sequential pulses after the main mass failure. Furthermore, the fish-tail lobe bulldozed the snow while moving downward (Figure 4.16D). This mechanism and the deviation of the

debris from the main runout path have, in previous studies, been attributed to differential mobility of debris within the debris mantle, especially in debris avalanches on glacier surfaces (Delaney and Evans, 2014). I infer that the more fluid component of the falling mass was instead transferred downwards during the main mass failure.

The fall component of the Móafellshyrna failure is not limited to the boulders now found at the foot and on the surface of the talus slope below the source area, which fell during the Móafellshyrna event and up to months after the occurrence of the landslide. The isolated molards or cones of debris found scattered at the foot of the talus slope are the result of the degradation of blocks of ice-rich deposits that also fell from the source area (see Chapter 6 for further details). Coherent blocks were still visible nine days after the occurrence of the failure, unstably perched at the edge of the topographic bench (see Figure 4.13). Some of them were not transported downslope, but degraded in place resulting in cones of debris faintly preserved in the source area (see Figure 4.13). However, the question remains as to how the molards in the accumulation zone came to be there: did they fall or were they pushed? Since the reach angle model is one of the universally recognised methods to analyse travel distance of small rock falls (<100 m^3), I have compared the reach angle and size of the cones of debris left during the Móafellshyrna event to those of normal boulders that fell in the same area of the landslide (Figure 4.28). Normally, “the larger the falling boulder, the smaller the value of the reach angle” (e.g. Copons et al., 2009; Corominas, 1996). According to this principle, both boulders and particularly molards in Móafellshyrna show a high mobility. In Figure 4.30, I compared the reach angle and size of the Móafellshyrna molards to the shadow angle (same as reach angle, but calculated from the apex of the talus slope) of blocks of similar size in

Spain, where Copons et al. (2009) found that the rock fall size has a strong influence on the travel distance also for block size <10^5 m^3. Copons et al. (2009) plotted individual block volumes and the farthest boulders found at the study area, since they represent the largest volumes and largest travel distances from past rock falls at the same site. They found a negative relationship between block volume and the shadow angle ratio value. Both boulders and molards in Móafellshyrna have high mobility (horizontal travel distance L values are high), but coherent with the mobility of 'normal' rock-fall boulders analysed by Copons et al. (2009). In the case of molards, this slightly higher mobility could also be partially attributed to a 'compound' transport mechanism, as it is possible that, once fallen, they landed on the still mobile landslide debris material. They might then have been rafted on the surface of a viscous flow (as shown by the compressional ridges) and transported to greater distances.

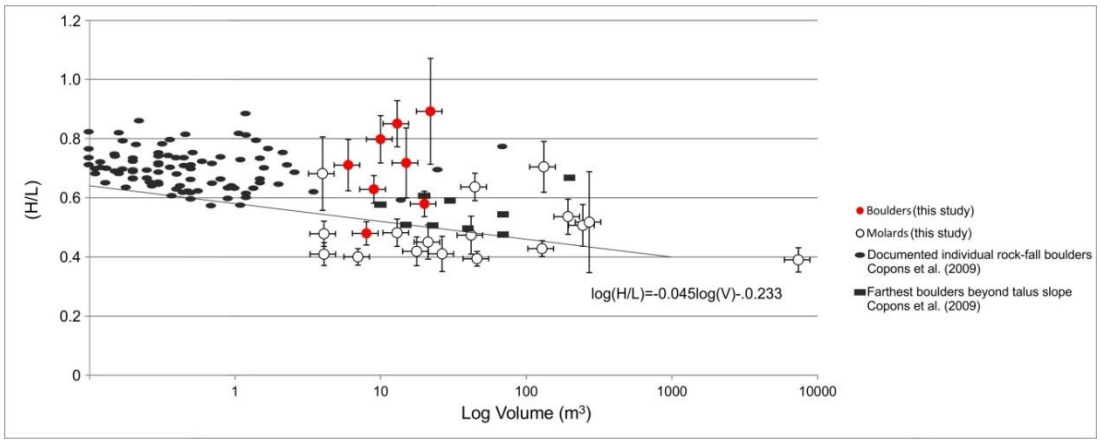

Figure 4.30. Semilogarithmic plot of volume (m^3) versus reach angle for the molards and boulders of Móafellshyrna landslide (error bars are the same for Figure 4.28) and shadow angle of documented individual boulders and farthest boulders beyond talus slope from Copons et al., (2009). Copons et al., (2009) fitted a regression equation by the lower envelope of plotted data, estimating the maximum travel distance of rock blocks by taking into account their volume.

The fluid-dominated phase of the Móafellshyrna landslide is evident in the landforms downslope of the flat accumulation area. The presence of sand-boil structures in the terminal lobe of the landslide could be an indicator of liquefaction, as similar features were observed in analogous landslides (for example in the Frank landslide in Alberta; McConnell and Brock, 1903) and attributed to liquefaction (Xu et al., 2012). In the same area of the landslide, segregation of coarse and fine material in discrete zones is observed, and probably occurred due to the fines leaking out of accumulations of coarse material in topographic traps. The presence of a straight channel with poorly-defined lateral levees, and of a terminal lobe with coarse and fine deposits in discrete zones, could also be related to a fluid-dominated phase, similar to a debris flow/slide (Costa, 1984). The fluid component of the failing mass overshot the flat accumulation area and even crossed a slight topographic high, and then flowed along the line of steepest descent. The transition from a rock/debris slide to a debris flow is a common process that has been related to liquefaction (Boultbee et al., 2006; Capra and Macías, 2000; Crosta, 2001; Scott et al., 2002; Tost et al., 2014; Vallance and Scott, 1997; Voight and Sousa, 1994; Xu et al., 2012). Back analysis using RAMMS (see Section 4.4.2.3) did not predict this transition, as the parameters introduced for the simulation were those for a granular flow. This suggests that a source of fluid was necessary for producing saturation and to transfer of material downslope. There are two possible sources of fluid that caused the evolution of the Móafellshyrna landslide into a debris flow/slide-like mass movement. The first could have come from the fluid saturating the debris material before it was mobilised. In Chapter 5, I show that abundant precipitation preceded the Móafellshyrna event, so it is likely that the talus material both on and below the topographic bench was saturated. It is possible that the initial falling debris mass

encountered the talus slope below the topographic bench, and that here the fluid phase separated from the solid-dominated phase and slid further downwards, as it was more mobile. This is a common process that has been reported in other debris slides/avalanches (Geertsema et al., 2006b; Huggel et al., 2007; Hungr and Evans, 2004; Roberti et al., 2017a). The separation of a fluid dominated phase from a dry phase has also been reproduced by two-phase numerical modelling (Pudasaini, 2012; Pudasaini and Krautblatter, 2014). The second possible source of fluid could have been the thawing of the ground ice cementing the source debris material. I discuss this point in Section 4.5.2 below. Furthermore, in rock-ice avalanches on snow-covered glaciers, ice and snow are thought to reduce the friction by 50% (Schneider et al., 2011b; Sosio et al., 2012). The presence of a thin (few tens of centimetres) layer of snow on ground at the time of the failure could have had a role lubricating the movement, even if minor considering that in rock-ice avalanches the path material entrained is for the vast majority snow or ice, which is not the case for Móafellshyrna.

To summarize the evolution of the Móafellshyrna landslide, the failure developed through four different chronological steps:

- Step 1 – Rotational slide and rock/debris fall: The source mass formed by ice-cemented talus deposits detached with a rotational sliding process. Because of an abrupt topographic jump (the presence of a topographic bench), the source talus debris disaggregated and was transferred downslope through the process of rock/debris fall.
- Step 2 – Debris entrainment: The source mass then encountered a talus slope lying below the topographic bench, and entrained part of the talus deposits and moved further downslope. Once the debris mass reached the

first flat accumulation area, the landslide material divided into two different rheology types: solid-dominated and fluid-dominated.

- Step 3 – Fluid-dominated phase: The fluid dominated phase was transferred downslope and produced forms similar to those of a debris flow/slide, such as sand-boil structures, leveed channels and a terminal lobe with segregation of coarse and fine material in discrete zones.
- Step 4 – Solid-dominated phase: The solid dominated phase left thick (up to meters) coarse debris ridges and depressions that show the direction of the movement. It also produced secondary lobes – one of which bulldozed the snow covering the ground at the time of the failure – which show a granular behaviour and reveal debris emplacement in sequential pulses after the main mass failure.
- Step 5 – Rock/debris fall: Rock and debris fall processes occurred onto the landslide body when it was still mobile and rafted small boulders and molards landing on its surface/ The fall activity continued for months (probably even years) after its occurrence.

4.5.2 The dynamics of the Árnesfjall landslide

Similarly to the Móafellshyrna landslide, the Árnesfjall landslide initiation and emplacement involved different dynamic processes. The Árnesfjall landslide is characterised by a distinctive curved slip surface in the scarp zone, hence initial downslope movement is also attributable to rotational sliding. The presence of elongated conical ridges of loose deposits (molards), which were cemented by ground ice at the time of the failure, are further evidence of rotational-sliding motion, since they appear to be produced by *en echelon* concave-upward rupture surfaces (rotated ice-cemented ridges of debris), and they preserve the original

stratification of the talus slope. This process was only possible in talus material because the ground ice gave the loose debris a more rigid rheology. Similar conical features in debris slides that formed through an analogous process were observed by Brideau et al. (2009) in the Little Salmon Lake debris slide, Canada, where ice-rich deposits were transported by the surrounding sliding saturated material. Furthermore, most of the molards lie in the depletion zone, which is separated from the accumulation zone by an abrupt transition in slope. This subdivision is typical of rock/debris slides (Varnes, 1978), and the Árnesfjall landslide shows a Fahrböschung of 32° (Table 4.7) that is consistent with debris slides.

In addition, the Árnesfjall landslide shows a different dynamic at its periphery, where debris material was mobilised as debris flows, which have lateral levees and terminal lobes. This is not an uncommon characteristic of debris slides, but the presence of secondary debris flows indicates the renewed presence of fluid saturating the material after the initial landslide. The eastern debris flow has the same length as the accumulation zone, and follows a channelized morphology that was already present at the time of the failure. It is therefore likely that this debris flow developed contemporaneously to the debris slide, and the pre-existing channel acted as a preferential path for the fluid component of the failing mass. However, I have shown that the western debris flow developed subsequently to the debris slide, likely triggered by the degradation of the ground ice within the material mobilised by the failure, providing fluid for sediment transport downslope. At the same time (or soon before or after), a block of ice-rich sediment rolled and slid downslope and arrived at repose in the terminal lobe of the debris flow, and then degraded to form a molard. In this terminal lobe the debris are only up to 30-50 cm thick and are dispersed in multi-directional flow lines, so it is expected that

this thin sheet of debris was produced by the degradation of the ground ice that was cementing the source material at the time of the failure.

4.5.3 Ground ice and fluid: estimation and role in the Móafellshyrna and Árnesfjall landslide dynamics

The Móafellshyrna and Árnesfjall landslides are two rare examples of landslides where blocks of ice-rich deposits were found immediately after the occurrence of the failure. Both the landslides are complex and show various forms related to different dynamic processes in different location of the landslides. The two landslides show dynamics analogous to those of rock-ice avalanches. The mobility of these types of mass movement can change during their propagation due to entrainment of ice, snow and substrate material; such mixing with the source material can reduce the friction coefficient altering the runout (Evans and Clague, 1988; Huggel et al., 2005; McSaveney, 1978; Schwab et al., 2003; Sosio et al., 2012). In general, the mobility of rock/debris slides/avalanches is not affected by their volume, but is mainly controlled by the availability and distribution of a source of liquid along their path (Hungr and Evans, 2004). I infer that there were two sources of liquid that changed the emplacement of the Móafellshyrna and Árnesfjall failures to a debris-flow/slide like movement: the entrainment of saturated material from the talus slope in Móafellshyrna and the ground ice thaw in both of the landslides. As I will show in Chapter 5, abundant precipitation fell in the Móafellshyrna area before the event. This probably caused the saturation of both the source material and the talus material below the source area, generating enough fluid to causing a transition to a debris-flow emplacement.

The total potential energy (PE) released by the falling mass in Móafellshyrna is 2.36×10^{13} J. This can be calculated using the equation

$$PE = \Delta z g \gamma V, \quad (2)$$

where Δz is the vertical distance between the centres of gravity from the initial position (arbitrarily estimated at the centre of the source mass at elevation of 800 m a.s.l.) to the final position (arbitrarily estimated following Lucchitta (1978), at 380 m a.s.l.), g is the gravitational constant, γ is the unit weight of the material and V is the volume mobilised (Erismann and Abele, 2001). This PE is calculated assuming an average density of 1863 kg/m^3. This density is obtained by considering 80% of the failed mass having a density of an average granular flow (2100 kg/m^3; Iverson, 1997), and 20% of the mass having the density of ice (917 kg/m^3). This assumption is based on the content of ground ice that was visually estimated at the time of the failure. Knowing the potential energy, it is possible to estimate the amount of ice melt through transmission of energy generated by the falling ice-cemented debris mass. Theoretically, the impact energy of the Móafellshyrna landslide could have melted up to 7.7×10^4 m^3 of ice (assuming 3.35×10^5J/kg necessary for melting ice at 0°C). Of course, an extensive amount of energy is dissipated during the collapse, fall and impact of the material, so the actual amount of energy available to melt is probably much less. However, considering that only part of the ground ice was still preserved after the failure in blocks of ice-rich sediment, the potential energy released by the initial Móafellshyrna mass (151,400 m^3) could have contributed to melt at least part of the ground ice contained in it.

If we assume that the fluid content of the landslide was coming only from the source material (151,400 m^3), and that the content of ground ice is 20%, this would lead to an estimate of meltwater of ~3.0×10^4 m^3 at maximum (since blocks

of ice-rich sediments had ground ice preserved in the source area and in the landslide body). The energy produced by the failure could have impacted the talus slope below the source area and caused an increase in temperature that generated a further source of fluid from the thawing of the ground ice. This would be also in agreement with laboratory studies: with an initial dry granular flow with an ice content above 40%, water supply by ice and snow melting caused liquefaction of the material and a reduction of the friction coefficient by more than 50%, allowing the transition from a dry to a fully saturated flow (Schneider et al., 2011b; Sosio et al., 2012). As shown in Figure 4.31, greater mobility is predicted for rock/debris avalanches interacting with ice during propagation than for those that do not (Evans and Clague, 1988). De Blasio (2014) lists as landslide characteristics affected by icy conditions and lubrication "strong stretching, longitudinal stripes, long runout, outrunner blocks, digitations, and marked spread of the landslide". Some of these characteristics are also found in Árnesfjall, where I found an outrunner molard at the end of its debris flow, and a multi-directional thin sheet of debris. Similarly to rock-ice avalanches, Árnesfjall and Móafellshyrna propagated on rough terrains and divided into several lobes. Tongue-shaped deposits, digitate margins and minor surface relief — features similar to wet snow avalanches — are found in rock/debris avalanches involving ice or propagating on ice surfaces (Sosio, 2015).

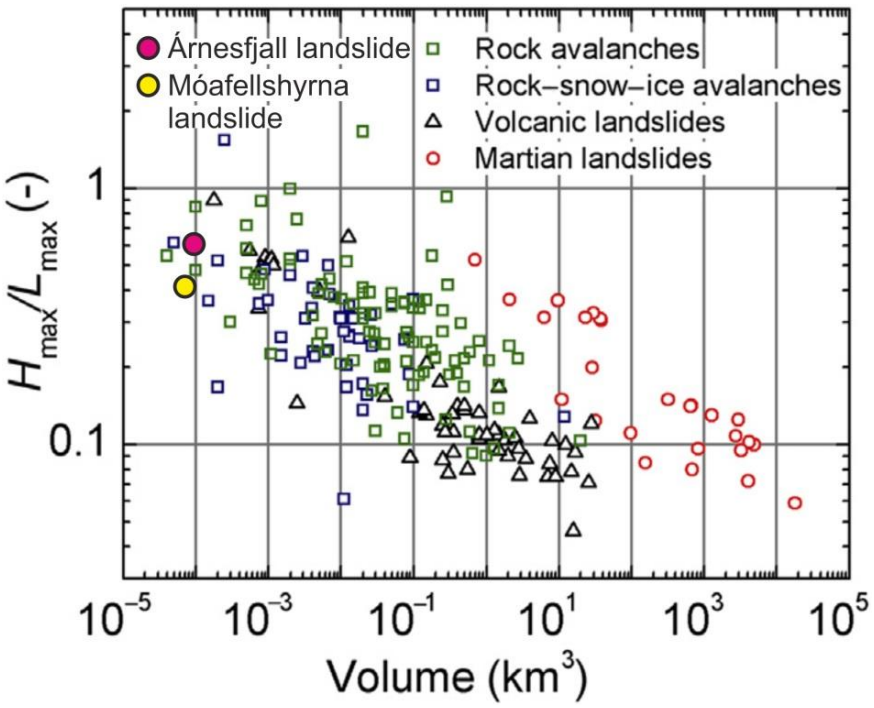

Figure 4.31. Logarithmic plot of the relative runout (H/L) versus volume (V) of rock/debris avalanches from different settings, with the values for Móafellshyrna and Árnesfjall superposed (modified after Sosio (2015)).

The dynamics of both Móafellshyrna and Árnesfjall landslides are complex and this can raise problems when evaluating potential hazard. Their complexity is determined by different factors, such as topography, the entrainment of new saturated material in the case of Móafellshyrna, and the nature of the source material, composed of talus deposits cemented by ground ice. In Árnesfjall, two different mechanisms (rotational slide and debris flow) characterised the development of the landslide, while in Móafellshyrna there were three (rotational slide, debris flow/slide and rock/debris fall). This complexity is difficult to interpret and reconstruct. Models of the dynamics of rapid flow slides, debris flows and avalanches can accurately predict the runout extensions whenever the rheological parameters are well defined (McDougall and Hungr, 2004). Dynamic analyses of rock avalanches entraining large quantities of saturated debris were

carried out using numerical modelling showing that these are a complex type of landslide, transitional between rock avalanche and debris avalanche (Hungr and Evans, 2004). Rock avalanches in permafrost environments can be even more hazardous than in non-permafrost ones, as real runouts have been shown to exceed predicted ones by 30%, probably because of fluidization processes (Bottino et al., 2002). The presence of ground ice is another factor to be accounted for whenever considering the hazard of landslides involving ground ice. Landslides like the Móafellshyrna and the Árnesfjall ones are therefore more difficult to characterise and model, and this can generate problems when predicting similar rapid mass movements in analogous settings.

4.6 Conclusions

Landslides involving loose debris cemented by ground ice are unreported, but could have a large destructive potential and cause casualties if impacting on inhabited regions. In this chapter, I have analysed the dynamics of the Móafellshyrna and Árnesfjall landslides, two failures that occurred in the last decade in northern Iceland and that mobilised ground-ice cemented talus deposits. I have shown that the different morphological and morphometric characteristics of these landslides reveal their complex and dynamic nature. This fulfils one of the main aims of the thesis, to understand the connections between the degradation of ground ice and the occurrence of rapid mass movements in mountainous areas of Iceland with discontinuous permafrost by studying their morphological signatures. In particular, I draw the following conclusions:

1. In both landslides, the nature of the movement evolved during the event, changing the mobility and trajectories of the landslides. In

Móafellshyrna, the failure started as a rotational slide and involved a component of rock/debris fall. The failure then evolved from a sliding motion to a more dispersive debris slide/avalanche motion. The failing mass then became more mobile due to liquefaction and began its emplacement as a debris flow/slide. In Árnesfjall, the landslide initiated with a rotational slide motion, with a more fluid lateral component that evolved as a debris flow. Once the main landslide body was deposited, secondary debris flows activated as a result of thawing ground ice cementing the source material, generating also a single outrunner.

2. The complexity of the morphological features of these landslides reveal that mass movements involving ground ice can be multi-phase, comprising a fluid dominated phase and multiple pulses of a solid dominated phase. The solid dominated phase could derive from two sources, namely the entrainment of new saturated material and the thaw of ground ice. The potential energy of 2.36×10^{13} J released by the failing Móafellshyrna mass could have contributed to melt at least part of the ground ice, with the production of a new source of fluid (a maximum of 3.0×10^{5} m^3 of water) available for fluidization. The separation of a fluid dominated phase from a dry phase is a common phenomenon observed in rock and debris avalanches.
3. The presence of ground ice and its role make this kind of landslides difficult to simulate in a back analysis environment. However, morphological and dynamic analogies with rock-ice avalanches confirm that the mobility of mass movements involving ice is enhanced, and that the ice melting can cause a more complex propagation of the failure, with a possible debris-flow like evolution.

4. I have shown that different rapid mass movements processes were involved during both Móafellshyrna and Árnesfjall failures due to the presence of ground ice, and they can be classified as complex (Hungr et al., 2014; Varnes, 1978). For this reason, this type of movement is difficult to model, making it more difficult to assess their hazard, and more difficult to predict similar rapid mass movements in comparable settings.
5. These complex type of landslides might be more common than expected from the reports in the literature, as when such failures are not witnessed, the ground ice can completely degrade by the time that the landslide is surveyed. The concepts reported in this chapter might apply to other similar mass movements involving terrains affected by ground ice. It would be important in terms of hazard assessment to better understand the complex dynamics of these landslides in case they occur in inhabited areas.

Chapter 5. The preparatory and triggering factors of the Móafellshyrna and Árnesfjall landslides in northern Iceland[2]

5.1 Introduction

As reported in Chapter 2, rapid mass movements, including rock falls, rock avalanches, debris flows and debris slides, are common geomorphological processes in Iceland and present a significant and direct threat to many towns, villages and farmhouses (Decaulne, 2005, 2007). Precipitation, snow melt, temperature variations and earthquake activity are the most common triggering factors for landslides in Iceland (Sæmundsson et al., 2003; Sæmundsson and Decaulne, 2007; Smith et al., 2009). However, during the last decade, two, somewhat unusual, rapid mass movements have occurred in northern Iceland.

[2] Part of the work contained in this chapter of the thesis is based on a paper that was published in the journal Science of the Total Environment on 31 October 2017 entitled "The triggering factors of the Móafellshyrna debris slide in northern Iceland: intense precipitation, earthquake activity and thawing of mountain permafrost". The full citation of this paper is:

Sæmundsson Þ, Morino C, Helgason JK, Conway SJ, Pétursson HG. 2018. The triggering factors of the Móafellshyrna debris slide in northern Iceland: intense precipitation, earthquake activity and thawing of mountain permafrost. Science of the Total Environment 621: 1163–1175. DOI: 10.1016/j.scitotenv.2017.10.111

Since the published manuscript focussed on the preparatory and triggering factors of the Móafellshyrna landslides alone, I have added new data, analysis and discussion of the preparatory and triggering factors of the Árnesfjall landslide for this chapter. This material was not published in the paper. Typological changes to the paper have been made to ensure consistency with the rest of the thesis. These changes are: change of the title, addition of relevant sections and figures regarding Árnesfjall landslide preparatory and triggering conditions, removal and/or changes of sections repeating descriptions and concepts already reported elsewhere in the thesis, the use of the first person singular instead of the first person plural where appropriate, and the inclusion of references to other parts of the thesis.

As reported in Chapter 4, the first occurred on the Móafellshyrna Mountain on 20th September 2012 in the Tröllaskagi peninsula (Figure 5.1A), and the second on the Árnesfjall Mountain on 10th July 2014 in the Westfjords (Figure 5.1B; Sæmundsson et al., 2013, 2014a, 2014b). In all these landslides, ice-cemented debris was found within the deposits; to the best of my knowledge, this has never been previously reported in Iceland. The source areas of these landslides are all located on steep (above 40°) NW to NE facing-slopes, where discontinuous permafrost might be expected (e.g., Gorbunov, 1988; King, 1986). The source area at Móafellshyrna landslide is located at elevations of 870 m a.s.l., within the zone of discontinuous permafrost in Iceland as calculated by Etzelmüller et al. (2007), whereas at Árnesfjall the source area is located at about 400 m a.s.l., a much lower altitude than previously observed for mountain permafrost in Iceland (Etzelmüller et al., 2007). This has led to the hypothesis that degradation of permafrost in these areas of the island has played an important role in the occurrence of these mass failures, although other exogenous and endogenous factors could have conditioned the source region or triggered the release of the landslides. In this Chapter, I aim to fulfil one of the main aims of this thesis: to identify the exogenous and endogenous factors that caused the release of these landslide, focussing my attention to the role of permafrost degradation.

In Chapter 4, I reported and discussed the morphological and morphometric characteristics of the Móafellshyrna and Árnesfjall landslides. In this chapter, I examine how intense precipitation and ground-ice degradation (via increased annual temperatures) could have contributed to the Móafellshyrna and Árnesfjall failures. Furthermore, since the Móafellshyrna landslide occurred after seismic activity, this aspect is also analysed for this case study. To examine these factors,

data from weather stations, seismometers, witness reports and field observations were used. I place emphasis on the field evidence of ground ice-thaw, because permafrost degradation has never previously been considered as a triggering factor for gravitational mass movements in Iceland, although other recent landslides elsewhere have been attributed to the melting of permafrost (e.g., Bottino et al., 2002; Dramis et al., 1995; Geertsema et al., 2006; Harris et al., 2001; Huggel et al., 2012; Schwab et al., 2003).

I described the state of knowledge of permafrost in Iceland in Chapter 2, so in the following sections I firstly describe the seismic conditions in central northern Iceland and their role in previous mass wasting events, and then I give an overview of the general meteorological conditions in Iceland. I then report the results, reconstructing the conditions that favoured the occurrence of the landslides. Next is discussion of the results, identifying the preparatory and triggering factors (as per McColl (2012) for paraglacial landslides) that induced the landslides. I posit that Móafellshyrna landslide was induced by a combination of intense precipitation in the weeks prior to the failure, and seismic activity on the 18th and 19th September, and that the degradation of ground ice was the final trigger. Finally, I propose that the Árnesfjall landslide originated after sudden precipitation, and the degradation of ground ice contributed as a final trigger in generating the failure.

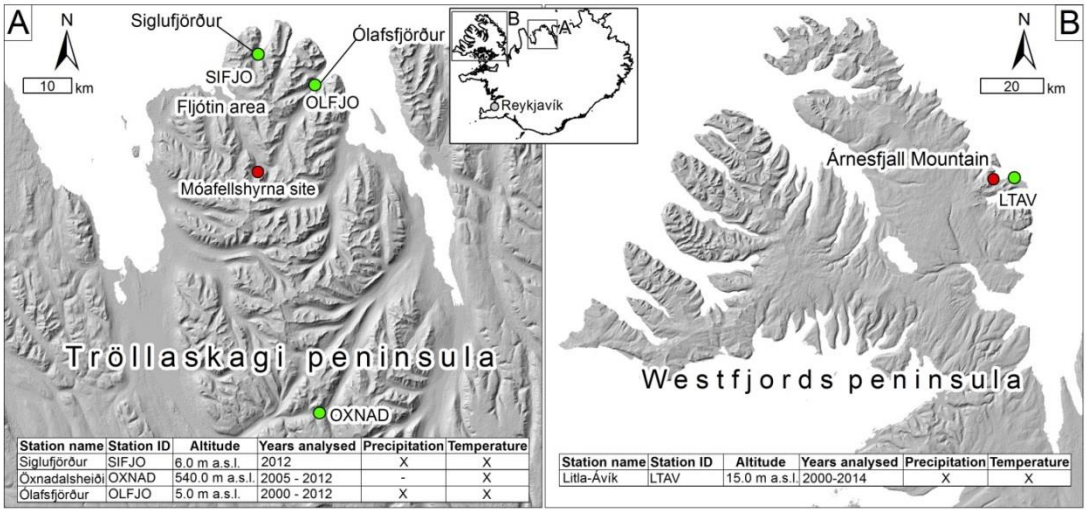

Station name	Station ID	Altitude	Years analysed	Precipitation	Temperature
Siglufjörður	SIFJO	6.0 m a.s.l.	2012	X	X
Óxnadalsheiði	OXNAD	540.0 m a.s.l.	2005 - 2012	-	X
Ólafsfjörður	OLFJO	5.0 m a.s.l.	2000 - 2012	X	X

Station name	Station ID	Altitude	Years analysed	Precipitation	Temperature
Litla-Ávík	LTAV	15.0 m a.s.l.	2000-2014	X	X

Figure 5.1. The Móafellshyrna site, located in the Tröllaskagi peninsula, northern Iceland (A), and the Arnesfjall site, located in the Westfjords peninsula (B). The green dots mark the locations of the weather stations used for this study. The hillshaded digital elevation model used as a basis of these maps is from the Digital Elevation Model over Europe (EU-DEM) from the Global Monitoring for Environment and Security service for geospatial reference data access project (GMES RDA). The tables provide details on the Icelandic Meteorological Office and Icelandic Road and Coastal Administration weather stations, whose datasets have been used for this study. Symbols "X" and "-" mean that data are or are not available at the stations, respectively.

5.1.1 Seismic activity in central northern Iceland

The seismic activity in Iceland is related to its position on the Mid-Atlantic plate boundary, which crosses the island and its location over the Icelandic Hotspot (Allen, 2002; Bjarnason, 2008; Einarsson, 2008; Thordarson and Hoskuldsson, 2002; Tryggvason et al., 1983; Wolfe et al., 1997). The seismic activity in the northernmost region of the island is related to the Tjörnes Fracture Zone (Einarsson and Björnsson, 1979; Sæmundsson, 1974), which is defined by three seismically active lineaments - the Grímsey Oblique Rift, the Húsavík Flatey Fault and the Dalvík lineament (e.g., Gudmundsson, 2007, 2000; Sæmundsson, 1974) - and includes the Eyjafjarðaráll N-S extensional graben, located offshore north

of the Tröllaskagi peninsula (Figure 5.2). Activity on this fault system caused the earthquakes prior to the Móafellshyrna landslide (Gudmundsson, G.B., Hensch et al., 2013), as shown in Section 5.3.3.3).

Earthquakes are known to have contributed to the initiation of landslide and rock fall in Iceland in the past (e.g., Ágústsson and Pétursson, 2013; Halldórsson, 1984; Jónsson, 1957; Jonsson et al., 1992; Sæmundsson et al., 2003; Thorarinsson, 1937; Thorarinsson et al., 1959), but no study has explored in detail the role of earthquake activity as a preparatory and/or triggering factor on rock fall or landslides in Iceland, as has been done elsewhere in the world (Harp and Jibson, RW, 1996; Yin et al., 2009). The above mentioned Icelandic studies relate mass movements to larger earthquakes than those prior to the failure in Móafellshyrna; e.g. in June 2000, two earthquakes of magnitude 6.4 occurred in Iceland, with the epicentre in the middle of the southern lowlands. Rock fall activity was reported as a result of this event as far as 75 km from the epicentre (Sæmundsson et al., 2003).

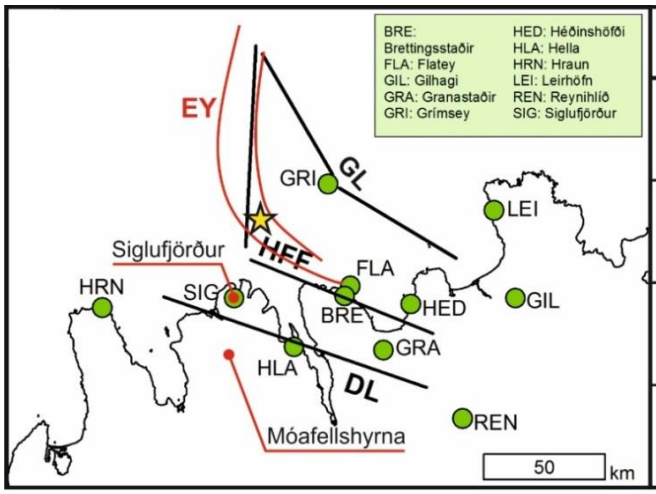

Earthquakes	
Time	**Magnitude (Richter scale)**
19th September 2012, 7.57 am	M 4.5
19th September 2012, 8.28 am	M 4.3
20th September 2012, 9.27 am	M 4.2

Figure 5.2. The structural elements of the Tjörnes Fracture Zone marked in black (Grímsey lineament (GL), Húsavík-Flatey fault (HFF) and Dalvík lineament (DL); from Stefánsson et al., 2008) and the Eyjafjarðaráll graben marked in red (EY); the position of the epicenter zone for the earthquakes preceding the Móafellshyrna landslide is marked with a yellow star, the Icelandic Meteorological Office (IMO)

seismometers in the area marked with the green dots and the labels refer to their abbreviated names, as given in full in the key. On the right are reported the timing and magnitude of the earthquake sequence in the Eyjafjarðaráll graben from 19th to 20th September 2012 (from Gudmundsson et al., 2014).

5.1.2 General weather conditions in Iceland and in the study areas

Weather patterns in Iceland are highly variable, with frequent and strong variations in precipitation and temperature; this is mainly because Iceland is located on the main path taken by North Atlantic low-pressure systems (Einarsson, 1984). The mean annual air temperature for the period 1971–2000 was 4–5°C in the south, 3–4°C in the east and west and 2–3°C in northern coastal parts of the country (Tveito et al., 2000). Hence precipitation can fall as either snow or rain. The two dominant precipitation-bringing wind directions in the Tröllaskagi area are NE and SW (Arnalds et al., 2001a; Brynjólfsson and Ólafsson, 2009). The precipitation is heavier during strong NE winds. Consequently, mean annual precipitation increases from about 500 – 1000 mm per year in the central and northern parts of the country to more than 3000 mm/yr in the southeast (Crochet et al., 2007).

In the Tröllaskagi peninsula, during the winter months, from October to April, the precipitation in the outer part of the peninsula is almost exclusively snow or sleet, and the main period of snow avalanche activity is associated with strong north-easterly wind (Arnalds et al., 2001a). The northern part of Tröllaskagi peninsula is generally a heavy snow prone area, and Siglufjörður and Fljótin area are commonly considered to be one of the heaviest snow prone areas in Iceland (Arnalds et al., 2001a). According to Crochet et al. (2007), the annual precipitation

from 1971-2000 in the Tröllaskagi area varies from 1000-1500 mm in the coastal lowlands up to 2000-2500 mm on the summits. Localised orographic effects mean that in the Tröllaskagi peninsula precipitation is higher near the coastline when there are northerly winds (Brynjólfsson and Ólafsson, 2009). Conversely, the precipitation is likely to be higher in the lowlands in the interior of the Tröllaskagi peninsula area than at the coast during periods with southerly winds. In the mountains of the peninsula, the orographic effect also play a role during precipitation brought by southerly winds, increasing at higher elevation. The Mean Annual Air Temperature (MAAT) for the period 1971-2000 was 2-3°C in the northern coastal areas of Iceland (Crochet et al., 2007; Tveito et al., 2000). The data series for the Tröllaskagi area between 1940-1970 show MAAT of 2-4°C in the coastal areas and -2 to -4°C at the summits (Einarsson, 1984).

In the Westfjords, the Mean Annual Air Temperature for the period 1961-1990 is 3.2° (Glade and Jensen, 2004), and the decadal anomaly recorded for the periods 1991-2000 and 2001-2010 with respect to the reference period 1961-1990 is respectively -0.25 – 1.25°C and 1 – 1.25°C (Crochet et al., 2007). For the same period (1961-1990), in Kvígindisdalur, a station on the south side of the Westfjords that has continuous data, the annual mean was 1380 mm (Glade and Jensen, 2004), while for the period 1949-1992, 770 mm of mean annual precipitation was recorded at the station of Gjögri, in the western side of the Westfjords. Average annual precipitation of 969 mm was calculated compiling data from the stations of Lambavatn, Galtarviti, Hornstrandir and Aedey in the Westfjords (Decaulne, 2001). In the Westfjords, the strongest winds are most often north-easterly and bring abundant precipitation (Jónsson et al., 2004).

5.2 Methods

The preparatory and triggering factors of the Móafellshyrna and Árnesfjall landslides were analysed using meteorological data from the Icelandic Meteorological Office (IMO) for three and two months prior to the landslides respectively, and for the period 2000-2012 for the Móafellshyrna landslide and the period 2000-2014 for the Árnesfjall landslide. Data for the seismic activity of the north coast in 2012 were also obtained from the IMO. My supervisor Þorsteinn Sæmundsson and collaborators at the Icelandic Meteorological Office also interviewed the inhabitants of the Þrasastaðir farm Móafellsdalur valley regarding the Móafellshyrna event, while I interviewed them three years after the occurrence of the landslide. Jón Kristinn Helgason (IMO) interviewed the inhabitants of the Melar farm, located a few hundred meters from the terminal deposits of the landslide, about the failure at Árnesfjall. In Móafellshyrna, fieldwork was performed a few hours, four days and nine days after the landslide event, and then three years after the event in summer 2015. In Árnesfjall, fieldwork was performed two days after the occurrence of the landslide and then two years after the landslide event.

5.2.1 Direct report from witnesses

The local residents of the Þrasastaðir farm, located at the junction between the Móafellsdalur and the Stífludalur valleys and 1.7 km from the terminal deposits of the landslide, witnessed the release of the landslide, and were interviewed on the day of the event regarding the earthquake activity prior to the failure, the landslide evolution, timing of the landslide and the events that occurred during the first few hours of the failure and in the years after its occurrence.

The Melar farm is located in the Meladalur valley along the Strandavegur road 343, at the foot of the northern slope of the Árnesfjall mountain. The terminal deposits of the landslide reached the bottom of the slope, few hundred meters from the farm. The inhabitants of the farm witnessed the release of the landslide, and were interviewed two days after the event regarding the landslide evolution, timing of the landslide and the events that occurred during the first few hours of the landslide and in the days after its occurrence.

5.2.2 Meteorological data

For Móafellshyrna only two weather stations in the northern part of the Tröllaskagi peninsula measure both precipitation and temperature, one located in the town of Siglufjörður (WMO (World Meteorological Organization) ID: 4157) at 6 m a.s.l. (25 km north of the site) and the other one in the town of Ólafsfjörður (WMO ID: 4155) at 5 m a.s.l. (21 km northeast of the site). A third station is located at the Öxnadalsheiði highlands pass (WMO ID: 4859) at 540 m a.s.l. (40 km south of the site), can measure only temperature and is operated by the Icelandic Road and Coastal Administration (Figure 5.1). A problem in the approach of this study is that the majority of the stations used to establish mean atmospheric temperatures for the Móafellshyrna site are located near the coast and therefore at low altitude. This leads to a potential bias when evaluating trends in temperature, because such stations may not be representative of the atmospheric temperatures experienced in the highlands. To overcome this, the environmental lapse rate of 0.649°C per 100 m (Sheridan *et al.* 2010) was applied to the mean temperatures recorded at all three stations as an estimate of the temperature at the source zone of the Móafellshyrna landslide. The correction of the precipitation data collected near the coast for the inland conditions was not

attempted, because this would not only require a temperature correction, but would need to take into account variations in wind speed, wind direction and pressure in a meteorological model, which is beyond the scope of this work.

At the time of the failure, the closest weather station to the Árnesfjall site was the manned synoptic station of Litla-Ávík, operated by the Icelandic Road and Coastal Administration. The station (WMO ID: 4031) and is located along the coast at 15 m a.s.l., 5 km east to the Árnesfjall landslide and 7 km south-east to the village of Norðufjörður. Unfortunately, there is no other weather station located within 40 km of the Árnesfjall mountain recording precipitation and/or temperature. The closest automated station, Gjögur, located at 31.0 m a.s.l. 9 km east-south-east of the Árnesfjall mountain, was not operative at the time of the failure or during the time range considered (2000-2014).

5.3 Results

5.3.1 Witness report of the Móafellshyrna landslide

The residents of the Þrasastaðir farm recounted that on the 20th of September 2012 at around 12.30 p.m. they heard a rumbling noise, which originated from the Móafellshyrna mountain. They also recounted that a black tension crack, in the snow covered mountain, progressively formed above the colluvial cone at around 850 m a.s.l. They saw large blocks of debris that broke off the frontal part of the cone and fell onto the talus slope below. This activity was most intense in the first 1-1.5 hours, but they reported that there were intermittent noises and rock fall activity throughout the day.

The residents of the Þrasastaðir farm felt all the three earthquakes that occurred on the 19th and 20th September, with the last one only three hours before the landslide event. It was estimated that less than 1 m of snow was on the ground at the time of the failure.

5.3.2 Witness report of the Árnesfjall landslide

The resident of the Melar farm witnessed the Árnesfjall landslide on 10th July 2014. In the morning, they saw debris movement of few meters, cracks forming in the source area of the landslide, and minor rock falls accompanying these precursory events. The failure happened at 1.30 p.m., and it was accompanied by a dust cloud that travelled in the same direction as the flow. After the landslide came to rest, they saw one of the blocks transported by the landslide, and they realised it was a block of frozen debris. They recounted that the ice melted throughout the day, and a few days later it had become a conical pile of debris. The farmers reported that some minor debris fall occurred throughout the day of the failure and some days after the main event.

5.3.3 Antecedent conditions to the Móafellshyrna landslide

5.3.3.1 Precipitation

The spring and summer months preceding the Móafellshyrna event were dry, and the autumn was unusually wet (Figure 5.3Figure 5.4) (Jónsson, 2013). From April until 28th August 2012, dry conditions prevailed in the outer part of the Tröllaskagi peninsula, with only one day with precipitation greater than 10 mm:

23rd to 24th July, when 70 to 90 mm of rain was recorded at Siglufjörður and Ólafsfjörður weather stations (Figure 5.5).

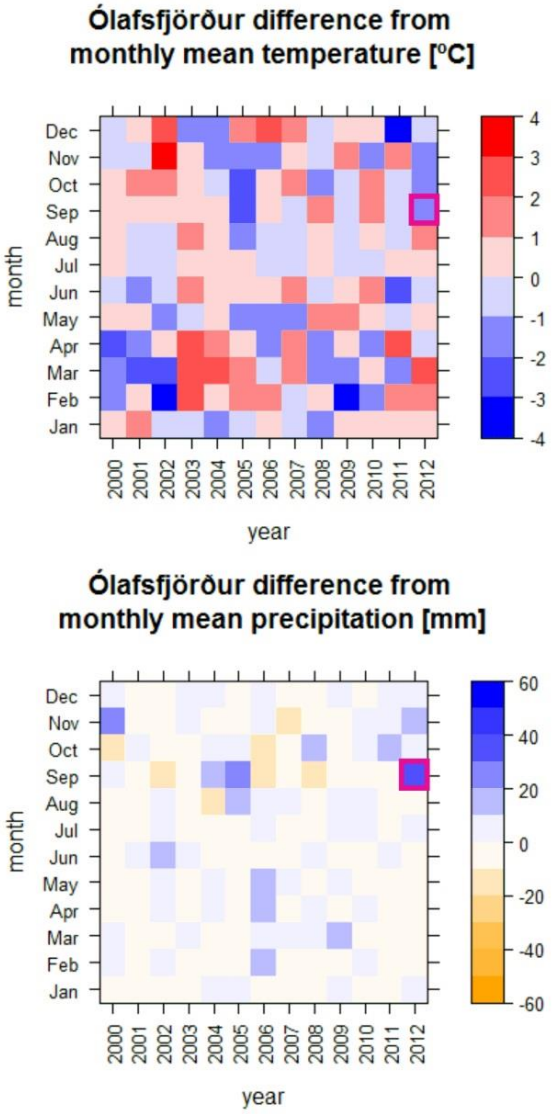

Figure 5.3. Matrix plots of the difference between the average monthly temperature (top) and precipitation (bottom) and the average value for that month for the period 2000-2012 for the Ólafsfjörður station (Data supplied by the IMO in 2016). The pink squares mark the month of the occurrence of the Móafellshyrna event.

From 20th August to 20th September around a third of the total precipitation for 2012 fell in the area (~400-550 mm). For comparison, the average annual precipitation in the town of Ólafsfjörður is ~400 mm for the period 2000-2012

(Figure 5.3Figure 5.4). In detail, from 28th August to 8th September the cumulative precipitation in Siglufjörður was 190 mm and 120 mm in Ólafsfjörður, with an additional 30 to 40 mm precipitation at these stations on the 3rd, 6th and 7th September. From 9th to 11th September an unseasonal and severe snowstorm hit the north eastern and northern parts of the country (Hermannsdóttir, 2012; Jónsson, 2013). Following this snowfall, around 100 mm rain was measured in only two days at Siglufjörður and almost 150 mm at Ólafsfjörður. The precipitation continued from 11th to 17th September, either as snow, sleet or rain at these weather stations. From September 17th to 19th less than 10 mm of precipitation was recorded, but at the time of the Móafellshyrna event 540 mm precipitation had been recorded in Siglufjörður and 490 mm at Ólafsfjörður weather stations since 23rd July, which corresponds to 40-45% of the mean annual precipitation from 2000-2012 (Figure 5.3). The monthly precipitation data from Ólafsfjörður station from 2000 to 2012 show that September is the month with maximum precipitation for any given year, with a range between 70 and 250 mm (Figure 5.3, 5.4). The year of 2012, however, had precipitation exceeding the average for this month (Figure 5.3).

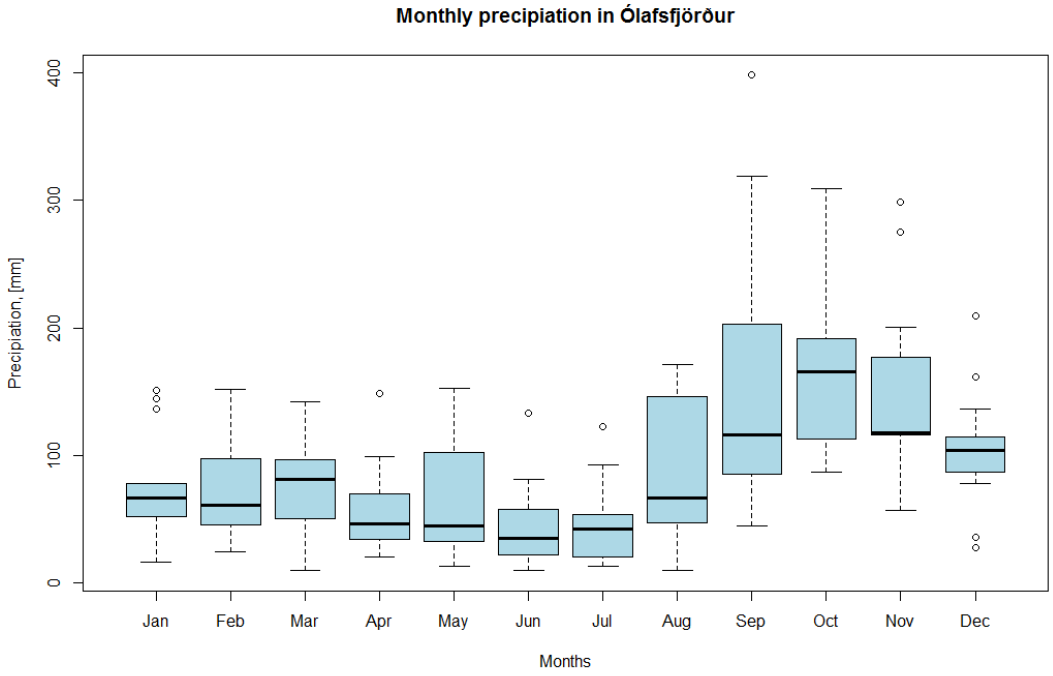

Figure 5.4. A boxplot of the precipitation data from the Ólafsfjörður station for each month between the years 2000 to 2012 (Data from IMO 2016). The end of the dotted lines is where the max and min values of precipitation were measured for each month, excluding the outliers that are displayed as dots (outliers are defined as values which lie outside 1.5 times the interquartile range above the upper quartile and bellow the lower quartile). The blue boxes is where the 50% of accumulated measured precipitation falls and the black lines are the medians for each month.

Unfortunately, there is no weather station located in the mountainous region of Tröllaskagi and, as previously mentioned, there is no weather station in the Fljótin area. This means that absolute precipitation data for the Móafellshyrna site cannot be reported, but it is reasonable to assume that, on a month by month basis, the trends should be similar to those of surrounding weather stations. Predicting whether precipitation falls as snow or rain at Móafellshyrna is outside the scope of this study and is complicated by a number of factors including snow drifting, wind-dependant snowmelt and variable orographic effects dependant on wind direction (Brynjólfsson and Ólafsson, 2009; see Section 5.1.2). Snow was visible on the ground on the day of the failure and was less than 1m thick from

eye witness accounts (equivalent to ~100 mm of precipitation, depending on snow density) Therefore, the majority of the precipitation received up to 20th September had been absorbed by the ground. The fact that snow was present on the ground argues against a sudden influx of water into the ground via snowmelt, known to trigger other mass wasting phenomena in Iceland (e.g. Decaulne et al., 2005). Hence, an analysis of the wind data from the weather stations was not pursued, because this would only be important if melt or precipitation were the primary triggers for the failure.

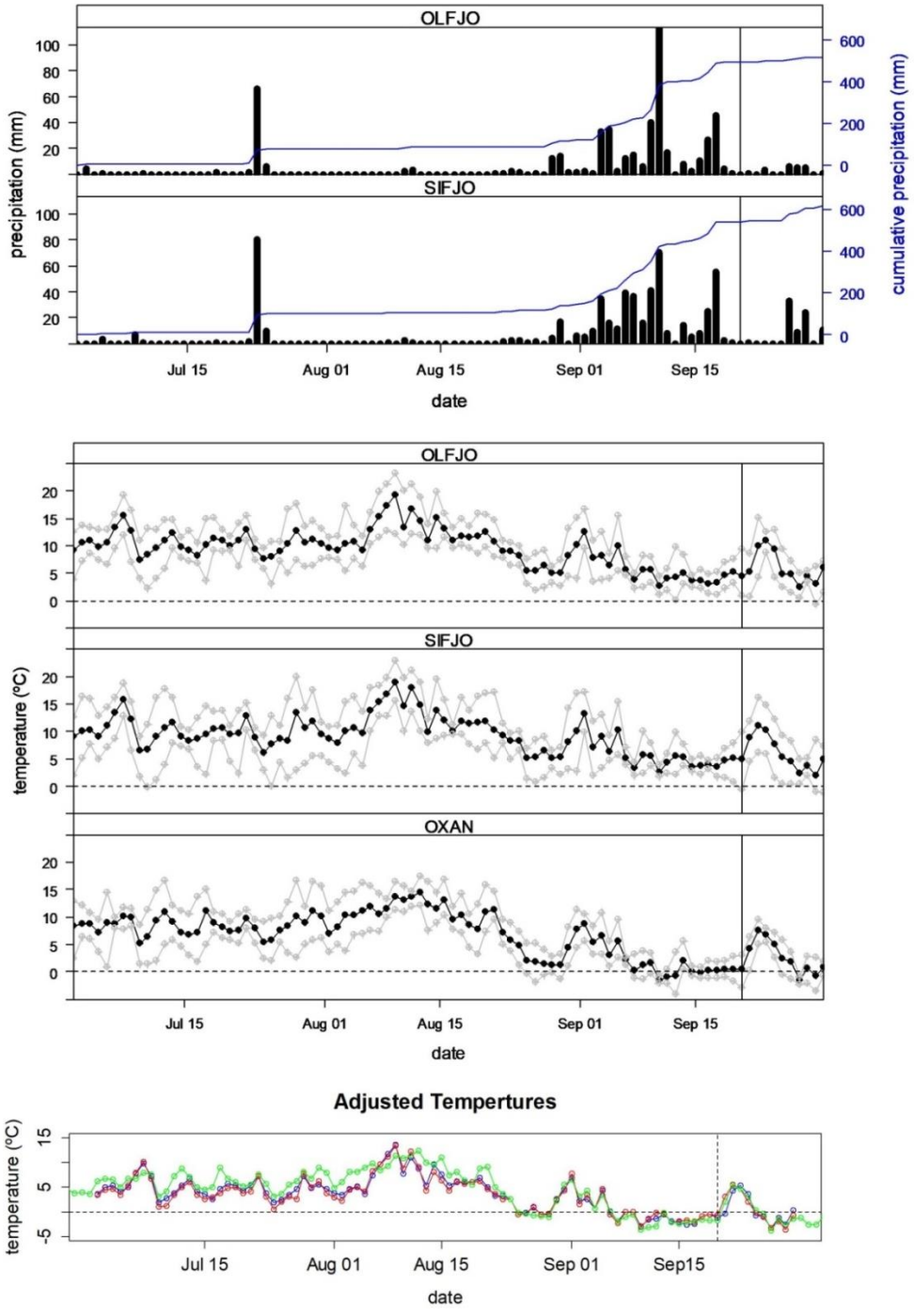

Figure 5.5. Precipitation and temperature in Siglufjörður and Ólafsfjörður in summer 2012. Top: daily precipitation (black bars), cumulative precipitation (blue lines) for temperature measurements from the Siglufjörður (SIFJO) and Ólafsfjörður (OLFJO) weather stations. Middle: daily temperature data from the Siglufjörður (SIFJO), Ólafsfjörður (OLFJO) and Öxnadalsheiði (OXAN) weather stations. Bottom: mean temperature data for all three stations adjusted to 880 m altitude of Móafellshyrna (red= SIFJO, green=

OXAN and blue= OLFJO). All data from 1st July to 30th September 2012 (Data obtained from IMO in 2016). The vertical line is the date of the Móafellshyrna event.

5.3.3.2 Temperature

At Móafellshyrna the temperature patterns in 2012 were also unusual, as the summer and spring were unusually warm, but the autumn was particularly cold (Figure 5.3; Jónsson, 2013). The average temperature measured in the town of Ólafsjörður was 10.4°C in July and 10.9°C in August in 2012. The average temperatures for these months for the period 2000-2012 are 9.8°C and 9.6°C respectively. On the other hand, the average temperature for September 2012 was 5.7°C compared to an average of 7.2°C for 2000-2012.

The average daily air temperature from 6th to 20th September at the Siglufjörður and Ólafsfjörður stations varied between 3 to 6°C, and at the Öxnadalsheiði weather station, fluctuated around zero, but reached approximately -3°C the night before the failure (Figure 5.5). Our corrected temperature data indicate average daily temperatures at the altitude of the Móafellshyrna event of around -1 to -2°C in the days preceding the failure, and hence night-time temperatures would have been even lower. During the evening of 19th September, a drop below 0°C in the atmospheric temperature in the mountains was measured in the Öxnadalsheiði weather station (Fig. 7). The snow on the ground at the time of the Móafellshyrna landslide shows that similar sub-freezing conditions also prevailed at this altitude prior to the event. These low temperatures combined with the snow cover are strong evidence that sudden influx of water from precipitation was not the trigger for the Móafellshyrna landslide.

5.3.3.3 Earthquake sequence

In the Eyjafjarðaráll graben, three earthquakes with magnitudes M 4.2 to M 4.5 were registered on 19th and 20th September (Gudmundsson, G.B., Hensch et al., 2013). Their epicentres are located 25-27 km north-northeast of the town of Siglufjörður, and 60 km north-northeast of the Móafellshyrna site (Figure 5.2). On the morning of 19th September, one day prior to the failure, two earthquakes with magnitudes M 4.5 and M 4.3 occurred at 07:57 and 08:28 respectively. Following these earthquakes, smaller aftershocks occurred throughout the day. Another earthquake of magnitude M 4.2 occurred at 9:27 on the 20th September, approximately three hours prior to the first observations of the Móafellshyrna landslide (Figure 5.2).

5.3.4 Antecedent conditions to the Árnesfjall landslide

5.3.4.1 Precipitation

The spring months preceding the Árnesfjall event were dry (Figure 5.6). From May to 30th June 2014, dry conditions prevailed in Litla-Ávík. Ten days before the occurrence of the failure, almost 90 mm of rain fell in the area close by the Árnesfjall mountain, of which 62 mm were recorded between 4th to 6th July (Figure 5.7). From the beginning of May to 9th July the cumulative precipitation in Litla-Ávík was 140 mm (Figure 5.7). July was the month with the maximum precipitation registered for the year 2014 (Figure 5.6), with the peak recorded in the ten days before the landslide (Figure 5.7).

It must be noted that the weather station of Litla-Ávík was the only weather station available for the area, and it lies in a rain shadow from easterly winds, shielded by the mountain next to the weather station. This means that the precipitation might be more abundant and intense at the site of the event, especially with northerly, north-easterly and easterly winds.

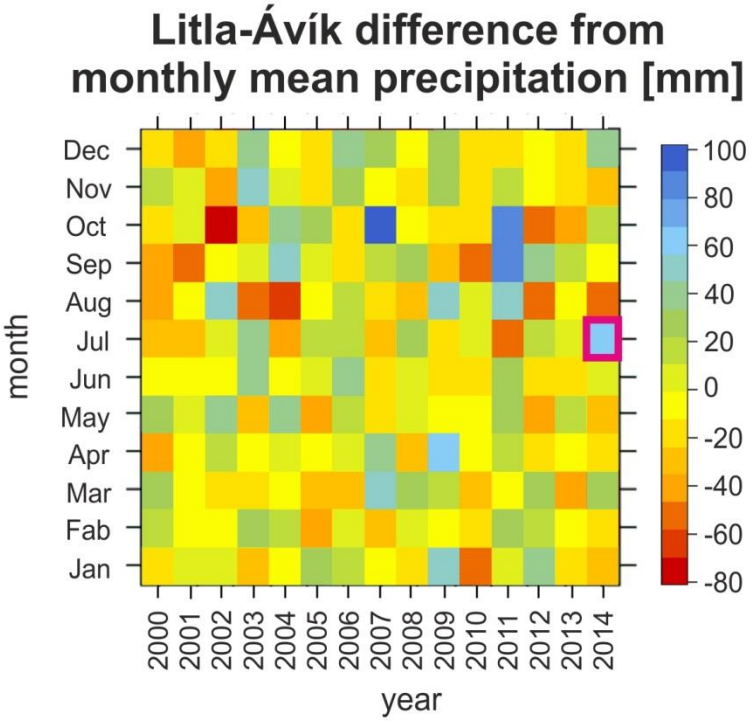

Figure 5.6. Matrix plot of the difference between the average monthly precipitation and the average value for that month for the period 2000-2014 for the Litla-Ávík station (Data supplied by the IMO in 2018). The pink square marks the month of the occurrence of the Árnesfjall event.

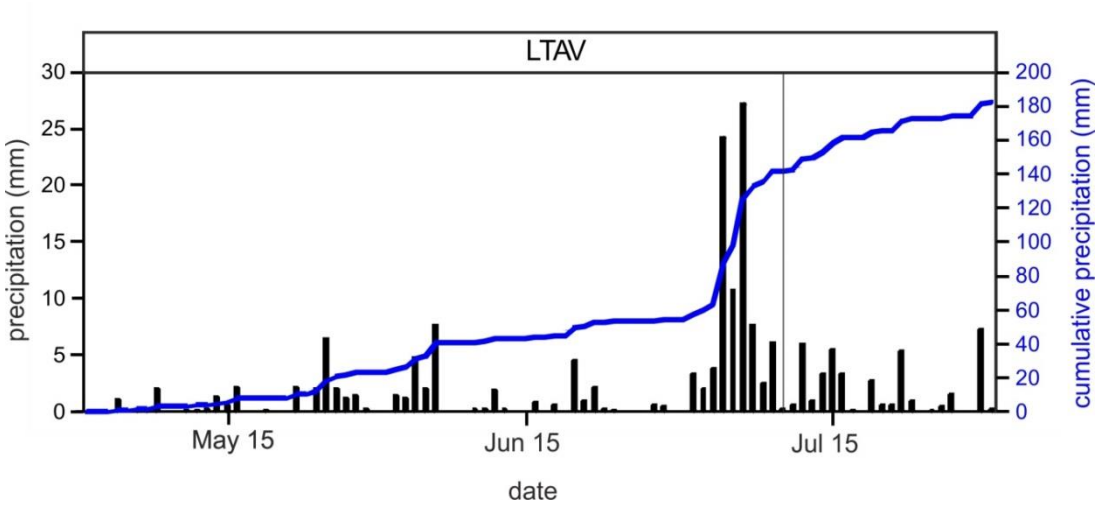

Figure 5.7. Daily precipitation (black bars) and cumulative precipitation (blue lines) for precipitation measurements from the Litla-Ávík (LTAV) weather station (Data obtained from IMO in 2018). The vertical bar is the date of the Árnesfjall event.

The cumulative precipitation recorded in Litla-Ávík in this period was 90 mm, but probably more rainfall felt on the Árnesfjall area. Figure 5.8 shows a wind rose for the weather station of Gjögur (9 km ESE to the Árnesfjall mountain) for the period 2000-2016, with the condition that the precipitation must be higher than 1 mm (data plot from IMO), most of the precipitation-carrying winds in the area are north-north-easterly winds. This is coherent with the general wind trend of the Westfjords (Jónsson et al., 2004). As the station of Litla-Ávík is positioned on the west-south-western side of the Reykjarneshyrna mountain, the orographic part of the precipitation is probably missing. With only the precipitation data from the weather station of Litla-Ávík (the Gjögur weather station was not operative at the time of the failure), a careful interpretation suggests that a sudden rainfall, probably more intense that the one recorded, hit the region near the Árnesfjall Mountain and triggered the landslide. On the day of the event, almost no

precipitation occurred (0.2 mm). It is not unusual, and it is well documented in literature, that the onset of landslides can occur from a few hours to a days after intense precipitation (Baum and Godt, 2010; Iverson and Major, 1987; Iverson, 2000; Matsuura et al., 2008).

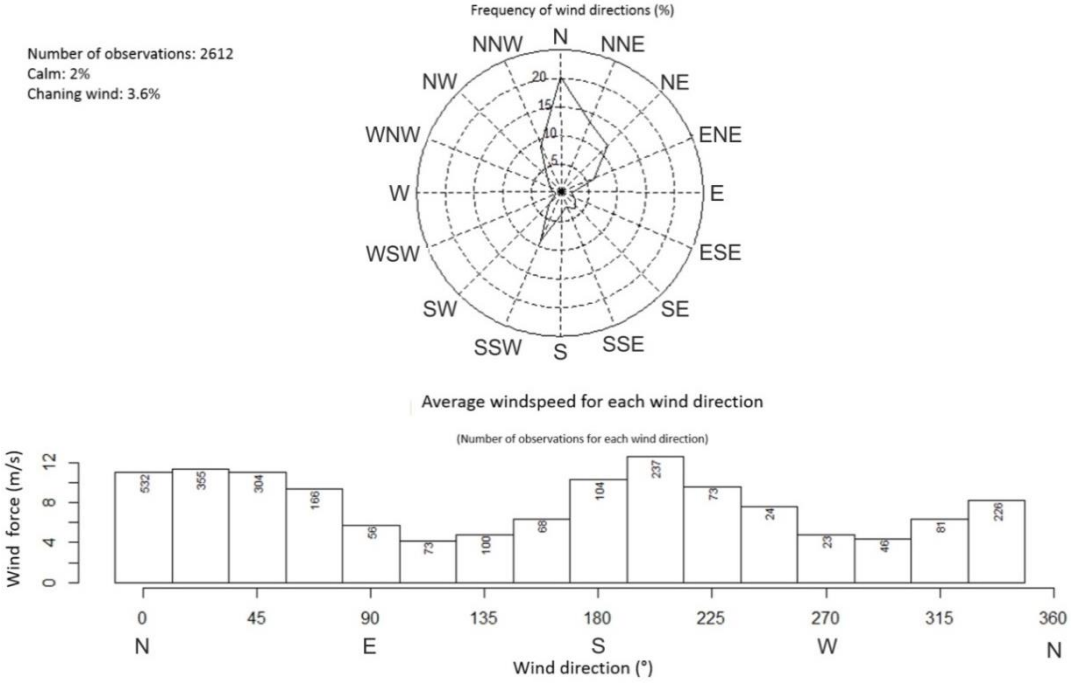

Figure 5.8. Wind in the Westfjords. On the top, wind rose for the weather station of Gjögur for the period 2000-2016, with the condition that the precipitation must be higher than 1 mm; at the bottom, average wind speed for each wind direction (Data supplied by the IMO in 2018).

5.3.4.2 Temperature

The temperature patterns in 2014 were not unusual for the region (Figure 5.9). The average temperature measured in Litla-Ávík was 9.2°C in June and 9.8°C in July in 2014 (Figure 5.10), which are values that fall within the average range recorded for the period 2000-2014 (Figure 5.9). The average temperatures for these months for the period 2000-2012 are 7.4°C and 9.3°C respectively. However, on 8th June, two days before the occurrence of the Árnesfjall event, the

temperature raised from an average of 7.8°C (temperature recorded the week before), to an average of 11.0°C from 8th to 10th July (Figure 5.11).

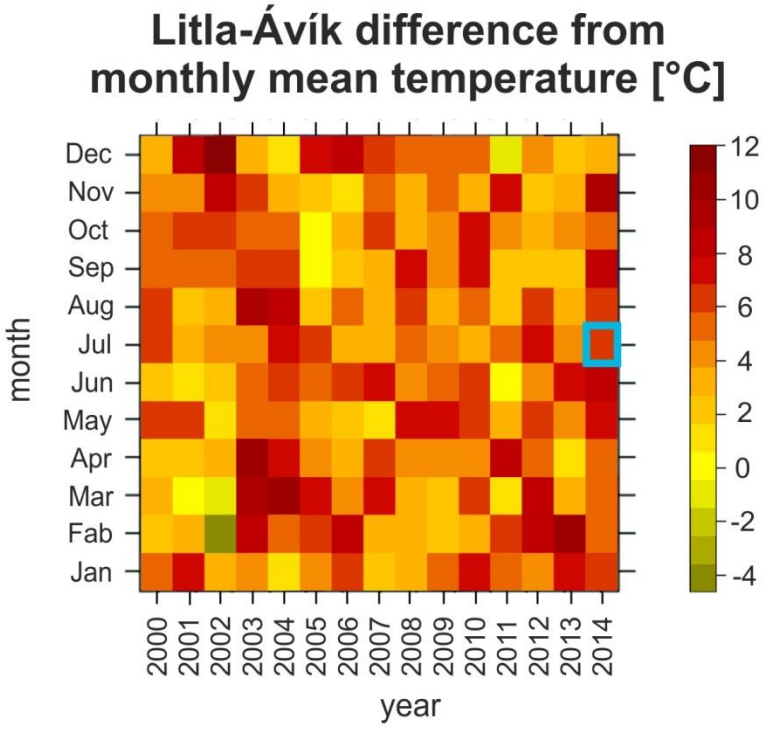

Figure 5.9. Matrix plots of the difference between the average monthly temperature and the average value for that month for the period 2000-2014 for the Litla-Ávík station (Data supplied by the IMO in 2018). The blue square marks the month of the occurrence of the Árnesfjall event.

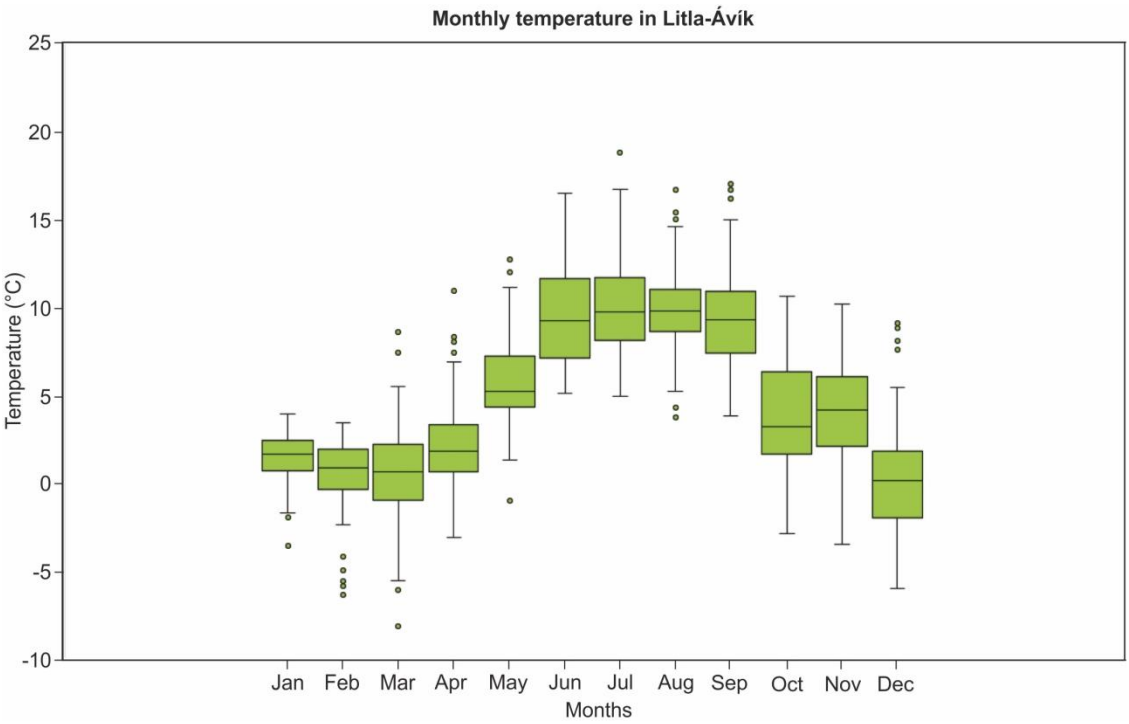

Figure 5.10. A boxplot of the temperature data from the Litla-Ávík station for each month between the years 2000 to 2012 (Data supplied by the IMO in 2018). The end of the lines is where the max and min values of temperature were measured for each month, excluding the outliers that are displayed as dots (outliers are defined as values which lie outside 1.5 times the interquartile range above the upper quartile and bellow the lower quartile). The green boxes is where the 50% of accumulated measured precipitation falls and the black lines are the medians of each month.

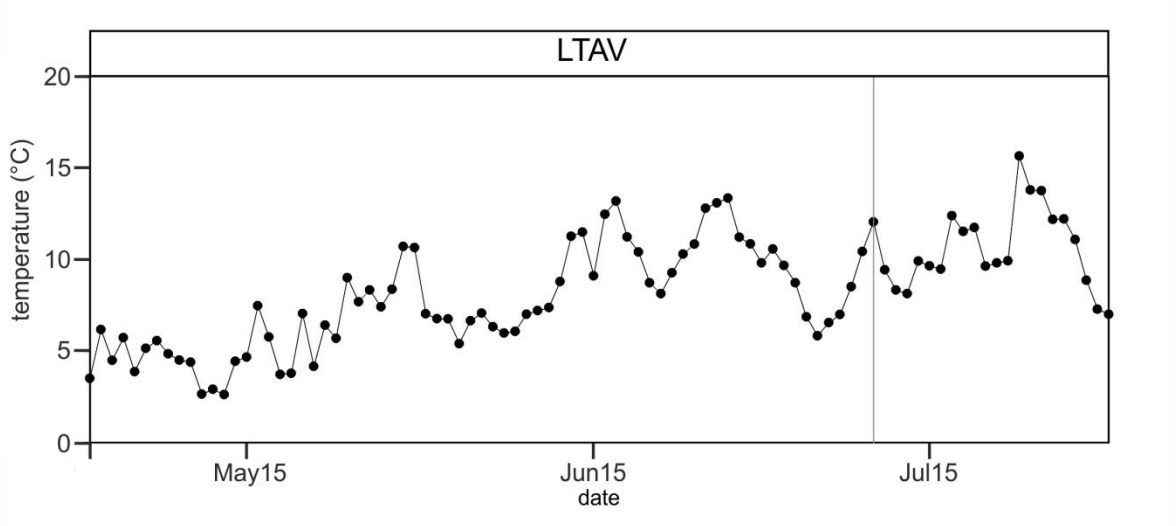

Figure 5.11. Daily temperature data from the Litla-Ávík (LTAV) weather station for the months of May, June and July 2014 (Data supplied by the IMO in 2018). The vertical bar is the date of the Árnesfjall event.

5.4 Discussion

Several factors might have contributed to the failure of the Móafellshyrna and Árnesfjall landslides: heavy precipitation, ground ice degradation (via a rise in average surface temperatures), and earthquake activity in the case of Móafellshyrna. For the Móafellshyrna landslide, it is possible to infer that precipitation was the main preparatory factor (but not the trigger) for this landslide for the following reasons: heavy prolonged precipitation was recorded across the area, where nearly half of the usual annual precipitation fell in less than one month (Figure 5.3). Many case studies have shown that high magnitude water input, either by rainfall (e.g., Rapp and Nyberg, 1981) or snowmelt (e.g., Decaulne et al., 2005), leads to oversaturation of soil, which can directly trigger debris flows and shallow landslides. These studies also point out the role of intense rainfall as a preparatory (rather than direct trigger) factor to failure (Addisson, 1987; Becht, 1995; Cannon and Reneau, 2000; Guzzetti et al., 2007; Innes, 1983; Johnson and Rahn, 1970; Johnson and Rodine, 1984; Luckman, 1992; Rapp, 1995, 1964, 1985; Rapp and Nyberg, 1981; Sæmundsson et al., 2003; Sæmundsson and Decaulne, 2007; Smith et al., 2009). However, the role of water infiltration in triggering shallow landslides and debris flow in permafrost areas is rarely well-documented (Harris and Gustafsson, 1993). Precipitation was probably not a *direct* trigger of the Móafellshyrna landslide, because snow was present on the ground at the time of the failure. However, saturation appears to have been a key preparatory condition for the failure to occur.

In the case of Árnesfjall landslide, precipitation was probably the main trigger for the landslide. Sudden and heavy precipitation occurred in the ten days before

the occurrence of the landslide (Figure 5.7), after a spring dominated by dry conditions (Figure 5.6).

Only for Móafellshyrna was seismic activity a potential trigger for the landslide. The direct influence of the seismic activity and associated ground acceleration on the motion of the debris in the source area seems unlikely, as the event did not occur immediately following any seismic event. Earthquakes are a common triggering factor for landslide activity and are considered as a major cause for landslides worldwide (e.g. Keefer, 2002, 1994, 1984; Malamud et al., 2004). Yet, no other rapid mass movement was reported on the northern part of the Tröllaskagi area on 19th or 20th September, which might be expected if ground acceleration were sufficient to trigger landslides. However, the short time interval (three hours) between the last earthquake and the failure indicates a possible connection between the failure and the seismic events.

Selby (1993) argued that “stability of the slope, orientation of the earthquake in relation to the slide mass, earthquake magnitude, focal depth, seismic attenuation and after-shock distribution” are factors that determine whether earthquakes trigger landslides. According to Keefer (1984), the maximum area likely to be affected by landslides in a seismic event increases from approximately none at M 4.0 up to 500.000 km^2 at M 9.2. According to (Malamud et al., 2004), the lowest earthquake-magnitude is M 4.3 +/-0.4. for triggering gravitational mass movements. Tatard et al. (2010) state that earthquakes of M 4 and lower have little or no influence on landslide triggering. Nevertheless, different studies (e.g.,Sassa et al., 2007; Walter and Joswig, 2008) mention that small earthquakes (maximum M 3.6 in southern Italy according to Del Gaudio et al. (2000) and repeated shocks can influence hydrogeological settings and can

possibly cause landslides, sometimes with delay between the earthquake and the mass movement. Jibson et al. (1994) also discuss delayed landslide movements, from larger earthquakes (M 7.0), and state that the simplest explanation for the delay is a change in the ground-water conditions. Based on the above mentioned studies, it is unlikely that an earthquake of M 4.3 was the only triggering factor for the Móafellshyrna landslide, having taken place 60 km away from the epicentre. On the other hand, since the Móafellshyrna landslide occurred only three hours after a seismic event, the seismic sequence is likely playing some indirect role.

The ground water flow systems of the talus deposits composing the source material of the Móafellshyrna and Árnesfjall landslide is expected to be very limited. This is due to several factors: i) the catchment areas above the source areas are not very large (around 350 m long in Móafellshyrna and 250 m long in Árnesfjall); ii) the talus cones were confined uphill by a vertical rockwall, and in the case of Móafellshyrna, downhill by the edge of a topographic bench; iii) the presence of ground ice cementing the deposits; iv) the sub-horizontal dipping of the bedrock layers where the deposits are perched. However, it has been shown that talus slopes can contain multiple and distinct groundwater flow systems beneath or within them, and that they have a rapid and localised response to precipitation and melt inputs (McClymont et al., 2010; Roy and Hayashi, 2009). One component of the groundwater flow in the talus cones of both landslides may originate in the pervasive systems of sub-horizontal and sub-vertical discontinuities affecting the bedrock. If a groundwater system was present before the failure, the response of the water table should have been rapid. In the case of Móafellshyrna, since seismic activity can release water by co-seismic liquefaction or consolidation of loose sediments (e.g., Manga et al., 2003;

Montgomery and Manga, 2003), a change in the hydrogeological equilibrium of the colluvial cone caused by seismic activity could have contributed to the occurrence of the failure.

Field evidence from the Móafellshyrna and Árnesfjall landslides suggests the involvement of ground ice thaw in triggering the event. In the case of Árnesfjall landslide, the annual trend of temperature does not seem to differ from the past years (Figure 5.9). According to an Icelandic technical report (Sigfússon et al., 2016), in the period 1949-1992 and 1995-2015 for the Gjögur and Litla-Avik stations, there were more than 150 frost days per year, but four months (December-March) had an average temperature below the freezing point. The combination of sudden and probably intense precipitation, and an abrupt rise of temperature up to 12.5°C in the days before the failure could have caused the degradation of the ground ice present in the source area, which is a combination of factors that have been attributed to the release of rapid mass movements elsewhere worldwide (Crosta et al., 2004; Huggel et al., 2005; Huscroft et al., 2003). In Móafellshyrna, because the month of the event had temperatures lower than average and the days prior to the event were mostly below zero Celsius (as evidenced by snow on the ground), thaw water from the ground ice in the perched talus likely did not contribute significantly to the event. However, longer term, deeper thawing caused by an annual rise in temperature and therefore a shift in the permafrost table, including an anomalously warm preceding summer, is a more likely contributor.

In recent years, there has been an increasing interest worldwide in the influence of climate warming and associated decline of mountain permafrost on the occurrence of mass wasting phenomena (e.g., Damm and Felderer, 2013;

Fischer et al., 2006; Gruber et al., 2004; Gruber and Haeberli, 2007; Rebetez et al., 1997; Sattler et al., 2011; Stoffel et al., 2014; Stoffel and Huggel, 2012). The increasing frequency of rapid mass movements, such as debris flows, debris slides, rock falls and rock avalanches, in mountainous areas have been linked in several cases to mountain permafrost degradation (Clague et al., 2012; Darrow et al., 2016; Haeberli et al., 2017; Wirz et al., 2013). Loss of ice-cementation, the presence of segregated ice, increased hydrostatic pressure and the associated reduction of shear strength can all lead to reduction of stability with increasing atmospheric temperature via permafrost degradation (Gruber and Haeberli, 2007; Krautblatter et al., 2013; Pogliotti et al., 2015). Although, these previous studies have focused on the stability of massive rock masses, a similar (perhaps exaggerated) effect might be expected in ice-cemented talus.

The increase of mean annual temperature, which has been observed in Iceland over the last few decades, is probably causing degradation of discontinuous permafrost in Iceland (Björnsson et al., 2008), and this process is thought to be present in the Tröllaskagi peninsula, but not in the Westfjords (Etzelmüller et al., 2007). Our observations of the ice-cemented deposits shows that the Móafellshyrna and Árnesfjall landslides originated from deposits containing pore-filling ground ice and equally that these deposits were still frozen at the time of the failures (see Chapter 4). Together, these argue for a permafrost origin for this ground ice in the Móafellshyrna case study. In the case of the Westfjords, and therefore of the Árnesfjall landslide, permafrost has not previously been expected to be present in the area. However, the proximity of the Drangajökull glacier could affect the presence of sporadic permafrost predicted in the permafrost map by Brown et al. (1997), and it has been shown in other

studies that permafrost conditions — even if sporadic — are present in areas near glaciers (Bolch and Marchenko, 1990; Etzelmuller and Hagen, 2005; Gruber and Haeberli, 2009; Haeberli and Beniston, 1998; Kneisel and Kääb, 2007). The existence of a glacier at 26 km from the Árnesfjall site, and the presence of ground ice cementing the deposits of the landslide are two arguments supporting a permafrost origin for the ground ice in its source material. The increasing average temperatures over the last decades in Iceland (Björnsson et al., 2008; Jónsson, 2013) before the landslide events may have initiated the degradation of ground ice in the talus cones where the landslides initiated, not from the top-down, but from the base-up. This thawing may have: i) lubricated the base of the cemented talus cones, ii) lowered the effective friction angle (reducing cohesion), and hence iii) caused the downslope movement of the talus cones. In both landslides (north-northwest facing), the warming of the rock mass onto which the colluvial deposit was previously cemented could have been brought about by a combination of propagation of the thermal wave through the rock mass from the warmer southeast-facing side (e.g., Noetzli et al., 2007) and the delivery of warmer liquid water (derived from the intense precipitation) to the talus-rock interface from the south-westward dipping strata in Móafellshyrna and the east-south-eastward dipping strata in Árnesfjall. Hence, the rupture occurred beneath the permafrost table. Perhaps the ice-cemented colluvium was in effect forming an underground “ice dam” that was holding back water-saturated debris until its own weight caused it to fail, with the additional contribution of the seismic shaking in the case of Móafellshyrna landslide. However, it is not possible to substantiate this link with certainty, due to the lack of direct temperature measurements in the talus cones. Our hypothesis is supported by (i) the slow widening of the tension cracks

at the top of the source areas as observed by eye-witnesses, (ii) the presence of multiple rupture surfaces in the Árnesfjall landslide as an indicator of cohesive rotational sliding downwards, and (iii) the fact that both the landslides were fluidised (a water content higher than expected for such a small catchment).

Ice-cemented deposits have been observed in these two landslides and in a third in Iceland occurred in 2011 on the Torfufell mountain (source area at ~750 m a.s.l.). The source zones for the Móafellshyrna and the Torfufell slides are at the lower elevation limit of discontinuous mountain permafrost in northern Iceland (i.e., 800 m a.s.l.; Etzelmüller et al., 2007). On the other hand, the source zone of the landslide in the Árnesfjall Mountain is at an unexpectedly lower elevation (source area at ~350 m a.s.l.). This event provides additional evidence to support the hypothesis that the lower limit of permafrost degradation extends to lower altitudes, and shows that knowledge of mountain permafrost in Iceland is incomplete. The setting of talus perched on benches or flat topographic surfaces is not a rare situation in Iceland because of the sub-horizontal basalt layers create topographic benches on which loose material can accumulate. Hence, investigating whether those benches with permafrost conditions, particularly above inhabited areas, contain ground ice and establishing its condition, should be a priority.

5.5 Conclusions

Following the analysis of the weather and seismic data prior to the Móafellshyrna landslide, I have defined what are the exogenous and endogenous factors that brought to the release of the Móafellshyrna and Árnesfjall landslides, including a new factor that has never been conceived for Iceland: permafrost degradation. It can be concluded that heavy precipitation prior to the failure was the main preparatory factor, with over 400 mm of precipitation recorded in one month prior to the event after an unusually dry summer season. Weather data prior the Árnesfjall landslide were also analysed and sudden and intense precipitation was the main triggering factor for the occurrence of the landslide. In Móafellshyrna, the influence of seismic activity is unclear, but the close temporal association between the last earthquake series and the failure suggests that the shaking could have contributed to the initiation of the failure, weakening the cohesion between the ice-cemented deposits and the bedrock and/or changing the hydrology. The presence of ice-cementing in source talus deposits in the Móafellshyrna landslide at 870 m confirms the presence of discontinuous mountain permafrost at that elevation in the Tröllaskagi peninsula, while the presence of ground ice in the source deposits of the Árnesfjall landslide at 350 m a.s.l. highlights the possibility that unexpected zones of discontinuous permafrost could be present in areas of the island where permafrost has not been predicted by previous models. The partial thaw of these deposits was a trigger for the failures for these reasons: i) mean annual air temperatures are generally increasing in Iceland, ii) the talus cones initially slid as a single cohesive mass suggesting basal lubrication/melting, iii) the Móafellshyrna landslide followed an usually warm spring and summer. The fact that another recent landslide contains

similar ice-cemented deposits suggests that mountain permafrost degradation could be more prevalent in triggering landslides in Iceland than has previously been thought.

The ice-cemented deposits within the slides of the Móafellshyrna, Torfufell and Árnesfjall Mountains have highlighted the need for a more detailed understanding of the distribution and condition of mountain permafrost within perched talus deposits in Iceland. These three landslides occurred in uninhabited areas, but future similar landslides might not, and these could represent a potential risk to society and infrastructure in the island. This is why Chapter 4 and 6 focus on the relationship between rapid mass wasting processes and the degradation of mountain permafrost in loose deposits in Iceland, and particularly on how the ground-ice can affect the mobility of the failures and how to interpret the geomorphic signatures of these landslides.

Chapter 6. Molards as an indicator of permafrost degradation and landslide processes[3]

6.1 Introduction

This chapter uncovers the main finding of this thesis: the formation of a particular landform called “molards”, and its importance in both the understanding of permafrost degradation in cold environments and the landslide dynamics in ground-ice affected terrains. This particular type of landslides leaves clear morphological signatures, as I have shown in Chapter 4, and molards are a further feature that shows the different behaviour of permafrost-degradation induced landslides and their impact on the periglacial landscape.

Glacial and periglacial environments are particularly sensitive to the effects of climate change (Haeberli and Beniston, 1998; Hinzman et al., 2005). However, few easily recognisable landforms in cold landscapes are reliable indicators of increasing atmospheric temperature. Here, I propose that molards, landforms

[3] The work contained in this chapter of the thesis is based on a paper that is in review on the journal Earth Planetary Science Letters entitled “Molards as a marker of permafrost degradation and landslide processes”. The manuscript has been reviewed and is awaiting moderate corrections. The full citation of this paper is:

Morino, C, Conway, S. J., Sæmundsson, Þ., Helgason, J. K., Hillier, J., Butcher, F. E. G., Balme,, M. R., Jordan, C., Argles, T. 2018. Molards as an indicator of permafrost degradation and landslide processes. Earth Planetary Science Letters, under review.

In addition to my supervisory team, this manuscript benefits from the collaboration with Jon Kristin Helgason, who provided photographs of the landslides and field observations, and Frances E. G. Butcher, who provided images of Mars. Both collaborators, with my supervisors, contributed to the manuscript preparation, which is the result of my own work. Typological changes to the paper have been made to ensure consistency with the rest of the thesis. These changes are: removal of the abstract, removal or changes of parts of the Introduction and Methods to avoid repetition with the rest of the thesis, the use of the first person singular instead of the first person plural where appropriate.

poorly reported in the literature, can help to fill this gap. Molards have been described as mounds of debris occurring in landslide deposits (Cassie et al., 1988; Goguel and Pachoud, 1972; Mollard and Janes, 1984). They are generally ~0.3-12 m high (Brideau et al., 2009; Jermyn and Geertsema, 2015), up to 12 m wide (Milana, 2016), have a single, central, rounded to pointed summit (Jermyn and Geertsema, 2015; Xu et al., 2012), and flank slope angles of 27°-45° (Cassie et al., 1988; McConnell and Brock, 1903). Molards have been found in the distal zones, at the margins of the displaced mass, and/or below the main scarp of landslides (Cruden, 1982; Geertsema et al., 2006b).

Molards have recently been identified in a variety of periglacial environments, including northern Canada, the Andes, and the Tibetan Plateau (Jermyn and Geertsema, 2015; Milana, 2016; Xu et al., 2012). Only three recent studies have hypothesised a link between molards and permafrost degradation (Brideau et al., 2009; Lyle et al., 2014; Milana, 2016). These studies propose that movement of landslide material in permafrost regimes causes blocks of frozen material to detach and be transported downslope (Brideau et al., 2009; Lyle et al., 2014). When the blocks come to rest, the ground ice cementing them thaws, leaving conical mounds of rocks and debris. Although no previous studies have observed the full cycle of molard evolution, original ground ice contents of 50-80% have been estimated (Brideau et al., 2009; Milana, 2016) as sufficient for blocks of ice-cemented sediments to survive both initial failure and transport.

I combine field and remote sensing studies of molards found in the deposits of the recent Móafellshyrna and Árnesfjall landslides in Iceland to constrain their complete evolution, providing the first observations before and after ice loss. My data dispel any lingering doubts about the direct link between these landforms and permafrost degradation. I show that molards are a critical marker of

permafrost degradation, and they can reveal important information on the mobility of landslides in terrains affected by permafrost. I distinguish molards from other cone-shaped landforms, such as hummocks occurring in debris/rock avalanche deposits (Shea and van Wyk de Vries, 2008), and I detail characteristics that can be used to identify them in the field and from remote sensing data.

6.2 Methods

6.2.1 Fieldwork

My supervisors Þorsteinn Sæmundsson and collaborators at the Icelandic Meteorological Office performed fieldwork of the Móafellshyrna landslide 9 days after its occurrence, and Jón Kristinn Helgason (Icelandic Meteorological Office) visited the Árnesfjall landslide two days after the event. I revisited the Móafellshyrna site in summer 2015 and the Árnesfjall site in summer 2016, in order to i) perform field observations, ii) collect Structure from Motion (SfM) photogrammetry datasets, iii) perform differential GPS (dGPS) surveys of the landslides using two GNSS Leica VIVA GS10 Systems (one as rover unit and one as base station; average accuracy of samples is around 1cm in plan and 2cm in height), and iv) ground-support the collection of airborne data for the Móafellshyrna site (for more details see Section 4.3.2 in Chapter 4).

6.2.2 Airborne data

In September 2015, the U.K. Natural Environment Research Council's Airborne Research Facility (NERC-ARF) on behalf of the European Facility for Airborne Research (EUFAR) collected aerial photography and LiDAR data for the Móafellshyrna area in Iceland, three years after the Móafellshyrna landslide occurred. 170 aerial photographs were collected with a Leica RCD105 digital

camera, and 15 lines were flown to collect 126 M LiDAR points with 1.7 points/m^2 using a Leica ALS50-II. A GNSS Leica VIVA GS10 dGPS was used in a fixed location at 1 Hz during the flight to collect base station data for the on-board dGPS. The processing of the LiDAR point cloud was performed by NERC-ARF-DAN (Data Analysis Node). I used the LAStools extension for ArcGIS to convert the point clouds into gridded data at 1 m/pixel, using the return time of the last peak of light to reach the receiver from the LiDAR laser shot, which is usually assumed to be the ground return. I used Agisoft Photoscan to produce a seamless orthomosaic from the airphotos, where the position of the images was controlled using ten well-spread ground control points derived by locating matching positions in a hillshaded version of the LiDAR DEM and the air photos.

6.2.3 Structure from motion

For the Árnesfjall site, I processed digital photos with the ground-based Structure from Motion (SfM) photogrammetry technique (Westoby et al., 2012) to produce a 3-D topographic model, from which an orthomosaic at 9 cm/pixel and DEM at 18 cm/pixel (Digital Elevation Model) were derived. 73 photos were collected in July 2016, two years after the Árnesfjall landslide occurrence, using a single-lens reflex (SLR) camera. I applied an absolute coordinate system to the 3D model by identifying clearly visible blocks and features on the landslide - a total of 19 ground control points (GCPs) - and obtaining their coordinates using a GNSS Leica VIVA GS10 System differential GPS, with an accuracy of 1 cm horizontally and 2 cm vertically. I produced the orthomosaic and the DEM using Agisoft Photoscan software, and then imported them into ArcGIS for further analysis (for more detail see Section 4.3.3 in Chapter 4).

6.2.4 Morphometric analysis of molards

In order to link the landslides' processes to the morphology of the molards, I i) analysed their distribution and geomorphic characteristics, ii) compared the slope angle of their longer and shorter flanks, iii) calculated their eccentricity, and iv) plotted the orientation of their long axes with respect to those of the landslides.

6.2.4.1 Area, height, volume and slope characteristics

The molards were first digitised as a polygon in ArcGIS using their contrast in terms of texture and shading on the aerial photographs. The area of molards was estimated by calculating the area of the resulting polygon (Figure 6.6E). To measure their height (Figure 6.6E), for each molard I used a topographic profile placed parallel to the contour lines outside the molard and passing through the molard' peak, in order to obtain the elevation of the molards' peaks and of their bases. The elevation data for these profiles was derived from LiDAR in the case of Móafellshyrna and SfM in the case of Árnesfjall. The volume of material composing the molards was calculated following Conway and Balme (2014), reconstructing the surface of the landslide without the molards, and deriving the deposited volumes by subtracting this surface from the surface with the molards (Figure 6.6E). Error propagation calculations by Conway and Balme (2014) suggest that such volume estimates are accurate to within 15%. Slope of the basal area where molards lie was calculated by creating a slope map of the surface of the landslide without the molards and taking the mean value. The slope angle for the long and short flanks of molards was the mean value of the slope obtained from the slope map of the original DEMs (Figure 6.6E).

I performed two-sample t-tests assuming unequal variances for the volume, area, height, slope angle of the basal area and eccentricity of molards, using the values of Móafellshyrna and Árnesfjall respectively as variables. I used the values

of each site separately for testing the slope angles of short and long flanks of their molards (see Table 6.1).

A dispersion parameter $\psi=\sigma/\mu$ (where σ is the standard deviation and μ is the mean) for height, axes and volumes of molards, show less homogeneous sizes in Móafellshyrna compared to those of Árnesfjall (see Table 6.2). This is confirmed by Pearson correlation coefficient calculated for height- long axis, height- short axis and long- short axis, showing a strong correlation in Móafellshyrna, suggesting a circular shape in plan- view and casually linked dimensions, while in Árnesfjall lower values suggest more elliptical shapes (see Table 6.2).

The volume-frequency distribution for the molards in Móafellshyrna shows a power-law distribution, while the volume-frequency distribution for the molards in Árnesfjall conforms to an exponential distribution (see Figure 6.5). Both were determined by comparing three different plots of the volume-frequency distribution (i.e., linear-linear, logarithmic-linear, bi-logarithmic), where I considered the best distribution the one fitting the more to a straight line.

6.2.4.2 Eccentricity and direction

To measure the eccentricity of the molards, an ellipse was fitted to approximate the perimeter of each molard, with the area of each ellipse being equal to the area of the perimeter of the represented molard. Then, the eigenvalue and eigenvectors of each zone were calculated, with the orientation of the ellipse being in the direction of the first eigenvector. Finally, the geometric characteristics of the ellipse were calculated, specifically the centroids, the major and the minor axes (the ratio of the major and minor axes of the ellipse is the same as the ratio of their eigenvalues). I plotted the orientation of the long axes of the molards

against the propagation direction of the landslides using GeoRose open-source software (Figure 6.6B,D).

6.3 Results

6.3.1 Landslide observations and molard formation

I studied molards that developed on the two landslides that are the object of study of Chapter 4 and Chapter 5: the Móafellshyrna landslide (Tröllaskagi peninsula, Figure 6.1A) and the Árnesfjall landslide (Westfjords, Figure 6.1B), which, as reported in Chapter 4, both originated from talus deposits perched on topographic benches. Both landslides can be classified as complex landslides (Varnes, 1978), but molards have allowed me to identify different dynamic component in the failure processes.

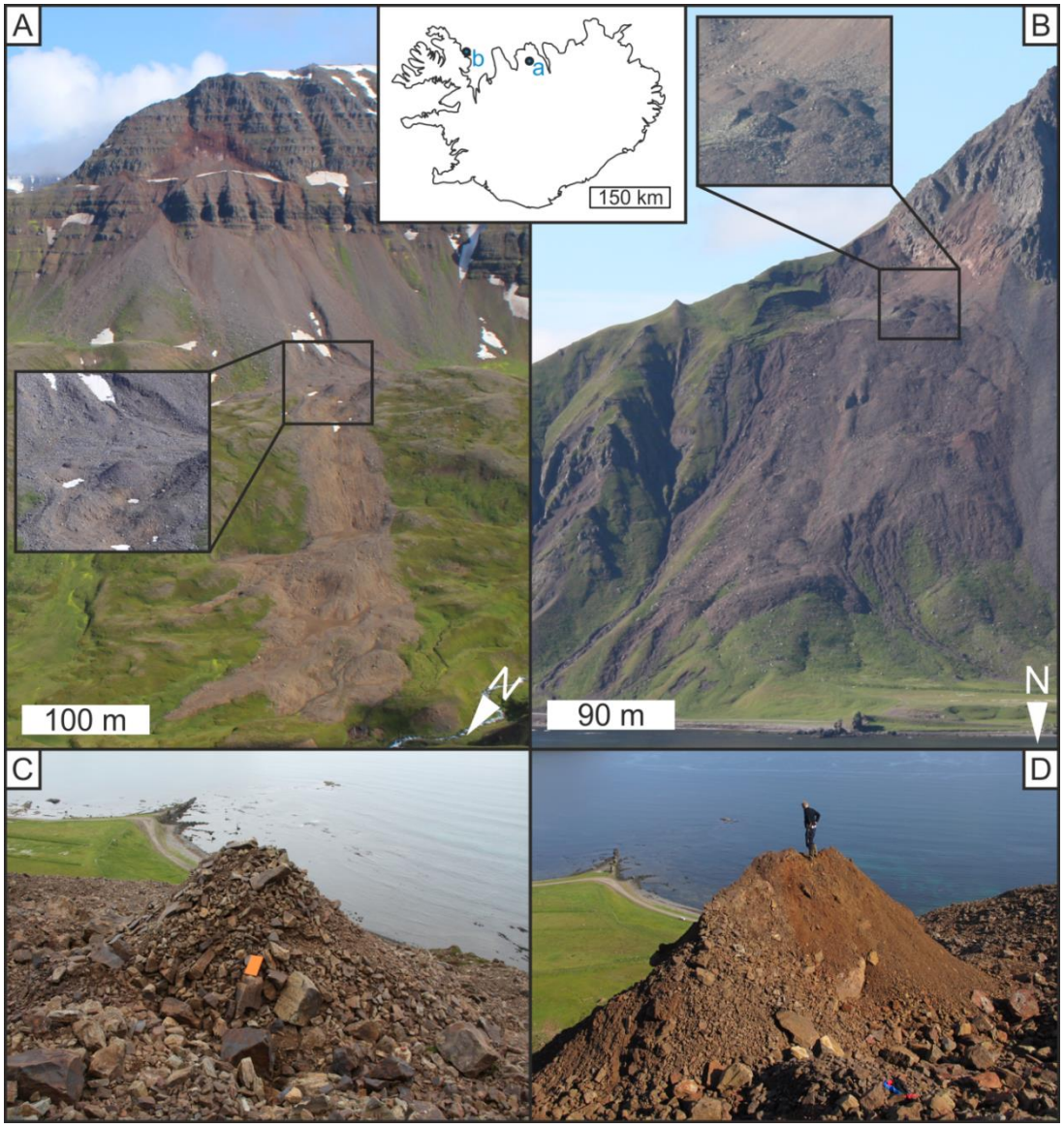

Figure 6.1. The Móafellshyrna and Árnesfjall field sites. (A) The Móafellshyrna landslide photographed in summer 2015, with enlarged frontal view of molards. (B) The Árnesfjall landslide photographed in summer 2016. (C) A molard in Árnesfjall preserving the original stratification of the source material. (D) A molard few days after the occurrence of Árnesfjall landside, preserving abundant fine deposits.

During the field observations performed immediately after the failures, in the Móafellshyrna landslide deposits my supervisor Þ. Sæmundsson and collaborators found isolated pseudo-cubic and angular blocks of ice-rich sediments (Figure 6.2A,E) that came to rest at the foot of the talus slope and on a flat surface 295-390 m below the source area (Figure 6.2A). At Árnesfjall, J. K.

Helgason and collaborators found a spatially dense group of angular, elongated ice-cemented ridges of debris 40-150 m below the top of the main scarp of the landslide (Figure 6.2C), and an isolated block at the toe of the landslide. In both landslides, the blocks and ridges were composed of poorly sorted clast-supported talus deposits. Ground ice was cementing all the material, allowing the blocks and ridges to preserve a cubic or angular shape (Figure 6.2A,C) both during and after the failure. The lithological and grain-size composition of the blocks and ridges of ice-rich sediments were examined. They comprised slightly imbricated mixture of angular boulders, cobbles, and pebbles embedded in sandy silt to silty clay matrix. The colour of the matrix varied from brown to red, and the lithology of the clasts reflected the bedrock of the area (Tertiary Basalt Formation, see Chapter 4), being composed of basalts, rhyolites and weathered tephra layers (Mioc.-Lower Plioc.) (Jóhannesson, 2014).

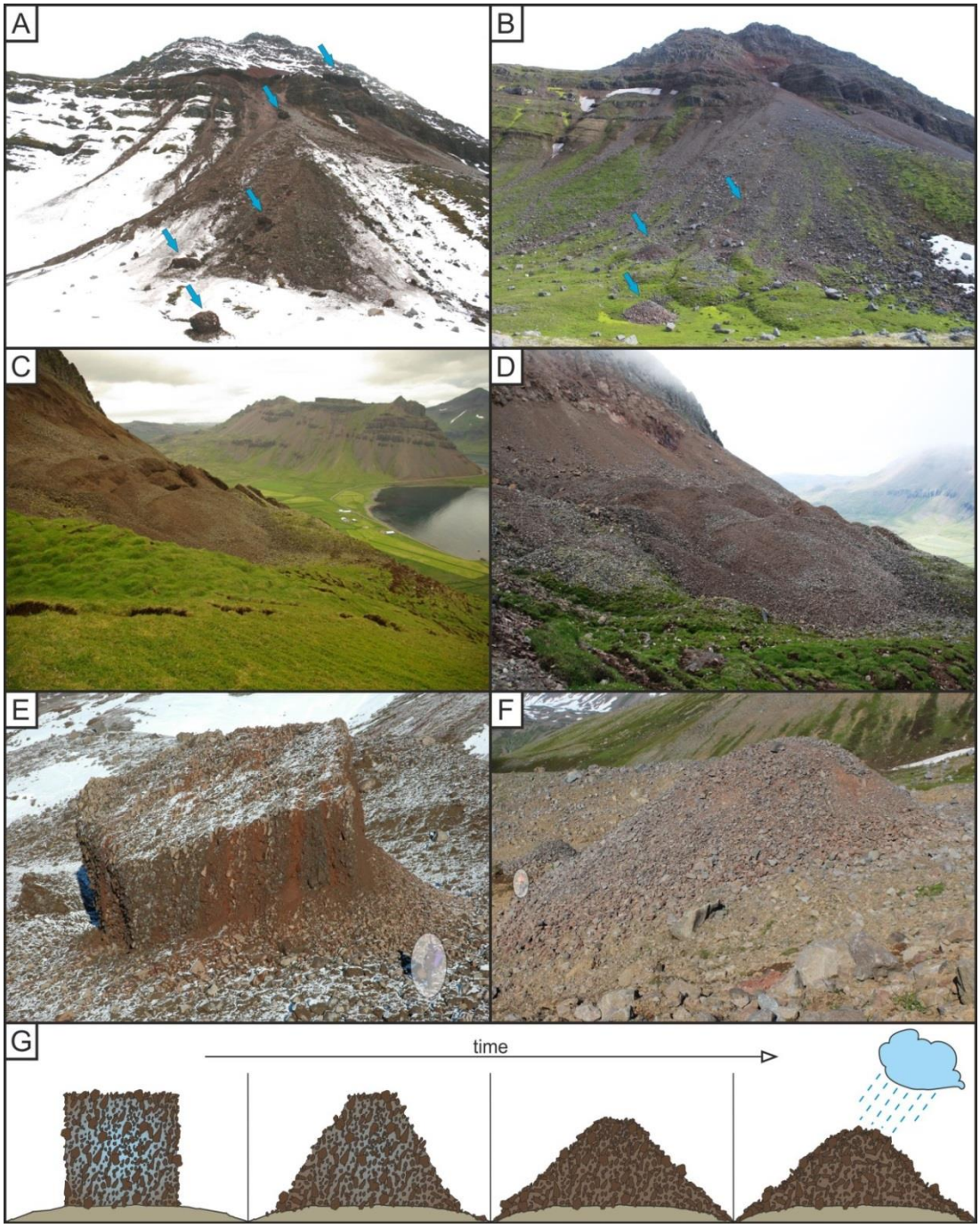

Figure 6.2. The formation of molards. In each pair of images, ice-cemented blocks are on the left; the resulting molards are on the right. (A) Cubic and angular blocks of ice-rich sediments (blue arrows) at the Móafellshyrna site that are perched on the source area and have fallen onto the talus slope below. Photo taken the day after the failure (courtesy of G. Hansson). (B), Same perspective as Figure 6.2A, but three years after the failure, with remnants of the blocks of ice-rich sediments preserved as molards (blue arrows). (C) Angular ridges generated by tilting of ice-cemented talus at the Árnesfjall site. Photo taken two days after the failure (courtesy of V. Benediktsson). (D) Same perspective as Figure 6.2C, but two years after the failure, where remnants of the ice-cemented ridges have degraded into densely-packed, elongated mounds

of debris. € The largest block of ice-rich sediments that fell during the Móafellshyrna event; note different layers of deposits composed of imbricated gravel embedded in brown to red sandy to silty clay. (F) The remnant of the block in Figure 6.2E three years after the failure, preserved as a molard. (G) Schematic evolution of a molard, from the block of clast-supported imbricated deposits cemented by ground ice to the collapsed conical mound of debris, preserving sorted gravel deposits on its surface, with fine deposits being leached out.

I revisited the sites 2 and 3 years after the failures, respectively. In Móafellshyrna, I found conical molards with rounded summits in the place of the original ice-cemented blocks (Figure 6.2B,F). In Árnesfjall, the group of elongate ridges below the main scarp had become smaller (with maximum height up to 3.7 m) molards with the same elongated shape and pointed summits (Figure 6.2D). At both sites, at the surface most molards are clast-supported (by boulders, cobbles and pebbles, Figure 6.1C; Figure 6.3A), with fine material sometimes present, but there are rare cases of molards composed of matrix-supported gravelly sand to silty clay material (Figure 6.1D). However, the surface material does not necessarily reflect the inner composition of molards; I investigated the interior of one molard at each site to find that the deposits are richer in matrix just a few decimetres below the surface (Figure 6.3B). Once the blocks disaggregated into molards, I observed that some of them were still preserving a faint original layering of the source deposits (Figure 6.1C), with imbricated unsorted gravel in sandy silt to silty clay matrix, which is further proof that the deposits must have been ice-cemented during the failure. However, in most of the cases, molards' deposits were non-stratified unsorted gravel to clay material, and I did not observe any radial grain size gradation (Figure 6.3A,B).

Figure 6.3. Material comprising molards. (A) A molard in Móafellshyrna showing coarse deposits on the surface with no gradation. (B) Typical internal granulometry of a molard, composed of unsorted gravel in sandy silt to silty clay matrix.

A schematic evolution of the degradation of an ice-cemented block into a cone of debris has been recently proposed (Milana, 2016), reconstructing their degradation assuming a theoretical initial shape of a sphere. I observed that differently shaped molards are a direct result of the originally differently shaped blocks of ice-cemented material. From a cubic or angular block, the resulting molard has a rounded and symmetrical conical shape (Figure 6.2E-G); alternatively, in the case of ice-cemented elongated ridges, the final molards preserve the elongated shape. In both cases, I have measured that molards can be 30% lower than the initial block, because thaw results in the debris located at the top of the block/ridge collapsing to the base (Figure 6.2G).

I have modelled how to estimate the original size of a block of ice-rich sediments from the resulting molard. Knowing the height (h) and length of the flank (L) of a molard, it is possible to estimate the width (B) – and then the area and volume – of the original block as shown in equation (3) (Figure 6.4):

$$B = 2\sqrt{L^2 - h^2} \quad (3)$$

I have tested this model through field measurements of the size of the largest block of ice-rich sediment. A molard of L=11.9 m and h=10.2 m will result from a block with B=12.2 m, which is the measured length of the biggest block in Móafellshyrna after the failure. So for example, from a cubic and angular block 10.2 to 14.8 m high and with an area from 924.24 to 1002 m^2, the resulting molard would have a rounded and symmetrical conical shape, would stand 10.2 m high maximum and cover an area of 1193 m^2. In the future, this model could give important estimations of the initial ground ice content of the original blocks.

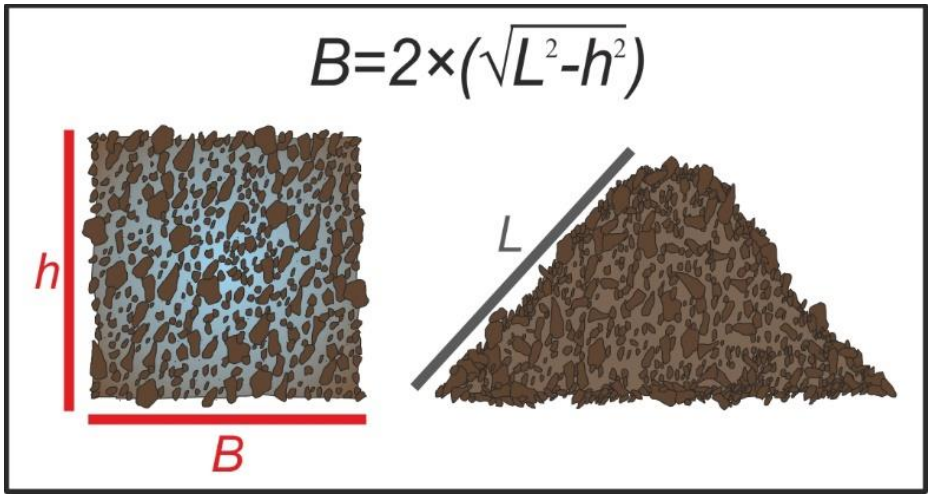

Figure 6.4. Model for estimating the width of the original block of ice-rich sediment (assumed to have a rectangular section) knowing height and length of the flank of the molard, which is assumed to have a triangular section.

.

A similar surface lowering (35%) has been recorded in hummocks of thawing ice-cored moraines in the terminal region of outlet-glaciers in Iceland (Krüger and Kjær, 2000). Hummocks of ice-cored moraines are similar to molards not only in their conical shape, but also in their mode of formation: ice-cored moraines retain massive ice cores and form hummocks when the ice melts (Dyke and Savelle, 2000). Similarly to molards, the form of the hummocks is determined by thaw and gravitational collapse. They can have similar flank slope angles of between 25°

and 35° (Hambrey et al., 1997) or higher. Many meters of ice can be buried under only a few centimetres to meters of till (Schomacker and Kjær, 2008), meaning that the resulting feature can easily disappear when all the ice is melted (Mercer, 1963). The ratio of ice to debris within molards in Móafellshyrna is much lower (15-20% ground ice content; Sæmundsson et al., 2018), giving them a much higher preservation potential. This is why molards remain recognisable even after the ice has gone. I posit that molards should vary in shape and size depending on the slope where they form. In Móafellshyrna, molards rest on a slope of 17 ° and have circular shapes and rounded summits, whereas those in Árnesfjall are on slopes of up to 28° and have elongated shapes and angular summits. I further hypothesise that molards' shape and size should also depend on the granulometry of the source material (more rounded molards are expected for courser granulometry), and on their initial ground ice content (the more ground ice, the lower the final height of the molard). Finally, I infer that the lack of matrix on the surface of the molards is due to the action of precipitation, washing out the fines through the coarse debris by percolation (Figure 6.2G).

6.3.2 Molards distribution and morphology: indicators of landslide dynamics

The morphometry and the spatial distribution of molards in Móafellshyrna and Árnesfjall landslides can provide information about the failure dynamics of the landslides. Molards in Móafellshyrna have different characteristics to those in Árnesfjall, although the average height, basal area and volume of the molards do not differ significantly between the two landslides (see Table 6.1).

Table 6.1 – Two-tailed t-test assuming unequal variances for correlating the morphometric measurements of molards in Moafellshyrna and Arnesfjall landslides, including: volume, area, height, slope of the basal area, slopes of the short and long axes respectively in Moafellshyrna and Arnesfjall, eccentricity, long flanks, and short flanks. df indicates degree of freedom.

Volume

t-Test: Two-Sample Assuming Unequal Variances

	Móafellshyrna	Árnesfjall
Mean	504.3476135	759.0220391
Variance	3142722.376	497282.9869
Observations	17	23
Hypothesized Mean Difference	0	
Df	20	
t Stat	-0.560452687	
P(T<=t) one-tail	0.290697652	
t Critical one-tail	1.724718243	
P(T<=t) two-tail	0.581395303	
t Critical two-tail	2.085963447	

Area

t-Test: Two-Sample Assuming Unequal Variances

	Móafellshyrna	Árnesfjall
Mean	118.5581894	166.2943023
Variance	77895.87538	12952.49165
Observations	17	23
Hypothesized Mean Difference	0	
Df	20	
t Stat	-0.665492706	
P(T<=t) one-tail	0.256668957	
t Critical one-tail	1.724718243	
P(T<=t) two-tail	0.513337914	
t Critical two-tail	2.085963447	

Height

t-Test: Two-Sample Assuming Unequal Variances

	Móafellshyrna	Árnesfjall
Mean	2.021764706	1.937826087
Variance	5.072590441	0.932126877
Observations	17	23
Hypothesized Mean Difference	0	
df	20	
t Stat	0.144183801	
P(T<=t) one-tail	0.443399156	
t Critical one-tail	1.724718243	
P(T<=t) two-tail	0.886798313	
t Critical two-tail	2.085963447	

Eccentricity

t-Test: Two-Sample Assuming Unequal Variances

	Slope short side	Slope long side
Mean	0.535586297	0.737150731
Variance	0.035206619	0.017255267
Observations	17	23
Hypothesized Mean Difference	0	
df	27	
t Stat	-3.794866109	
P(T<=t) one-tail	0.000379784	
t Critical one-tail	1.703288446	
P(T<=t) two-tail	0.000759568	
t Critical two-tail	2.051830516	

Short flanks

t-Test: Two-Sample Assuming Unequal Variances

	Móafellshyrna	Árnesfjall
Mean	3.604113	3.465630957
Variance	9.158176306	5.140505046
Observations	17	23
Hypothesized Mean Difference	0	
df	28	
t Stat	0.158618668	
P(T<=t) one-tail	0.437553922	
t Critical one-tail	1.701130934	
P(T<=t) two-tail	0.875107845	
t Critical two-tail	2.048407142	

Long flanks

t-Test: Two-Sample Assuming Unequal Variances

	Móafellshyrna	Árnesfjall
Mean	6.271242118	9.190356087
Variance	27.68073931	17.02352545
Observations	17	23
Hypothesized Mean Difference	0	
df	29	
t Stat	-1.896795826	
P(T<=t) one-tail	0.03392757	
t Critical one-tail	1.699127027	
P(T<=t) two-tail	0.06785514	
t Critical two-tail	2.045229642	

Slope basal area

t-Test: Two-Sample Assuming Unequal Variances

	Móafellshyrna	Árnesfjall
Mean	17.77304706	26.1175
Variance	23.26567952	25.20092774
Observations	17	23
Hypothesized Mean Difference	0	
df	35	
t Stat	-5.31562627	
P(T<=t) one-tail	3.0843E-06	
t Critical one-tail	1.689572458	
P(T<=t) two-tail	6.16861E-06	
t Critical two-tail	2.030107928	

Slope short-long axes Móafellshyrna

t-Test: Two-Sample Assuming Unequal Variances

	Slope short side	Slope long side
Mean	16.64106294	20.90587059
Variance	40.5219231	41.41413294
Observations	17	17
Hypothesized Mean Difference	0	
df	32	
t Stat	-1.942613405	
P(T<=t) one-tail	0.03045321	
t Critical one-tail	1.693888748	
P(T<=t) two-tail	0.060906419	
t Critical two-tail	2.036933343	

Slope short-long axes Árnesfjall

t-Test: Two-Sample Assuming Unequal Variances

	Slope short side	Slope long side
Mean	33.47453478	27.29548261
Variance	30.05328937	33.25067893
Observations	23	23
Hypothesized Mean Difference	0	
df	44	
t Stat	3.724520017	
P(T<=t) one-tail	0.000276948	
t Critical one-tail	1.680229977	
P(T<=t) two-tail	0.000553896	
t Critical two-tail	2.015367574	

For instance, the Móafellshyrna molards have a larger range in volume (Figure 6.6E). Also, the slope angles of the short and long flanks of molards are roughly equal in Móafellshyrna (Figure 6.6E), while the downslope faces of the Árnesfjall molards are longer and less steep than the scarp-facing short flanks (see Table 6.2, Figure 6.6E). The Árnesfjall molards are consistently elliptical in shape (Figure 6.6E), whereas molards in Móafellshyrna are variable, but generally

closer to circular (Figure 6.6E). Finally, while Móafellshyrna molards do not show a preferential orientation in their long axes with respect to the landslide's runout-direction (Figure 6.6B), the long axes of the molards in Árnesfjall are oriented roughly perpendicular to the landslide's runout direction, and parallel to the main scarp (Figure 6.6D).

Table 6.2 - Morphometric measurements of molards in Móafellshyrna and Árnesfjall, including: height, length of long and short axes, area, volume, slope of the basal area, slope of the short and long flanks, eccentricity, and length of the short and long flanks. Mean, standard deviation and dispersion parameter are reported for every measurement. Pearson correlation coefficient is reported for the correlation of height, long and short axes.

Móafellshyrna

ID	Height (m)	Long axis (m)	Short axis (m)	Area (m^2)	Volume (m^3)	Slope basal area (°)	Short flank slope (°)	Long flank slope (°)	Eccentricity	Short flank lenght (m)	Long flank lenght (m)
MM01	2.20	12.16	9.55	96.51	244.18	26.55	12.72	31.41	0.62	5.11	7.66
MM02	2.25	11.85	7.69	73.62	193.52	27.15	23.01	28.67	0.76	4.13	7.33
MM03	2.65	18.23	7.22	101.71	270.77	24.62	15.30	27.23	0.92	10.23	8.05
MM04	0.41	3.70	3.14	8.77	4.00	18.00	16.36	16.85	0.53	1.69	2.03
MM05	0.34	4.84	3.75	14.21	4.09	13.50	16.56	12.69	0.63	1.71	2.05
MM06	1.80	8.82	8.41	64.84	41.83	14.90	14.69	14.10	0.30	2.51	7.17
MM07	1.50	8.50	7.78	55.37	17.70	11.07	30.07	11.44	0.40	3.76	4.46
MM08	10.20	39.48	37.90	1193.23	7375.36	16.36	26.45	30.34	0.28	11.96	24.70
MM09	0.58	3.87	3.14	9.34	4.09	14.28	6.56	17.10	0.59	1.65	1.54
MM10	2.15	7.69	7.32	43.03	26.45	20.49	21.71	25.78	0.31	2.44	4.50
MM11	2.15	7.60	6.79	40.74	45.97	20.00	12.15	22.95	0.45	2.08	5.17
MM12	2.25	10.37	9.49	82.32	132.03	21.23	17.22	26.24	0.40	2.29	7.31
MM13	1.98	9.29	8.11	55.61	44.41	15.80	18.28	21.86	0.49	1.80	6.34
MM14	1.95	12.88	11.56	119.60	128.33	15.39	18.26	14.30	0.44	3.99	7.97
MM15	0.80	4.87	4.39	15.45	7.00	12.84	4.73	16.32	0.44	1.33	3.60
MM16	0.92	7.08	4.47	22.05	21.21	14.35	16.04	19.02	0.78	2.81	4.50
MM17	0.24	6.99	4.45	19.07	12.99	15.58	12.79	19.10	0.77	1.78	2.25
Mean	2.02	10.48	8.54	118.56	504.35	17.77	16.64	20.91	0.54	3.60	6.27
Standard deviation	2.25	8.34	7.95	279.10	1772.77	4.82	6.37	6.44	0.19	2.94	5.10
Dispersion parameter	1.11	0.80	0.93	2.35	3.51	4.82	6.37	6.44	0.19	0.81	0.81

Correlation (Pearson's R)					
Height - Long axis	0.96	Short - Long axis	0.95	Height - Short axis	0.98

Árnesfjall

ID	Height (m)	Long axis (m)	Short axis (m)	Area (m^2)	Volume (m^3)	Slope basal area (°)	Short flank slope (°)	Long flank slope (°)	Eccentricity	Short flank lenght (m)	Long flank lenght (m)
AM01	1.25	7.53	6.11	34.19	48.60	25.81	31.80	25.89	0.58	1.65	4.04
AM02	1.16	19.72	11.88	203.21	1228.68	30.23	37.61	33.29	0.80	1.95	17.67
AM03	2.55	21.63	19.66	359.32	2124.89	32.23	37.54	35.76	0.42	3.88	16.60
AM04	1.15	19.31	17.59	262.36	1409.54	32.37	37.62	33.11	0.41	2.51	14.66
AM05	3.30	27.44	18.74	405.17	2302.63	26.86	37.27	29.32	0.73	2.35	15.46
AM06	1.19	16.87	9.78	118.93	656.66	35.99	35.66	21.26	0.81	4.31	2.16
AM07	1.45	18.97	10.17	148.61	948.44	31.26	34.39	25.78	0.84	3.15	7.36
AM08	3.25	24.64	20.36	388.06	2274.11	29.76	38.64	33.30	0.56	6.38	13.04
AM09	2.25	16.58	8.92	121.41	551.56	24.87	38.72	29.54	0.84	1.89	7.18
AM10	1.95	22.50	12.29	211.09	814.22	25.08	36.39	24.90	0.84	5.74	5.37
AM11	3.70	18.63	11.75	163.63	568.26	22.34	38.46	31.57	0.78	4.95	9.62
AM12	3.30	25.21	14.61	271.34	1023.36	23.11	39.27	34.72	0.81	10.54	7.90
AM13	1.35	14.29	6.89	84.36	273.45	24.88	26.61	22.92	0.88	2.46	11.53
AM14	3.50	23.92	14.09	268.31	1009.44	20.22	35.57	27.02	0.81	5.59	9.15
AM15	2.15	16.22	12.12	170.25	361.54	15.29	27.23	23.69	0.66	6.43	8.65
AM16	3.10	16.43	11.04	161.36	710.89	19.61	29.16	24.30	0.74	2.07	10.00
AM17	1.30	12.85	8.30	90.66	177.35	21.52	21.76	16.97	0.76	1.55	6.99
AM18	1.15	16.18	10.42	127.37	455.86	20.55	32.37	30.78	0.76	1.17	10.00
AM19	1.30	10.50	5.68	47.09	41.77	23.90	35.46	27.97	0.84	1.11	5.01
AM20	1.35	10.09	6.78	49.30	54.39	25.12	19.22	11.93	0.74	3.00	4.28
AM21	1.18	10.95	6.91	59.32	176.89	29.61	30.38	30.11	0.78	2.88	9.58
AM22	0.65	10.62	5.11	42.38	119.00	29.61	33.85	30.01	0.88	2.75	9.14
AM23	1.04	8.54	6.36	37.05	125.99	30.48	34.93	23.66	0.67	1.42	5.99
Mean	1.94	16.94	11.11	166.29	759.02	26.12	33.47	27.30	0.74	3.47	9.19
Standard deviation	0.97	5.68	4.61	113.81	705.18	5.02	5.48	5.77	0.13	2.22	4.04
Dispersion parameter	0.50	0.34	0.41	0.68	0.93	5.02	5.48	5.77	0.13	0.64	0.44

Correlation (Pearson's R)

Height - Long axes	0.72	Short - Long axis	0.87	Height - Short axis	0.64

In Móafellshyrna, the molards are clustered in an area with a mean slope of 17° at the foot of, or beyond, the talus slope located below the topographic bench (Figure 6.6A). Their position matches that expected for rock falls, where competent fragments detach and fall, and come to rest either within, at the foot, or beyond the base of the talus slope (Evans and Hungr, 1993; Varnes, 1978). The large size variation of molards in Móafellshyrna mirrors that in rock fall (Figure 6.6E), where their power-law frequency–volume distribution (see Figure 6.5) is related to rock fragmentation (Einstein, 1937). Their final position on a low slope allowed the blocks to degrade into isolated cones with a circular base, radially symmetrical flank slopes (see Figure 6.6E; see Table 6.2), and no preferential orientation.

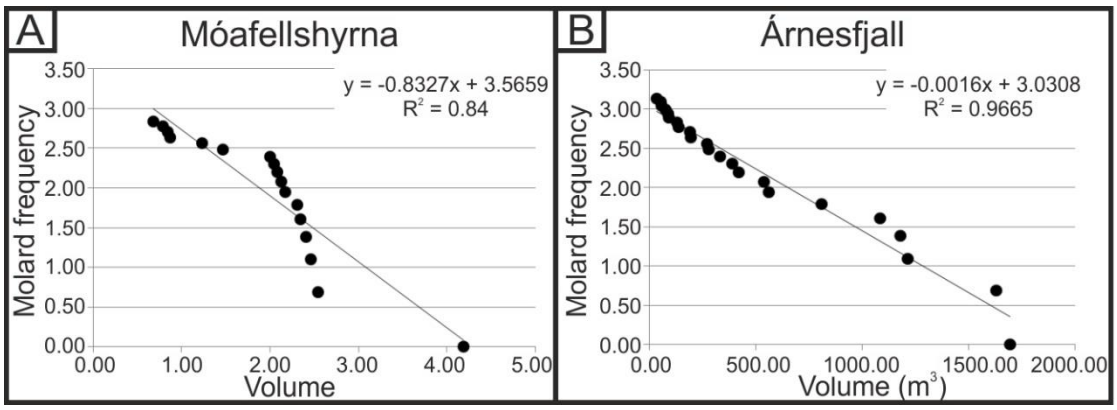

Figure 6.5. Volume-frequency distribution of molards. (A) Volume-frequency distribution (bi-logarithmic distribution) for the molards of Móafellshyrna, showing a power-law distribution. (B) Volume-frequency distribution for the molards of Árnesfjall (log-linear distribution), showing an exponential distribution.

Molards in Árnesfjall lie on an average slope of 26° and are concentrated less than 30 m below the base of the failure scarp (Figure 6.6C). This position is typical of the location of *en echelon* concave-upward rupture surfaces in debris slides. These ruptures are oriented perpendicular to the flow direction, and blocks of material often move downward with little internal deformation (Varnes, 1978).

Molards in Árnesfjall derive from the degradation of densely packed, elongated ridges exposed by the rotational-sliding motion of the source material, cut by several curved planes of movement. These dynamics are reflected in their more homogeneous size (see Table 6.1) and their elliptical shape (Figure 6.6E), a result of the degradation of elongated cusps of ice-cemented precursor units produced by relatively coherent rotational sliding. This process can be deduced by the orientation of the mounds' long axes, perpendicular to the main movement downslope (Figure 6.6D). Furthermore, the steep upslope-facing short flanks of these molards (Figure 6.2C,D; Figure 6.6E) reflects a common behaviour of rotational slides, where the upper part of the units produced by curved rupture surfaces tilt backwards toward the scarp.

By measuring the size, morphology and distribution of molards, I have been able to discriminate between the processes of simple gravitational fall and of rotational sliding. I recognise that other types of motion might also transport ice-cemented materials, forming molards with morphometry and distribution different to those described here. For example, molards with a wide-range of dimensions scattered across the mobilised mass could be expected in rock/debris avalanches, due to their extremely rapid flow-like motion (Hungr et al., 2001), while molards accumulated in the terminal lobe could result from debris flows, due to their tendency of producing longitudinal sorting near the front of the surge (Iverson, 1997).

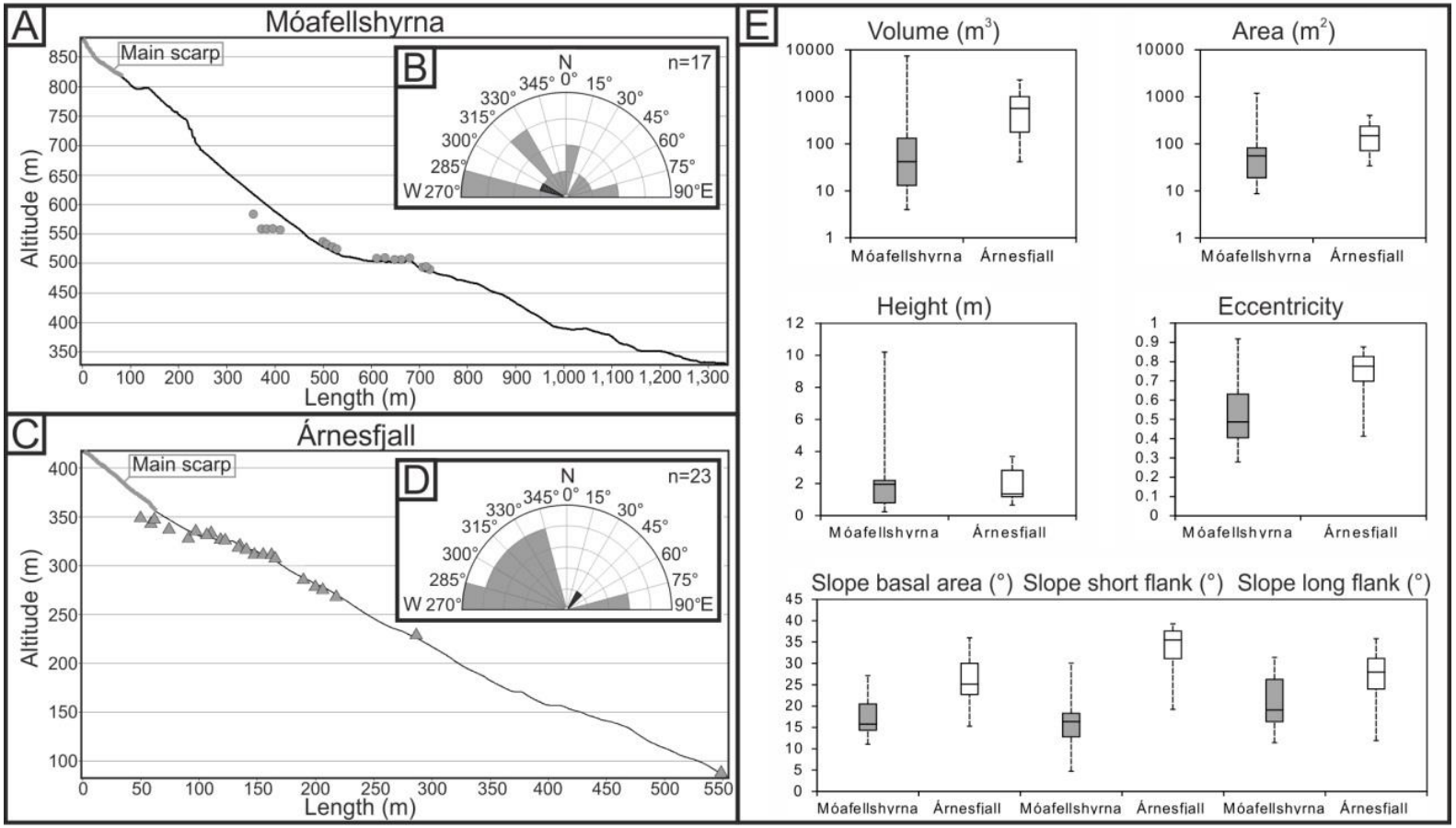

Figure 6.6. Dimensions and distribution of molards. (A) The topographic profile of the Móafellshyrna landslide, with the position of molards marked as grey points, and the main scarp zone marked with a grey line. (B) Rose diagram of the orientation of molards' long axes where the orientation of the Móafellshyrna landslide is marked as a hatched texture. (C) The topographic profile of the Árnesfjall landslide, with the position of molards marked as grey triangles, and the main scarp zone marked with a grey line. (D) Rose diagram of the orientation of molards' long axes where the orientation of the Árnesfjall landslide is marked as a hatched texture. (E) Boxplots of the volume, area, height, slope of the basal area, slope of the short and long flanks, and eccentricity of the molards in Móafellshyrna and Árnesfjall; note that the vertical axis for volume and area use a logarithmic scale. The whiskers indicate the maximum and minimum values, the boxes mark the interquartile range, and the black lines are the medians of each population. For all the measurements, in Móafellshyrna n=17, in Árnesfjall n=23.

6.3.3 Molards in remote sensing data

Identifying molards reliably is crucial if they are to give insights into the geomorphological and climatic condition of the landscape where they form. Conical mounds can be generated by many processes, but molards are always associated with a landslide. They could, however, perhaps be confused with hummocky terrains found in rock avalanche deposits. Hummocks can be used to determine the kinematics of a landslide (Shea and van Wyk de Vries, 2008), but they have the following characteristics that distinguish them from molards: (i) they usually decrease in size with runout distance (Yoshida et al., 2012) and towards the margins of the flow (Clavero et al., 2002), unlike molards, which have a heavy-tailed size distribution if generated by falling, or more homogeneous sizes if generated by sliding, (ii) hummocks in rock and debris avalanches can have volumes of up to 10^6 m^3 (Clavero et al., 2002), while molards in Iceland have volumes of thousands of cubic meters at most, and (iii) hummocks tend to have their long axes parallel or orthogonal to the direction of the mass movement (Clavero et al., 2002; Yoshida, 2014), while I have demonstrated that molards are expected to have axes with no preferential orientation with respect to the flow if produced by fall. Hence, in addition to molards being readily identifiable in the field, I propose that in most cases they can also be reliably identified in remote sensing data, although in some areas field studies would be needed to confirm the identification.

In Figure 6.7, I show a plan view image of molards in Móafellshyrna landslide (Figure 6.7A,B), a location with putative molards elsewhere on Earth (Figure 6.7C,D), and possible candidates on Mars (Figure 6.7E,F). In Figure 6.6D, cone-shaped landforms of ~1-46 meters-diameter are scattered across the surface of

deposits mobilised by a rock avalanche (Pedersen et al., 2002) in Greenland. The failure falls within a region where continuous permafrost has been reported (Van Tatenhove and Olesen, 1994); hence, I infer that these conical mounds are molards, but *in situ* investigation would be needed to test this hypothesis. Landslides have been active in this area since at least 1985 (Benjamin, 2014), and cones of debris were reported to be present in 2000 (Pedersen et al., 2002), so there is the potential that these cones are indicative of permafrost degradation in this area. Furthermore, many more putative molards are seen here than in my Icelandic examples, suggesting that more molards could be produced in areas with more pervasive ground-ice content.

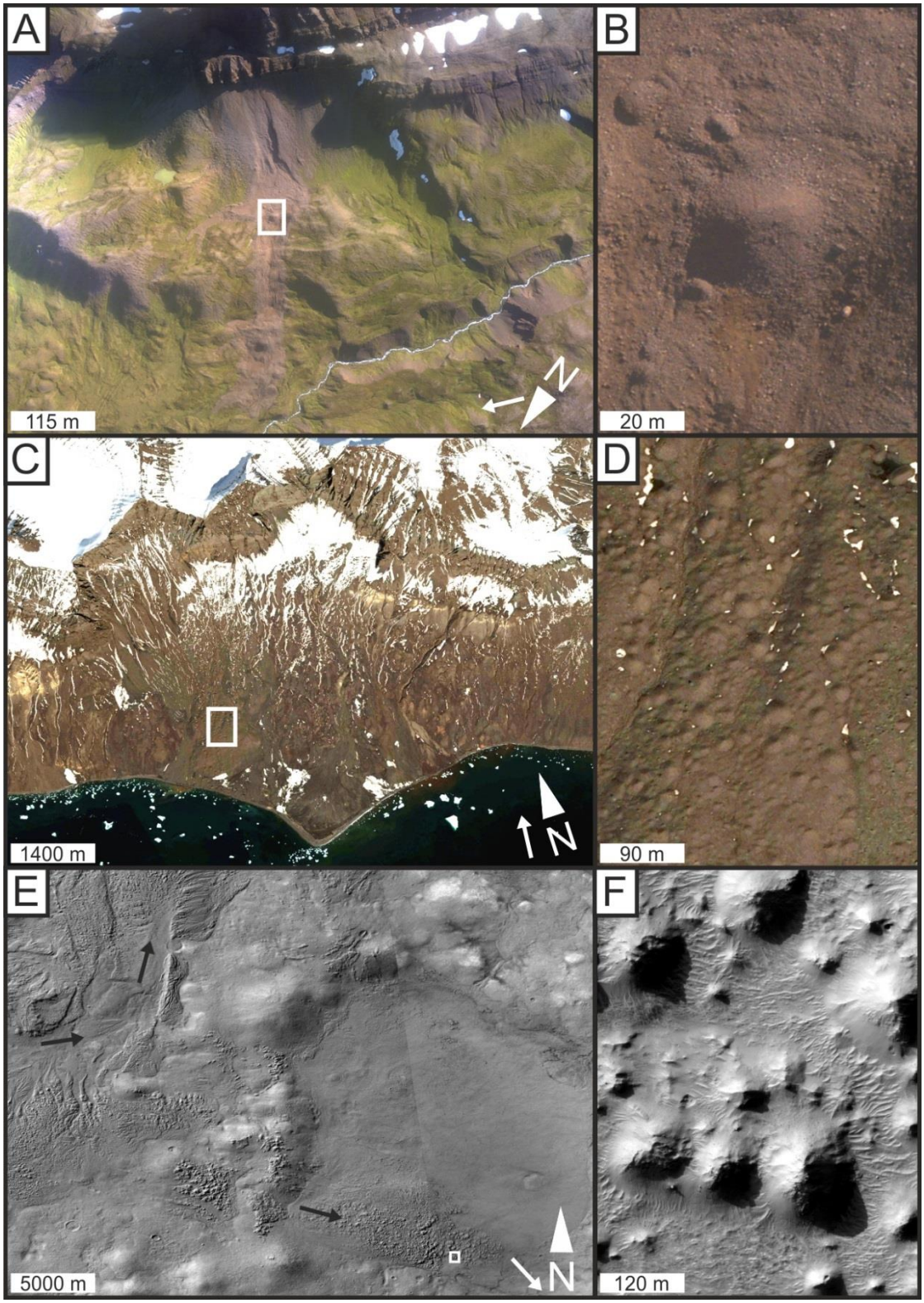

Figure 6.7. Molards from remote sensing. (A) Aerial image of Móafellshyrna landslide, with the extent of Figure 6.6B outlined by the white box. (B) Molards in Móafellshyrna landslide. (C) Aerial image of a rock avalanche on the south coast of Nuussuaq, west coast of Greenland (image from Google Earth) with the extent of Figure 6.6D outlined by the white box. (D) Putative molards in Nuussuaq (image from Google Earth). (E) Impact ejecta flow deposits from Hale Crater on Mars, (Context Camera images

G14_023858_1429 and G19_025704_1431, credit NASA/JPL-Caltech/MSSS), with black arrows indicating the inferred flow directions. (F) Conical landforms in the ejecta blanket of Hale Crater on Mars (High-resolution Imaging Science Experiment image ESP_052222_1425, credit NASA/JPL/University of Arizona). White arrows indicate lighting direction.

Similar scattered conical landforms are identifiable within impact ejecta originating from Hale Crater on Mars (Figure 6.7E,F). The ice-rich nature of the impact ejecta has already been proposed based on other landforms (Jones et al., 2011). I propose that conical landforms within the ejecta flow are molards, which with further study could yield important constraints on the ice-content of the original ejecta flow and insights into recent modification of ground ice reservoirs on Mars.

6.4 Discussion and Conclusions

Iceland has discontinuous permafrost (Brown et al., 1997; Rekacewicz, 2005), which in general is spatially and temporally heterogeneous (Rödder and Kneisel, 2012), and mountain permafrost has been modelled at elevations above 800-900 m a.s.l. in the central-northern regions of the island (Etzelmüller et al., 2007). This predicted permafrost distribution has been ground-truthed by comparison with the distribution of active rock glaciers and ice-cored moraines in the Tröllaskagi peninsula (Farbrot et al., 2007a; Lilleøren et al., 2013).

The Móafellshyrna landslide falls within the predicted spatial zone and altitude band for mountain permafrost. In contrast, the Árnesfjall landslide occurred on the coastline of the Westfjords, 400 m below the predicted permafrost altitude in this area. Hence, the presence of molards here is the only unequivocal and pragmatically detectable indicator of permafrost conditions. Both landslides

originated from talus material. In general, coarse blocky talus material is a particularly favourable substrate for ice-rich permafrost (Etzelmüller et al., 2001; Harris and Pedersen, 1998). In talus slopes, ground ice can be formed by burial of snow by mass wasting debris, which protects the snow from ablation (Gruber and Hoelzle, 2008), and can lead to the development of ice-rich permafrost (Kenner et al., 2017). Annual freeze-thaw cycles in talus slopes in mountain permafrost environments can reach depths of ~3-7 m, but rarely decametres (Matsuoka et al., 1998). The ice-cemented blocks that detached in the Móafellshyrna landslide were 15-20 m thick, much larger than the expected maximum depths of annually-formed, ice-cemented ground. Hence, it is very likely that the source talus slopes were perennially-frozen ground and that the molards indicate permafrost degradation.

Molards reported in landslides have all involved terrains that are known to be affected by discontinuous permafrost (Brideau et al., 2009; Cruden, 1982; Lyle et al., 2014). In one case, the deposits of an active rock glacier were the source material for the landslide with molards (Milana, 2016). As I have shown that molards evolve from parent blocks of ice-rich sediments, to the light of this study previously reported molards provide new information: they are an indicator (perhaps the only indicator) of ongoing or past permafrost degradation. Furthermore, in Móafellshyrna molards are the first direct indication of ongoing permafrost degradation in this region of Iceland, in an area already thought to host only mountain permafrost (Etzelmüller et al., 2007; Farbrot et al., 2007a; Lilleøren et al., 2013). In Árnesfjall, molards mark both the presence of permafrost in an area thought to have no perennially frozen ground and its recent/ongoing degradation.

My new recognition that molards provide a way to track permafrost degradation is important, as similar indicator-landforms (such as retrogressive-thaw slumps (Ashastina et al., 2017), thermokarst lakes (Yoshikawa and Hinzman, 2003), baydjarakhs (Séjourné et al., 2015)) are scarce, and generally occur only in zones of continuous permafrost. Other indicators of permafrost, such as active rock glaciers, ice-cored moraines, composite ridges, ice-wedges, or palsas, need long-term monitoring of air/ground temperature to detect the state of permafrost, whereas molards directly reveal permafrost degradation. I propose that future studies can use molards with the purpose of mapping historic-permafrost conditions and geographically tracking past climate change.

By studying how the deposits of two landslides in northern Iceland evolved through time, I have shown for the first time that molards form in periglacial environments from the degradation of blocks and ridges of ice-cemented deposits into conical mounds of debris. Molards have distinctive spatial and geomorphic characteristics that reveal the dynamics of the landslides that formed them. Isolated molards indicate transport via fall, while densely-grouped elongated molards below the main scarp are generated by sliding. In this paper, I distinguish two different dynamic styles using molards, but future study is required to determine if molard characteristics could reveal other types of landslide motion. The relation between permafrost degradation and slope stability is well documented in the literature, but, in the light of my study, further efforts should be engaged in defining how molards can be used in risk mitigation. The types of landslide from which molards form are likely to become more common as ground temperatures in ice-rich permafrost zones increase, making thaw and slope instabilities in periglacial environments more probable. Furthermore, given that the presence of ice enables long runout and high velocity in mass movements

(Huggel et al., 2005), molards could be used to detect areas at risk of potentially disastrous ground ice thaw-induced landslides.

I have demonstrated that molards are a landform that can be readily recognised in the field as a marker of recent and ongoing permafrost degradation. I found few molards in Iceland compared to studies of molards in permafrost-rich terrains, hence the number-density of molards at a site may reveal the abundance of ground ice at the time of the failure. One of my study sites in northern Iceland is a region where mountain permafrost has not been modelled, and until my study there was no direct field evidence to prove its presence and/or condition. The recent formation of molards reveals the presence of permafrost in the area, and its ongoing degradation.

Finally, I have demonstrated that molards are not only readily recognisable in the field, but also via remote sensing. This opens up the possibility of efficiently identifying these landforms across large and remote areas, revealing the influence of ice thaw not only in mountain permafrost environments, but also on planetary surfaces such as Mars, where the role of volatiles in landscape evolution is vigorously debated.

The discovery of the formation of molards and of their role as cipher key in reading the periglacial landscape to understand permafrost degradation and landslide dynamics accomplish one of the aims of this thesis: to understand what is the morphological inheritance of landslides occurring in degrading ground-ice terrains, and to use this inheritance to decipher permafrost degradation and failure dynamics.

Chapter 7. Synthesis and conclusions

7.1 How do debris flows and landslides affect the Icelandic landscape?

The research contained in this thesis has shown that rapid mass movements can influence landscape evolution in Iceland, and has addressed some of the main problems that have been highlighted in previous studies concerning the triggers, the sediment supply and transfer of slope failures. Weathered and fractured volcanic bedrock, steep slopes mantled by loose deposits, changing climate conditions and earthquake activity have been identified as the main factors that lead to the initiation of landslides in Iceland (Sæmundsson et al., 2003; Sigurđsson and Williams, 1991). Many debris flows in Iceland are released because of rapid snowmelt (Decaulne and Sæmundsson, 2006), and have a high frequency (Decaulne et al., 2005). These studies highlighted the need to define the threshold values of the different parameters necessary to trigger mass movements, such as atmospheric temperature increase, accumulated precipitation, or sediment accumulation, in order to efficiently predict landslides and debris-flows. A further knowledge gap was identified by Glade (2005), who advised that since hazard scenarios are dependent on sediment availability, debris-flow hazard assessment in Iceland and other locations should rely on geomorphic analysis. Bell and Glade (2004) reported that in the Westfjords of Iceland debris flows and rock falls pose a high risk to the local communities. They suggest that future research should determine the sediment supply rate from the source areas to the slopes, which is crucial when quantifying the risk that these processes can pose. I have quantified the material mobilised and the potential for

new sediment supply in different sections of debris flows affecting the town of Ísafjörður in the Westfjords (Chapter 3), and by two landslides in the Westfjords and in the Tröllaskagi peninsula (Chapter 4). This has allowed me to identify and characterise different failure mechanisms that are geomorphically distinct and that have affected the slopes of Iceland by mobilising large quantities of debris. I have recognised that in Iceland mass wasting phenomena are extremely prone to activation and re-activation, and occur through a range of processes that leave distinctive spatial geomorphic characteristics. Some of these processes result from heavy and intense precipitation, seismic activity and permafrost degradation, the magnitude of which I have estimated (Chapter 5). These different factors can cause an acute geomorphic response of the Icelandic landscape, resulting in a major mobilization of sediment by rapid mass movements.

These new findings on the rapid mass movements in Iceland can be extended to other contexts worldwide, as my geomorphic analysis have permitted to detect, quantify and characterise debris accumulated at high gradients and debris transfer in complex landslides, without the assistance of any other monitoring system, and could be easily applied to other similar failures around the globe. The novel discovery that permafrost is degrading in Iceland and causing gravitational movements is a further evidence that we do not know enough about permafrost degradation in discontinuous mountain permafrost environments and the consequent hazard that could derive. This highlight the importance that future studies should focus on the field evidence of permafrost degradation, and how to link them to the regional extension of permafrost and its degrading state.

7.2 Is permafrost degrading in Iceland?

The findings of my thesis feed into and complement the findings of the last 40 years of research into permafrost in Iceland. Harris (1981) and Priesnitz and Schunke (1978) were the first to highlight that permafrost is present with different continuity of coverage in Iceland, and confined the permafrost distribution in Iceland to the central highlands. The same areas in central Iceland fall within the zones of sporadic permafrost in the official International Permafrost Association (IPA) map (Brown et al., 1997). Etzelmüller et al. (2007) modelled the overall extent of permafrost in Iceland, identifying that its lower limit decreases from southeast to north, and it is limited to above 800 m a.s.l in the north and east, and above 1000 m in the south. The authors found that permafrost covers around 15% of the total land area of Iceland, and is probably degrading. Farbrot et al. (2007a, 2007b) and Lilleøren et al. (2013) outlined the distribution of permafrost at regional scale in north and eastern Iceland, recognising active permafrost landforms to determine the widespread occurrence of mountain permafrost above 800-900 m a.s.l., with above 400 m a.s.l. in the northernmost zones of the country. An ongoing degradation of permafrost on the island was suggested by Kneisel et al. (2007), who detected shallow and heterogeneous distribution patterns of permafrost in different sites in the highlands of central Iceland, and acknowledged its sensitiveness to climate change. This was locally confirmed by Saemundsson et al. (2012), who recorded a deterioration of permafrost landforms such as palsas and a thickening of the active layer.

Despite the exceptional progress achieved in understanding the distribution and state of permafrost in Iceland, unexpected events have proved that we are still far from having obtained conclusive findings. I have reported on two different

landslides that occurred in northern Iceland where ground ice was found in the landslide deposits immediately after their occurrence (Chapter 4). These two rapid mass movements resulted in changes in permafrost on the landscape that has never been reported before in Iceland. The Móafellshyrna landslide is located in an area where permafrost is expected by the model of Etzelmüller et al. (2007). In contrast, the Árnesfjall landslide occurred on the coastline in an area where permafrost had not been modelled, and at a lower altitude than the predicted permafrost elevation. I demonstrated that both landslides originated from talus material, a particularly favourable substrate for ice-rich permafrost (Harris and Pedersen, 1998). Both landslides mobilised material at a depth that exceeds the expected maximum depths of annually-formed, ice-cemented ground (Matsuoka et al., 1998). Hence, it is very likely that the source talus slopes were perennially-frozen ground. The occurrence of this type of landslide in a short period of time after an increase of the mean annual air temperatures in Iceland is a further indication that permafrost degradation is one of the foremost causes for the release of these unusual rapid mass movements. The Móafellshyrna and Árnesfjall landslides are unexpected events that show that similar events might occur not only in Iceland, but also in similar mountain permafrost environments, where unstable loose ice-cemented deposits could fail due to ground-ice degradation with increasing atmospheric temperatures.

After that my supervisors and I disseminated our observations and results regarding the Móafellshyrna and Árnesfjall landslides, we received the news that blocks of ice-rich sediments similar to those ones that we observed have been photographed on a landslide that occurred in eastern Iceland in April 1947 (see Figure 7.1.). This opens the possibility for future research on other past Icelandic

landslides triggered by ground-ice thaw, as they could give us important information of the distribution and state of permafrost in the past decades.

Figure 7.1. A block of ice-rich sediments on the deposits of a landslide occurred in spring 1947 on the south-west facing slope of the Hoffell mountain in eastern Iceland. Note the path ploughed in the snow by the block (courtesy of R. Þorvaldsson).

My study is at a local scale, so the conclusions drawn in this thesis cannot be extrapolated to reflect the conditions of permafrost in the whole country. However, if indications of permafrost degradation are locally present in different areas of Iceland, it is reasonable that the same state of degradation can be expected in other regions of Iceland. In Iceland, long-term standard air and ground-surface and subsurface temperature measurements should be implemented and validated with extensive topographic and geophysical monitoring, in order to successfully predict the evolution of ground temperature in a changing climate and analyse its potential impact. Since the periglacial environments in Iceland are predicted to react rapidly to changes of the environmental boundary

conditions (Kneisel et al., 2007), monitoring the effects of variations in permafrost on sediment stability and transport should be of primary importance, as these could have serious destructive consequences on Icelandic landscape and society.

7.3 Is there a geomorphological marker for permafrost degradation?

Landforms related to permafrost can be associated with its aggradation — permafrost growth — or its degradation — permafrost thaw. Surface features related to permafrost aggradation such as thermal-contraction-crack polygons, palsas or rock glaciers have been studied in Iceland and worldwide to monitor the extension and state of permafrost (Emmert and Kneisel, 2017; Haeberli et al., 2006; Hubbard et al., 2013; Kneisel et al., 2007; Sæmundsson et al., 2012), as modifications in their morphometric characteristics can reveal changing conditions of permafrost. Monitoring techniques such as air/ground thermal monitoring or repeat geophysical surveys, even if very effective, can however be logistically difficult and require a long-term approach (Hachem et al., 2009; Hilbich et al., 2008). Landforms associated with permafrost degradation, such as retrogressive-thaw-slumps and mass movements, indicate ongoing permafrost degradation wherever the state of permafrost is well known, which again requires a long-term record of thermal, geothermal and geophysical monitoring and modelling. However, the link between these landforms and the presence and/or degradation of permafrost is difficult to ascertain wherever these datasets are not available and the distribution and conditions of permafrost are not clearly constrained, such as places at the border between discontinuous and patchy

permafrost. By studying landslides affecting permafrost terrains in northern Iceland, I have found that molards are landforms that can be used as a marker of permafrost degradation (Chapter 6). Molards are cones of debris that are found in landslide deposits and that form from the degradation of ice-cemented blocks involved in the development of landslides in periglacial environments. In the Móafellshyrna landslide, which falls in an area of Iceland where permafrost is expected (Etzelmüller et al., 2007; Farbrot et al., 2007a; Lilleøren et al., 2013), molards are the first direct indication of ongoing permafrost degradation. In the Árnesfjall landslide, located in a region where mountain permafrost has not been expected from model results (Etzelmüller et al., 2007; Rekacewicz, 2005), molards are the only evidence to prove permafrost presence and its degrading condition. As opposed to other landforms associated with permafrost, I have shown that molards can directly reveal recent or ongoing permafrost degradation using field observations or remote sensing.

Using molards as an indicator of permafrost degradation is not only possible in Iceland. The fact that molards are readily recognisable in the field and using remote sensing opens up the possibility of identifying these landforms in other remote areas. I have shown that candidate molards are also observable within impact ejecta originating from Hale Crater on Mars. In Chapter 6, I have reported an example of cone-shaped landforms lying on the deposits of a rock avalanche in the western coasts of Greenland. With further study, molards could reveal the influence of ice thaw in permafrost environments, and clarify the role of volatiles in landscape evolution of Mars and other planets. These are only two examples, but similar conical features are also identifiable in other regions of the globe, such on the accumulation zone of a landslide in eastern Kashmir (Figure 7.2). As for

the case in Greenland, here a great number of debris cones seem to be scattered on the landslide deposits, compared to the few molards that I found in Iceland.

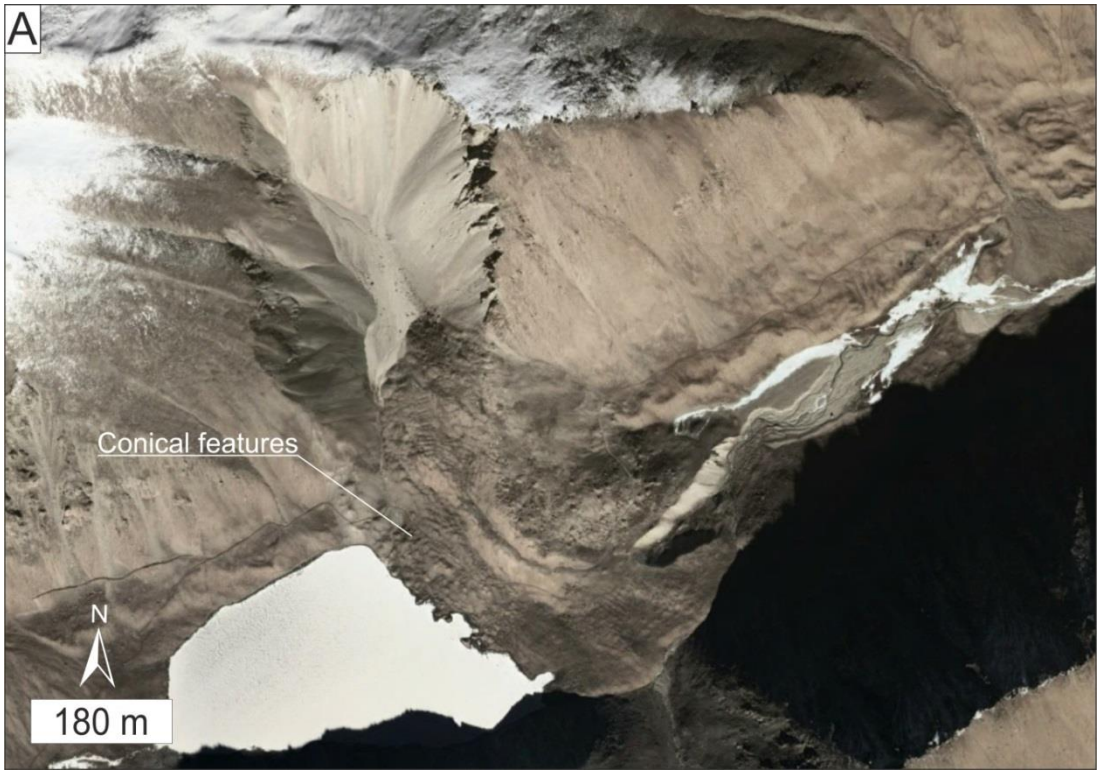

Figure 7.2. Aerial image of a landslide in the eastern Kashmir with conical features scattered in the accumulation zone (image from Google Earth).

Other cones of debris have been observed in the Mount Meager debris avalanche in British Columbia (Roberti et al., 2017a), and molards were identified on the deposits of the Brazeau Lake slide in Alberta (Cruden, 1982; Figure 7.3). In both landslides, permafrost thaw was recognised to have a role in the release of the failures, but the cones of debris were not linked to this process. The Himalayas, Canada and Greenland are areas where continuous and discontinuous permafrost is expected (Brown et al., 1997); therefore further studies should clarify how the number and density of molards can depend on the abundance of ground ice in the terrains affected by failures. In general, a more thorough characterisation of molards in other contexts should be accomplished

with the purpose of linking their morphology and distribution to the presence of permafrost, its coverage and state. A second avenue for future research is to better understand the landslide processes that result in the formation of molards, as I have shown in Chapter 6, as different mass movement dynamics can bring diverse morphometric characteristics to molards. This thesis has qualitatively shown that molards are differentiable from landforms that share morphological similarities with them, such as hummocks in rock and debris avalanches, and hummocks in ice-cored moraines. However, quantitative geomorphological comparisons would be advisable to avoid confusion and misleading interpretations when distinguishing these landforms. Finally, experimental simulations of formation of molards should be performed on a wide variety of materials with different granulometry, rheology and ground-ice/debris ratio, with the aim of quantifying their relative control of the shape of the cones of debris deriving from the decay of the blocks of ice-rich deposits.

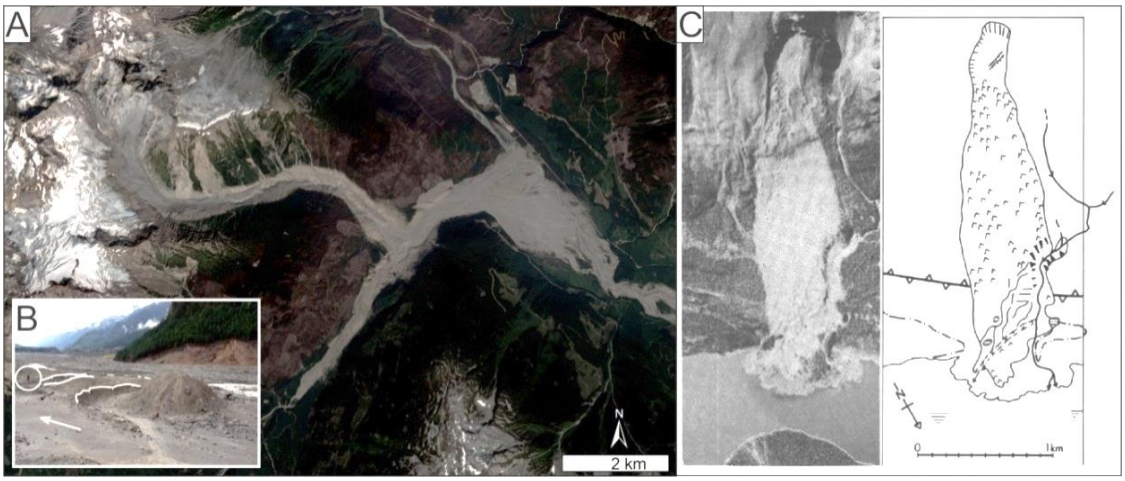

Figure 7.3. Candidate molards in Canada. (A) The aerial view of the Mount Meager debris avalanche (photos DS_PHR1A_201508121923233_FR1_PX_W124N50_0718_02305 and DS_PHR1A_201508121923233_FR1_PX_W124N50_0718_02305 from Airbus Defence & Space); (B) a detail of one of the cones of debris on the surface of the Mount Meager debris avalanche (from Roberti et al. (2017)); (C) aerial view of the Brazeau Lake slide in Alberta and its structures, with inverted V to indicate molards (from (Cruden, 1982)).

7.4 Can permafrost degradation be traced back in the past?

Reconstructing paleo-permafrost with accuracy is of great importance for understanding the origin of current landscapes, as their shape could precondition the occurrence of new mass movements. However, large uncertainties still exist on the maximal extent in Europe and Iceland during the Last Glacial Maximum (LGM) (Andrews et al., 2000; Clark et al., 2009; Hubbard et al., 2006; Jost et al., 2005). Moreover, the paleo-permafrost development, its extent and degradation and the glacier-permafrost interaction during the LGM are difficult to constrain. One way of approaching this complex problem, is the spatial and temporal analysis of paraglacial and periglacial forms. Various studies have led to great progress in our knowledge of paraglacial and periglacial landforms developed during the LGM and the Holocene in Iceland. There is a strong relationship between deglaciation and slope instabilities during the paraglacial phase in Iceland (Mercier et al., 2017). In the Westfjords, almost two hundred rockslides have been identified in an area deglaciated during the LGM to Younger Dryas transition (Peras et al., 2016). In central northern Iceland (Skagafjörður), most landslides in the area occurred during the first half of the Holocene, and landslide susceptibility was enhanced when the post-glacial uplift was at its maximum (Coquin et al., 2015; Cossart et al., 2014; Mercier et al., 2012). Among periglacial forms, thufur, even if not directly linked to permafrost, expanded in Iceland over the Holocene, which is coherent with permafrost extent in peri-Atlantic regions and with glacier fluctuations (Van Vliet-Lanoë et al., 1998). Although huge efforts have been made to define the origin of the paraglacial and periglacial landscape of Iceland, it is difficult to find a marker that can aid in defining the limit of paleo-

permafrost degradation. In this thesis I have hypothesised that molards could be used to trace permafrost degradation in the past. This potential is illustrated via the following case studies. In Figure 7.4A, a rockslide in Tröllaskagi peninsula (north-western side of Tungudalur valley) has some conical features at the toe of its accumulation zone. Similar landforms are also present in the upper accumulation zone of a rockslide on the northern side of the Tindastóll ridge, on the western coast of Skagafjörður fjord (Figure 7.4B). These rockslide are amongst those which have been linked to a paraglacial origin after the glacial retreat following the maximal ice extent in Iceland (Mercier et al., 2017). Similar hummocky topographies have been observed in analogue landslides in northern Iceland and have been related to deep-seated gravitational slope deformation (Coquin et al., 2016; Mercier et al., 2012). Coquin et al. (2016) hypothesised a water supply from permafrost thaw for one of these rockslides. The similarities between the conical features found in these paraglacial rockslides and molards are remarkable: both are found scattered on landslide deposits, they share the same form and hence possibly a permafrost-thaw related origin. In visual investigations of aerial images of the western side of the Móafellsdalur valley (the same where the Móafellshyrna landslide developed) and in subsequent inspections in the field, I have found similar conical features at the foot of a talus slope lying on the south-east side of the Lambahnjúkur mountain. These conical debris features have the same shape and size as the fresh molards I have investigated, and they lay on the deposits of a rockslide of paraglacial origin (Mercier et al., 2017). Further *in situ* investigations, morphometric characterisation and dating of these features, could reveal if they are hummocks, like those found in rock avalanches as an expression of stretching around blocks by faults (e.g., Shea and van Wyk de Vries, 2008), or molards. Confirmation of

these landforms being molards would imply a permafrost-thaw related origin and support my hypothesis that molards can be used to track permafrost degradation in to the past.

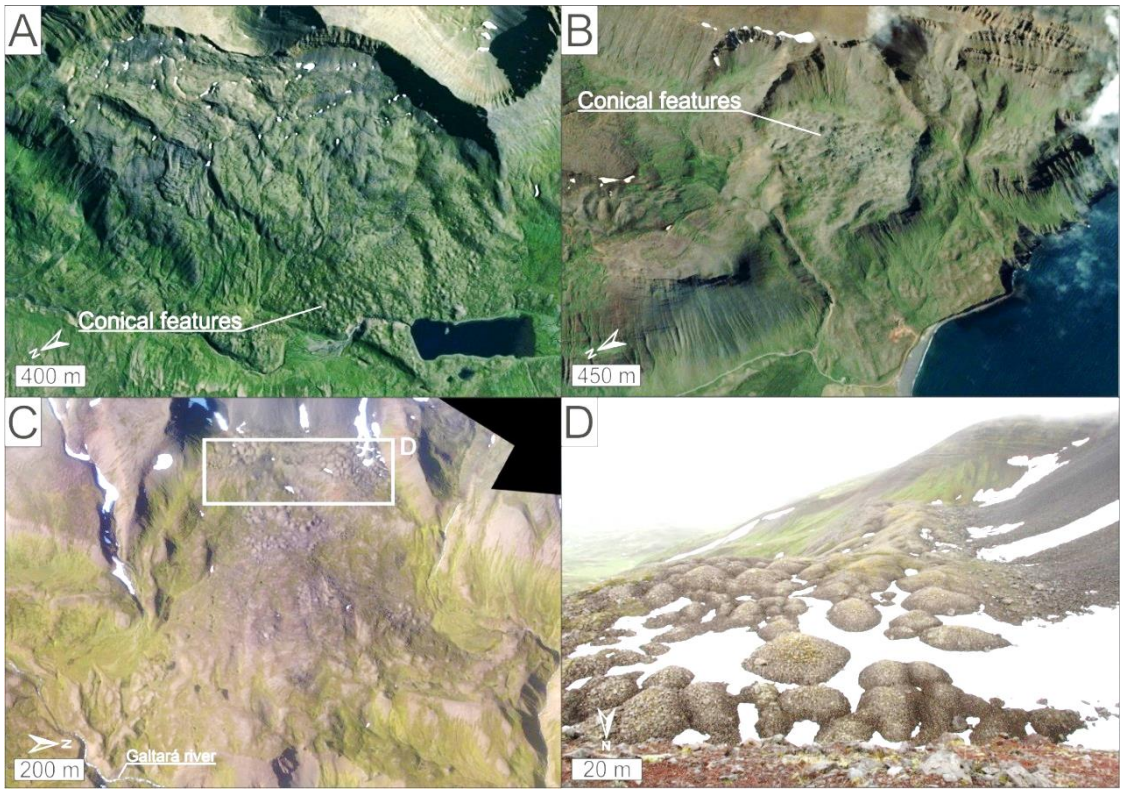

Figure 7.4. Candidate periglacial features in northern Iceland. (A) Aerial view of one of the paraglacial rockslides in the Tröllaskagi peninsula, with conical features at its toe (image from Google maps); (B) aerial view of other conical features present in the upper accumulation zone of a rockslide on the northern side of the Tindastóll ridge (western coast of Skagafjörður fjord; image from Google maps); (C) aerial view of conical features on the western side of the Móafellsdalur valley, on the south-east side of the Lambahnjúkur mountain; (D) oblique view of the conical features on the of the Lambahnjúkur mountain.

7.5 What is the hidden hazard of melting ground ice?

The mean surface temperature of the Earth has risen 0.6 to 0.9 degrees Celsius between 1906 and 2005 (IPCC, 2007). The response of hillslope geomorphic systems to climate change is expected to be acute, particularly at high latitudes (Harrison, 2009). Permafrost is degrading, as permafrost areal extent is decreasing and the active layer is deepening in different areas worldwide (Jorgenson et al., 2010; Smith and Riseborough, 1996; Zhang et al., 2007). It is well known that there is an influence of degrading permafrost on the occurrence of mass wasting phenomena (e.g., Fischer et al., 2006; Gruber et al., 2017; Gruber and Haeberli, 2007; Rebetez et al., 1997; Sattler et al., 2011; Stoffel and Huggel, 2012). Permafrost degradation has been identified in mountainous areas as one of the causes of rising frequency of rapid mass movements, such as debris flows, debris slides, rock falls and rock avalanches (Clague et al., 2012; Haeberli et al., 2017; Huggel et al., 2017; Wirz et al., 2016). Permafrost degradation can result in a loss of ground-ice cementation, the presence of segregated ice, increased hydrostatic pressure and the associated reduction of shear strength, and therefore to a reduction of stability (e.g., Gruber and Haeberli, 2007; Krautblatter et al., 2013). Slope position and aspect influence the response of slopes to increasing atmospheric temperatures: more rapid and deeper thermal responses are recorded at convex summits and ridges (Gruber and Haeberli, 2007), and north-facing slopes receive less solar radiation (Salzmann et al., 2007).

Little is known about the distribution and the state of permafrost in Iceland and its response to recent climate change. The occurrence in 2012 and 2014 of two

landslides affecting ground ice-rich terrains has highlighted the lack of knowledge of the present state of permafrost in Iceland and on the possible hazardous consequences of its degradation. I have shown that Móafellshyrna and Árnesfjall mobilised large volumes of material (see Chapter 4). Luckily, the Móafellshyrna landslide occurred at few kilometres from the nearest farm, and no one was on the road that was hit by the Árnesfjall landslide. However, this type of landslide might occur in more densely inhabited areas in the future, or could dam a valley, a circumstance that can cause outburst floods if the dam fails, with release down-valley of large amounts of water and sediments (e.g., Clague and Evans, 2000; Korup, 2002). A complication in evaluating the hazard that this type of landslide represents is the fact that few landslides involving ice-cemented debris have been observed and studied. Furthermore, a crucial problem in predicting slope adjustments, and in general geomorphological responses to climate change, is the lack of preserved analogues (Knight and Harrison, 2009). Therefore, studying the Icelandic hillslope responses to present-day climate change needs to deal with issues concerning magnitudes and rates of potential mass failures, considering the fact that it is expected that hazardous rapid mass movements induced by permafrost degradation will become more common in the near future due to predicted future warming (e.g., Allen et al., 2011; Geertsema et al., 2006; Harris et al., 2009; Keiler et al., 2010). No record of permafrost-induced landslides in Iceland exists, so we do not know if the occurrence of the landslides discussed here, which happened over a relatively short period of time, is the prelude to an increase in the frequency of rapid mass movements. Awareness of this type of failures should be raised among the local authorities and population.

The survey of the Móafellshyrna and Árnesfjall landslides immediately after the events, but before the ground ice completely thawed, was crucial to the

reconstruction of the history of the landslides' evolution, but this is not always possible if failures occur in remote areas or when no one can witness them. A possible way to improve our knowledge of this type of landslide would be the automatic detection of the landslides in remote areas of the island from satellite imagery, a technique that has been successfully applied in other locations for features such as landslides and karst landforms (e.g., Martha et al., 2010; Siart et al., 2009). This would allow the detection of active rapid mass movements in uninhabited areas where they cannot be witnessed, and their subsequent prompt field inspections would allow timely collection of important information about their potential release causes (importantly, including permafrost degradation), their distribution, and their frequency, all of which are crucial in the perspective of hazard assessment.

Another potential avenue for research, in order to improve the ability to predict the potential risk brought by rapid mass movements in Iceland and other mountain settings, is to identify zones with similar settings to those of Móafellshyrna, Árnesfjall and Ísafjörður. These case studies all share in common loose debris as source material that is located on a sub-horizontal topographic surface. Recognizing similar settings in other areas of Iceland would allow identification of possible at-risk locations and the installation of preventative measures, or at least monitoring systems. This is a possibility that could be applied in other at-risk periglacial environments. An effective monitoring of recurrent rapid mass movements could be the regular acquisition and differencing of topographic surfaces obtained through the technique of Structure from Motion (see Chapter 4). This approach can be used to monitor and quantify expeditiously and at low cost slopes affected by frequent mass movements like debris flows.

Another research strand arising from this thesis would be to investigate the role of soil creep and solifluction in contributing to the development of rapid mass movements in settings similar to those reported in this thesis. It has been reported in the literature that soil creep and solifluction could mobilise surficial debris in cold environments, providing new material to refill source areas of debris flows and debris slides (Glade, 2005; Sasaki et al., 2000). A similar process might be inferred for Ísafjörður, where creep features are observable in the deposits covering the Gleiðarhjalli bench above the town (Figure 7.5). Determining whether creep is active in this site will aid estimates of sediment availability and production, which in turn would allow a better estimates of magnitude and frequency of future debris-flow event. This could be applicable not only in Iceland, but wherever in cold environments debris flows and rapid mass movements recur regularly due to continuous sediment supply and threaten people and infrastructures on their path.

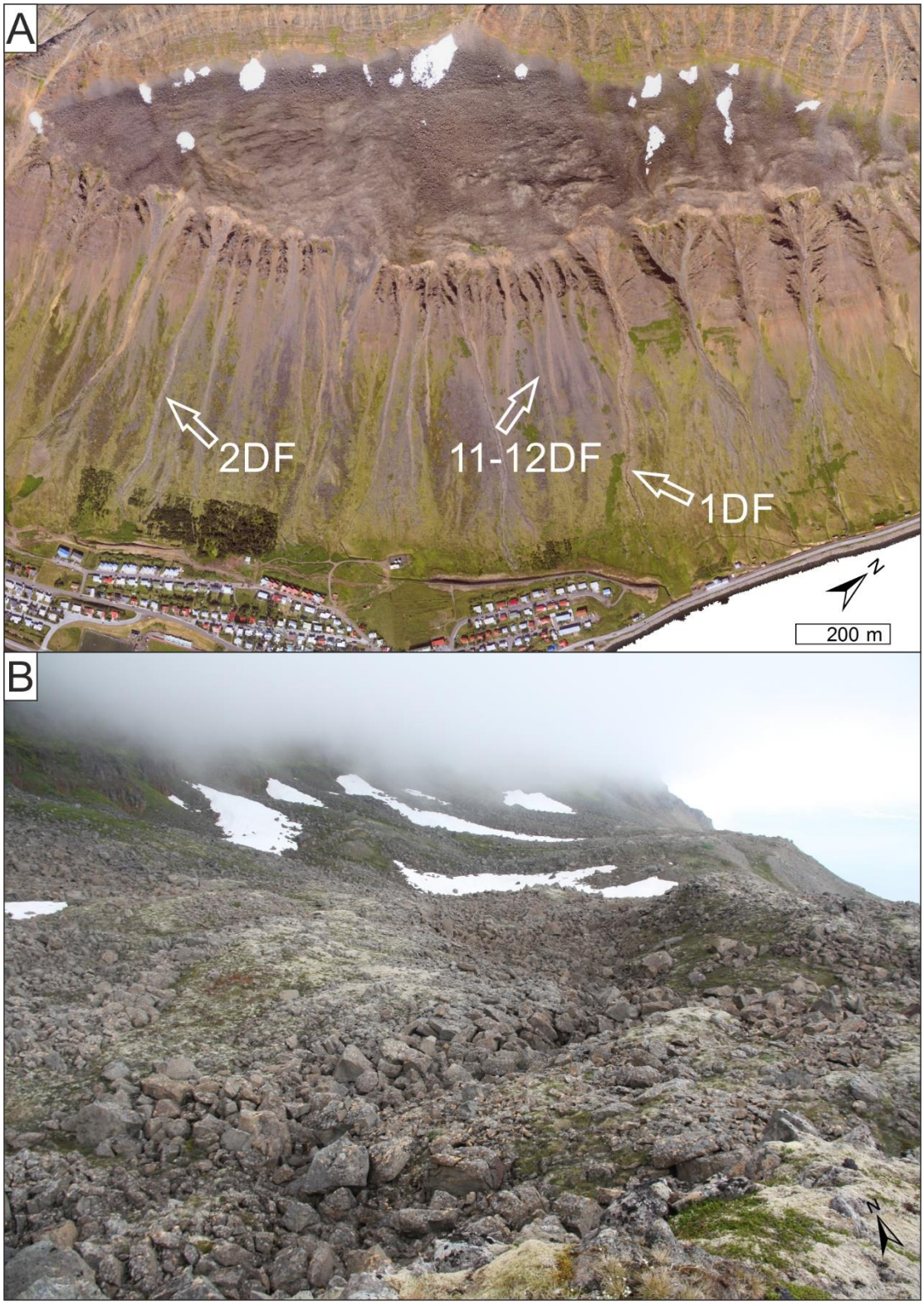

Figure 7.5. Possible creep structures above the town of Ísafjörður. (A) Aerial view of the slope affected by debris flows above the town of Ísafjörður, with potential creep structures on the Gleiðarhjalli bench; (B) an oblique view of the Gleiðarhjalli bench with stripes of coarse deposits.

7.6 Conclusions

This thesis has contributed to add new knowledge regarding rapid mass movements and their dynamics in cold environments. The first focus of this thesis was to identify signatures to distinguish different debris-flow release styles in northern Iceland, while the second focus was to understand the possible connections between the thawing of ground ice in mountainous areas of Iceland with discontinuous permafrost and the occurrence of landslides. I have demonstrated that a better understanding of landslides and debris flows is possible through quantitative geomorphological analysis. The melting of shallow ground ice in mountainous areas affected by permafrost was a “hidden hazard”, until the occurrence of two landslides sourced by ice-cemented talus deposits. Other zones in Iceland, even if not affected by ground-ice thaw, present even more hazardous phenomena, with debris flows recurring every 4-5 years above urban areas. The understanding of conditions and processes controlling rapid mass movements is crucial in the perspective of hazard assessment.

I have analysed the different triggering styles and evolution of debris flows in the Westfjords of Iceland, where debris flows have historically posed at risk local population. I have reconstructed the evolution of different debris flows by quantifying morphological and volumetric changes that, because gradually occurring and not directly observed in action, are “hidden” to human sight, and therefore potentially more hazardous for inhabited areas.

The morphologic study of two landslides in northern Iceland where ground ice was observed after their occurrence has included morphometric analysis of their features, quantification of the volumes mobilised, and characterisation of their different rheologies. This has allowed me to determine that ground ice had a

major role in the complex development of these landslides, promoting the failure and affecting the transport mechanisms. Therefore, understanding the mobility of such large slope failures is essential for mitigating the risk in the case of similar events in inhabited regions.

The same landslides have been analysed for their preparatory and triggering factors. I have described and discussed the relative importance of intense precipitation, earthquake activity and thawing of ground ice in contributing to the release of the landslides, identifying ground-ice thaw as a major trigger for the landslides, which suggests that mountain permafrost degradation is more prevalent in generating landslides in Iceland than was thought previous to this work.

In these two landslides of northern Iceland I found molards, conical mounds of debris that can form part of a landslide's deposits. I have shown the first conclusive evidence that molards result from thawing of frozen blocks of ice-rich sediments, which collapse into cones of debris. Molards can be used as a marker of permafrost degradation, and their morphometry and spatial distribution give valuable insights into landslide dynamics in periglacial terrains. I have also demonstrated that molards are readily recognisable not only in the field, but also in remote sensing data on the surface of Earth and other planets, and could be used as an indicator of current and past permafrost conditions.

7.7 Recommendations for future work

There are a lot of open opportunities for extending the novel findings of this thesis. My research has opened up new questions and research opportunities to study the spatial and temporal distribution of ground ice in unstable loose

sediments in periglacial terrains and the ice-rich nature of the surface of Mars. In particular, further directions that can branch off from this thesis are:

- To monitor zones of Iceland and periglacial environments potentially affected by rapid mass movements, which are expected to cause an acute geomorphic response to changing climate conditions. An extension of the hazard assessment of recurrent rapid mass movements like debris flows in Iceland and other mass-movements exposed areas would be to apply the same differencing of topographic surfaces that I have used in Ísafjörður for the monitoring of slopes affected by mass movements using repeated Structure from Motion. This is a user-friendly technique that can be effectively used by local authorities to monitor and quantify sediment transport by debris flows expeditiously and at low costs. At the same time, the information gathered could improve our understanding of how debris flows and landslides in cold environments are sediment supplied, initiate and develop.
- To better characterise the geographic extent and state of permafrost in Iceland and other periglacial environments, in order to be able to predict the changes of ground temperature in a changing climate and their potentially hazardous consequences on the landscape. An obvious extension in the perspective of preventing future hazardous landslides in permafrost terrains would be to identify zones with unstable loose deposits affected by permafrost, inspect their stability and put in place protective measurements for inhabited areas and/or infrastructures;
- To validate the work that I have done on molards in Iceland, verifying if molards reported elsewhere have the same distribution and morphologies, and if these show different dynamic processes. A further avenue would be

to track geographical distribution of landslides with molards in other zones where more detailed permafrost-distribution models are available and verify to what extent molards can be an index of permafrost degradation in the present. Dating candidate ancient molards could lead to evaluate if they can be used to map permafrost degradation in the past. Finally, the novel finding of the importance of molards in reading the periglacial environment can be exported to study the morphology of Mars and other planetary surfaces. The discovery of candidate molards in the ejecta of Hale Crater adds to the evidence that the impact was into ice-rich materials. The molards have the potential to constrain both the initial ground ice content at the Hale impact, but also the conditions during ejecta emplacement. Since the distribution and morphology of molards on Earth tell us about landslide dynamics, molards could then be used to probe the dynamics of impact ejecta emplacement on Mars and potentially other planetary surfaces.

References

Abele G. 1974. Bergsturze in den Alpen. Ihre Verbreitung, Morphologie und Folgeerscheinungen. Wiss. Alpenvereinshefte **25**: 230.

Addisson K. 1987. Debris flow during intense rainfall in Snowdonia, North Wales: a preliminary survey. Earth Surface Processes and Landforms **12**: 561–566.

Ágústsson K, Pétursson HG. 2013. Skriður og grjóthrun. 639–645.

Akca D. 2007. Least Squares 3D Surface Matching. Eidgenössische Technische Hochschule Zürich: Zurich; 92 pp.

Allen RM. 2002. Plume-driven plumbing and crustal formation in Iceland. Journal of Geophysical Research **107**: 2163. DOI: 10.1029/2001JB000584

Allen SK, Cox SC, Owens IF. 2011. Rock avalanches and other landslides in the central Southern Alps of New Zealand: A regional study considering possible climate change impacts. Landslides **8**: 33–48. DOI: 10.1007/s10346-010-0222-z.

Allen SK, Gruber S, Owens IF. 2009. Exploring steep bedrock permafrost and its relationship with recent slope failures in the Southern Alps of New Zealand. Permafrost and Periglacial Processes **20**: 345–356. DOI: 10.1002/ppp

Anderson RS, Anderson SP. 2010. Geomorphology: the mechanics and chemistry of landscapes. Cambridge University Press; 637 pp.

Anderson SA, Sitar N. 1995. Analysis of Rainfall-Induced Debris Flows. Journal of Geotechnical Engineering **121**: 544–552. DOI: 10.1061/(ASCE)0733-9410(1995)121:7(544)

Andersson JG. 1906. Solifluction, a Component of Subaërial Denudation. The Journal of Geology **14**: 91–112.

Andrés N, Tanarro LM, Fernández JM, Palacios D. 2016. The origin of glacial alpine landscape in Tröllaskagi Peninsula (North Iceland). Cuadernos de Investigación Geográfica **42**: 341. DOI: 10.18172/cig.2935

Andrews JT et al. 2000. The N and W Iceland Shelf: Insights into Last Glacial Maximum ice extent and deglaciation based on acoustic stratigraphy and basal radiocarbon AMS dates. Quaternary Science Reviews **19**: 619–631. DOI: 10.1016/S0277-3791(99)00036-0

Andrews JT, Hardardóttir J, Geirsdóttir Á, Helgadóttir G. 2002. Late Quaternary ice extent and glacial history from the Djúpáll trough, off Vestfirdir peninsula, north-west Iceland: A stacked 36 cal. Ky environmental record. Polar Research **21**: 211–226. DOI: 10.3402/polar.v21i2.6481

Arnalds Þ, Jónasson K, Sigurðsson S. 2004. Avalanche hazard zoning in Iceland based on individual risk. Annals of Glaciology **38**: 285–290. DOI: 10.3189/172756404781814816

Arnalds Þ, Sauermoser S, Jóhannesson T, Grímsdóttir T. 2001. Hazard zoning for Siglufjörður. Technical report, Reykjavík.

Arnalds Þ, Sauermoser S, Jóhannesson T, Jensen E. 2002. Hazard zoning for Seyðisfjörður.Technical report, Reykjavík.

Ashastina K, Schirrmeister L, Fuchs M, Kienast F. 2017. Palaeoclimate characteristics in interior Siberia of MIS 6-2: First insights from the Batagay permafrost mega-thaw slump in the Yana Highlands. Climate of the Past **13**: 795–818. DOI: 10.5194/cp-13-795-2017

Ballantyne CK. 2002. Paraglacial geomorphology. Quaternary Science Reviews **21**: 1935–2017. DOI: 10.1016/S0277-3791(02)00005-7

Ballantyne CK, Harris C. 1994. The Periglaciation of Great Britain . Cambridge University Press: Cambridge; 355 pp.

Bangen S, Hensleish J, McHugh P, Wheaton J. 2016. Error modeling of DEMs fromtopographic surveys of rivers using fuzzy inference systems. Water Resources Research **52**: 1176–1193. DOI: 10.1002/2014WR015716

Barla G, Dutto F, Mortara G. 2000. Brenva Glacier rock avalanche of 18 January 1997 on the Mont Blanc range, northwest Italy. Landslide News **13**: 2–5.

Baum RL, Godt JW. 2010. Early warning of rainfall-induced shallow landslides and debris flows in the USA. Landslides **7**: 259–272. DOI: 10.1007/s10346-009-0177-0

Becht M. 1995. Slope erosion processes in the Alps. In Steepland Geomorphology, Slaymaker O (ed). 54–61.

Bell R, Glade T. 2004. Quantitative risk analysis for landslides - Examples from Bíldudalur, NW-Iceland. Natural Hazards and Earth System Science **4**: 117–131. DOI: 10.5194/nhess-4-117-2004

Beniston M et al. 2018. The European mountain cryosphere: a review of its current state, trends, and future challenges. The Cryosphere **12**: 759–794. DOI: 10.5194/tc-12-759-2018

Benjamin J. 2014. Dynamic analysis of long run-out rock avalanches:A view from the Vaigat Strait,West Greenland, M.Sc.Thesis, Durham University;108 pp.

Berti M, Genevois R, Simoni A, Tecca PR. 1999. Field observations of a debris flow event in the Dolomites. Geomorphology **29**: 265–274. DOI: 10.1016/S0169-555X(99)00018-5

Berti M, Simoni A. 2005. Experimental evidences and numerical modelling of debris flow initiated by channel runoff. Landslides **2**: 171–182. DOI: 10.1007/s10346-005-0062-4

Besl P, McKay N. 1992. A method for registration of 3-D shapes. IEEE Transactions on Pattern Analysis and Machine Intelligence **14**: 239–256. DOI:

10.1109/34.121791

Beylich A. 2000. Geomorphology, Sediment Budget, and Relief Development in Austdalur, Austfirðir, East Iceland. Actic, Antartic, and Alpine Research **32**: 466–477.

Beylich AA, Decaulne A, Sandberg O. 2004. First Science Meeting of the European Science Foundation - Sedimentary Source-to-Sink-Fluxes in Cold Environments. Náttúrustofa Norðurlands vestra.

Beylich AA, Kneisel C. 2009. Sediment Budget and Relief Development in Hrafndalur, Subarctic Oceanic Eastern Iceland. Arctic, Antarctic, and Alpine Research **41**: 3–17. DOI: 10.1657/1938-4246(08-020)[BEYLICH]2.0.CO;2

Bjarnason IÞ. 2008. An Iceland hotspot saga. Jokull **58** : 3–16.

Björnsson H et al. 2008. Hnattrænar loftslagsbreytingar og áhrif þeirra á Íslandi. Skýrsla vísindanefndar um loftslagsbreytingar, Reykjavík.

Blais-Stevens A, Kremer M, Bonnaventure PP, Smith SL, Lipovsky P, Lewkowicz AG. 2015. Active Layer Detachment Slides and Retrogressive Thaw Slumps Susceptibility Mapping for Current and Future Permafrost Distribution, Yukon Alaska Highway Corridor: 449-452. In Engineering Geology for Society and Territory. Lollino G, A. M, Clague J, Shan W, and M. C (eds). Springer.

Blaschke PM, Trustrum NA, Hicks DL. 2000. Impacts of mass movement erosion on land productivity: A review. Progress in Physical Geography **24**: 21–52. DOI: 10.1191/030913300669154532

De Blasio FV. 2014. Friction and dynamics of rock avalanches travelling on glaciers. Geomorphology **213**: 88–98. DOI: 10.1016/j.geomorph.2014.01.001

De Blasio FV, Elverhøi A. 2008. A model for frictional melt production beneath large rock avalanches. Journal of Geophysical Research: Earth Surface **113** : 1–13. DOI: 10.1029/2007JF000867

De Blasio FV, Engvik LE, Elverhøi A. 2006. Sliding of outrunner blocks from submarine landslides. Geophysical Research Letters **33**: 8–11. DOI: 10.1029/2005GL025165

Blasone G, Cavalli M, Marchi L, Cazorzi F. 2014. Monitoring sediment source areas in a debris-flow catchment using terrestrial laser scanning. Catena **123**: 23–36. DOI: 10.1016/j.catena.2014.07.001

Bolch T, Marchenko S. 1990. Significance of glaciers, rockglaciers, and ice-rich permafrost in the Northern Tien Shan as water towers under climate change conditions. In Proceedings of the Workshop Assessment of Snow-Glacier and Water Resources in Asia; 132–143.

Bossi G, Cavalli M, Crema S, Frigerio S, Quan Luna B, Mantovani M, Marcato G, Schenato L, Pasuto A. 2015. Multi-temporal LiDAR-DTMs as a tool for modelling a complex landslide: A case study in the Rotolon catchment (eastern Italian Alps). Natural Hazards and Earth System Sciences **15**: 715–722. DOI: 10.5194/nhess-15-715-2015

Bottino G, Chiarle M, Joly A, Mortara G. 2002. Modelling rock avalanches and their relation to permafrost degradation in glacial environments. Permafrost and Periglacial Processes **13** : 283–288. DOI: 10.1002/ppp.432

Boultbee N, Stead D, Schwab J, Geertsema M. 2006. The Zymoetz River rock avalanche, June 2002, British Columbia, Canada. Engineering Geology **83**: 76–93. DOI: 10.1016/j.enggeo.2005.06.038

Bovis M., Jones P. 1992. Holocene history of earthflow mass movements in south-central British Columbia: the influence of hydroclimatic changes. Canadian Journal of Earth Sciences **29**: 1746–1755.

Bovis MJ, Dagg BR. 1992. Debris flow triggering by impulsive loading: mechanical modelling and case studies. Canadian Geotechnical Journal **29**: 345–

352.

Brasington J, Langham J, Rumsby B. 2003. Methodological sensitivity of morphometric estimates of coarse fluvial sediment transport. Geomorphology **53**: 299–316. DOI: 10.1016/S0169-555X(02)00320-3

Brasington J, Rumsby BT, Mcvey RA. 2000. Monitoring and Modelling Morphological Change in a Braided Gravel-Bed River Using High Resolution Gps-. Earth Surface Processes and Landforms **25**: 973–990. DOI: 10.1002/1096-9837(200008)25:9<973::AID-ESP111>3.0.CO;2-Y

Brayshaw D, Hassan MA. 2009. Debris flow initiation and sediment recharge in gullies. Geomorphology **109**: 122–131. DOI: 10.1016/j.geomorph.2009.02.021

Bremer M, Sass O. 2012. Combining airborne and terrestrial laser scanning for quantifying erosion and deposition by a debris flow event. Geomorphology **138**: 49–60. DOI: 10.1016/j.geomorph.2011.08.024

Brideau M, Stead D, Hopkinson C, Demuth M, Barlow J, Evans S, Delaney K. 2009. Preliminary description and slope stability analyses of the 2008 Little Salmon Lake and 2007 Mt . Steele landslides , Yukon. In Yukon Exploration and Geology: 119–134.

Brown J, Ferrians OJ, Heginbottom JA, Melnikov ES. 1997. Circum-Arctic map of permafrost and ground-ice conditions. US Geological Survey, Reston.

Brynjólfsson S, Ólafsson H. 2009. Precipitation in the Svarfaðardalur region, North-Iceland. Meteorology and Atmospheric Physics **103**: 57–66. DOI: 10.1007/s00703-008-0348-x

Brynjólfsson S, Schomacker A, Ingólfsson Ó, Keiding JK. 2015. Cosmogenic36Cl exposure ages reveal a 9.3 ka BP glacier advance and the Late Weichselian-Early Holocene glacial history of the Drangajökull region, northwest Iceland. Quaternary Science Reviews **126**: 140–157. DOI:

10.1016/j.quascirev.2015.09.001

Bull JM, Miller H, Gravley DM, Costello D, Hikuroa DCH, Dix JK. 2010. Assessing debris flows using LIDAR differencing: 18 May 2005 Matata event, New Zealand. Geomorphology **124**: 75–84. DOI: 10.1016/j.geomorph.2010.08.011

Burbank DW, Leland J, Fielding E, Anderson RS, Brozovic N, Reid MR, Duncan C. 1996. Bedrock incision, rock uplift and threshold hillslopes in the northwestern Himalayas. Nature **379**: 505–510.

Burrough PA, McDonnell RA, Lloyd CD. 2015. Principles of geographical information systems. Oxford University Press; 329 pp.

Campbell RH. 1975. Soil Slips, Debris Flows, and Rainstorms in the Santa Monica Mountains and Vicinity, Southern California. U.S. Geological Survey Professional Paper 851; 51 pp.

Cannon SH, Kirkham RM, Parise M. 2001. Wildfire-related debris-flow initiation processes, Storm King Mountain, Colorado. Geomorphology **39**: 171–188. DOI: 10.1016/S0169-555X(00)00108-2

Cannon SH, Reneau SL. 2000. Conditions for generation of fire-related debris flows, Capulin Canyon, New Mexico. Earth Surface Processes and Landforms **25**: 1103–1121. DOI: 10.1002/1096-9837(200009)25:10<1103::AID-ESP120>3.0.CO;2-H

Capra L, Macías JL. 2000. Pleistocene cohesive debris flows at Nevado de Toluca Volcano, central Mexico. Journal of Volcanology and Geothermal Research **102** : 149–167. DOI: 10.1016/S0377-0273(00)00186-4

Caseldine C, Geirsdóttir Á, Langdon P. 2003. Efstadalsvatn - A multi-proxy study of a Holocene lacustrine sequence from NW Iceland. Journal of Paleolimnology **30** : 55–73. DOI: 10.1023/A:1024781918181

Caseldine C, Stotter J. 1993. “Little Ice Age” glaciation of Trollaskagi peninsula, northern Iceland: climatic implications for reconstructed equilibrium line altitudes (ELAS). The Holocene **3**: 357–366. DOI: 10.1177/095968369300300408

Cassie JW, Van Gassen W, Cruden DM. 1988. Laboratory analogue of the formation of molards, cones of rock- avalanche debris. Geology **16** : 735–738. DOI: 10.1130/0091-7613(1988)016<0735:LAOTFO>2.3.CO;2

Cavalli M, Goldin B, Comiti F, Brardinoni F, Marchi L. 2017. Assessment of erosion and deposition in steep mountain basins by differencing sequential digital terrain models. Geomorphology **291**: 4–16. DOI: 10.1016/j.geomorph.2016.04.009

Cendrero A, Dramis F. 1996. The contribution of landslides to landscape evolution in Europe. Geomorphology **15**: 191–211. DOI: 10.1016/0169-555X(95)00070-L

Chen Y, Medioni G. 1992. Object modelling by registration of multiple range images. Image and vision computing **10**: 145–155.

Christen M, Kowalski J, Bartelt P. 2010. RAMMS: Numerical simulation of dense snow avalanches in three-dimensional terrain. Cold Regions Science and Technology **63** : 1–14. DOI: 10.1016/j.coldregions.2010.04.005

Clague JJ, Evans SG. 2000. A review of catastrophic drainage of moraine-dammed lakes in British Columbia . Quaternary Science Reviews A review of catastrophic drainage of moraine-dammed lakes in British Columbia. Quaternary Science Reviews **19**: 1763–1783. DOI: 10.1016/S0277-3791(00)00090-1

Clague JJ, Huggel C, Korup O, Mcguire B. 2012. Climate Change and Hazardous Processes in High Mountains. Revista de la Asociación Geológica Argentina **69** : 328–338. DOI: 10.5167/uzh-77920

Clark M. 1983. Icelandic perspectives on periglacial research. Polarforschung **53**: 21–29.

Clark PU, Dyke AS, Shakun JD, Carlson AE, Clark J, Wohlfarth B, Mitrovica JX, Hostetler SW, McCabe AM. 2009. The Last Glacial Maximum. Science **325**: 710–714. DOI: 10.1126/science.1172873

Clavero J, Sparks R, Huppert H, Dade W. 2002. Geological constraints on the emplacement mechanism of the Parinacota debris avalanche, Northern Chile. Bulletin of Volcanology **64**: 40–54. DOI: 10.1007/s00445-001-0183-0

Coe JA, Glancy PA, Whitney JW. 1997. Volumetric analysis and hydrologic characterization of a modern debris flow near Yucca Mountain, Nevada. Geomorphology **20**: 11–28. DOI: Doi 10.1016/S0169-555x(97)00008-1

Coe JA, Kinner DA, Godt JW. 2008. Initiation conditions for debris flows generated by runoff at Chalk Cliffs, central Colorado. Geomorphology **96**: 270–297. DOI: 10.1016/j.geomorph.2007.03.017

Conway SJ, Balme MR. 2014. Decameter thick remnant glacial ice deposits on Mars. Geophysical Research Letters **41**: 5402–5409. DOI: 10.1002/2014GL059980.

Conway SJ, Decaulne A, Balme MR, Murray JB, Towner MC. 2010. A new approach to estimating hazard posed by debris flows in the Westfjords of Iceland. Geomorphology **114**: 556–572. DOI: 10.1016/j.geomorph.2009.08.015

Copons R, Vilaplana JM, Linares R. 2009. Rockfall travel distance analysis by using empirical models (Soì a d ' Andorra la Vella , Central Pyrenees). Natural Hazards and Earth System Science **9**: 2107–2118. DOI: 10.5194/nhess-9-2107-2009

Coquin J, Mercier D, Bourgeois O, Cossart E, Decaulne A. 2015. Gravitational spreading of mountain ridges coeval with Late Weichselian deglaciation: Impact

on glacial landscapes in Tröllaskagi, northern Iceland. Quaternary Science Reviews **107**: 197–213. DOI: 10.1016/j.quascirev.2014.10.023

Coquin J, Mercier D, Burgeois O, Feuillet T, Decaulne A. 2016. Is gravitational spreading a precursor for the Stífluhólar landslide (Skagafjörður, Northern Iceland)? Géomorphologie : relief, processus, environnement **22**: 9–24.

Corominas J. 1996. The angle of reach as a mobility index for small and large landslides. Canadian Geotechnical Journal **33** : 260–271.

Cossart E, Braucher R, Fort M, Bourlès DL, Carcaillet J. 2008. Slope instability in relation to glacial debuttressing in alpine areas (Upper Durance catchment, southeastern France): Evidence from field data and 10Be cosmic ray exposure ages. Geomorphology **95**: 3–26. DOI: 10.1016/j.geomorph.2006.12.022

Cossart E, Mercier D, Decaulne A, Feuillet T, Jónsson HP, Sæmundsson T. 2014. Impacts of post-glacial rebound on landslide spatial distribution at a regional scale in northern Iceland (Skagafjörur). Earth Surface Processes and Landforms **39**: 336–350. DOI: 10.1002/esp.3450

Costa JE. 1984. Physical geomorphology of debris flows. In Developments and applications of geomorphology: 268–317. Springer, Berlin, Heidelberg DOI: 10.1007/978-3-642-69759-3_9

Crochet P, Jóhannesson T, Jónsson T, Sigurðsson O, Björnsson H, Pálsson F, Barstad I. 2007. Estimating the Spatial Distribution of Precipitation in Iceland Using a Linear Model of Orographic Precipitation. Journal of Hydrometeorology **8**: 1285–1306. DOI: 10.1175/2007JHM795.1

Crosta GB. 2001. Failure and flow development of a complex slide: The 1993 Sesa landslide. Engineering Geology **59**: 173–199. DOI: 10.1016/S0013-7952(00)00073-9

Crosta GB, Chen H, Lee CF. 2004. Replay of the 1987 Val Pola Landslide,

Italian Alps. Geomorphology 60: 127–146. DOI: 10.1016/j.geomorph.2003.07.015

Crozier MJ. 1989. Landslides: Causes, Consequences and Environment. Routledge, London; 252 pp.

Crozier MJ. 2010. Deciphering the effect of climate change on landslide activity: A review. Geomorphology 124: 260–267. DOI: 10.1016/j.geomorph.2010.04.009

Cruden DM. 1982. The Brazeau Lake slide, Jasper National Park, Alberta. Canadian journal of earth science 19: 975–981. DOI: 10.1139/e82-081

Cruden DM, Varnes D. 1996. Landslide types and processes. In Landslides investigation and mitigation, Transportation research board UNRC (ed). Washington, DC; 36–75.

Curry RR. 1966. Observation of alpine mudflows in the Tenmile Range, central Colorado. Geological Society of America Bulletin 77 : 771–776.

Dahl-Jensen T, Larsen LM, Pedersen SAS, Pedersen J, Jepsen HF, Pedersen GK, Nielsen T, Pedersen AK, Von Platen-Hallermund F, Weng W. 2004. Landslide and tsunami 21 November 2000 in Paatuut, West Greenland. Natural Hazards 31 : 277–287. DOI: 10.1023/B:NHAZ.0000020264.70048.95

Dai F., Lee C., Ngai Y. 2002. Landslide risk assessment and management: an overview. Engineering Geology 64: 65–87. DOI: 10.1016/S0013-7952(01)00093-X

Damm B, Felderer A. 2013. Impact of atmospheric warming on periglacial degradation and debris flow initiation – a case study from the eastern European Alps. Quaternary Science Journal. 62: 136–148.

Darrow MM, Gyswyt NL, Simpson JM, Daanen RP, Hubbard TD. 2016. Frozen debris lobe morphology and movement: An overview of eight dynamic features, southern Brooks Range, Alaska. Cryosphere 10: 977–993. DOI: 10.5194/tc-10-252

977-2016

Davies MC, Hamza O, Harris C. 2001. The effect of rise in mean annual temperature on the stability of rock slopes containing ice-filled discontinuities. Permafrost and Periglacial Processes **12**: 137–144. DOI: 10.1002/ppp

Davies TRH. 1986. Large debris flows: a macro-viscous phenomenon. Acta Mechanica **63**: 161–178.

Davies TRH, McSaveney MJ. 2012. Mobility of long-runout rock avalanches. In Landslides: Types, Mechanisms and Modeling, Cambridge University Press; 50–58.

Davis JL, Annan AP. 1989. Ground-Penetrating Radar for high-resolution mapping of soil and rock stratigraphy. Geophysical prospecting **37**: 531–55.

Decaulne A. 2001. Dynamique des versants et risques naturels dans les fjords d'Islande du nord-ouest, l'impact géomorphologique et humain des avalanches et des debris flows, PhD Thesis, University of Clermont II, France

Decaulne A. 2004. Combining geomorphological, historical and lichenometrical data for assessment of risk due to present-day slope processes, a case study from the Icelandic Westflords. Risk Analysis **4**: 177–186.

Decaulne A. 2005. Slope processes and related risk appearance within the Icelandic Westfjords during the twentieth century. Natural Hazards and Earth System Science **5** : 309–318. DOI: 10.5194/nhess-5-309-2005

Decaulne A. 2007. Snow-avalanche and debris-flow hazards in the fjords of north-western Iceland, mitigation and prevention. Natural Hazards **41**: 81–98. DOI: 10.1007/s11069-006-9025-x

Decaulne A, Sæmundsson Þ. 2003. Debris-flows characteristics in the Gleidarhjalli area , North-western Iceland. In Debris-Flow Hazards Mitigation: Mechanics, Prediction, and Assessment , D. Rickenmann D and Chen CL (eds).

Millpress, Rotterdam: Davos, Switzerland; 1107–1118.

Decaulne A, Sæmundsson Þ. 2006. Geomorphic evidence for present-day snow-avalanche and debris-flow impact in the Icelandic Westfjords. Geomorphology **80**: 80–93. DOI: 10.1016/j.geomorph.2005.09.007

Decaulne A, Sæmundsson Þ. 2007. Spatial and temporal diversity for debris-flow meteorological control in subarctic oceanic periglacial environments in Iceland. Earth Surface Processes and Landforms **32**: 1971–1983. DOI: 10.1002/esp.1509

Decaulne A, Sæmundsson Þ, Pétursson O. 2005. Debris flow triggered by rapid snowmelt: A case study in the Gleidarhjalli area, northwestern Iceland. Geografiska Annaler, Series A: Physical Geography **87**: 487–500. DOI: 10.1111/j.0435-3676.2005.00273.x

Decaulne A, Sæmundsson Þ, Pétursson HG, Jónsson HP, Sigurðsson IA. 2010. A large rock avalanche onto Morsarjökull glacier, south-east Iceland. Its implications for ice-surface evolution and glacier dynamics. In Iceland in the Central Northern Atlantic: hotspot, sea currents and climate change.

Decaulne A, Cossart E, Mercier D, Feuillet T, Coquin J, Jónsson HP. 2016. An early Holocene age for the Vatn landslide (Skagafjörður, central northern Iceland): Insights into the role of postglacial landsliding on slope development. Holocene **26**: 1304–1318. DOI: 10.1177/0959683616638432

Delaney KB, Evans SG. 2014. The 1997 Mount Munday landslide (British Columbia) and the behaviour of rock avalanches on glacier surfaces. Landslides **11**: 1019–1036. DOI: 10.1007/s10346-013-0456-7

Deline P, Broccolato M, Noetzli J, Ravanel L, Tamburini A. 2013. The December 2008 Crammont Rock avalanche, Mont Blanc Massif Area, Italy. Landslide Science and Practice: Global Environmental Change **4**: 403–408. DOI:

10.1007/978-3-642-31337-0-52

Deline P, Gruber S, Delaloye R, Fischer L, Geertsema M, Giardino M, Hasler A, Kirkbride M, Krautblatter M, Magnin F, McColl S, 2015. Ice loss and slope stability in high-mountain regions. In Snow and Ice-related Hazards, Risks and Disasters: 521-561.

Densmore AL, Hovius N. 2000. Topographic fingerprints of bedrock landslides. Geology **28**: 371–374. DOI: 10.1130/0091-7613(2000)28<371:TFOBL>2.0.CO

Dramis F, Govi M, Guglielmin M, Mortara G. 1995. Mountain permafrost and slope instability in the Italian Alps: the Val Pola Landslid. Permafrost and Periglacial Processes **6**: 73–82.

Dramis F, Sorriso-Valvo M. 1995. Deep-seated gravitational slope deformations, related landslides and tectonics. International Journal of Rock Mechanics and Mining Sciences and Geomechanics **5**: 203A.

Dyke AS, Savelle JM. 2000. Major end moraines of Younger Dryas age on Wollaston Peninsula, Victoria Island, Canadian Arctic: implications for paleoclimate and for formation of hummocky moraine. Canadian Journal of Earth Sciences **37** : 601–619. DOI: 10.1139/e99-118

Einarsson MA. 1984. Climate of Iceland. In World survey of climatology. Elsevier, Amsterdam; 673–697.

Einarsson P. 2008. Plate boundaries, rifts and transforms in Iceland. Jokull **58** : 35–58.

Einarsson P, Björnsson S. 1979. Earthquakes in Iceland. Jökull **29**: 37–46.

Einarsson T, Albertsson KJ. 1988. The Glacial History of Iceland During the Past Three Million Years. Philosophical Transactions of the Royal Society: Biological Sciences **318** : 637–644. DOI: 10.1098/rstb.1988.0027

Einstein, H.A., 1937. Bedload transport as a probability problem.

Sedimentation. Water Resources Publications, Colorado: 105–108.

Eiríksson J, Knudsen KL, Haflidason H, Henriksen P. 2000. Late-glacial and Holocene palaeoceanography of the North Icelandic shelf. Journal of Quaternary Science **15**: 23–42. DOI: 10.1002/(SICI)1099-1417(200001)15:1<23::AID-JQS476>3.0.CO;2-8

Elwell HA, Stocking MA. 1976. Vegetal cover to estimate soil erosion hazard in Rhodesia. Geoderma **15** : 61–70. DOI: 10.1016/0016-7061(76)90071-9

Emmert A, Kneisel C. 2017. Internal structure of two alpine rock glaciers investigated by quasi-3-D electrical resistivity imaging. Cryosphere **11**: 841–855. DOI: 10.5194/tc-11-841-2017

Erismann TH, Abele G. 2001. Dynamics of rockslides and rockfalls. Springer-Verlag: Berlin; 316 pp.

Etzelmüller B, Farbrot H, Guðmundsson Á, Humlum O, Tveito OE, Björnsson H. 2007. The regional distribution of mountain permafrost in Iceland. Permafrost and Periglacial Processes **18**: 185–199. DOI: 10.1002/ppp.583

Etzelmuller B, Hagen JO. 2005. Glacier-permafrost interaction in Arctic and alpine mountain environments with examples from southern Norway and Svalbard. Geological Society, London, Special Publications **242**: 11–27. DOI: 10.1144/GSL.SP.2005.242.01.02

Etzelmüller B, Hoelzle M, Flo Heggem ES, Isaksen K, Mittaz C, Mühll DV, Ødegård RS, Haeberli W, Sollid JL. 2001. Mapping and modelling the occurrence and distribution of mountain permafrost. Norsk Geografisk Tidsskrift, Norwegian Journal of Geography **55**: 186–194. DOI: 10.1080/00291950152746513

Evans DJA, Ewertowski M, Orton C. 2017. The glaciated valley landsystem of Morsárjökull, southeast Iceland. Journal of Maps **13**: 909–920. DOI: DOI: 10.1080/17445647.2017.1401491

Evans SG, Clague JJ. 1988. Catastrophic rock avalanches in glacial environments. In Proceedings of the 5th International Symposium on Landslides Vol. 2.; 1153–1158.

Evans SG, DeGraff JV. 2002. Catastrophic landslides: effects, occurrence, and mechanisms . Geological Society of America. Vol.15.; 411 pp.

Evans SG, Hungr O. 1993. The assessment of rockfall hazard at the base of talus slopes. Canadian Geotechnical Journal **30**: 620–636. DOI: 10.1139/t93-054

Evans SG, Mugnozza GS, Strom AL, Hernmanns RL, Ischuk A, Vinnichenko S. 2006. Landslides from massive rock slope failure and associated phenomena. In Landslides from massive rock slope failure: 3–52. Springer, Dordrecht.

Van Everdingen R. 2005. Multi-language glossary of permafrost and related ground-ice terms. National Snow and Ice Data Center/World Data Center for Glaciology, Boulder **1998** : 186pp. DOI: 10.2307/1551636

Fairchild LH. 1987. The importance of lahar initiation processes. Reviews in Engineering Geology **7** : 51–62.

Farbrot H, Etzelmüller B, Guðmundsson Á, Humlum O, Kellerer-Pirklbauer A, Eiken T, Wangensteen B. 2007a. Rock glaciers and permafrost in Tröllaskagi, northern Iceland. Zeitschrift für Geomorphologie **51**: 1–16. DOI: 10.1127/0372-8854/2007/0051S2-0001

Farbrot H, Etzelmüller B, Schuler T V., Guðmundsson Á, Eiken T, Humlum O, Björnsson H. 2007b. Thermal characteristics and impact of climate change on mountain permafrost in Iceland. Journal of Geophysical Research **112**: F03S90. DOI: 10.1029/2006JF000541

Favalli M, Fornaciai A, Pareschi MT. 2009. LIDAR strip adjustment: Application to volcanic areas. Geomorphology **111**: 123–135. DOI: 10.1016/j.geomorph.2009.04.010

Feuillet T, Coquin J, Mercier D, Cossart E, Decaulne A, Jónsson HP, Sæmundsson Þ. 2014. Focusing on the spatial non-stationarity of landslide predisposing factors in northern Iceland: Do paraglacial factors vary over space? Progress in Physical Geography **38**: 354–377. DOI: 10.1177/0309133314528944

Feuillet T, Mercier D, Decaulne A, Cossart E. 2012. Classification of sorted patterned ground areas based on their environmental characteristics (Skagafjörður, Northern Iceland). Geomorphology **139–140**: 577–587. DOI: 10.1016/j.geomorph.2011.12.022

Fischer L, Eisenbeiss H, Kääb A, Huggel C, Haeberli W. 2011. Monitoring topographic changes in a periglacial high-mountain face using high-resolution DTMs, Monte Rosa East Face, Italian Alps. Permafrost and Periglacial Processes **22** : 140–152. DOI: 10.1002/ppp.717

Fischer L, Kääb A, Huggel C, Noetzli J. 2006. Geology, glacier retreat and permafrost degradation as controlling factors of slope instabilities in a high-mountain rock wall: the Monte Rosa east face. Natural Hazards and Earth System Sciences **6** : 761–772. DOI: 10.5194/nhess-6-761-2006

Fonstad MA, Dietrich JT, Courville BC, Jensen JL, Carbonneau PE. 2013. Topographic structure from motion: A new development in photogrammetric measurement. Earth Surface Processes and Landforms **38**: 421–430. DOI: 10.1002/esp.3366

Frank F, McArdell BW, Huggel C, Vieli A. 2015. The importance of entrainment and bulking on debris flow runout modeling: Examples from the Swiss Alps. Natural Hazards and Earth System Sciences **15**: 2569–2583. DOI: 10.5194/nhess-15-2569-2015

French HM. 2007. The periglacial environment. Third Edit. John Wiley & Sons, Ltd.; 458 pp.

Fryxell FM, Horberg L. 1943. Alpine mudflows in Grand Teton National Park, Wyoming. Geological Society of America Bulletin **54**: 457–472.

Fuller IC, Large ARG, Charlton ME, Heritage GL, Milan DJ. 2003. Reach-scale sediment transfers: An evaluation of two morphological budgeting approaches. Earth Surface Processes and Landforms **28**: 889–903. DOI: 10.1002/esp.1011

Furukawa Y, Ponce J. 2010. Accurate, dense, and robust multiview stereopsis. IEEE Transactions on Pattern Analysis and Machine Intelligence **32**: 1362–1376. DOI: 10.1109/TPAMI.2009.161

Garcia S, Arnaud NO, Angelier J, Bergerat F, Homberg C. 2003. Rift jump process in Northern Iceland since 10 Ma from40Ar/39Ar geochronology. Earth and Planetary Science Letters **214**: 529–544. DOI: 10.1016/S0012-821X(03)00400-X

Gariano SL, Guzzetti F. 2016. Landslides in a changing climate. Earth-Science Reviews **162** : 227–252. DOI: 10.1016/j.earscirev.2016.08.011

Del Gaudio V, Trizzino R, Calcagnile G, Calvaruso a., Pierri P. 2000. Landsliding in seismic areas: the case of the Acquara-Vadoncello landslide (southern Italy). Bulletin of Engineering Geology and the Environment **59**: 23–37. DOI: 10.1007/s100640000054

Geertsema M, Clague JJ, Schwab JW, Evans SG. 2006a. An overview of recent large catastrophic landslides in northern British Columbia, Canada. Engineering Geology **83** : 120–143. DOI: 10.1016/j.enggeo.2005.06.028

Geertsema M, Highland L, Vaugeouis L. 2009. Environmental impact of landslides. In Landslides–Disaster Risk Reduction: 589–607. Springer, Berlin, Heidelberg DOI: 10.1007/978-3-540-69970-5

Geertsema M, Hungr O, Schwab JW, Evans SG. 2006b. A large rockslide - Debris avalanche in cohesive soil at Pink Mountain, northeastern British

Columbia, Canada. Engineering Geology **83**: 64–75. DOI: 10.1016/j.enggeo.2005.06.025

Geirsdóttir Á, Andrews JT, Ólafsdóttir S, Helgadótti G, Hardardóttir J. 2002. A 36 Ky record of iceberg rafting and sedimentation from north-west Iceland. Polar Research **21**: 291–298. DOI: 10.1111/j.1751-8369.2002.tb00083.x

Geirsdóttir A, Miller GH, Axford Y, Olafsdottir S. 2009. Holocene and latest Pleistocene climate and glacier fluctuations in Iceland. Quaternary Science Reviews **28**: 2107–2118. DOI: 10.1016/j.quascirev.2009.03.013

Glade T. 2005. Linking debris-flow hazard assessments with geomorphology. Geomorphology **66**: 189–213. DOI: 10.1016/j.geomorph.2004.09.023

Glade T, Jensen EH. 2004. Recommendations for landslide hazard assessments in Bolungarvik and Vesturbyggd, NW-Iceland. Technical report Reykjavik.

Glancy P., Bell JW. 2000. Landslide-induced flooding at Ophir Creek, Washoe County, western Nevada, May 30, 1983. U.S. Geological Survey Professional Paper 1617

Godt JW, Coe JA. 2007. Alpine debris flows triggered by a 28 July 1999 thunderstorm in the central Front Range, Colorado. Geomorphology **84** : 80–97. DOI: 10.1016/j.geomorph.2006.07.009

Goguel J, Pachoud A. 1972. Géologie et dynamique de l'écroulement du Mont Granier: dans le Massif de Chartreuse, en novembre 1248. Bulletin du Bureau de Recherche Geologiques et Minieres **III**, **1** : 29–38.

Gorbunov AP. 1988. The alpine permafrost zone of the USSR. In Proceedings of the Fifth International Permafrost Conference. Vol. 1 : 154-158. Tapir Publishers.

Goulden T, Hopkinson C. 2010. The Forward Propagation of Integrated

System Component Errors within Airborne Lidar Data. Photogrammetric Engineering & Remote Sensing **76** : 589–601. DOI: 10.14358/PERS.76.5.589

Griffiths PG, Webb RH. 2004. Frequency and initiation of debris flows in Grand Canyon, Arizona. Journal of Geophysical Research **109**: 1–14. DOI: 10.1029/2003JF000077

Gruber S, Fleiner R, Guegan E, Panday P, Schmid MO, Stumm D, Wester P, Zhang Y, Zhao L. 2017. Review article: Inferring permafrost and permafrost thaw in the mountains of the Hindu Kush Himalaya region. Cryosphere **11**: 81–99. DOI: 10.5194/tc-11-81-2017

Gruber S, Haeberli W. 2007. Permafrost in steep bedrock slopes and its temperatures-related destabilization following climate change. Journal of Geophysical Research: Earth Surface **112** : 1–10. DOI: 10.1029/2006JF000547

Gruber S, Haeberli W. 2009. Mountain permafrost. In Permafrost soils, . Springer, Berlin, Heidelberg; 33–44.

Gruber S, Hoelzle M. 2008. The cooling effect of coarse blocks revisited: a modeling study of a purely conductive mechanism. Proceedings of the 9th International Conference on Permafrost 2008 : 557–561. DOI: 10.5167/uzh-2823

Gruber S, Hoelzle M, Haeberli W. 2004. Permafrost thaw and destabilization of Alpine rock walls in the hot summer of 2003. Geophysical Research Letters **31**: 1–4. DOI: 10.1029/2004GL020051

Gudmundsson, G.B., Hensch M, Roberts M, Group the S monitoring. 2013. The fall 2012 earthquake sequence in Eyjafjarðaráll, western Húsavík-Flatey Fault. In Proceedings of the International Workshop on Earthquakes in North Iceland, Húsavík, North Iceland; 71–73.

Gudmundsson A. 2000. Dynamics of volcanic systems in Iceland: Example of Tectonism and Volcanism at Juxtaposed Hot Spot and Mid-Ocean Ridge

Systems Agust. Annual Review of Earth and Planetary Sciences **28**: 107–140.

Gudmundsson A. 2007. Infrastructure and evolution of ocean-ridge discontinuities in Iceland. Journal of Geodynamics **43**: 6–29. DOI: 10.1016/j.jog.2006.09.002

Günther F, Grosse G, Jones BM, Schirrmeister L, Romanovsky VE, Kunitsky V. 2016. Unprecedented permafrost thaw dynamics on a decadal time scale: Batagay mega thaw slump development, Yana Uplands, Yakutia, Russia.

Guodong C, Dramis F. 1992. Distribution of Mountain Permafrost and Climate - A state of the art report. Permafrost and Periglacial Processes **3**: 83–91.

Guzzetti F, Peruccacci S, Rossi M, Stark CP. 2007. Rainfall thresholds for the initiation of landslides in central and southern Europe. Meteorology and Atmospheric Physics **98** : 239–267. DOI: 10.1007/s00703-007-0262-7

Guzzetti F, Stark CP, Salvati P. 2005. Evaluation of flood and landslide risk to the population of Italy. Environmental Management **36**: 15–36. DOI: 10.1007/s00267-003-0257-1

Hachem S, Allard M, Duguay C. 2009. Using the modis land surface temperature product for mapping permafrost: An application to northern Quebec and Labrador, Canada. Permafrost and Periglacial Processes **20**: 407–416. DOI: 10.1002/ppp.672

Haeberli W. 1997. Slope stability problems related to glacier shrinkage and permafrost degradation in the Alps. Eclogae Geologicae Helvetiae **90** : 407-414.

Haeberli W et al. 2006. Permafrost creep and rock glacier dynamics. Permafrost and Periglacial Processes **17** : 189–214. DOI: 10.1002/ppp.561

Haeberli W, Beniston M. 1998. Climate change and its impacts on glaciers and pemafrost in the Alps. Ambio **27** : 258–265.

Haeberli W, Guodong C, Gorbunov AP, Harris SA. 1993. Mountain permafrost

and climatic change. Permafrost and Periglacial Processes **4**: 165–174. DOI: 10.1002/ppp.3430040208

Haeberli W, Noetzli J, Arenson L, Delaloye R, Gärtner-Roer I, Gruber S, Isaksen K, Kneisel C, Krautblatter M, Phillips M. 2011. Mountain permafrost: Development and challenges of a young research field. Journal of Glaciology **56**: 1043–1058. DOI: 10.3189/002214311796406121

Haeberli W, Rickenmann D, Zimmermann M. 1990. Investigation of 1987 debris flows in the Swiss Alps: general concept and geophysical soundings. Hydrology in Mountain Regions. II - Artificial Reservoirs, Water and Slopes. IAHS Publ. **194**: 303–310.

Haeberli W, Schaub Y, Huggel C. 2017. Increasing risks related to landslides from degrading permafrost into new lakes in de-glaciating mountain ranges. Geomorphology **293**: 405–417. DOI: 10.1016/j.geomorph.2016.02.009

Halldórsson P. 1984. Skagafjarðarskjálftinn 1963.

Hambrey MJ, Huddart D, Bennet MR, Glasser NF. 1997. Genesis of “hummocky moraines” by thrusting in glacier ice: evidence from Svalbard and Britain. Journal of the Geological Society **154**: 623–632. DOI: 10.1144/gsjgs.154.4.0623

Haque U et al. 2016. Fatal landslides in Europe. Landslides **13**: 1545–1554. DOI: 10.1007/s10346-016-0689-3

Harp E, Jibson, RW. 1996. Landslides triggered by the 1994 Northridge, Calfolnia, Earthquake. Bulletin of the Seismological Society of America **86**: S319–S332.

Harris C. 2005. Climate change, mountain permafrost degradation and geotechnical hazard. In Global change and mountain regions. An overview of current knowledge. Springer, Dordrecht; 215–224.

Harris C et al. 2009. Permafrost and climate in Europe: Monitoring and modelling thermal, geomorphological and geotechnical responses. Earth-Science Reviews **92** : 117–171. DOI: 10.1016/j.earscirev.2008.12.002

Harris C, Haeberli W, Vonder Mühll D, King L. 2001. Permafrost monitoring in the high mountains of Europe: the PACE Project in its global context. Permafrost and Periglacial Processes **12** : 3–11. DOI: 10.1002/ppp.377

Harris SA. 1981. Climatic relationships of permafrost zones in areas of low winter snow-cover. Arctic **34** : 64–70.

Harris SA, Gustafsson CA. 1993. Debris flow characteristics in an area of continuous permafrost, St Elias Range, Yukon Territory. Zeitschrift fur Geomorphologie **37** : 41–56.

Harris SA, Pedersen DE. 1998. Thermal regimes beneath coarse blocky materials. Permafrost and Periglacial Processes **9**: 107–120. DOI: 10.1002/(SICI)1099-1530(199804/06)9:2<107::AID-PPP277>3.0.CO;2-G

Harrison S. 2009. Climate sensitivity: implications for the response of geomorphological systems to future climate change. Geological Society, London, Special Publications **320**: 257–265. DOI: 10.1144/SP320.16

Hasler A, Geertsema M, Foord V, Gruber S, Noetzli J. 2015. The influence of surface characteristics, topography and continentality on mountain permafrost in British Columbia. Cryosphere **9** : 1025–1038. DOI: 10.5194/tc-9-1025-2015

Hauck C, Isaksen K, Mühll DV, Sollid JL. 2004. Geophysical surveys designed to delineate the altitudinal limit of mountain permafrost: An example from Jotunheimen, Norway. Permafrost and Periglacial Processes **15** : 191–205. DOI: 10.1002/ppp.493

Hauck C, Vonder Muhll D, Maurer H. 2003. Using DC resistivity tomography to detect and characterize mountain permafrost. Geophysical Prospecting **51** : 273–

284. DOI: 10.1046/j.1365-2478.2003.00375.x

Heginbottom JA, Dubreuil MA, Harker PA. 1995. Canada – Permafrost . 5th editio. Natural Resources Canada: Ottawa, MCR; 4177 p.

Heim A. 1932. Landslides and human lives . N. Skermer. Bi-Tech Publishers: Vancouver, B.C.

Hermannsdóttir K. 2012. Veðrið sem gekk yfir landið 9. – 11. September 2012. Icelandic Met Office [online] Available from: www.vedur.is/vedur/frodleikur/greinar/nr/2533 (Accessed 20 July 2009)

Hilbich C, Hauck C, Hoelzle M, Scherler M, Schudel L, Völksch I, Vonder Mühll D, Mäusbacher R. 2008. Monitoring mountain permafrost evolution using electrical resistivity tomography: A 7-year study of seasonal, annual, and long-term variations at Schilthorn, Swiss Alps. Journal of Geophysical Research: Earth Surface **113** : 1–12. DOI: 10.1029/2007JF000799

Hinzman LD et al. 2005. Evidence and implications of recent climate change in Northern Alaska and other Arctic regions. Climatic Change **72** : 251–298. DOI: 10.1007/s10584-005-5352-2

Hoelzle M, Wagner S. 1998. Surface movement and internal deformation of ice-rock mixtures within rock glaciers at Pontresina-Schafberg, Upper Engadin, Switzerland. In Proceedings of the Seventh International Conference on Permafrost. Vol. 2327. Université Laval; 465-471.

Hovius N, Stark CP, Allen PA. 1997. Sediment flux from a mountain belt derived by landslide mapping. Geology **25**: 231–234. DOI: 10.1130/0091-7613(1997)025<0231:SFFAMB>2.3.CO;2

Hsu K. 1975. Catastrophic debris streams (sturzstroms) generated by rockfalls. Geological Society of America Bulletin **86**: 129–140.

Hu W, Dong XJ, Xu Q, Wang GH, van Asch TWJ, Hicher PY. 2016. Initiation

processes for run-off generated debris flows in the Wenchuan earthquake area of China. Geomorphology **253**: 468–477. DOI: 10.1016/j.geomorph.2015.10.024

Hubbard A, Sugden D, Dugmore A, Norddahl H, Pétursson HG. 2006. A modelling insight into the Icelandic Last Glacial Maximum ice sheet. Quaternary Science Reviews **25**: 2283–2296. DOI: 10.1016/j.quascirev.2006.04.001

Hubbard SS et al. 2013. Quantifying and relating land-surface and subsurface variability in permafrost environments using LiDAR and surface geophysical datasets. Hydrogeology Journal **21**: 149–169. DOI: 10.1007/s10040-012-0939-y

Huggel C, Zgraggen-Oswald S, Haeberli W, Kääb A, Polkvoj A, Galushkin I, Evans SG. 2005. The 2002 rock/ice avalanche at Kolka/Karmadon, Russian Caucasus: assessment of extraordinary avalanche formation and mobility, and application of QuickBird satellite imagery. Natural Hazards and Earth System Science **5**: 173–187. DOI: 10.5194/nhess-5-173-2005

Huggel C, Gruber S, Caplan-Auerbach J, Wessels RL, Molnia BF. 2007. The 2005 Mt. Steller, Alaska, rock-ice avalanche: A large slope failure in cold permafrost. In Proceedings of the Ninth International Conference on Permafrost. Vol. 29 : 747–752. DOI: 10.5167/uzh-3097

Huggel C, Clague JJ, Korup O. 2012. Is climate change responsible for changing landslide activity in high mountains? Earth Surface Processes and Landforms **37**: 77–91. DOI: 10.1002/esp.2223

Hungr O. 1981. Dynamics of rock avalanches and other types of slope movements. Ph.D. thesis, University of Alberta, Edmonton

Hungr O. 1990. Momentum transfer and friction in the debris of rock avalanches: Discussion. Canadian Geotechnical Journal **27**: 697–697.

Hungr O, Evans SG. 2004. Entrainment of debris in rock avalanches: An analysis of a long run-out mechanism. Bulletin of the Geological Society of

America **116** : 1240–1252. DOI: 10.1130/B25362.1

Hungr O, Evans SG, Bovis MJ, Hutchinson JN. 2001. A review of the classification of landslides of the flow type. Environmental and Engineering Geoscience **7** : 221–238. DOI: 10.2113/gseegeosci.7.3.221

Hungr O, Corominas J, Eberhardt E. 2005a. Estimating landslide motion mechanism, travel distance and velocity. In Landslide risk management: 99–128.

Hungr O, McDougall S, Bovis M. 2005b. Entrainment of material by debris flows. In Debris-flow hazards and related phenomena. Springer Berlin Heidelberg; 135–158.

Hungr O, Leroueil S, Picarelli L. 2014. The Varnes classification of landslide types, an update. Landslides **11** : 167–194. DOI: 10.1007/s10346-013-0436-y

Hunter G, Fell R. 2003. Travel distance angle for “rapid” landslides in constructed and natural soil slopes. Canadian Geotechnical Journal **40** : 1123–1141. DOI: 10.1139/t03-061

Hürlimann M, Rickenmann D, Graf C. 2003. Field and monitoring data of debris-flow events in the Swiss Alps. Canadian Geotechnical Journal **40** : 161–175. DOI: 10.1139/t02-087

Huscroft C A, Lipovsky PS, Bond JD. 2003. Permafrost and landslide activity: Case studies from southwestern Yukon Territory. Inn Yukon Exploration and Geology : 107–119.

Hutchinson JN. 1968. Mass Movement. In Geomorphology. Encyclopedia of Earth Science. Springer, Berlin, Heidelberg; 688-696.

Hutchinson, J.H., 1988. Morphological and Geotechnical Parameters of Landslides in Relation to Geology and Hydrogeology, Landslides. In Proceedings of the fifth international symposium on landslides; 3-35.

Icelandic Metereological Office, Report. 2012. Ofanflóðavarnir neðan

Gleiðarhjalla á ÍsafirðiOfanflóðavarnir neðan Gleiðarhjalla á Ísafirði. Mat á umhverfisáhrifum Matsskýrsla.

Imaizumi F, Sidle RC, Tsuchiya S, Ohsaka O. 2006. Hydrogeomorphic processes in a steep debris flow initiation zone. Geophysical Research Letters **33**: 2–5. DOI: 10.1029/2006GL026250

Ingolfsson O, Norddahl H, Schomacker A. 2010. Deglaciation and Holocene Glacial History of Iceland. Development in Quaternary Science **13**: 51–69.

Innes JL. 1983. Debris flows. Progress in Physical Geography **7**: 469–501.

IPCC. 2007. Climate Change 2007: The Physical Science Basis. Summary for Policymakers. Intergovernmental Panel on Climate Change, Geneva; 333 pp.

Isaksen K, Ødegård RS, Eiken T, Sollid JL. 2000. Composition, flow and development of two tongue-shaped rock glaciers in the permafrost of Svalbard. Permafrost and Periglacial Processes **11**: 241–257. DOI: 10.1002/1099-1530(200007/09)11:3<241::AID-PPP358>3.0.CO;2-A

Iverson R. M, Major JJ. 1987. Rainfall, groundwaterf low, and seasonal motion at Minor Creek landslide, northwestern California: Physical interpretation of empirical relations. Geological Society of America Bulletin **99**: 579–594. DOI: 10.1130/0016-7606(1987)99<579:RGFASM>2.0.CO;2

Iverson RM. 1997. The Physics of Debris Flows. Review of Geophysics **3**: 245–296.

Iverson RM. 2000. Landslide triggering by rain infiltration. Water Resources Research **36** : 1897–1910. DOI: 10.1029/2000WR900090

Iverson RM, Denlinger RP, LaHusen RG, Logan M. 2000. Two-phase debris-flow across 3-D terrain: model predictions and experimental tests. In Debris-flow hazards mitigation: mechanics, prediction, and assessment. IOS Press: Davos, Switzerland; 521–529.

Iverson RM et al. 2015. Landslide mobility and hazards: Implications of the 2014 Oso disaster. Earth and Planetary Science Letters **412**: 197–208. DOI: 10.1016/j.epsl.2014.12.020

James MR, Robson S. 2012. Straightforward reconstruction of 3D surfaces and topography with a camera: Accuracy and geoscience application. Journal of Geophysical Research: Earth Surface **117** : 1–17. DOI: 10.1029/2011JF002289

James MR, Robson S. 2014. Mitigating systematic error in topographic models derived from UAV and ground-based image networks. Earth Surface Processes and Landforms **39** : 1413–1420. DOI: 10.1002/esp.3609

Javernick L, Brasington J, Caruso B. 2014. Modeling the topography of shallow braided rivers using Structure-from-Motion photogrammetry. Geomorphology **213** : 166–182. DOI: 10.1016/j.geomorph.2014.01.006

Jermyn C, Geertsema M. 2015. An Overview of Some Recent Large Landslide Types in Nahanni National Park, Northwest Territories, Canada. Engineering Geology for Society and Territory **1**: 315–320. DOI: 10.1007/978-3-319-09300-0_59

Jibson RW, Prentice CS, Borissoff B a, Rogozhin E a, Langer CJ. 1994. Some observations of landslides triggered by the 29 April 1991 Racha earthquake, Republic of Georgia. Bulletin Seismological Society of America **84**: 963–973.

Jóhannesson H. 2014. Geological Map of Iceland. Bedrock Geology. Scale: 1:600 000. 2nd edition Náttúrufræðistofnun Íslands – Icelandic Institute of Natural History [online] Available from: www.arcgis.com/home/item.html?id=c56c70100e21467891fde8f534da96c3#overview

Jóhannesson T, Arnalds Þ. 1992. Accidents and economic damage due to snow avalanches and landslides in Iceland. Jökull : 81–94.

Johnson AM, Rahn PH. 1970. Mobilization of debris flows. Zeitschrift fur Geomorphologie **9**: 168–185.

Johnson AM, Rodine JR. 1984. Debris flow. In Slope Instability , Brunsden D and Prior DB (eds). Wiley, Chichester; 257–361.

Jones AP, McEwen AS, Tornabene LL, Baker VR, Melosh HJ, Berman DC. 2011. A geomorphic analysis of Hale crater, Mars: The effects of impact into ice-rich crust. Icarus **211**: 259–272. DOI: 10.1016/j.icarus.2010.10.014

Jónsson HB, Norðdahl H, Pétursson HG. 2004. Myndaði Berghlaup Vatnsdalshóla? Náttúrufræðingurinn **72** : 129–138.

Jónsson Ó. 1957. Skriðuföll og snjóflóð, I bindi.

Jonsson O, Petursson HG, Rist S, Sigvaldsson J. 1992. Skriðuföll og snjóflóð, II bindi.

Jónsson T. 2013. The weather in Iceland 2012. Climate summary. Icelandic Met Office [online] Available from: http://en.vedur.is/weather/articles/nr/2614

Jordan CJ, Napier B. 2015. Developing digital fieldwork technologies at the British Geological Survey. Geological Society, London, Special Publications **436**: 1–11. DOI: http://doi.org/10.1144/SP436.6

Jorgenson MT, Romanovsky V, Harden J, Shur Y, O'Donnell J, Schuur EAG, Kanevskiy M, Marchenko S. 2010. Resilience and vulnerability of permafrost to climate changeThis article is one of a selection of papers from The Dynamics of Change in Alaska's Boreal Forests: Resilience and Vulnerability in Response to Climate Warming. Canadian Journal of Forest Research **40**: 1219–1236. DOI: 10.1139/X10-060

Jost A, Lunt D, Abe-Ouchi A, Abe-Ouchi A, Peyron O, Valdes PJ, Ramstein G. 2005. High-resolution simulations of the last glacial maximum climate over Europe: A solution to discrepancies with continental palaeoclimatic

reconstructions? Climate Dynamics **24**: 577–590. DOI: 10.1007/s00382-005-0009-4

Julian M, Anthony EJ. 1994. Landslides and climatic variables with specific reference to the Maritime Alps of southeasternFrance. In Temporal Occurrence and Forecasting of Landslides in the European Community, Programme EPOCH , Casale R, Fantechi R, and Flageollet JC (eds). 697–721.

Kaab A. 2008. Remote sensing of permafrost-related problems and hazards. Permafrost and Periglacial Processes **19**: 107–136. DOI: 10.1002/ppp

Kean JW, McCoy SW, Tucker GE, Staley DM, Coe JA. 2013. Runoff-generated debris flows: Observations and modeling of surge initiation, magnitude, and frequency. Journal of Geophysical Research: Earth Surface **118**: 2190–2207. DOI: 10.1002/jgrf.20148

Keefer DK. 1984. Landslides caused by earthquakes. Geological Society of America Bulletin **95**: 406–421.

Keefer DK. 1994. The importance of earthquake-induced landslides to long-term slope erosion and slope-failure hazards in seismically active regions. Geomorphology **10**: 265–284.

Keefer DK. 2002. Investigating landslide caused by earthquakes - a historical review. Survey in Geophysics **23**: 473–510.

Keiler M, Knight J, Harrison S. 2010. Climate change and geomorphological hazards in the eastern European Alps. Philosophical Transactions of the Royal Society A: Mathematical, Physical and Engineering Sciences **368**: 2461–2479. DOI: 10.1098/rsta.2010.0047

Kellerer-Pirklbauer A, Lieb GK, Avian M, Carrivick J. 2012. Climate change and rock fall events in high mountain areas: numerous and extensive rock falls in 2007 at Mittlerer Burgstall, central Austria. Geografiska Annaler. Series A,

Physical Geography **94**: 59–78.

Kenner R, Phillips M, Hauck C, Hilbich C, Mulsow C, Bühler Y, Stoffel A, Buchroithner M. 2017. New insights on permafrost genesis and conservation in talus slopes based on observations at Flüelapass, Eastern Switzerland. Geomorphology **290**: 101–113. DOI: 10.1016/j.geomorph.2017.04.011

King L. 1986. Zonation and Ecology of High Mountain Permafrost in Scandinavia. Geografiska Annaler. Series A, Physical Geography **68** : 131–139.

King LC. 1953. Canons of landscape evolution. Geological Society of American, Bullettin **64**: 721–752.

Kjekstad O, Highland L. 2009. Economic and Social Impacts of Landslides. Landslides. In Landslides–disaster risk reduction; 573-587. Springer, Berlin, Heidelberg. DOI: 10.1007/978-3-540-69970-5

Kneisel C, Kääb A. 2007. High spatial resolution data acquisition for the geosciences: kite aerial photography. Earth Surface Processes and Landforms **32**: 1797–1810. DOI: 10.1002/esp

Kneisel C, Sæmundsson P, Beylich AA. 2007. Reconnaissance surveys of contemporary permafrost environments in central Iceland using geoelectrical methods: Implications for permafrost degradation and sediment fluxes. Geografiska Annaler, Series A: Physical Geography **89**: 41–50. DOI: 10.1111/j.1468-0459.2007.00306.x

Kneisel C, Emmert A, Kästl J. 2014. Application of 3D electrical resistivity imaging for mapping frozen ground conditions exemplified by three case studies. Geomorphology **210**: 71–82. DOI: 10.1016/j.geomorph.2013.12.022

Knight J, Harrison S. 2009. Periglacial and paraglacial environments: a view from the past into the future. Geological Society, London, Special Publications **320**: 1–4. DOI: 10.1144/SP320.1

Kokelj S, Tunnicliffe J, Lacelle D, Lantz TC, Fraser RH. 2015. Retrogressive thaw slumps: From slope process to the landscape sensitivity of northwestern Canada. In 68e Conférence Canadienne de Géotechnique et 7e Conférence Canadienne sur le Pergélisol, Québec. Vol. 17.

Kokelj S V., Lacelle D, Lantz TC, Tunnicliffe J, Malone L, Clark ID, Chin KS. 2013. Thawing of massive ground ice in mega slumps drives increases in stream sediment and solute flux across a range of watershed scales. Journal of Geophysical Research: Earth Surface **118**: 681–692. DOI: 10.1002/jgrf.20063

Korup O. 2002. Recent research on landslide dams-a literature review with special attention to New Zealand. Progress in Physical Geography **26** : 206–235. DOI: 10.1191/0309133302pp333ra

Krautblatter M, Funk D, Günzel FK. 2013. Why permafrost rocks become unstable: A rock-ice-mechanical model in time and space. Earth Surface Processes and Landforms **38**: 876–887. DOI: 10.1002/esp.3374

Kristjánsson L, Pätzold R, Preston J. 1975. The palaeomagnetism and geology of the Patreksfjördur-Arnarfjördur region of Northwest Iceland. Tectonophysics **25** DOI: 10.1016/0040-1951(75)90027-X

de Krom V. 1990. Retrogressive thaw slumps and active layer slides on Herschel Island, Yukon. M.Sc. Thesis, McGill University, Montréal, Québec

Krüger J, Kjær KH. 2000. De-icing progression of ice-cored moraines in a humid, subpolar climate, Kötlujökull, Iceland. The Holocene **10**: 737–747. DOI: 10.1191/09596830094980

Lacelle D, Bjornson J, Lauriol B. 2010. Climatic and geomorphic factors affecting contemporary (1950-2004) activity of retrogressive thaw slumps on the Aklavik plateau, Richardson mountains, NWT, Canada. Permafrost and Periglacial Processes **21**: 1–15. DOI: 10.1002/ppp.666

Lane SN, Westaway RM, Hicks DM. 2003. Estimation of erosion and deposition volumes in a large, gravel-bed, braided river using synoptic remote sensing. Earth Surface Processes and Landforms **28**: 249–271. DOI: 10.1002/esp.483

Lantuit H, Pollard WH. 2008. Fifty years of coastal erosion and retrogressive thaw slump activity on Herschel Island, southern Beaufort Sea, Yukon Territory, Canada. Geomorphology **95**: 84–102. DOI: 10.1016/j.geomorph.2006.07.040

Lantuit H, Pollard WH, Couture N, Fritz M, Schirrmeister L, Meyer H, Hubberten HW. 2012. Modern and Late Holocene Retrogressive Thaw Slump Activity on the Yukon Coastal Plain and Herschel Island, Yukon Territory, Canada. Permafrost and Periglacial Processes **23**: 39–51. DOI: 10.1002/ppp.1731

Larsen IJ, Pederson JL, Schmidt JC. 2006. Geologic versus wildfire controls on hillslope processes and debris flow initiation in the Green River canyons of Dinosaur National Monument. Geomorphology **81**: 114–127. DOI: 10.1016/j.geomorph.2006.04.002

Legros F. 2002. The mobility of long-runout landslides. Engineering Geology **63** : 301–331. DOI: 10.1016/S0013-7952(01)00090-4

Lewin J, Warburton J. 1994. Debris Flows in an Alpine Environment. Geography **79** : 98–107.

Lewkowicz AG. 1990. Morphology, frequency and magnitude of active-layer detachment slides, Fosheim Peninsula, Ellesmere Island, N.W.T. In Proceedings of the 5th Canadian permafrost conference.Vol. 54; 111–118.

Lewkowicz AG, Harris C. 2005a. Morphology and geotechnique of active-layer detachment failures in discontinuous and continuous permafrost, northern Canada. Geomorphology **69** : 275–297. DOI: 10.1016/j.geomorph.2005.01.011

Lewkowicz AG, Harris C. 2005b. Morphology and geotechnique of active-layer detachment failures in discontinuous and continuous permafrost, northern Canada. Geomorphology **69** : 275–297. DOI: 10.1016/j.geomorph.2005.01.011

Lilleøren KS, Etzelmüller B, Gärtner-Roer I, Kääb A, Westermann S, Gumundsson Á. 2013. The Distribution, Thermal Characteristics and Dynamics of Permafrost in Tröllaskagi, Northern Iceland, as Inferred from the Distribution of Rock Glaciers and Ice-Cored Moraines. Permafrost and Periglacial Processes **24** : 322–335. DOI: 10.1002/ppp.1792

Líndal J. 1936. Hvernig eru Vatnsdalshólar til orðnir. Náttúrufræðingurinn **6** : 65–75.

Lippert J, Wastl M, Stötter J, Moran AP, Geist T, Geitner C. 2003. Measuring and modelling ablation and accumulation on glaciers in Northern Iceland. Zeitschrift fur Gletscherkunde und Glazialgeologie **39** : 87–98.

Lowe DG. 2004. Distinctive image features from scale invariant keypoints. International Journal of Computer Vision **60**: 91–11020042. DOI: http://dx.doi.org/10.1023/B:VISI.0000029664.99615.94

Loye A, Jaboyedoff M, Isaac Theule J, Liébault F. 2016. Headwater sediment dynamics in a debris flow catchment constrained by high-resolution topographic surveys. Earth Surface Dynamics **4** : 489–513. DOI: 10.5194/esurf-4-489-2016

Lucchitta BK. 1978. A large landslide on Mars. Bulletin of the Geological Society of America **89**: 1601–1609. DOI: 10.1130/0016-7606(1978)89<1601:ALLOM>2.0.CO;2

Lucieer A, Jong SM d., Turner D. 2014. Mapping landslide displacements using Structure from Motion (SfM) and image correlation of multi-temporal UAV photography. Progress in Physical Geography **38**: 97–116. DOI: 10.1177/0309133313515293

Luckman BH. 1992. Debris flows and snow avalanches landforms in the Lairig Ghru, Cairngorn Mountains, Scotland. Geografiska Annaler **74** : 109–121.

Lukas S, Nicholson LI, Ross FH, Humlum O. 2005. Formation, Meltout Processes and Landscape Alteration of High-Arctic Ice-Cored Moraines—Examples From Nordenskiold Land, Central Spitsbergen. Polar Geography **29**: 157–187. DOI: 10.1080/789610198

Lyle RR, Hutchinson DJ, Preston Y. 2004. Landslide processes in discontinuous permafrost, Little Salmon Lake (NTS 105L/1 and 2), south-central Yukon. In Yukon Exploration and Geology: 193–204.

Lyle RR, Brideau M, Lipovsky P, Hutchnson DJ. 2014. Landslides on ice-rich slopes – a geohazard in a changing climate. Geohazards **6** : 10.

MacKay JR. 1972. Te world of underground ice. Annals of the Association of American Geographers **62** : 1-22. DOI: 10.1111/j.1467-8306.1972.tb00839.x

Malamud BD, Turcotte DL, Guzzetti F, Reichenbach P. 2004. Landslides, earthquakes, and erosion. Earth and Planetary Science Letters **229**: 45-59. DOI: 10.1016/j.epsl.2004.10.018

Mancini F, Dubbini M, Gattelli M, Stecchi F, Fabbri S, Gabbianelli G. 2013. Using unmanned aerial vehicles (UAV) for high-resolution reconstruction of topography: The structure from motion approach on coastal environments. Remote Sensing **5** : 6880-6898. DOI: 10.3390/rs5126880

Manga M, Brodsky EE, Boone M. 2003. Response of streamflow to multiple earthquakes. Geophysical Research Letters **30**: 18-1—18-4. DOI: 10.1029/2002GL016618

Marchi L, Arattano M, Deganutti AM. 2002. Ten years of debris-flow monitoring in the Moscardo Torrent (Italian Alps). Geomorphology **46**: 1-17. DOI: 10.1016/S0169-555X(01)00162-3

Martha TR, Kerle N, Jetten V, van Westen CJ, Kumar KV. 2010. Characterising spectral, spatial and morphometric properties of landslides for semi-automatic detection using object-oriented methods. Geomorphology **116** : 24–36. DOI: 10.1016/j.geomorph.2009.10.004

Matsuoka N, Hirakawa K, Watanabe T, Haeberli W, Keller F. 1998. The role of diurnal, annual and millennial freeze-thaw cycles in controlling alpine slope instability. Proceedings of the 7th International Conference on Permafrost, Yellowknife, 23–27 June 1998 **55** : 711–717.

Matsuura S, Asano S, Okamoto T. 2008. Relationship between rain and/or meltwater, pore-water pressure and displacement of a reactivated landslide. Engineering Geology **101** : 49–59. DOI: 10.1016/j.enggeo.2008.03.007

McArdell BW, Bartelt P, Kowalski J. 2007. Field observations of basal forces and fluid pore pressure in a debris flow. Geophysical Research Letters **34**: 2–5. DOI: 10.1029/2006GL029183

McClymont AF, Hayashi M, Bentley LR, Muir D, Ernst E. 2010. Groundwater flow and storage within an alpine meadow-talus complex. Hydrology and Earth System Sciences **14**: 859–872. DOI: 10.5194/hess-14-859-2010

McColl ST. 2012. Paraglacial rock-slope stability. Geomorphology **153–154**: 1–16. DOI: 10.1016/j.geomorph.2012.02.015

McConnell RG, Brock RW. 1903. Report on the great landslide at Frank, Alberta, 1903. Dominion of Canada, Department of the Interior, Annual Report **VIII** : 3–17.

McDougall S, Hungr O. 2004. A model for the analysis of rapid landslide motion across three-dimensional terrain. Canadian Geotechnical Journal **41**: 1084–1097. DOI: 10.1139/t04-052

McSaveney MJ. 1978. Sherman glacier rock avalanche, Alaska, USA.

Developments in Geotechnical Engineering **14**: 197–258.

Mercer JH. 1963. Glacial geology of Ohio Range, Central Horlick Mountains, Antarctica. Research Foundation and the Institute of Polar Studies, The Ohio State University; 12 pp.

Mercier D, Cossart E, Decaulne A, Feuillet T, Jónsson HP, Sæmundsson Þ. 2012. The Hofthaholar rock avalanche (sturzstrom): Chronological constraint of paraglacial landsliding on an Icelandic hillslope. The Holocene **23**: 432–446. DOI: 10.1177/0959683612463104

Mercier D, Coquin J, Feuillet T, Decaulne A, Cossart E, Jónsson HP, Sæmundsson Þ. 2017. Are Icelandic rock-slope failures paraglacial? Age evaluation of seventeen rock-slope failures in the Skagafjörður area, based on geomorphological stacking, radiocarbon dating and tephrochronology. Geomorphology **296** : 45–58. DOI: 10.1016/j.geomorph.2017.08.011

Micheletti N, Chandler JH, Lane SN. 2015. Investigating the geomorphological potential of freely available and accessible structure-from-motion photogrammetry using a smartphone. Earth Surface Processes and Landforms **40** : 473–486. DOI: 10.1002/esp.3648

Milan DJ, Heritage GL, Hetherington D. 2007. Application of a 3D laser scanner in the assessment of erosion and deposition volumes and channel change in a proglacial river. Earth Surface Processes and Landforms **32**: 1657–1674. DOI: 10.1002/esp

Milana JP. 2016. Molards and Their Relation to Landslides Involving Permafrost Failure. Permafrost and Periglacial Processes **27**: 271–284. DOI: 10.1002/ppp.1878

Mollard J, Janes J. 1984. Airphoto Interpretation and the Canadian landscape. Energy, Mines, and Resources Canada; 415 pp.

Monnier S, Kinnard C. 2015. Internal Structure and Composition of a Rock Glacier in the Dry Andes, Inferred from Ground-penetrating Radar Data and its Artefacts. Permafrost and Periglacial Processes **26**: 335–346. DOI: 10.1002/ppp.1846

Montgomery DR, Manga M. 2003. Streamflow and Water Well Earthquakes. Science **300** : 2047–2049.

Moss JL. 2000. Using the Global Positioning System to monitor dynamic ground deformation networks on potentially active landslides. International Journal of Applied Earth Observation and Geoinformation **2**: 24–32. DOI: 10.1016/S0303-2434(00)85023-0

Mühll DV, Hauck C, Gubler H. 2002. Mapping of mountain permafrost using geophysical methods. Progress in Physical Geography **26**: 643–660. DOI: 10.1191/0309133302pp356ra

Murton JB. 2001. Thermokarst sediments and sedimentary structures, Tuktoyaktuk Coastlands, western Arctic Canada. Global and Planetary Change **28** : 175–192. DOI: 10.1016/S0921-8181(00)00072-2

Murton JB et al. 2017. Preliminary paleoenvironmental analysis of permafrost deposits at Batagaika megaslump, Yana Uplands, northeast Siberia. Quaternary Research (United States) **87** : 314–330. DOI: 10.1017/qua.2016.15

Nelson F, Anisimov O, Shiklomanov N. 2002. Climate change and hazard zonation in the circum-Arctic permafrost regions. Natural Hazards **26**(3) : 203-225.

Noetzli J, Gruber S, Kohl T, Salzmann N, Haeberli W. 2007. Three-dimensional distribution and evolution of permafrost temperatures in idealized high-mountain topography. Journal of Geophysical Research: Earth Surface **112** : 1–14. DOI: 10.1029/2006JF000545

Norðdahl H, Pétursson HG, 2005. Relative sea-level changes in Iceland: new aspects of the Weichselian deglaciation of Iceland. In Developments in Quaternary Sciences. Elsevier; 25-78.

Palmquist RC, Bible G. 1980. Conceptual modelling of landslide distribution in time and space. Bullettin of the International Association of Engineering Geology **21** : 178– 186.

Pedersen S a S, Larsen LM, Dahl-jensen T, Jepsen HF, Krarup G, Nielsen T, Pedersen AK, Platen-hallermund F Von, Weng W. 2002. Tsunami-generating rock fall and landslide on the south coast of Nuussuaq , central West Greenland. Geology of Greenland Survey Bulletin **191**: 73–83.

Peras A, Decaulne A, Cossart E, Coquin J, Mercier D. 2016. Distribution and spatial analysis of rockslides failures in the Icelandic Westfjords: first results. Géomorphologie : relief, processus, environnement **22**: 25–35. DOI: 10.4000/geomorphologie.11303

Permafrost Subcommittee. 1988. Glossary of permafrost and related ground-ice terms. Associate Committee on Geotechnical Research, National Research Council of Canada, Ottawa; 90 pp.

Petley D. 2012. Global patterns of loss of life from landslides. Geology **40**: 927–930. DOI: 10.1130/G33217.1

Pétursson HG. 1999. Skriðuföll á Siglufirði. Náttúrufræðingurinn **NÍ-99011** : 1-23.

Pétursson HG, Sæmundsson Þ, Jónsson HP, Brynjólfsson S. 2010. Landslides in Iceland, a short review. In Proceedings of the International Workshop on Earthquakes in North Iceland, Húsavík, North Iceland; 44–45.

Pétursson HG, Norðdahl H, Ingólfsson Ó. 2015. Late Weichselian history of relative sea level changes in Iceland during a collapse and subsequent retreat of

marine based ice sheet. Cuadernos de Investigación Geográfica **41**: 261. DOI: 10.18172/cig.2741

Phillips M, Wolter A, Lüthi R, Amann F, Kenner R, Bühler Y. 2017. Rock slope failure in a recently deglaciated permafrost rock wall at Piz Kesch (Eastern Swiss Alps), February 2014. Earth Surface Processes and Landforms **42** : 426–438. DOI: 10.1002/esp.3992

Pogliotti P, Guglielmin M, Cremonese E, Morra Di Cella U, Filippa G, Pellet C, Hauck C. 2015. Warming permafrost and active layer variability at Cime Bianche, Western European Alps. Cryosphere **9**: 647–661. DOI: 10.5194/tc-9-647-2015

Pollard WH. 2005. Thermokarst. Encyclopedia of the Arctic: 2021–2023.

Pollard WH, French HM. 1980. A first approximation of the volume of ground ice, Richards Island, Pleistocene Mackenzie Delta, 33 Northwest Territories, Canada. Canadian Geotechnical Journal **17** : 509–516.

Priesnitz BK, Schunke E. 1983. The Significance of Periglacial Phenomena in Ieeland. Polarforschung **53** : 9–19.

Priesnitz K, Schunke E. 1978. An approach to the ecology of permafrost in Central Iceland. In Third International Conference on Permafrost, Edmonton, Canada. National Research Council of Canada, Ottawa; 474–479.

Pudasaini SP. 2012. A general two-phase debris flow model. Journal of Geophysical Research: Earth Surface **117** : 1–28. DOI: 10.1029/2011JF002186

Pudasaini SP, Krautblatter M. 2014. A two-phase mechanical model for rock-ice avalanches. Journal of Geophysical Research : Earth Surface : 1–19. DOI: 10.1002/2014JF003183.Received

Rapp A. 1964. Recordings of mass wasting in the Scandinavian Mountains. Zeitschrift fur Geomorphologie **5** : 204–205.

Rapp A. 1985. Extreme rainfall and rapid snowmelt as causes of mass

movements in high latitude mountains. In Field and theory: lectures in geocryology , Church M and Slaymaker O (eds). University of British Columbia Press: Vancouver; 36–56.

Rapp A. 1995. Case studies of geoprocesses and environmental changes in mountains of northern Sweden. Geografiska Annaler **77** : 189–198.

Rapp A, Nyberg R. 1981. Alpine Debris Flows in Northern Scandinavia. Geografiska Annaler, Series A: Physical Geography **63** : 183–196.

Ravanel L, Deline P. 2011. Climate influence on rockfalls in high-alpine steep rockwalls: The north side of the aiguilles de chamonix (mont blanc massif) since the end of the "Little Ice Age." Holocene **21**: 357–365. DOI: 10.1177/0959683610374887

Rebetez M, Lugon R, Baeriswyl P. 1997. Climatic change and debris flows in high mountain regions: the case study of the Ritigraben torrent (Swiss Alps). Climatic change **36** : 371–389. DOI: 10.1023/A:1005356130392

Rekacewicz P. 2005. Permafrost distribution in the Arctic. UNEP/GRID-Arendal [online] Available from: http://www.grida.no/resources/7000

Remondino F, Spera MG, Nocerino E, Menna F, Nex F. 2014. State of the art in high density image matching. The Photogrammetric Record **29**: 144–166. DOI: 10.1111/phor.12063

Reuter HI, Hengl T, Gessler P, Soille P. 2009. Preparation of DEMs for geomorpometric analysis. Developments in Soil Science **33**: 87–120. DOI: 10.1016/S0166-2481(08)00004-4.

Rickenmann D. 1999. Empirical relationships for debris flows. Natural Hazards **19** : 47–77. DOI: 10.1023/A:1008064220727

Rickenmann D, Koschni A. 2010. Sediment loads due to fluvial transport and debris flows during the 2005 flood events in Switzerland. Hydrological Processes

24 : 993–1007. DOI: 10.1002/hyp.7536

Rickenmann D, Zimmermann M. 1993. The 1987 debris flows in Switzerland: documentation and analysis. Geomorphology **8** : 175–189.

Roberti G, Friele P, van Wyk de Vries B, Ward B, Clague JJ, Perotti L, Giardino M. 2017a. Rheological evolution of the mount meager 2010 debris avalanche, southwestern british columbia. Geosphere **13**: 1–22. DOI: 10.1130/GES01389.1

Roberti G, Ward B, van Wyk de Vries B, Friele P, Perotti L, Clague JJ, Giardino M. 2017b. Precursory slope distress prior to the 2010 Mount Meager landslide, British Columbia. Landslides **15**: 1–11. DOI: 10.1007/s10346-017-0901-0

Rödder T, Kneisel C. 2012. Influence of snow cover and grain size on the ground thermal regime in the discontinuous permafrost zone, Swiss Alps. Geomorphology **175–176** : 176–189. DOI: 10.1016/j.geomorph.2012.07.008

Rodolfo KS, Umbal JV, Alonso RA, Remotigue CT, Paladio-Melosantos ML, Salvador JH, Evangelista D, Miller Y. 1996. Two years of lahars on the western flank of Mount Pinatubo: Initiation, flow processes, deposits, and attendant geomorphic and hydraulic changes. In Fire and mud: eruptions and lahars of Mount Pinatubo, Philippines. 989–1013.

Roy JW, Hayashi M. 2009. Multiple, distinct groundwater flow systems of a single moraine-talus feature in an alpine watershed. Journal of Hydrology **373** : 139–150. DOI: 10.1016/j.jhydrol.2009.04.018

Sæmundsson K. 1973. Straumrákaðar klappir í kringum Ásbyrgi. Náttúrufræðingurinn **43** : 52–60.

Sæmundsson K. 1974. Evolution of the axial rifting zone in Northern Iceland and the Tjörnes Fracture Zone. Geological Society of America Bulletin **85** : 495–504. DOI: 10.1130/0016-7606(1974)85<495

Sæmundsson K. 1980. Outline of the geology of Iceland. Jökull **29** : 7–28.

Sæmundsson Þ, Pétursson HG. 2000. The Solvadalur debris-slide. Local Authorities Confronting Disasters and Emergencies, Reykjavk, Iceland. Abstract book **26**.

Sæmundsson Þ, Decaulne A. 2007. Meteorological triggering factors and threshold conditions for shallow landslides and debris-flow activity in Iceland. In First North America Landslide Conference; 1475–1484.

Sæmundsson Þ, Pétursson HG, Decaulne A. 2003. Triggering factors for rapid mass movements in Iceland. In Debris-flow hazards mitigation: mechanics, prediction, and assessment, Rickenman D and Chen CI (eds). Mill Press: Rotterdam; 167–178.

Sæmundsson Þ, Sigurðsson IA, Pétursson GH, Jónsson, P. H, Decaulne A, Roberts MJ, Jensen EH. 2011. Bergfóðið sem féll á Morsárjökull 2007 Mar 22. Náttúrufræðingurinn **81**: 131–141.

Sæmundsson Þ, Arnalds O, Kneisel C, Jonsson HP, Decaulne A. 2012. The Orravatnsrustir palsa site in Central Iceland-Palsas in an aeolian sedimentation environment. Geomorphology **167**: 13–20. DOI: 10.1016/j.geomorph.2012.03.014

Sæmundsson Þ, Helgason JK, Pétursson HP. 2013. The debris slide in the Móafellshyrna Mountain on the 20th of September 2012. Was it triggered by intense precipitation and earthquake activity or simply by melting of the permafrost? In International Proceedings of 8th IAG International Conference on Geomorphology.

Sæmundsson Þ, Helgason JK, Petursson H. 2014a. The decline of mountain permafrost and the occurrence of recent large debris slides in Iceland. In European Geosciences Union, General Assembly 2014.

Sæmundsson Þ, Helgason JK, Pétursson HP. 2014b. The melting of mountain

permafrost and the Móafellshyrna debris slide in Northern Iceland. In Proceeding of the 31st Nordic Geological Winter Meeting.

Sæmundsson Þ, Morino C, Helgason JK, Conway SJ, Pétursson HG. 2018. The triggering factors of the Móafellshyrna debris slide in northern Iceland: Intense precipitation, earthquake activity and thawing of mountain permafrost. Science of the Total Environment **621**: 1163–1175. DOI: 10.1016/j.scitotenv.2017.10.111

Salzmann N, Frei C, Vidale PL, Hoelzle M. 2007. The application of Regional Climate Model output for the simulation of high-mountain permafrost scenarios. Global and Planetary Change **56**: 188–202. DOI: 10.1016/j.gloplacha.2006.07.006

Sasaki Y, Fujii A, Asai K. 2000. Soil creep process and its role in debris slide generation-field measurements on the north side of Tsukuba Mountain in Japan. Developments in Geotechnical Engineering **84**: 199–219. DOI: 10.1016/S0165-1250(00)80017-6

Sassa K, Fukuoka H, Wang F, Wang G. 2007. Landslides induced by a combined effect of earthquake and rainfall. In Progress in Landslide Science : 193–207. Springer, Berlin, Heidelberg.

Sattler K, Keiler M, Zischg A, Schrott L. 2011. On the Connection between Debris Flow Activity and Permafrost Degradation: A Case Study from the Schnalstal, South Tyrolean Alps, Italy. Permafrost and Periglacial Processes **22**: 254–265. DOI: 10.1002/ppp.730

Schaffrath KR, Belmont P, Wheaton JM. 2015. Landscape-scale geomorphic change detection: Quantifying spatially variable uncertainty and circumventing legacy data issues. Geomorphology **250**: 334–348. DOI: 10.1016/j.geomorph.2015.09.020

Scheidegger AE. 1973. On the prediction of the reach and velocity of catastrophic landslides. Rock Mechanics and Rock Engineering **5** : 231–236.

Scheidl C, Rickenmann D, Chiari M. 2008. The use of airborne LiDAR data for the analysis of debris flow events in Switzerland. Natural Hazards and Earth System Science **8**: 1113–1127. DOI: 10.5194/nhess-8-1113-2008

Schmidt KM, Montgomery DR. 1995. Limits to relief. Science **270**: 617–621.

Schneider D, Huggel C, Haeberli W, Kaitna R. 2011a. Unraveling driving factors for large rock-ice avalanche mobility. Earth Surface Processes and Landforms **36** : 1948–1966. DOI: 10.1002/esp.2218

Schneider D, Kaitna R, Dietrich WE, Hsu L, Huggel C, McArdell BW. 2011b. Frictional behavior of granular gravel-ice mixtures in vertically rotating drum experiments and implications for rock-ice avalanches. Cold Regions Science and Technology **69**: 70–90. DOI: 10.1016/j.coldregions.2011.07.001

Schoeneich P, Dall'Amico M, Deline P, Zischg A. 2011. Hazards related to permafrost and to permafrost degradation. PermaNET project, state-of-the-art report 6.2

Schomacker A, Kjær KH. 2008. Quantification of dead-ice melting in ice-cored moraines at the high-Arctic glacier Holmströmbreen, Svalbard. Boreas **37**: 211–225. DOI: 10.1111/j.1502-3885.2007.00014.x

Schuster RL. 1996. Socioeconomic significance of landslides. In Landslides: Investigation and Mitigation, Turner AK and Schuster RL (eds). National Academy Press: Washington, DC; 12-35.

Schwab JW, Geertsema M, Evans SG. 2003. Catastrophic rock avalanches, west-central BC, Canada. In 3rd Canadian conference on geotechnique and natural hazards, Edmonton, AB; 252–259.

Schwamborn G, Heinzel J, Schirrmeister L. 2008. Internal characteristics of

ice-marginal sediments deduced from georadar profiling and sediment properties (Brøgger Peninsula, Svalbard). Geomorphology **95**: 74–83. DOI: 10.1016/j.geomorph.2006.07.032

Scott KM, Macias JL, Vallance JW, Naranjo JA, Rodriguez-Elizarraras SR, McGeehin JP. 2002. Catastrophic debris flows transformed from landslides in volcanic terrains: mobility, hazard assessment and mitigation strategies. U.S. Geological Survey Professional Paper **1630** : 59 pp.

Segal RA, Lantz TC, Kokelj S V. 2016. Acceleration of thaw slump activity in glaciated landscapes of the Western Canadian Arctic. Environmental Research Letters **11**(3): p.034025. DOI: 10.1088/1748-9326/11/3/034025

Séjourné A, Costard F, Fedorov A, Gargani J, Skorve J, Massé M, Mège D. 2015. Evolution of the banks of thermokarst lakes in Central Yakutia (Central Siberia) due to retrogressive thaw slump activity controlled by insolation. Geomorphology **241**: 31–40. DOI: 10.1016/j.geomorph.2015.03.033

Selby MJ. 1993. Hillslope Materials and Processes. 2nd editio. Oxford University Press, U.S.A.; 480 pp.

Shea T, van Wyk de Vries B. 2008. Structural analysis and analogue modeling of the kinematics and dynamics of rockslide avalanches. Geosphere **4**: 657-686. DOI: 10.1130/GES00131.1

Shreve RL. 1966. Sherman Landslide, Alaska. Science **154**: 1639–1643.

Shreve RL. 1968. The Blackhawk Landslide. The Geological Society of America, Inc.: Boulder, Colorado; 47 pp.

Siart C, Bubenzer O, Eitel B. 2009. Combining digital elevation data (SRTM/ASTER), high resolution satellite imagery (Quickbird) and GIS for geomorphological mapping: A multi-component case study on Mediterranean karst in Central Crete. Geomorphology **112**: 106–121. DOI:

10.1016/j.geomorph.2009.05.010

Sidle RC, Ochiai H. 2006. Landslides: Processes, Prediction, and Land Use. . Water Reso. American Geophysical Union: Washington, DC; 312 pp.

Sidle RC, Swanston DN. 1982. Analysis of a small debris slide in coastal Alaska. Canadian Geotechnical Journal **19**: 167–174.

Sigfússon AÞ, Thoroddsen Á, Aðalsteinsdóttir ÁK, Vignisdóttir E, Gunnarsdóttir H, Gíslason. S, Snorrason SP, Leiffsson ÞS, Guðmundsdóttir Þ. 2016. Hvalárvirkjun í Ófeigsfirði Matsskýrsla . Reykjavík, Iceland.

Sigurðsson O, Williams RSJ. 1991. Rockslides on the Terminus of "Jökulsárgilsjökull ", Southern Iceland. Geografiska Annaler: Series A, Physical Geography **73** : 129–140.

Smith JS, Chandler J, Rose J. 2009. High spatial resolution data acquisition for the geosciences: kite aerial photography. Earth Surface Processes and Landforms **34** : 155–161. DOI: 10.1002/esp

Smith MW, Carrivick JL, Quincey DJ. 2015. Structure from motion photogrammetry in physical geography. Progress in Physical Geography **40**: 247–275. DOI: 10.1177/0309133315615805

Smith MW, Riseborough DW. 1996. Permafrost monitoring and detection of climate change. Permafrost and Periglacial Processes **7**: 301–309. DOI: 10.1002/(SICI)1099-1530(199610)7:4<301::AID-PPP231>3.0.CO;2-R

Snavely N, Seitz SM, Szeliski R. 2008. Modeling the world from Internet photo collections. International Journal of Computer Vision **80** : 189–210. DOI: 10.1007/s11263-007-0107-3

Sofia G, Pirotti F, Tarolli P. 2013. Variations in multiscale curvature distribution and signatures of LiDAR DTM errors. Earth Surface Processes and Landforms **38** : 1116–1134. DOI: 10.1002/esp.3363

Sosio R. 2015. Rock-Snow-Ice Avalanches. In Landslide Hazards, Risks, and Disasters , Davies T (ed). Academic Press; 191-240.

Sosio R, Crosta GB, Chen JH, Hungr O. 2012. Modelling rock avalanche propagation onto glaciers. Quaternary Science Reviews **47**: 23–40. DOI: 10.1016/j.quascirev.2012.05.010

Sosio R, Crosta GB, Hungr O. 2008. Complete dynamic modeling calibration for the Thurwieser rock avalanche (Italian Central Alps). Engineering Geology **100** : 11–26. DOI: 10.1016/j.enggeo.2008.02.012

Spagnolo M, Clark CD. 2009. A geomorphological overview of glacial landforms on the Icelandic continental shelf. Journal of Maps **5** : 37–52. DOI: 10.4113/jom.2009.1049

Stoffel M, Huggel C. 2012a. Effects of climate change on mass movements in mountain environments. Progress in Physical Geography **36** : 421–439.

Stoffel M, Huggel C. 2012b. Effects of climate change on mass movements in mountain environments. Progress in Physical Geography **36**: 421–439. DOI: 10.1177/0309133312441010

Stoffel M, Mendlik T, Schneuwly-Bollschweiler M, Gobiet A. 2014. Possible impacts of climate change on debris-flow activity in the Swiss Alps. Climatic Change **122** : 141–155. DOI: 10.1007/s10584-013-0993-z

Stötter J. 1991. Geomorphologische und landschaftsgeschichtliche,Untersuchungen im Svarfaöardalur-Skiöadalur, Tröllaskagi, N-Island. Münchener Geographische Abhandlungen **9**; 1-166

Stötter J, Wastl M, Caseldine C, Häberle T. 1999. Holocene palaeoclimatic reconstruction in northern Iceland: Approaches and results. Quaternary Science Reviews **18** : 457–474. DOI: 10.1016/S0277-3791(98)00029-8

Strom A, Korup O. 2006. Extremely large rockslides and rock avalanches in

the Tien Shan Mountains, Kyrgyzstan. Landslides **3**: 125–136. DOI: 10.1007/s10346-005-0027-7

Tatard L, Grasso JR, Helmstetter A, Garambois S. 2010. Characterization and comparison of landslide triggering in different tectonic and climatic settings. Journal of Geophysical Research: Earth Surface **115**: 1–18. DOI: 10.1029/2009JF001624

Van Tatenhove FGM, Olesen OB. 1994. Ground temperature and related permafrost characteristics in west Greenland. Permafrost and Periglacial Processes **5** : 199–215.

Terzaghi K, Peck R, Mesri G. 1996. Soil mechanics in engineering practice. John Wiley & Sons.; 729 pp.

Theule JI, Liébault F, Laigle D, Loye A, Jaboyedoff M. 2015. Channel scour and fill by debris flows and bedload transport. Geomorphology **243**: 92–105. DOI: 10.1016/j.geomorph.2015.05.003

Theule JI, Liébault F, Loye A, Laigle D, Jaboyedoff M. 2012. Sediment budget monitoring of debris-flow and bedload transport in the Manival Torrent, SE France. Natural Hazards and Earth System Science **1** : 731–749. DOI: 10.5194/nhess-12-731-2012

Thomas HR, Cleall P, Li Y-C, Harris C, Kern-Luetschg M. 2009. Modelling of cryogenic processes in permafrost and seasonally frozen soils. Géotechnique **59** : 173–184. DOI: 10.1680/geot.2009.59.3.173

Thorarinsson S. 1937. Das Dalvik-Beben in Nord-island, 2. juni 1934. Geografiska Annaler **19** : 232–277.

Thorarinsson S. 1951. Notes on patterned ground in Iceland. Geografiska Annaler **33** : 144–156.

Thorarinsson S, Einarsson T, Kjartansson G. 1959. On the geology and

geomorphology of Iceland. Geografiska Annaler **41** : 135–169.

Thordarson T, Hoskuldsson A. 2002. Iceland. Classic Geology in Europe 3 . Terra Publishing: Harpenden, UK; 200 pp.

Tost M, Cronin SJ, Procter JN. 2014.Transport and emplacement mechanisms of channelised long-runout debris avalanches, Ruapehu volcano, New Zealand. Bulletin of Volcanology **76**:1–14. DOI: 10.1007/s00445-014-0881-z

Toyos G, Gunasekera R, Zanchetta G, Oppenheimer C, Sulpizio R, Favalli M, Pareschi MT. 2008. GIS-assisted modelling for debris flow hazard assessment based on the events of May 1998 in the area of Sarno, Southern Italy: II. Velocity and dynamic pressure. Earth Surface Processes and Landforms **33** : 1693–1708. DOI: 10.1002/esp.1640

Tryggvason K, Husebye ES, Stefansson R. 1983. Seismic image of the hypothesized Icelandic hot spot. Tectonophysic **100** : 97–118.

Tveito OE, Førland E, Heino R, Hanssen-Bauer I, Alexandersson H, Dahlström BA, Drebs, Kern-Hansen. C., Jónsson T, Vaarby Laursen E, Westman Y. 2000. Nordic temperature maps.. Oslo, Report 4 09/00.

Vallance JW, Scott KM. 1997. The Osceola Mudflow from Mount Rainier: Sedimentology and hazard implications of a huge clay-rich debris flow. Bulletin of the Geological Society of America **109**: 143–163. DOI: 10.1130/0016-7606(1997)109<0143:TOMFMR>2.3.CO;2

Valsson T, Sigurbjornsson R. 1996. Natturuva a Islandi. Arkitektur, Vertaekni and Skipulag **17** : 15–40.

Varnes DJ. 1978. Slope Movement Types and Processes. Transportation Research Board Special Report : 11–33. DOI: In Special report 176: Landslides: Analysis and Control, Transportation Research Board, Washington, D.C.

Varnes DJ. 1984. Landslide hazard zonation: a rewiew od principles and

practise. Natural Hazard Series **3**: 63 pp. DOI: 10.1007/BF02594720

Van Vliet-Lanoë B, Bourgeois O, Dauteuil O. 1998. Thufur formation in Northern Iceland and its relation to holocene climate change. Permafrost and Periglacial Processes **9**: 347–365. DOI: 10.1002/(SICI)1099-1530(199810/12)9:4<347::AID-PPP299>3.0.CO;2-4

Voight B, Sousa J. 1994. Lessons from Ontake-san: A comparative analysis of debris avalanche dynamics. Engineering Geology **38**: 261–297. DOI: 10.1016/0013-7952(94)90042-6

Walter M, Joswig M. 2008. Seismic monitoring of fracture processes from a creeping landslide in the Vorarlberg Alps. Geophysical Research Abstracts Vol.10.

Wangensteen B, Gudmundsson Á, Eiken T, Kääb A, Farbrot H, Etzelmüller B. 2006. Surface displacements and surface age estimates for creeping slope landforms in Northern and Eastern Iceland using digital photogrammetry. Geomorphology **80** : 59–79. DOI: 10.1016/j.geomorph.2006.01.034

Washburn AL. 1979a. Geocryology: A Survey of Periglacial Processes and Environments. Edward Arnold, London.

Wegmann M, Gudmundsson GH, Haeberli W. 1998. Permafrost changes in rock walls and the retreat of alpine glaciers: a thermal modelling approach. Permafrost and Periglacial Processes **9**: 23–33. DOI: 10.1002/(SICI)1099-1530(199801/03)9:1<23::AID-PPP274>3.0.CO;2-Y

Wells WG. 1981. Some effects of brushfires or erosion processes in coastal southern California. In Erosion and sediment transport in Pacific-rim steeplands, Proceedings to the Christchurch symposium, vol. 132, In International Association of Hydrological Sciences: Christchurch, New Zealand; 305–342.

Wells WG. 1987. The effects of fire on the generation of debris flows in

southern California. Reviews in Engineering Geology **7** : 105–114.

Westoby MJ, Brasington J, Glasser NF, Hambrey MJ, Reynolds JM. 2012. “Structure-from-Motion” photogrammetry: A low-cost, effective tool for geoscience applications. Geomorphology **179**: 300–314. DOI: 10.1016/j.geomorph.2012.08.021

Whalley BW, Palmer CF, Hamilton SJ, Martin HE. 1995a. An assessment of rock glacier sliding using seventeen years of velocirty data: Nautardalur Rock Glacier, North Iceland. Arctic and Alpine Research **27** : 345–351.

Whalley W, Douglas G, Jonsson A. 1983. The magnitude and frequency of large rockslides in Iceland in the postglacial. Geografiska Annaler. Series A, Physical Geography **65** : 99–110. DOI: 10.2307/520724

Whalley WB, Hamilton SJ, Palmer CF, Gordon JE, Martin HE. 1995b. The dynamics of rock glaciers: data from Tröllaskagi , North Iceland. In Steepland Geomorphology , Slaymaker O (ed). John Wiley & Sons, Ltd; 129–145.

Whalley WB, Martin HE. 1994. Rock glaciers in Trollaskagi: their origin and climatic significance. Münchener Geographische Arbeiten **12** : 289–308.

Wheaton JM, Brasington J, Darby SE, Sear DA. 2010. Accounting for uncertainty in DEMs from repeat topographic surveys: Improved sediment budgets. Earth Surface Processes and Landforms **35**: 136–156. DOI: 10.1002/esp.1886

Wieczorek GF, Glade T. 2005. Climatic factors influencing occurrence of debris flows. In Debris-flow hazards and related phenomena , Jakob M and Hungr O (eds). Springer: Chichester; 325–362.

Wirz V, Beutel J, Buchli B, Gruber S, Limpach P. 2013. Temporal Characteristics of Different Cryosphere- Related Slope Movements in High Mountains. In Landslide Science and Practice. Springer, Berlin, Heidelberg; 329-

333.

Wirz V, Geertsema M, Gruber S, Purves RS. 2016. Temporal variability of diverse mountain permafrost slope movements derived from multi-year daily GPS data, Mattertal, Switzerland. Landslides **13**: 67–83. DOI: 10.1007/s10346-014-0544-3

Wolfe CJ, Bjarnason IT, VanDecar JC, Solomon SC. 1997. Seismic structure of the iceland mantle plume. Nature **385** : 245–247. DOI: 10.1038/385245a0

Wright J, Conway SJ, Rothery DA, Balme MR. 2018. Post-Deposition (and Ongoing?) Modification of Caloris Ejecta Blocks. In Mercury: Current and Future Science of the Innermost Planet, Abstract 6071.

Xu Q, Shang Y, van Asch T, Wang S, Zhang Z, Dong X. 2012. Observations from the large, rapid Yigong rock slide – debris avalanche, southeast Tibet. Canadian Geotechnical Journal **49** : 589–606. DOI: 10.1139/t2012-021

Yin Y, Wang F, Sun P. 2009. Landslide hazards triggered by the 2008 Wenchuan earthquake, Sichuan, China. Landslides **6**: 139–151. DOI: 10.1007/s10346-009-0148-5

Yoshida H. 2014. Hummock alignment in Japanese volcanic debris avalanches controlled by pre-avalanche slope of depositional area. Geomorphology **223**: 67–80. DOI: 10.1016/j.geomorph.2014.06.024

Yoshida H, Sugai T, Ohmori H. 2012. Size-distance relationships for hummocks on volcanic rockslide-debris avalanche deposits in Japan. Geomorphology **136**: 76–87. DOI: 10.1016/j.geomorph.2011.04.044

Yoshikawa K, Hinzman LD. 2003. Shrinking thermokarst ponds and groundwater dynamics in discontinuous permafrost near Council, Alaska. Permafrost and Periglacial Processes **14** : 151–160. DOI: 10.1002/ppp.451

Zhang T, Nelson FE, Gruber S. 2007. Introduction to special section:

Permafrost and seasonally Frozen Ground Under a Changing Climate. Journal of Geophysical Research: Earth Surface **112** : 1–2. DOI: 10.1029/2007JF000821

Zhang Z. 1994. Iterative point matching for registration of free-form curves and surfaces. International Journal of Computer Vision **13**: 119–152. DOI: 10.1007/BF01427149

Zimmermann M. 1990. Debris flows 1987 in Switzerland : geomorphological and meteorological aspects. Hydrology in Mountainous Regions. II - Artificial Reservoirs; Water and Slopes **1**: 387–394.

Zimmermann M, Haeberli W. 1992. Climatic change and debris flow activity in high-mountain areas - a case study in the Swiss Alps. Catena **22** : 59–72.

Þorarinsson S. 1956. Séð frá Þjóðvegi. Náttúrufræðingurinn **24** : 7–15.

Appendix 1

Ground Penetrating Radar results

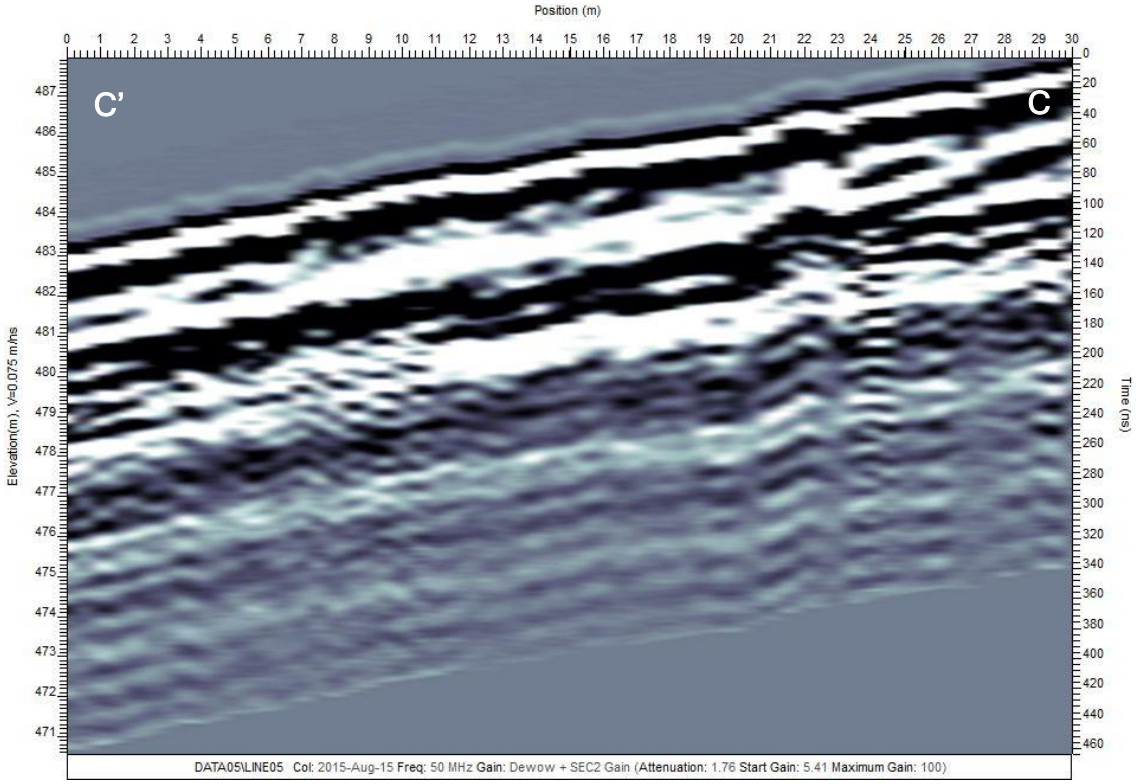

Figure A. 4. Results of GPR measurements at profile GPR L3.

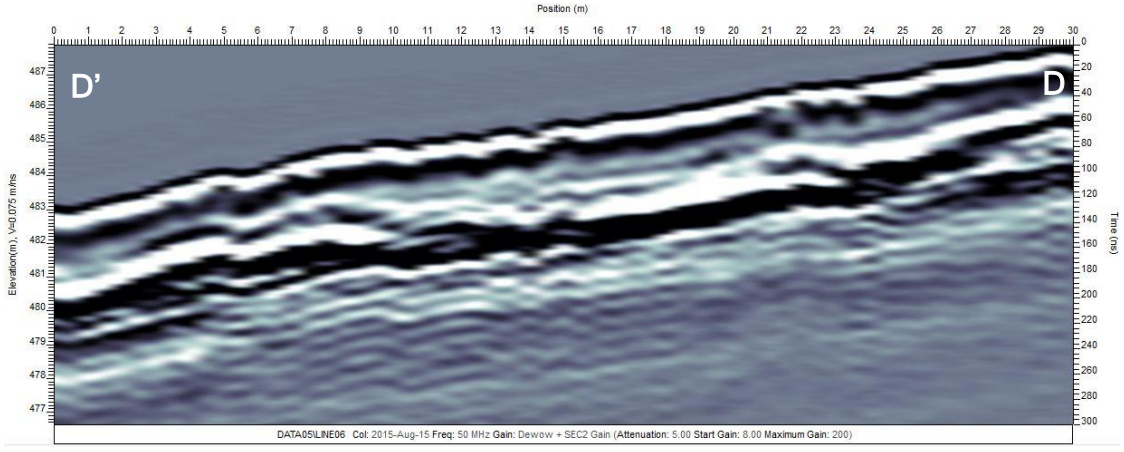

Figure A. 5. Results of GPR measurements at profile GPR L4.

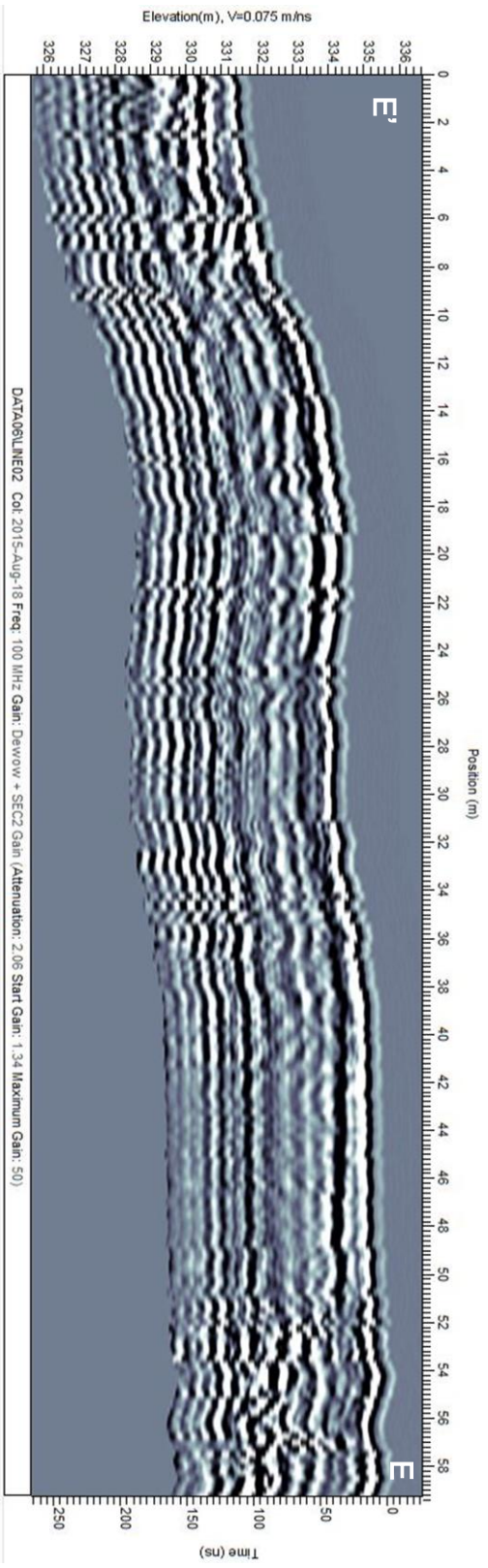

Figure A. 6. Results of GPR measurements at profile GPR L7.

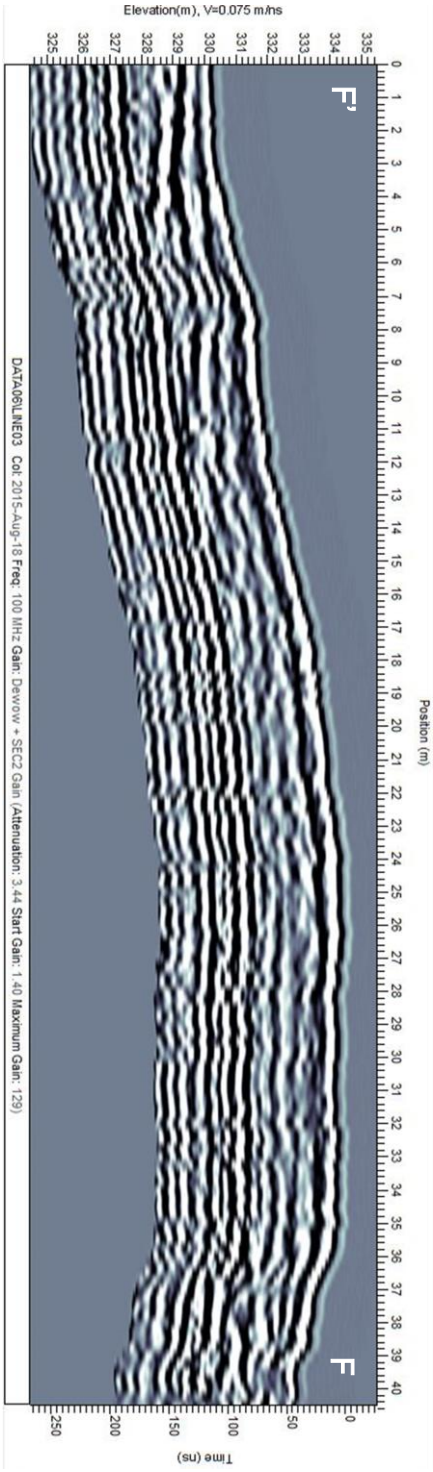

Figure A. 7. Results of GPR measurements at profile GPR L8.

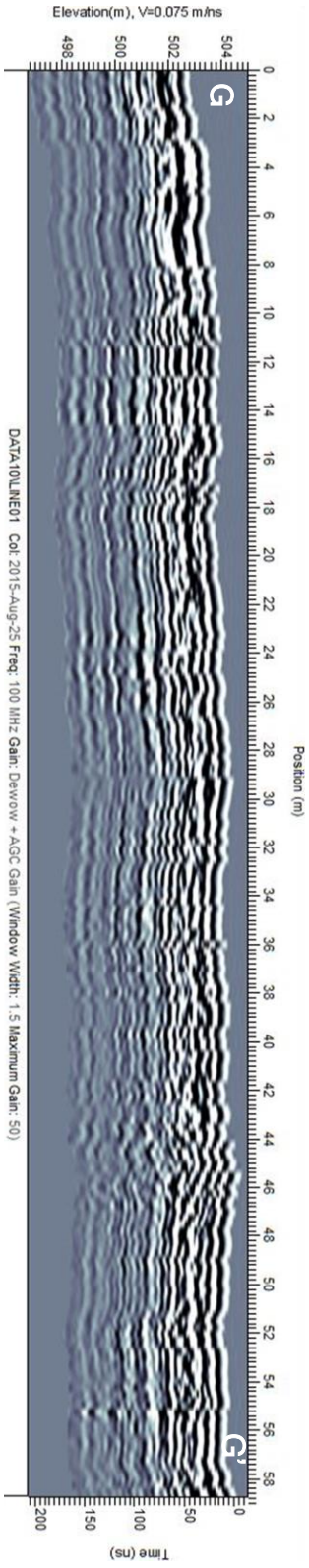

Figure A. 8. Results of GPR measurements at profile GPR L9.

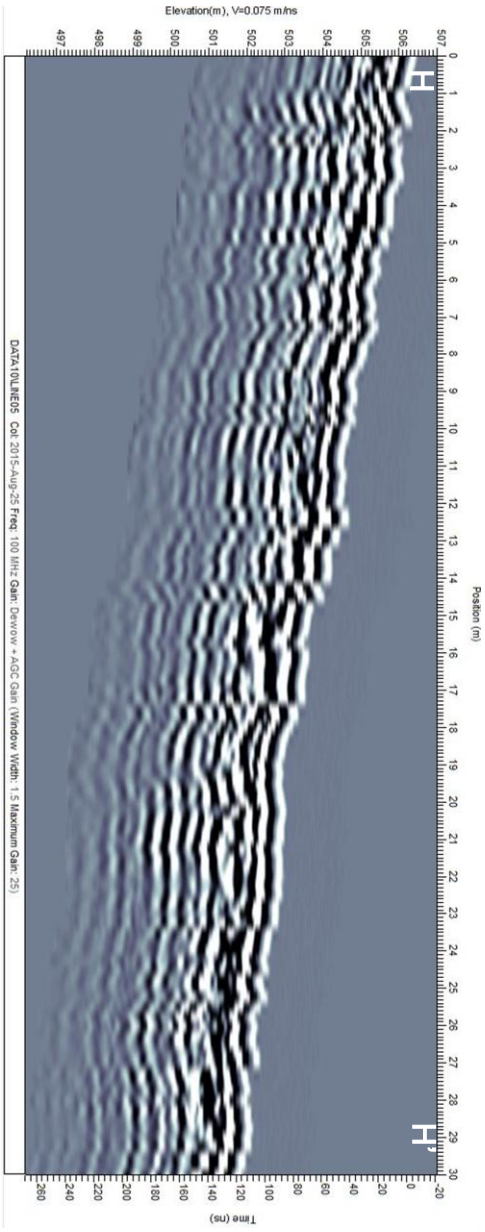

Figure A. 9. Results of GPR measurements at profile GPR L10.

Figure A. 10. Results of GPR measurements at profile GPR L11.